

## N O T I C E

THIS DOCUMENT HAS BEEN REPRODUCED FROM  
MICROFICHE. ALTHOUGH IT IS RECOGNIZED THAT  
CERTAIN PORTIONS ARE ILLEGIBLE, IT IS BEING RELEASED  
IN THE INTEREST OF MAKING AVAILABLE AS MUCH  
INFORMATION AS POSSIBLE

NASA Contractor Report 159698

(NASA-CR-159698) STUDIES OF THE ACOUSTIC  
TRANSMISSION CHARACTERISTICS OF COAXIAL  
NOZZLES WITH INVERTED VELOCITY PROFILES,  
VOLUME 1 Final Report (Lockheed-Georgia  
Co., Marietta.) 186 p HC A09/MF A01

N80-11870

Unclass

G3/71 46003

VOLUME I

STUDIES OF THE ACOUSTIC TRANSMISSION  
CHARACTERISTICS OF COAXIAL NOZZLES  
WITH INVERTED VELOCITY PROFILES

P. D. Dean, M. Salikuddin, K. K. Ahuja,  
H. E. Plumblee, and P. Mungur

LOCKHEED-GEORGIA COMPANY  
Marietta, GA 30063

CONTRACT NAS3-20797  
MAY 1979

**NASA**

National  
Aeronautics and  
Space  
Administration

Lewis Research Center  
Cleveland, Ohio 44135



NASA Contractor Report 159698

VOLUME I

STUDIES OF THE ACOUSTIC TRANSMISSION  
CHARACTERISTICS OF COAXIAL NOZZLES  
WITH INVERTED VELOCITY PROFILES

P. D. Dean, M. Salikuddin, K. K. Ahuja,  
H. E. Plumblee, and P. Mungur

LOCKHEED-GEORGIA COMPANY  
Marietta, GA 30063

CONTRACT NAS3-20797  
MAY 1979

**NASA**

National  
Aeronautics and  
Space  
Administration

Lewis Research Center  
Cleveland, Ohio 44135

## FOREWORD

This report was prepared by the Lockheed-Georgia Company, Marietta, Georgia, for the NASA-Lewis Research Center, Cleveland, Ohio, under Contract NAS3-20797.

Dr. Allen Karchmer was the Project Manager for the NASA-Lewis Research Center. Lockheed's Program Manager was Dr. Harry E. Plumblee, Jr.

The authors would like to express their sincere acknowledgements to Mr. Robert H. Burrin for his help in both designing the test rig and conducting the experiments.

# CONTENTS

	Page
SUMMARY . . . . .	1
1. INTRODUCTION . . . . .	3
2. PROGRAM OUTLINE AND PRELIMINARY INVESTIGATION . . . . .	5
2.1 Program Requirements . . . . .	5
2.2 Preliminary Investigation . . . . .	7
2.2.1 Measurement Considerations . . . . .	8
2.2.2 Source Type . . . . .	9
2.2.2.1 Broadband Excitation . . . . .	9
2.2.2.2 Discrete Tone Excitation . . . . .	10
2.2.2.3 Impulsive Excitation . . . . .	12
2.2.2.4 Summary of Source Types . . . . .	20
2.2.3 Internal Source Measurement Configurations . . . . .	20
2.2.4 Data Analysis . . . . .	23
2.3 Validation of Acoustic Impulse Technique . . . . .	27
2.3.1 Impedances and Absorption Coefficients of Absorbing Material . . . . .	27
2.3.2 Reflection Coefficients and Radiation Impedances of an Open Duct . . . . .	27
2.3.3 Far-Field Directivity . . . . .	31
2.4 Applications: Acoustic Properties of Conical Nozzles . . . . .	36
2.4.1 Effect of Nozzle Geometry . . . . .	36
2.4.2 Theory vs. Measurements . . . . .	38
2.4.2.1 Directivity . . . . .	42
2.4.2.2 Radiated Acoustic Power . . . . .	42
2.4.3 Effect of Flow . . . . .	42
2.5 Conclusions from Preliminary Investigation . . . . .	49
3. TEST CONFIGURATIONS AND PROCEDURE . . . . .	53
3.1 Facility Description . . . . .	53
3.1.1 Nozzle Description . . . . .	53
3.1.2 Source Section . . . . .	54
3.1.3 Spark Circuit . . . . .	62
3.2 Test Plan . . . . .	62
3.3 Data Acquisition and Analysis . . . . .	67
3.3.1 Facility Instrumentation . . . . .	67
3.3.2 Transient Capture and Editing . . . . .	69
3.3.3 Calibrations of Far-Field Microphones with Respect to the In-Duct Transducer . . . . .	70
3.3.4 Transformation and Smoothing . . . . .	70
3.3.5 Data Normalization . . . . .	73

	Page
4. TEST RESULTS . . . . .	79
4.1 Source in Core Flow . . . . .	80
4.1.1 Mach Number Effects . . . . .	80
4.1.2 Effect of L/h Ratio . . . . .	87
4.1.3 Summary . . . . .	87
4.2 Source in Fan . . . . .	91
4.2.1 Mach Number Effects . . . . .	91
4.2.1.1 Twenty-Degree Convergence Angle . . . . .	91
4.2.1.2 Forty-Degree Convergence Angle . . . . .	96
4.2.1.3 Summary . . . . .	102
4.2.2 Effect of L/h Ratio . . . . .	105
4.2.2.1 Twenty-Degree Convergence Angle . . . . .	105
4.2.2.2 Forty-Degree Convergence Angle . . . . .	111
4.2.2.3 Summary . . . . .	111
4.2.3 Convergence Angle Effects . . . . .	116
4.2.3.1 Summary . . . . .	119
4.3 Comparison of Sources in Core and Fan . . . . .	119
4.3.1 Summary . . . . .	133
4.4 Effects of Heating in Core and Fan . . . . .	133
4.4.1 Fan Temperature 750K . . . . .	134
4.4.2 Fan Temperature 900K . . . . .	138
4.4.3 Constant Temperature Ratio Comparisons . . . . .	138
4.4.4 Summary . . . . .	142
4.5 Conclusions . . . . .	145
APPENDIX A. RADIATION IMPEDANCE OF CONICAL NOZZLES WITH MEAN FLOW .	147
APPENDIX B. ACOUSTIC TRANSMISSION ACROSS A SYSTEM OF PLANE PARALLEL MULTILAYER FLOW FIELDS . . . . .	153
APPENDIX C. ANALYTICAL STUDIES OF THE ACOUSTIC PROPERTIES OF CONVERGING CONICAL NOZZLES IN THE ABSENCE OF MEAN FLOW .	169
APPENDIX D. SYMBOL LIST . . . . .	183
REFERENCES . . . . .	185

## SUMMARY

The work described in this report represents a first step in understanding and evaluating how internal noise within a jet engine radiates through a coannular exhaust nozzle with an inverted velocity profile.

The objective of this program was to conduct a series of tests to determine the efficiency of internal noise radiation using a model coannular jet system.

The approach used to achieve this objective was influenced by a lack of published experimental data. A preliminary investigation was undertaken (1) to define the test parameters which influence the internal noise radiation, (2) to develop a test methodology which could realistically be used to examine the effects of the test parameters, and (3) to validate this methodology. The result was the choice of an acoustic impulse as the internal noise source in the jet nozzles.

A coaxial test rig and coannular nozzle system was designed subsequently and a series of tests performed to determine the noise transmission characteristics of selected realistic nozzle configurations with practical inverted profile flow conditions. The parameters considered include: (a) those of geometry, viz. convergence angle of fan nozzle and core extension length to fan annulus height ratio and (b) those of flow, viz. jet nozzle Mach number (subsonic and supersonic) and temperature.

The results of the tests are presented as normalized directivity plots and reveal complex parametric interrelationships with few well-defined trends. These trends, where noted, are discussed as fully as possible, supported both by physical and analytical arguments.

## 1. INTRODUCTION

Turbofan engines currently are and will continue to be the primary propulsion system for commercial transport aircraft for the foreseeable future. There is no doubt that the general public at large considers these engines to be noisy, with the net result being the imposition of FAA Part 36 noise limitations as a certification requirement. As a consequence, both government agencies and industries have expended considerable resources in the search for both the origins and the control of turbofan engine noise.

The primary sources of this noise are the fan and exhaust jet. Suppression techniques for these sources have resulted in notable noise reductions. However, the predicted model scale or measured static noise reductions have not in fact been fully realized when tested in full-scale flight situations. In some cases these discrepancies can be traced to a noise floor dominated by radiation from within the core engine (see refs. 1.1, 1.2). Indeed, internal or core noise is possibly the dominant limitation in noise reduction efforts on the turbojet engines of current supersonic transport aircraft.

A new concept of interest for reducing the noise of engines with coannular jet exhaust streams is the inverted coannular jet velocity profile. Model-scale tests of this concept indicate jet exhaust noise reductions of the order of 6-8 EPNdB. However, before full-scale flight testing of new engines designed to produce such profiles is undertaken, all aspects of engine noise must be understood, including core noise generation, core noise radiation, and flight effects on fan/jet noise generation and radiation.

Since no experiments have been conducted to determine the efficiency of internal noise radiation for inverted velocity profile configurations, such tests are viewed as an essential first step in examining and understanding the total noise characteristics of this new, potentially quieter, engine/exhaust concept. The objective of this program was to conduct a series of such tests using a model coannular jet system with inverted velocity profiles and determine its noise transmission characteristics from a well-defined internal noise source.

To achieve this objective, it was necessary to first establish a satisfactory definition of the parameter(s) used to express the acoustic transmission characteristics of the nozzle system. Following this, the practical problems of establishing a test methodology for measuring the parameter(s) defined above had to be understood and resolved. This included not only the evaluation of alternate experimental approaches, but also the validation of the technique ultimately selected. Finally, following the successful completion of developing and validating a test methodology, a coaxial test rig and coannular nozzles were designed and fabricated and a series of tests were conducted and the resulting nozzle acoustic transmission data was reduced and evaluated.

This work is described in the following sections. Section 2 describes the detailed objectives and requirements of the test program. It then



describes a preliminary investigation which had the objective of developing experimental techniques and configurations. Section 3 contains a description of facilities used for the production testing and the data reduction and analysis procedures developed. Section 4 presents the test results with a discussion of the parametric trends observed in the test data.

## 2. PROGRAM OUTLINE AND PRELIMINARY INVESTIGATION

### 2.1 PROGRAM REQUIREMENTS

The overall objective of this program, as stated in the introduction, was to conduct a series of experiments using a coaxial nozzle system, operating with an inverted velocity profile, to determine the acoustic efficiency (or transmission coefficient) for internal noise radiation to outside ambient conditions. In order to fully appreciate the implications of this objective, more specific details of the program requirements are necessary:

(1) The nozzle system was to be modeled after typical Supersonic Cruise Aircraft Research (SCAR) study engine configurations. The nozzles were to be coaxial with a conical convergence angle. The primary nozzle exit was to be extended beyond the secondary nozzle exit by a distance,  $L$ , equal to 1, 3 and 5 times the secondary nozzle annulus width,  $h$ , (see fig. 2.1). In addition, based on test frequency considerations, appropriate size constraints were imposed. The primary nozzle diameter was selected to be 7.5 cm. As a result of the desire to retain a configuration similar to SCAR study engines, the radius ratio  $r_1/r_2$  was constrained to a value of 0.75. Based on the above and the primary nozzle convergence angle of  $15^\circ$ , the other relevant nozzle geometric parameters are tabulated as part of fig. 2.1.

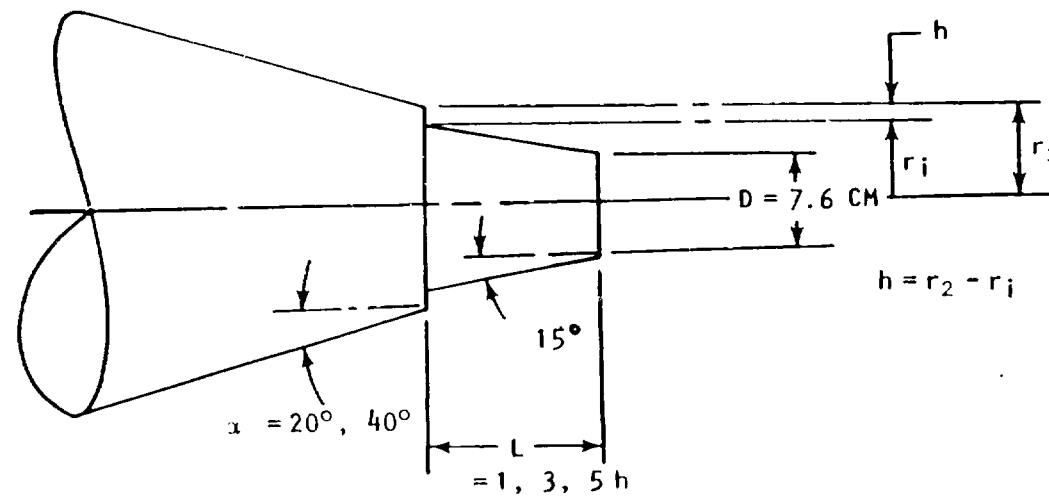
(2) The coaxial nozzle operating conditions, which determine to some extent the problems to be encountered are:

Outer Stream Mach No.	$0.6 \leq M_{J2} \leq 1.5$
Inner Stream Mach No.	$0.4 \leq M_{J1} \leq 1.2$
Mach No. Ratio	$M_{J2}/M_{J1} > 1.0$
Stagnation Temperature Ratio	$1.0 \leq T_2/T_1 \leq 3.0$

These parameters were to be varied according to a prespecified test plan in an attempt to isolate some of the dominant operating variables such as the ratio of secondary-to-primary velocity and temperature on the acoustic transmission characteristics of the coaxial nozzle system.

(3) The test results were required over a broad frequency range. The parameter  $kh$  was thought to be a dominant frequency parameter for the annulus. It was originally desired by NASA to determine the transmission characteristics of the nozzle system from  $0.63 \leq kh \leq 25$ . The upper limit of this frequency requirement corresponded to a frequency of 100 KHz based on the geometric data given in figure 2.1.

(4) It was required to produce the acoustic transmission characteristics, but:



$L/h$	$h \text{ (cm)}$	$L \text{ (cm)}$	$r_i \text{ (cm)}$	$r_2$	Annulus Area $A_2 \text{ (cm}^2\text{)}$	Area Ratio** $A_2/A_1$
1	1.37	1.37	4.12	5.49	41.45	0.91
3	1.71	5.12	5.12	6.83	64.14	1.41
5	2.26	11.30	6.78	9.04	112.21	2.46

\* $A_1 = \text{Primary Exit Area} = 45.60 \text{ cm}^2$ .

Figure 2.1 Relevant geometric parameters for coaxial nozzle system.

- (a) a definition of acoustic transmission coefficient for the nozzle system was unspecified;
- (b) a method for determining the internal and radiated sound fields in the presence of contaminating noise fields was unspecified;
- (c) the method for analyzing the data to be acquired was unspecified; and
- (d) a method for dealing with the duct modal structure in the internal noise measurement and data analysis was not available.

Based on the above, there were several problems that had to be resolved before tests could be conducted on the coaxial nozzle system. These problems could be broadly classified as listed below:

- (1) Acoustic Nozzle Transmission Coefficient (NTC): A definition of NTC was required. Based on previously published results, the NTC could assume one of several definitions, with the source specification being a governing factor in the ultimate selection.
- (2) Test Method: There were also several methods for measuring NTC, with the approach being linked to the NTC definition.
- (3) Data Analysis: The data analysis method is also interrelated to the above two problems, but must also be capable of rejecting extraneous noise both from inside the nozzle duct system and from externally generated jet noise.

In order to develop a test method that would satisfactorily deal with the above problems and still permit achievement of the test goals, it was found necessary to conduct a preliminary investigation. This investigation, discussed in the following subsections, deals with all the above problems.

## 2.2 PRELIMINARY INVESTIGATION

The major problems listed at the end of section 2.1 led to a series of studies in the preliminary investigation. First, it was necessary, based on data measurement considerations, to define the most logical measure of nozzle transmission coefficient (NTC). Following this, in line with the NTC definition, the source type and test technique had to be developed. Then, based on these considerations and constraints, the measurement procedures had to be established. Finally, the data analysis techniques necessary for determination of NTC had to be specified and developed, where required.

### 2.2.1 Measurement Considerations

In ultimately choosing the measurement technique for defining the source characteristics, it is necessary to decide what level of complexity is required. It is always necessary to specify a source distribution in duct acoustics studies. Earlier work in computing sound propagation through unlined and lined ducts and sound radiation from nozzles or inlets relied on the assumption of a plane mode pressure distribution from the source. Later analyses, based on experimental observation, indicated that perhaps this should be modified to assume that all the energy was contained in the least attenuated mode (a most conservative assumption) or else that equal energy should be assigned to all propagating modes.

Whatever the decision on source specification for analytical studies, it seems that the following possibilities exist for practical measurement of source characteristics: (1) mean square sound pressure distribution in the duct, (2) incident sound power in the duct, (3) equivalent acoustic source distribution, based on analytical modeling, and (4) far-field measurement for inference of source characteristics.

Based on measurement complexity, (4) above is probably simplest with item (3) being most complex. However, from the standpoint of providing most information, item (2) would rank quite high, whereas the measurement that would most likely be conducted in an actual engine situation is item (1). Methods (3) and (4) were rejected on complexity (item 3) and inadequate information (item 4). Of the remaining two methods, the incident power technique was preferred.

Methods of measuring incident power were considered and several types of intensity probes were evaluated. It was found to be possible to measure intensity by using a two point probe (ref. 2.1) or by using a combination microphone/hot-wire anemometer probe (ref. 2.2).

After considerable evaluation it was decided that, for the purposes of this study, the incident power measurement was most effective and the rest of this preliminary investigation is devoted to development of an experimental technique for measuring nozzle transmission coefficient based on incident power.

In line with the above, the nozzle transmission coefficient, based on the ratio of radiated power\* to incident power ( $W_{inc}$ ) in the duct, is:

$$NTC = \frac{4\pi R_m^2 \bar{p}_{rad}^2}{(\bar{\rho} \bar{c})_{amb}} \frac{1}{W_{inc}}, \quad (2-1)$$

where  $\bar{p}_{rad}^2$  is far-field microphone mean square pressure measured at radius  $R_m$  from the duct exit and  $\bar{\rho} \bar{c}$  is the characteristic impedance.

---

\*From standard texts (ref. 2.4) acoustic power is defined as the surface integral of far-field acoustic mean square pressure normalized to characteristic impedance ( $\bar{\rho} \bar{c}$ ).

This is equivalent to the ratio of the measured acoustic intensity to that produced at the measured point by an acoustic point monopole source of equivalent power equal to  $W_{inc}$  and located at the nozzle exit (see section 3.3.5).

With this decision on the definition of NTC, it is now possible to evaluate the potential types of source excitation, measurement techniques and data analysis methods. All three aspects are interrelated. Once the source type is chosen, the options remaining for measurement are reduced. Following the selection of source type and measurement option, the data analysis choices are minimized. However, the following criteria were applied in making the choices: simplicity, speed, and accuracy. The following subsections discuss the investigation leading to the ultimate experimental techniques chosen.

### 2.2.2 Source Type

The choice of acoustic source depended on (1) the frequency range, (2) the amplitude and linearity of the source, and (3) its environmental characteristics. The source had to be capable of producing sound within either the inner or outer nozzle duct-work up to the environmental test limits, i.e. greater than 207 KN/m<sup>2</sup> stagnation pressure and 900 K stagnation temperature.

Three basic source types were considered, namely broadband, discrete tone and impulsive. Implicit in the following discussion of all three types is the fact that, as the nozzle transfer function is defined in terms of some ratio of transmitted wave to incident wave parameter, some means must be available to remove or isolate the effects of any nozzle reflected wave from the in-duct measurement.

2.2.2.1 Broadband Excitation. - A broadband source has the obvious advantage that, since all frequencies are present, a one-time measurement of NTC should be sufficient, leading to minimized experimental time. However, the time average energy in any one narrow frequency band is relatively low and signal-to-noise problems will occur in far-field measurements at high velocity jet conditions.

The high-frequency requirement of 100 KHz effectively ruled out conventional electro-dynamic or electro-pneumatic driver systems. The primary candidate was a system of intersecting air jets.

Before attempting to build a high-frequency random acoustic noise generator, the problems of using random sound were evaluated by conducting lower frequency tests in an existing duct/nozzle system. In order to realistically evaluate the random noise test technique for determining NTC, it was necessary to choose the most suitable data analysis method. Since it was determined that incident sound power is the most meaningful quantity to use in describing the source characteristics upstream of the nozzle, it was necessary to develop a technique for eliminating reflected energy from incident energy.

It is obvious that a single point in-duct measurement would encompass the incident as well as the reflected energy. This is the situation whether

the measurement is of sound pressure or intensity. Thus, it is necessary to devise a technique for eliminating the reflected wave field.

In the ideal situation in free space, a two-point correlation of band-unlimited white noise produces an ideal impulse with the time delay corresponding to the propagation time between the two points. If the situation in the duct were similar to the ideal situation mentioned above, then a method for separating incident from reflected wave energy could be devised. In principle, this idea could be developed one step further by considering a cross-correlation between an in-duct signal and an outside far-field signal. The in-duct transducer would contain, as discussed, both incident and reflected energy, whereas the far-field transducer contains only transmitted energy. A cross-correlation should produce two peaks; the earlier one should correspond to the incident energy that is coherent with the far-field signal and the latter peak should correspond to coherence between the reflected signal and the far-field signal. If some process for removing the peak in the cross-correlation function corresponding to the reflection could be devised, then a Fourier transform of the edited cross-correlation would provide a cross-spectrum between the incident and transmitted signals. This could be suitably normalized, based on the in-duct incident spectrum to produce the required NTC.

However, with band limited noise in a real duct, the situation is somewhat different. The ideal impulsive cross-correlation functions become more like that shown in figure 2.2. The reason for this very confused cross-correlation function is due to two factors. First, the noise does not have a flat spectrum and is not band limited. Second, the noise excites multiple acoustic modes in the duct, each having different phase speeds. Thus, the cross-correlation modification referred to above is not practical.

Actually, the duct in figure 2.2 has been treated with an absorbent liner to minimize the higher-order duct modes, thereby permitting detection of a cross-correlation peak between the in-duct and far-field signals. Without the absorbent liner, it was not possible to detect this peak.

It should be noted that any continuous source will set up a sound field containing all possible modes of vibration travelling both towards the exit and from it. Thus, in order to have any real meaning the nozzle transmission coefficient should be specified based on a *known* modal content in the duct. Thus, even if the broadband noise source could be seriously considered, a modal analysis should strictly be performed. This would require that a large number of in-duct microphones be spaced circumferentially, radially and axially and simultaneously recorded for cross-spectrum analysis. This approach was not considered feasible in this work.

2.2.2.2 Discrete Tone Excitation. - Continuous tone excitation has one major advantage over random noise excitation in that the amount of source power available in a narrow frequency band is much greater, thus correspondingly reducing any signal-to-noise problems within that band. However, in order to cover the desired frequency range, a large number of test frequencies must be used, greatly increasing the test time. In addition, the complications of higher-order acoustic modes within the duct still require a complex modal analysis in order to determine the incident sound energy, as mentioned above.

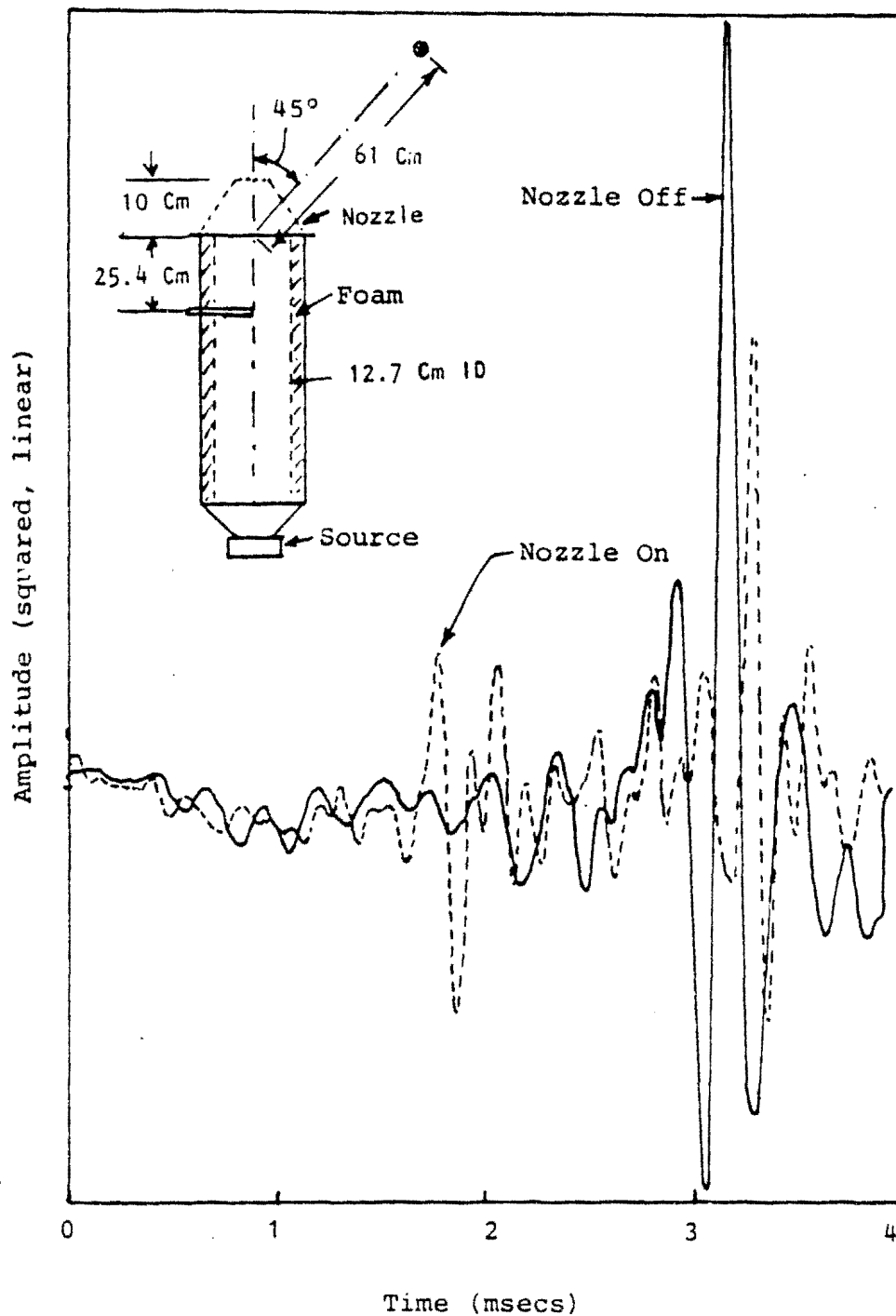


Figure 2.2 Comparison of nozzle-on and nozzle-off cross correlations between in-duct and far-field microphones with random excitation.



The use of *pulsed* discrete tone excitation would eliminate the need for *axial* sound field measurements in the duct since the incident pulses could be separated in time from the reflected pulses. However, the circumferential and radial sound field measurement requirement would remain in order to determine incident modal content.

The greatest practical difficulty experienced with this type of excitation is the lack of a suitable driver which can function at the ultrasonic frequencies required. The only known device with adequate power is the Hartmann generator which is unfortunately not readily controllable in power output and frequency content. A major disadvantage of this type of source for this application is the increase in test time in order to adequately cover the frequency range of interest from zero to 100 KHz. Consequently, this method was not pursued further as a viable source candidate.

2.2.2.3 Impulsive Excitation. - The third basic source type considered was an acoustic impulse. A major advantage of this type of source is its broadband spectral content. If the impulse time history is a true delta function, then its Fourier transform is a flat spectrum up to infinite frequency. In addition, in this ideal situation the impulse response of the nozzle is the nozzle transfer function, which if the reflected energy is removed, is the desired nozzle transmission coefficient (NTC).

Another major advantage of this type of source is that the reflected pulse from the nozzle can be separated in time from the incident pulse by the proper positioning of the in-duct transducer, thus simplifying the in-duct measurement of incident energy. In practice an ideal impulse does not exist. Acoustic impulses from practical sources have a finite width and do not have the ideal rectangular shape. The Fourier transform of a finite width rectangular impulse produces a spectrum with characteristic zeros. Figure 2.3 shows the effect on spectral content of rectangular pulses of varying widths. To achieve the 100 KHz frequency requirement, the optimum compromise would be a pulse-width of about 7  $\mu$ sec. However, an acoustic impulse from practical sources, even though of finite width, is not rectangular.

*Spark Source vs. Gun Shot.* - Two practical sources were investigated, a blank gun shot and an electrical spark discharge. Typical time histories are shown in figure 2.4. Both time histories are characterized by rapid pressure rises followed by a slower decay and rarefaction before recovery to ambient pressure. The basic difference between the two is the slower decay of the gun shot, probably due to extended burning. The transformed spectra of each pulse are compared in figure 2.5, and it can be seen that the longer pulse length of the gun-shot results in a much higher level of low-frequency content.

Significant problems with the gun shot arose from two other burning-associated characteristics. The first being that of contamination from unburned powder and wadding, while the second effect was a lack of pulse consistency from shot to shot. This latter effect was the most serious, since amplitude and pulse durations could vary by a factor of 2 or more between consecutive shots.

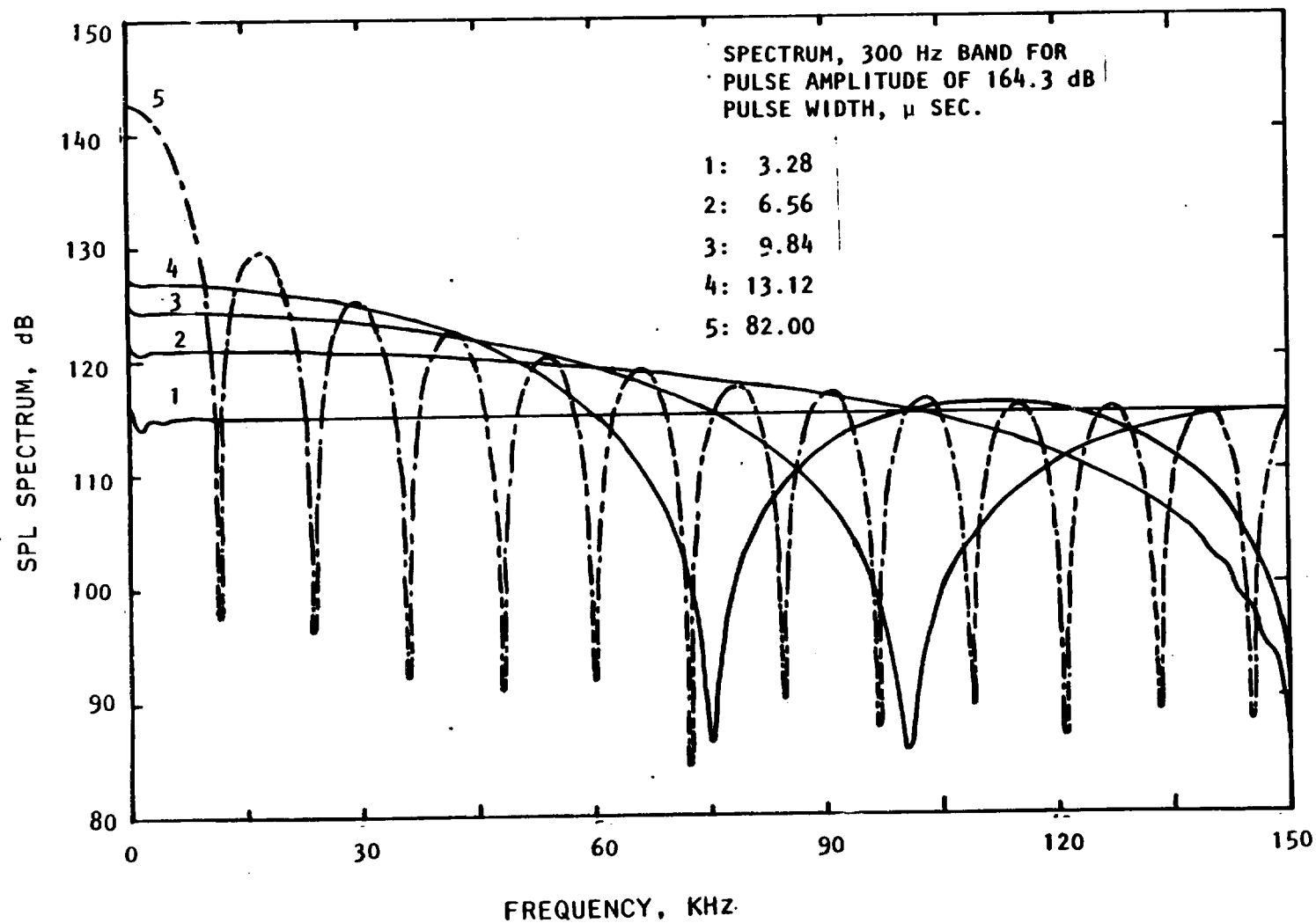


Figure 2.3 Effect of pulse width on ideal impulse spectrum shape.

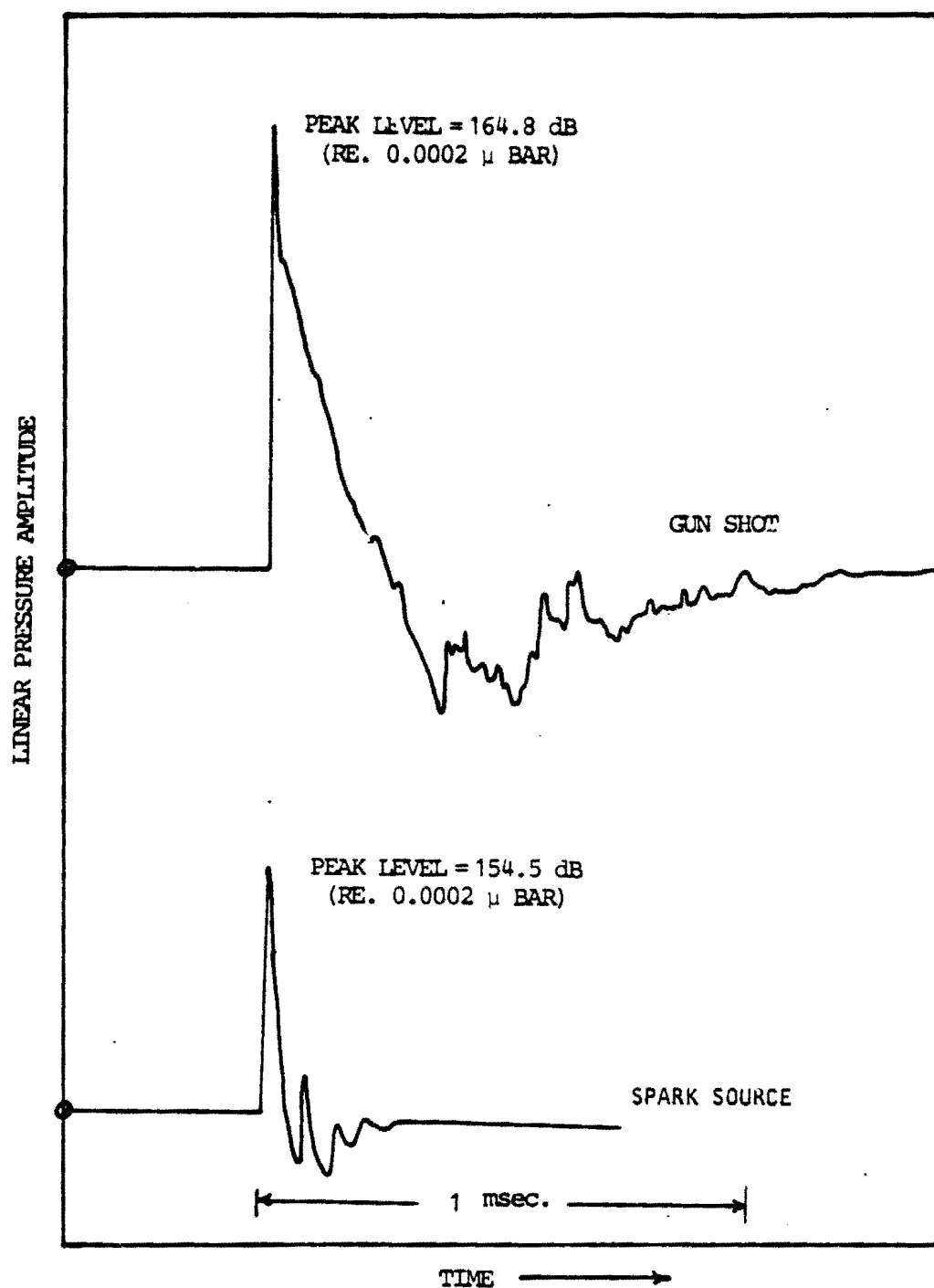


Figure 2.4 Free field pressure signal time histories from spark source and gun shot.

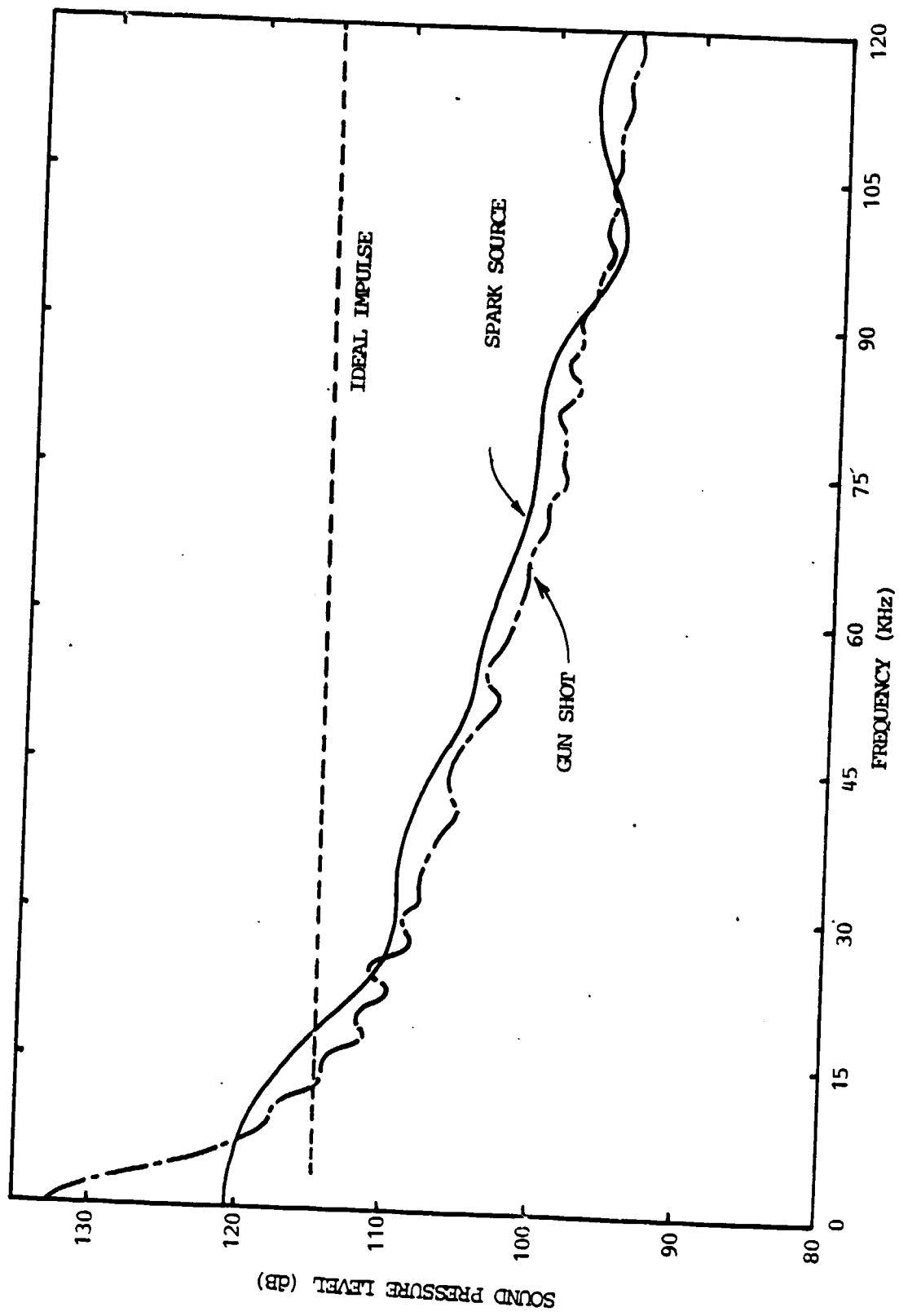


Figure 2.5 SPL spectra of pulse signals (300 Hz bandwidth).

The spark source on the other hand was more consistent, provided a more uniform and flatter spectrum, with the added practical advantage that no mechanical reloading, triggering devices, etc. were necessary. The fundamental operation consisted simply of closing a high-voltage switch, which then discharged a capacitor through the spark gap (for more details see section 3.1.3). Thus, the investigation concentrated on the suitability of a spark discharge as the most practical impulsive source.

*In-Duct Wave Structure from Point Impulsive Source.* - An impulsive point source in a free-field environment will radiate spherically. At some point in the far field, the wave front will have such a large radius of curvature that it will appear essentially as a plane wave, which is the desired in-duct condition. Shock tube studies have shown that a point source will propagate down the tube as a spherical wave followed by a reflected wave structure from the wall. This reflected wave field is a function of axial distance from the source. Figure 2.6 shows the evolution of this wave structure as a function of time and distance from the source. As a result of propagation nonlinearities, the wave fronts of the reflections gradually catch up to and coalesce with the initial spherical shock and produce a relatively clean wave front. However, multiple reflections of those parts of the initial spherical wave which are at high angles of incidence to the duct wall are unable to coalesce with the initial spherical wave due to their long travel times. This is illustrated in Figure 2.7(a). It can be shown that after  $n$  reflections, a ray between an on-axis source and an on-axis receiver  $x$  distance apart in a duct of diameter  $D$ , will arrive at  $\Delta t$  seconds after the direct ray such that

$$\Delta t \approx \frac{n^2 D^2}{2x c_0}$$

It can be seen from figure 2.7(a) that as the angle of incidence,  $\theta$  is increased, the number of reflections,  $n$ , for the corresponding ray also increases, which in turn increases the value of  $\Delta t$ . This phenomenon introduces a "train" of oscillations following the incident pulse in the pressure time history of the point impulsive source. This phenomenon is quite pronounced when the source section of the duct is unlined. These oscillations can, however, be minimized by the addition of an absorbent lining to attenuate the high angle reflections as illustrated in figure 2.7(b). This process, which effectively limits the pulse length, also reduces the total available energy by reducing the conical "capture window"  $\theta_c$  of the test duct. This reduction can however be optimized by proper selection of the absorption material and the length " $l$ " of absorbent lining downstream of the impulsive source. In the present work, 2.5 cm thick polyurethane foam lining in the 10 cm diameter duct with 15 cm length was used and produced an acceptable in-duct time history at  $x = 60D$  as shown in figure 2.8.

First, the incident (*outgoing*) pulse is seen in figure 2.8 to be a steep-fronted positive pressure wave followed by a rarefaction wave. It is similar to a one-dimensional travelling shock wave. The width of the pulse is a function of the distance from the source and the initial pulse amplitude. The second feature is the reflected (*ingoing*) pulse, which is shown to be a steep-fronted *negative* pressure wave. Close examination reveals that the leading

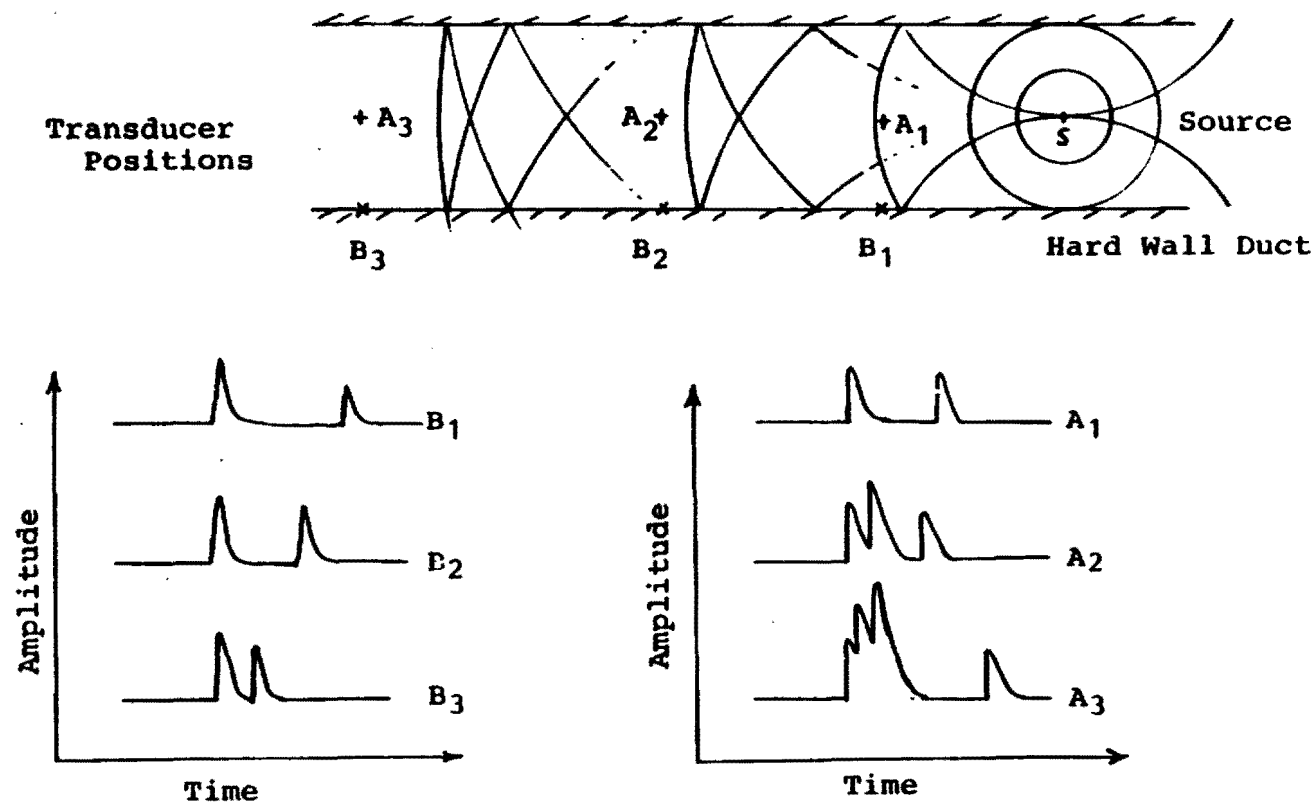


Figure 2.6 Characteristic effects of source/microphone position on measured time histories.

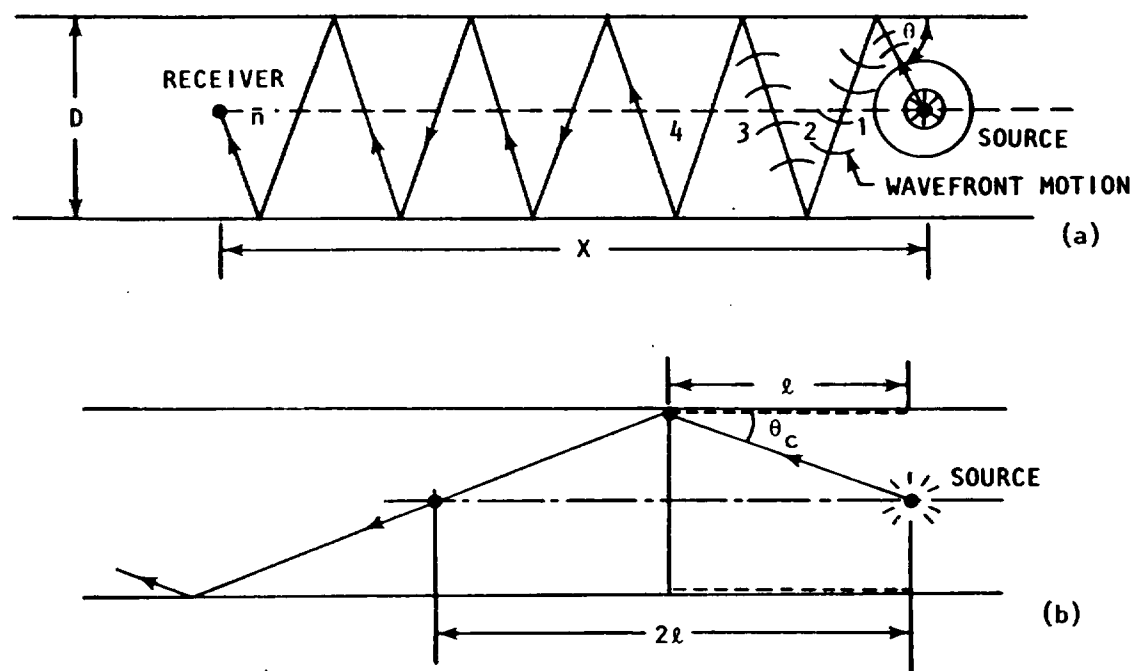


Figure 2.7 (a) Structure of pressure time-history from point impulsive source. (b) Effect of absorbent duct lining around the source.

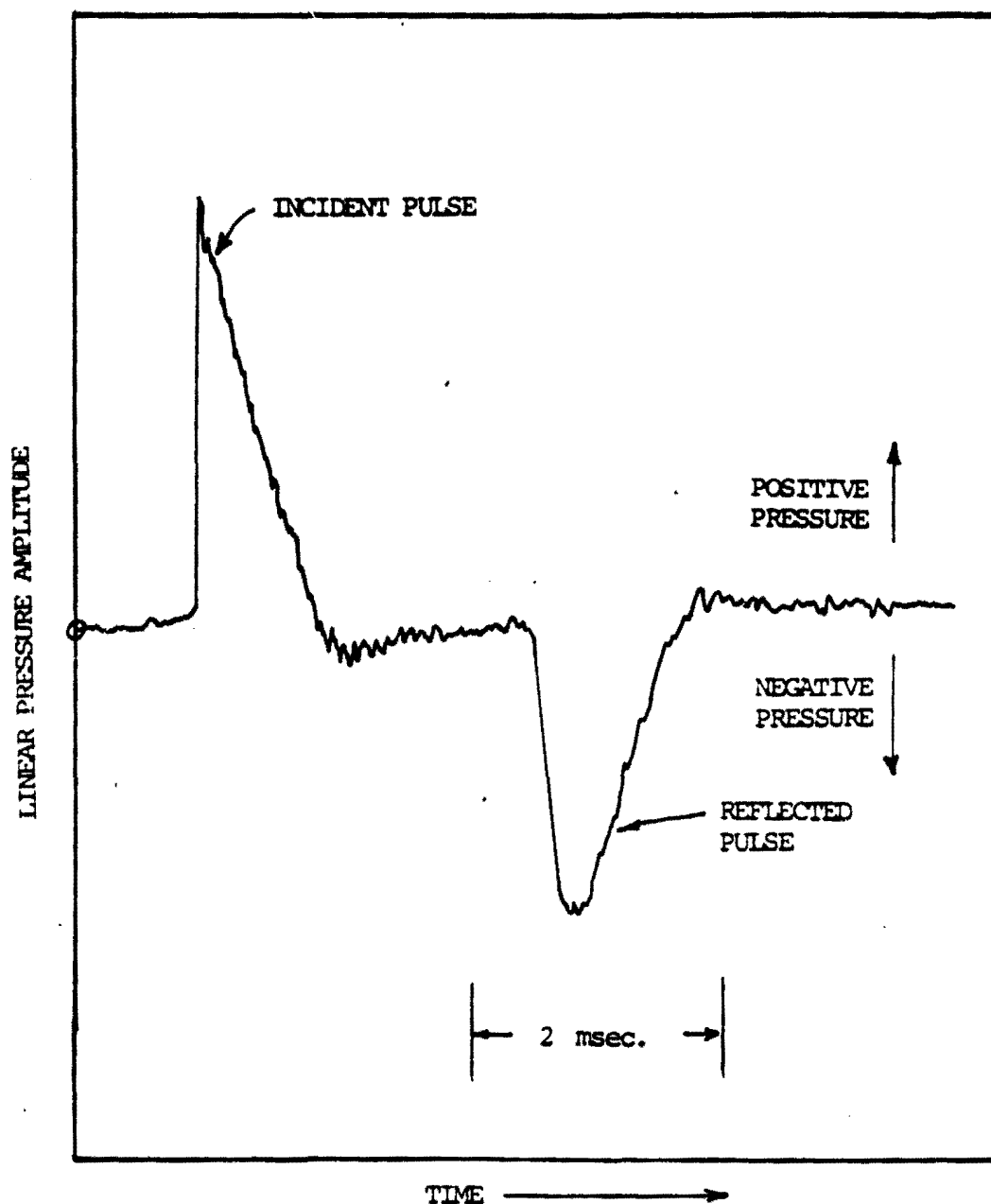


Figure 2.8 In-duct time history for 10 cm diameter duct at zero flow.



edge slope is not as sharp as that of the incident wave. Physically, this signifies an escape of high-frequency energy at the termination. Since each pulse is propagating at approximately the ambient speed of sound, pulse separation in time can only be achieved by proper transducer placement upstream of the termination. Another point worthy of mention is that the measured time interval between the incident and reflected pulse leading edges fairly accurately defines the geometric location at which reflection takes place.

**2.2.2.4 Summary of Source Types.** - Figure 2.9 summarizes the essential features of each source type discussed above. The impulse source stands out by virtue of its combination of short test time, high-spectral content, compactness and convenience of operation, and inherent ability to separate incident energy from reflected energy. This latter aspect not only applies within the duct, but also in the far field, which implies less rigorous and time-consuming attention to anechoic details in the vicinity of the far-field microphones.

### 2.2.3 Internal Source Measurement Configurations

The choice of an internal measurement configuration is inextricably linked to the type of source used. Continuous source excitation definitely requires a multiple in-duct detection scheme in order to separate and quantify the incident energy to the nozzle if the practical problem of higher-order mode excitation could be avoided. For low-frequency excitation (in the plane mode region), only axially spaced microphones are necessary. However, for higher frequencies, a complex array of in-duct microphones is necessary in order to perform a modal analysis. Such complexity was considered too time-consuming and inappropriate for this work.

For an impulse source it is necessary to define the sound pressure cross-sectional distribution only at one axial plane no matter what the modal content of the pulse. If the pulse could be constrained to a plane wave distribution, then a single wall-mounted pressure transducer would be all that is necessary to describe the incident and reflected sound field. The simplicity of such a measurement technique is obviously appealing and the preliminary investigation thus concentrated on establishing the conditions under which such a situation would be valid.

**Test Configuration.** - To confirm the suitability of this approach, a test setup as shown in figure 2.10 was used. A spark source was placed on the centerline of a 10 cm diameter pipe, 6 meters from its termination in an anechoic room. A 0.64 cm (1/4 in.) diameter transducer was mounted flush in the duct wall, 58.5 cm upstream of the termination. The termination options included 10 cm, 5 cm and 2.5 cm conical nozzles. In addition, 0.64 cm (1/4 in.) diameter far-field microphones were spaced on a 2.44 meter radius at 10° intervals of polar angle from the axis (zero degrees) to 120°.

**Initial Problems with the Test Configuration.** - Initial measurements of the pulse confirmed that within the test duct, a wave structure with peak amplitudes in excess of 2000 Pa (160 dB re. 20  $\mu$ Pa) could be produced. However, a serious problem with the operation of the spark source had to be

## EXCITATION OPTIONS

### DISCRETE

- LONG TEST TIME
- OUTGOING POWER NEEDS MODAL ANALYSIS
- HIGH FREQUENCY LIMITATIONS
- HIGH POWER PER Hz

### RANDOM

- SHORT TEST TIME
- OUTGOING POWER NEEDS MODAL ANALYSIS
- HIGH FREQUENCY LIMITATIONS
- LOW POWER PER Hz
- DIFFICULT TO ACHIEVE

### IMPULSE

- SHORT TEST TIME
- CONVENIENT INCIDENT POWER DETERMINATION
- GOOD FREQUENCY RANGE
- ADEQUATE POWER PER Hz

Figure 2.9 Essential features of three sources.

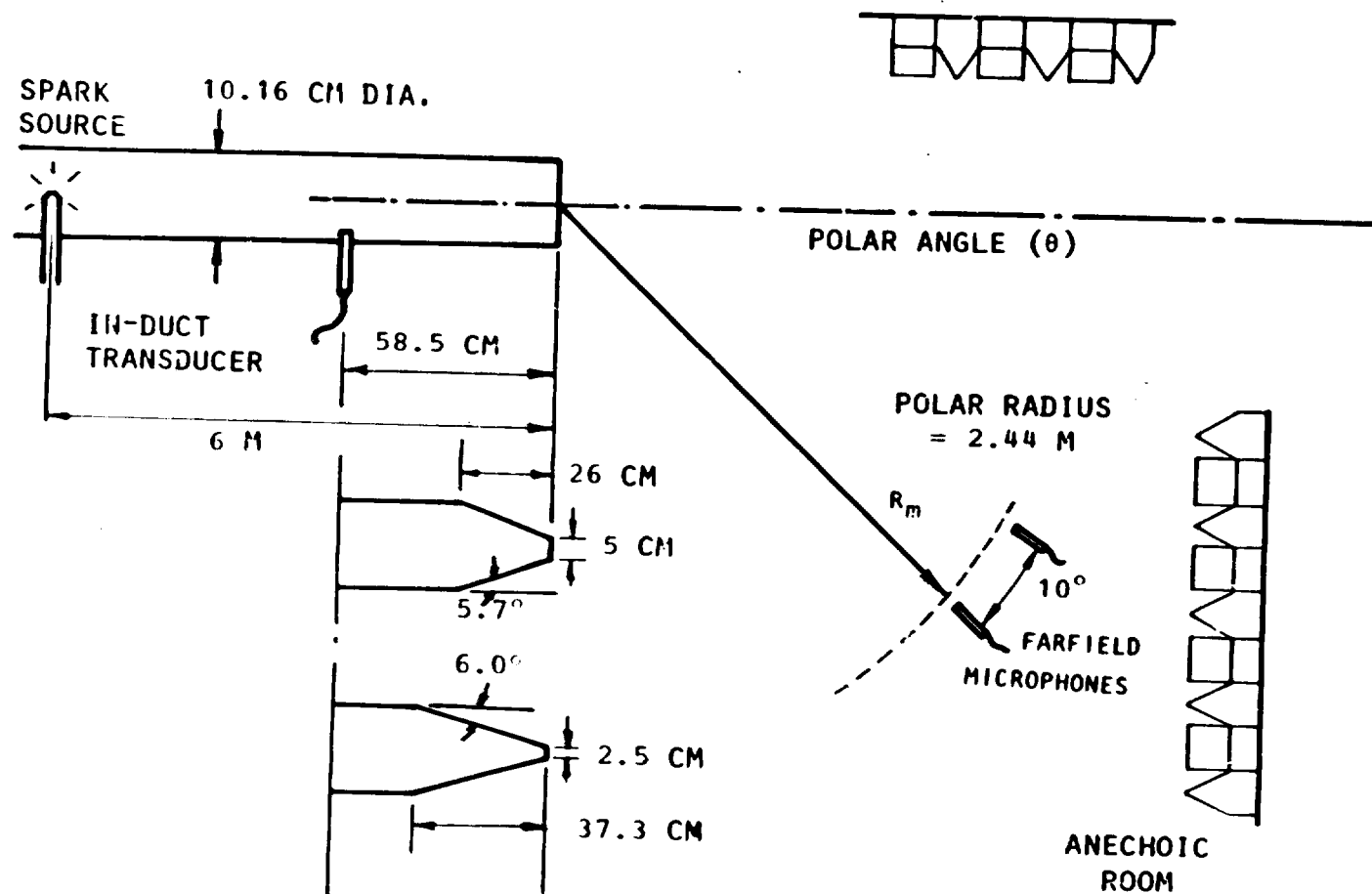


Figure 2.10 In-duct/far-field measurement configuration.

overcome at the outset of this investigation. The problem concerned the in-duct microphone which suffered both high electro-magnetic (E.M.) interference and saturation related nonlinearities. Each time the spark was discharged, the electromagnetic radiation from the gap, and its connecting leads was found to saturate microphones with temporary D.C. voltage shifts, to cause cable "ringing", to overload signal conditioners and even blow-out fuses of certain other electronic equipment in the laboratory. The problem became more severe the closer to the spark gap the pulse detection system was. Various combinations of instrumentation grounding and shielding finally reduced this effect considerably. The in-duct measurement problem was solved by the use of a piezoelectric (quartz type) transducer which was electrically isolated from the duct wall. A built-in amplifier minimized the E. M. pickup to acceptable levels, however, the lower limits of sensitivity of this transducer was considerably larger than that of the microphone, the smallest detectable signal being about 120 dB (re. 20  $\mu$ Pa). The E.M. interference could not be completely eliminated but owing to its rapid rate of decay, it decayed long before the acoustic pulse reached the in-duct transducer or the far-field microphones.

#### 2.2.4 Data Analysis

From the above discussion, it was obviously not practical to conduct modal analyses as part of the standard test procedure. Thus, the incident modal structure produced by the source had to be accepted and assumed constant for all tests. In this preliminary investigation, the spatial pulse pattern was taken as plane.

Based on this assumption then, only one in-duct pressure transducer is required to represent the pressure field across the entire duct. This situation is obviously desirable in the practical sense since (1) in-duct space is limited, (2) access is limited, and (3) stagnation conditions of pressure and temperature would require special attention to mounting and cooling problems.

Two basic measurements are of interest in this work. First, the nozzle reflection coefficient is of interest in the context of validating the impulse method by direct comparison with results from other methods. Second, the nozzle transmission coefficient is the fundamental property defining far-field radiation for the nozzle systems of interest. In this context nozzle transmission coefficient, given by equation (2-1), has been defined in terms of a nozzle transfer function between incident in-duct sound and far-field transmitted sound. Specifically, the measured property of interest is the transfer function in mean-square pressure terms between far field and in-duct incident sound.

Thus, with reference to figure 2.11, the nozzle transmission coefficient is referred to hereafter as the nozzle transfer function and is defined by

$$NTF = \bar{p}_{rad}(\theta) \frac{4\pi R_m^2}{A_0 \bar{p}_i^2} \frac{(\bar{p}\bar{e})_{duct}}{(\bar{p}\bar{e})_{amb}} \frac{1}{(1 + M_0)^2} \quad (2-2)$$

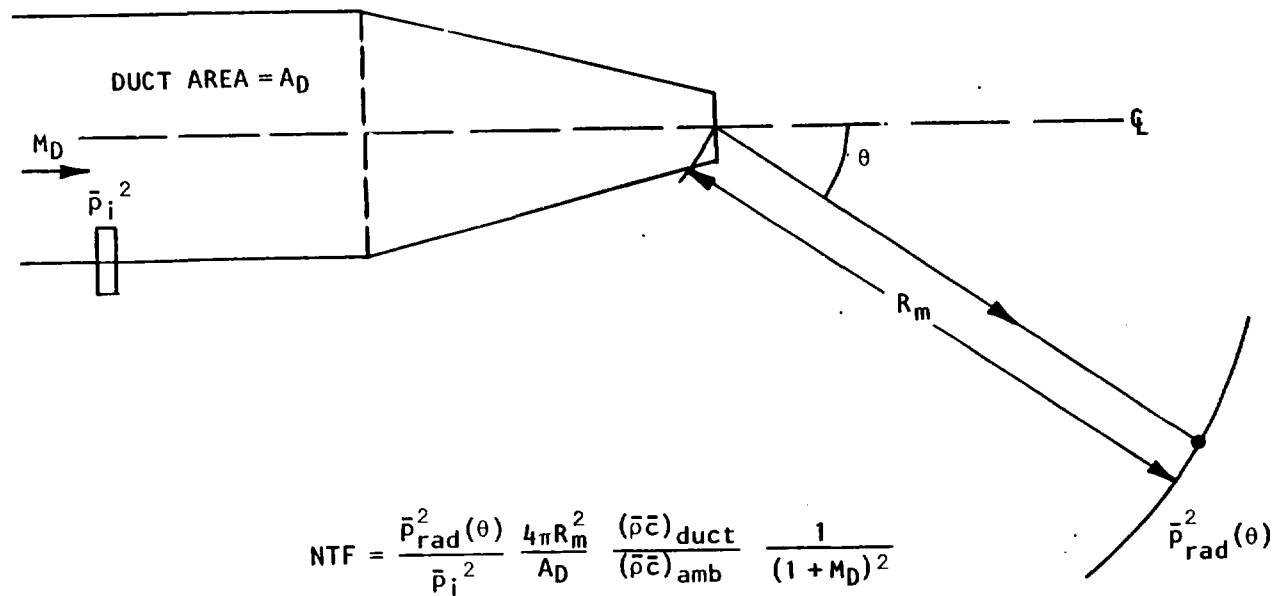


Figure 2.11 Basic definition of nozzle transmission coefficient.

where  $\bar{p}_{\text{rad}}^2(\theta)$  is the mean square far-field pressure at polar angle  $\theta$ .  $R_m$  is far-field radius,  $A_D$  is nozzle duct area, and  $\bar{p}_i^2$  is incident mean square in-duct pressure. Here,  $M_D$  is the duct Mach number and  $\bar{p}_i^2/(\bar{\rho}\bar{c})_{\text{duct}}(1+M_D)^2$  is the incident acoustic power  $W_{\text{inc}}$ .

Three basic characteristics are implicit in this definition:

- (1) A single-point in-duct measurement is representative of the average mean square pressure over the duct cross-section.
- (2) The far-field mean square pressure is azimuthally axisymmetric.
- (3) Below the first higher-mode cut-on frequency the incident plane mode will be transmitted as plane-mode radiation to the far-field.

Above this frequency, higher modes will be reflected from the nozzle and will also contribute to the far-field pressures even though the incident wave may be plane. Thus, nozzle reflection and transmission coefficients cannot *rigorously* be ascribed to any one mode or combination of in-duct modes. In this work, however, it is tacitly assumed that the *dominant* mode component reflected inside the duct and transmitted out of the duct is a plane wave.

Figures 2.8 and 2.12 show typical incident, reflected and transmitted (far-field) pulse time histories. The spectral content of each can be represented by their respective power spectra computed via the generalized Fourier transform relationship (see ref. 2.3). All the above manipulations were performed using a dual-channel digital Fast Fourier transform (FFT) analyzer with transient capture capability. This instrument has the convenience, not only of capturing the incident and reflected time histories, but also of editing and relative time translation (rotation) of the data. Since both these in-duct time histories are detected by one transducer, both analyzer memory channels are loaded with the same input of figure 2.8. Channel A is then modified to remove all signals except the *incident* time history and Channel B is similarly modified to remove all except the *reflected* time history. However, these signals also have a relative time separation due to pulse propagation time, since the transducer is upstream of the termination. The reflected pulse must, therefore, be rotated in the time domain to bring it into alignment with the incident pulse. Without the rotation, the influence of pulse propagation time has the effect of producing a frequency-dependent phase shift that is *not* related to the termination properties. This rotation procedure can be visualized as equivalently translating the transducer measurement point to the termination plane. The complex transfer function (B/A) can now be performed by the FFT analyzer.

Similarly, the transfer function between incident in-duct and far-field microphones can be determined. In this case, of course, the transmission coefficient, not the reflection coefficient, is the derived quantity. In this work we have defined this transfer function as the nozzle transfer function (NTF). Its variation as a function of polar angle in the radiated field defines the nozzle directivity as a function of frequency.

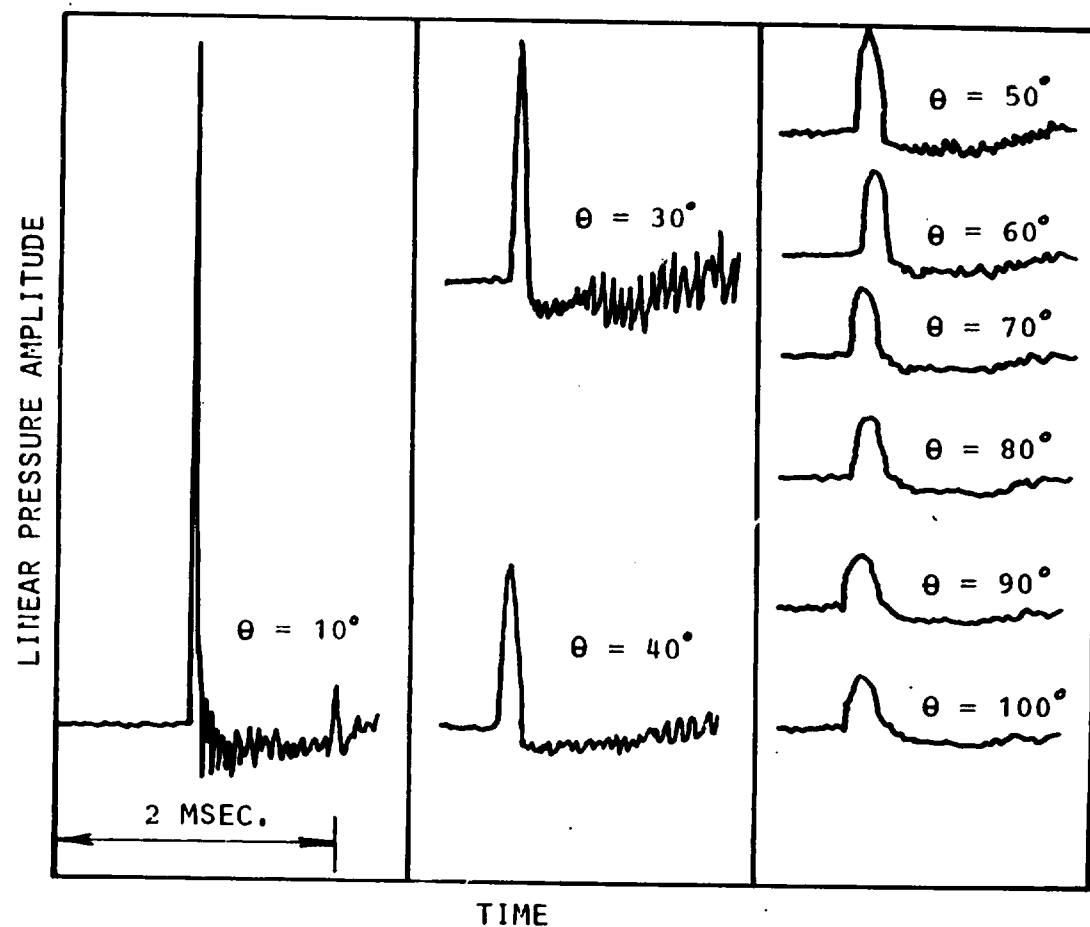


Figure 2.12 Variation of far-field time histories with polar angle  $\theta$ , for 10 cm duct at zero flow velocity.

In the present context, reflection coefficient  $\sigma(f)$  at a given frequency  $f$  is defined to be the ratio of the reflected intensity to the incident intensity at that frequency. For the in-duct signals the complex reflection coefficient  $[\sigma(f)]$  is identically equal to the complex transfer function  $[h(f)]$ . The termination impedance of the duct can be computed from the relationship (see standard texts e.g. ref. 2.4)  $Z_R = [1 + \sigma(f)]/[1 - \sigma(f)]$ . This relationship holds for any point in the parallel section of the duct under no flow conditions in the plane mode frequency regime. This impedance defines explicitly the amount of power propagation out of the duct system and is the major acoustical property of interest in the comparisons of impulse data with classical measurements described below in Section 2.3.

## 2.3 VALIDATION OF ACOUSTIC IMPULSE TECHNIQUE

In this section experimental results obtained using the acoustic impulse technique are compared with the results obtained from other established methods - both experimental and theoretical. These comparisons include (1) absorption coefficients and impedances of an absorbing material tested in a standard impedance tube, (2) reflection coefficients and radiation impedances of a straight unflanged duct exit computed using the Levine and Schwinger (ref. 2.5) analysis, and (3) far-field directivity of an unflanged straight duct computed using Lansing's (ref. 2.6) extension of the Levine and Schwinger analysis. These comparisons are described below in detail.

### 2.3.1 Impedances and Absorption Coefficients of Absorbing Material

A sample of 2.5 cm thick polyurethane foam was mounted to a steel plate at the exit plane of the 10 cm pipe shown in Figure 2.10. The incident and reflected wave pressure time history was captured and the editing process and transfer function analysis procedures were used in the manner described earlier. The same sample was then placed in a B&K 10 cm diameter impedance tube apparatus. The impedance tube data were acquired by the classical standing wave measurement technique up to the first cross mode frequency in the tube.

The results of the impedance tube test are compared with those of the impulse technique in figures 2.13 through 2.15. The measured reflection coefficients, derived impedances and absorption coefficients show excellent agreement from  $kR_D = 0.2$  up to  $kR_D = 3$ , where the second circumferential mode begins to propagate.

### 2.3.2 Reflection Coefficients and Radiation Impedances of Open Duct

Levine and Schwinger (ref. 2.5) developed an exact mathematical analysis of the sound field within and outside an unflanged circular pipe for a plane mode source. This analytical solution is directly applicable for comparison with the present results. The basic difference in geometry is that the duct used in the present study had a finite wall thickness whereas Levine and Schwinger (ref. 2.5) analysis assumes zero wall thickness. In a more recent analysis, Ando (ref. 2.7) examined the effect of pipe wall thickness and showed that the reflection coefficient amplitude reduces with increasing pipe wall thickness.



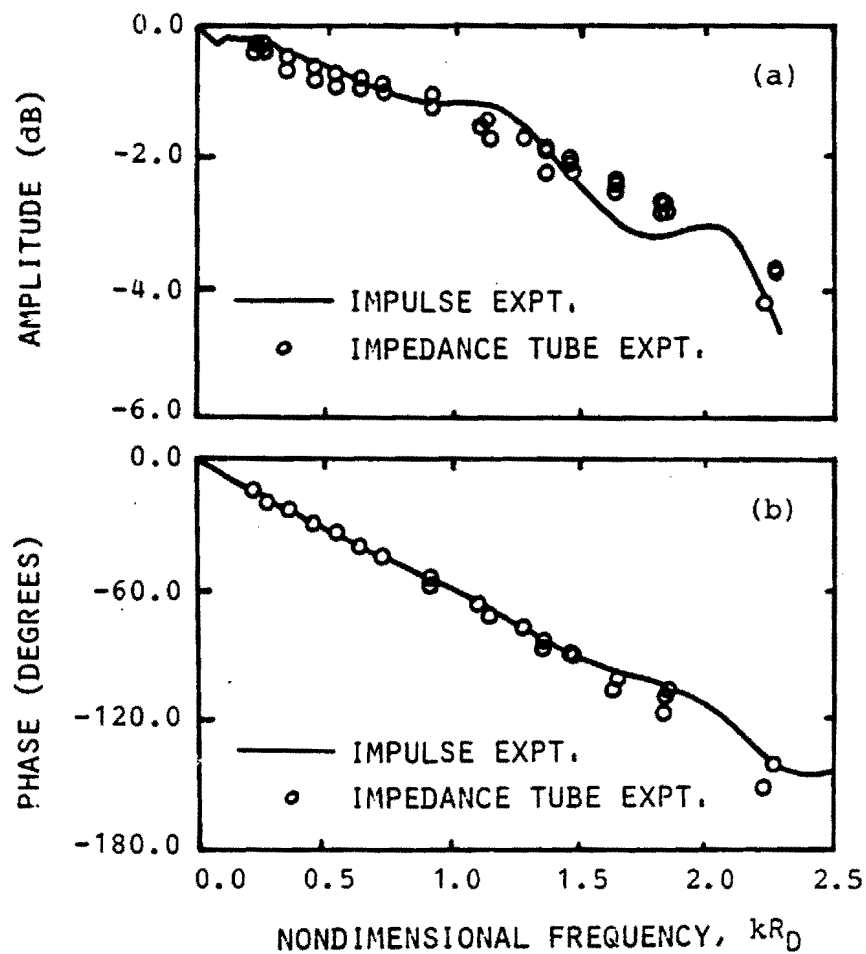


Figure 2.13 Reflection coefficient amplitude and phase comparisons between impulse method and impedance tube.

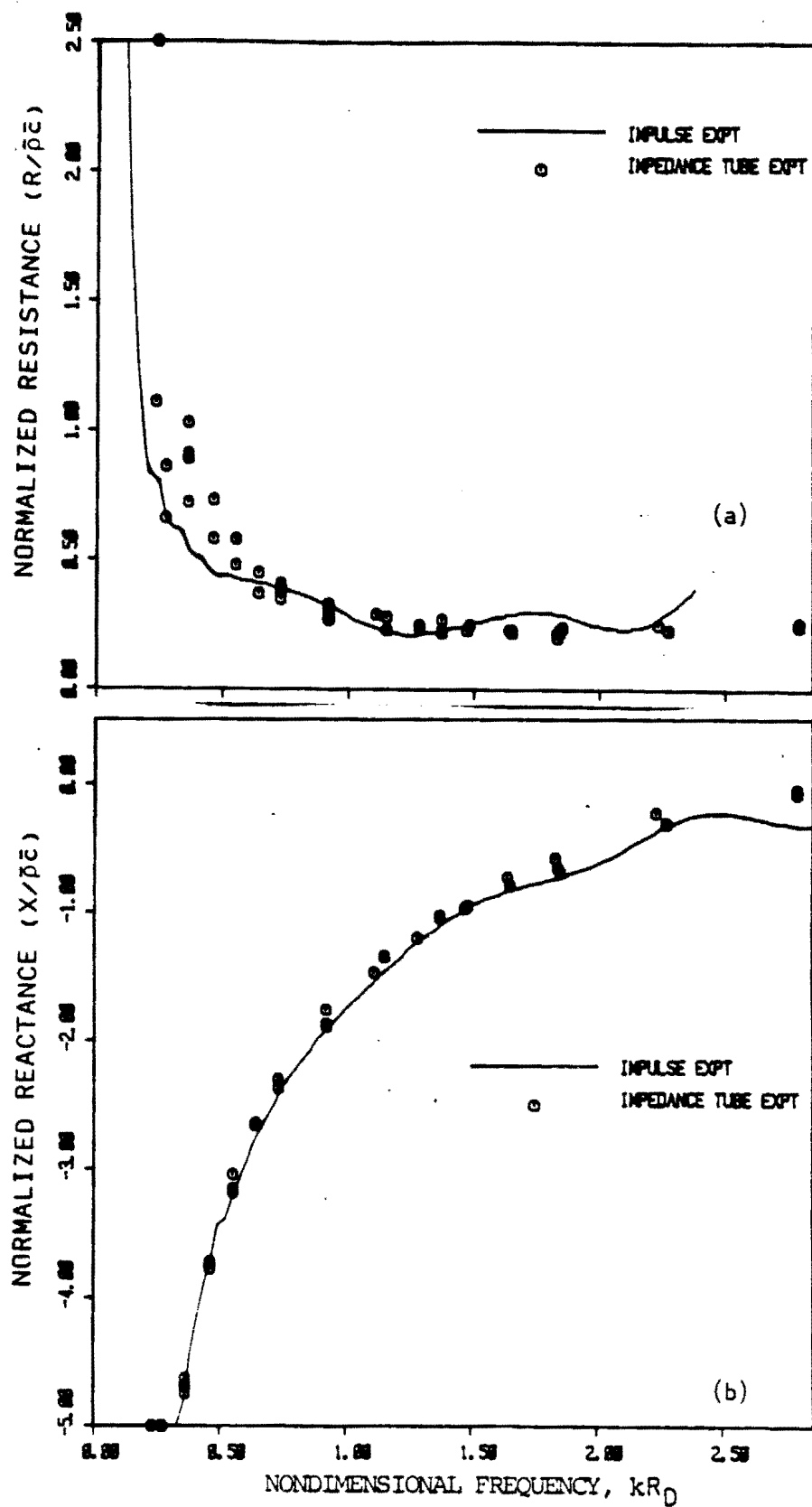


Figure 2.14 Acoustic impedance comparisons between impulse method and impedance tube.

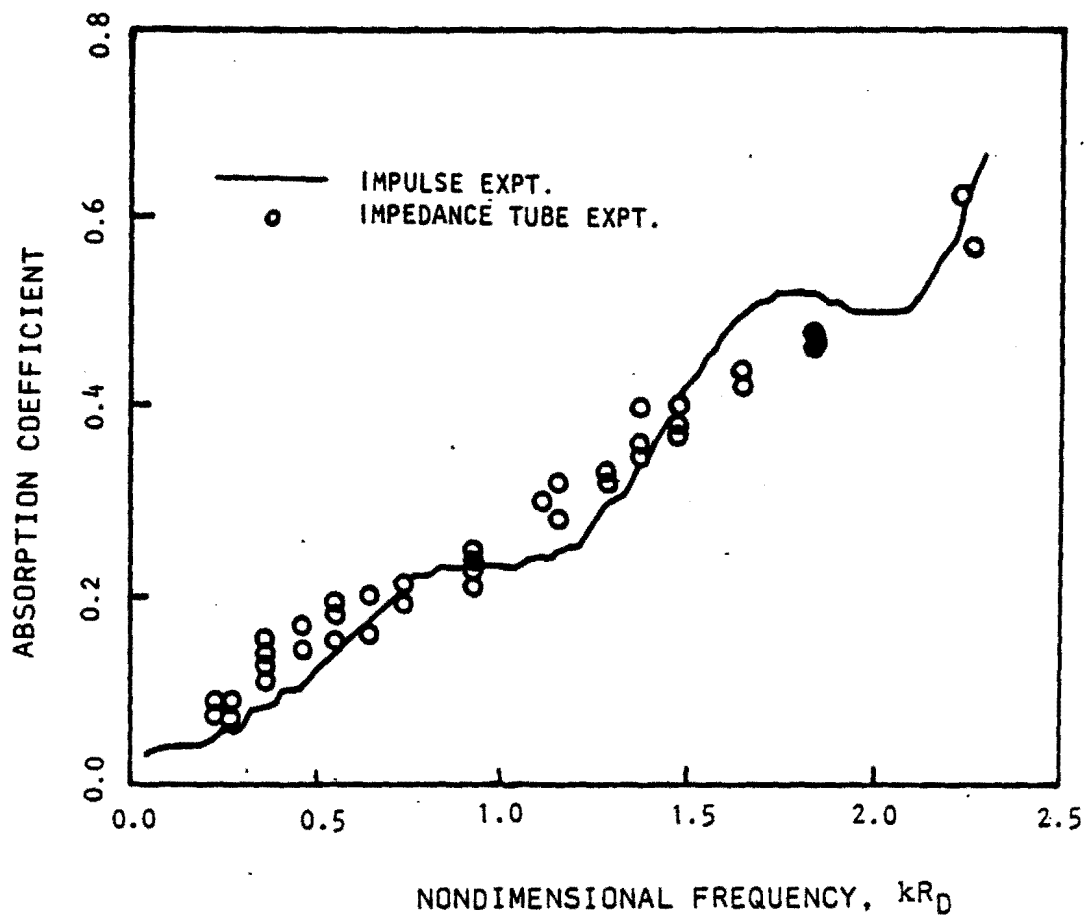


Figure 2.15 Absorption coefficient comparisons between impulse method and impedance tube.

The experimentally determined values of reflection coefficient amplitude and phase are shown in figure 2.16, together with Levine and Schwinger's solution. The phase comparison is remarkably accurate out to  $kR_0 = 3$ . Above this frequency the experimental data are contaminated by the first radial mode cut-on frequency. The amplitude comparison is not quite as good, with the measured value falling off more rapidly with increasing frequency than predicted by Levine and Schwinger (ref. 2.5). On figure 2.16, Ando's (ref. 2.7) results show that the trend due to the wall thickness is in a direction agreeing with the acoustic impulse technique experiments, however, it is not enough to account for all the difference.

The observed difference could also be partly due to nonlinear propagation. To test this hypothesis, a perfectly rigid termination was installed at the open end. The reflected signal measured at 48.5 cm from the end had thus propagated 97 cm further than the incident signal. The spectral difference of the reflected to incident signals in this situation provides an upper limit on the amount of change due to nonlinear propagation. The observed nonlinear effect was a slight reduction in high frequency energy (see fig. 2.17). For example at  $kR_0 \approx 4$ , the reduction is approximately 0.2 to 0.4 dB.

The net effect of correcting the measured results for both the pipe wall thickness and nonlinear propagation effects is to improve the comparison to such an extent that the difference becomes less than one dB out to  $kR_0 = 3$ . This excellent agreement is considered to fully justify the use of the impulse technique for termination reflection coefficient measurements. Figure 2.18 presents the radiation impedance as derived from the reflection coefficient measurements of figure 2.16, with the differences between theory and experiment explained above.

### 2.3.3 Far-Field Directivity

The analysis of Lansing et al. (ref. 2.6) for the radiated field and nozzle transfer function was used as the basis for comparison with the measured directivities. In Lansing's analysis a numerical solution of the situation analyzed by Levine and Schwinger was produced. The radiated far-field results from the impulse technique were obtained after correcting for the propagation time between the corresponding far-field signal and the in-duct signal. However, in Lansing's analysis the end-correction was included. Thus, in order to compare the results obtained by these two methods, the transfer function phase obtained in Lansing's computations was modified empirically to remove the end-correction. These results are presented in figure 2.19 together with the impulse measurements for a range of frequencies up to  $kR_0 = 3.7$ . Above this frequency, there are some discrepancies due to the existence of higher modes excited in the duct, which are not accounted for analytically.

These comparisons of the acoustic impulse technique experimental data, with classical theoretical and experimental results, demonstrate the validity of using the impulse technique for the measurement of acoustic transmission, reflection and absorption characteristics.

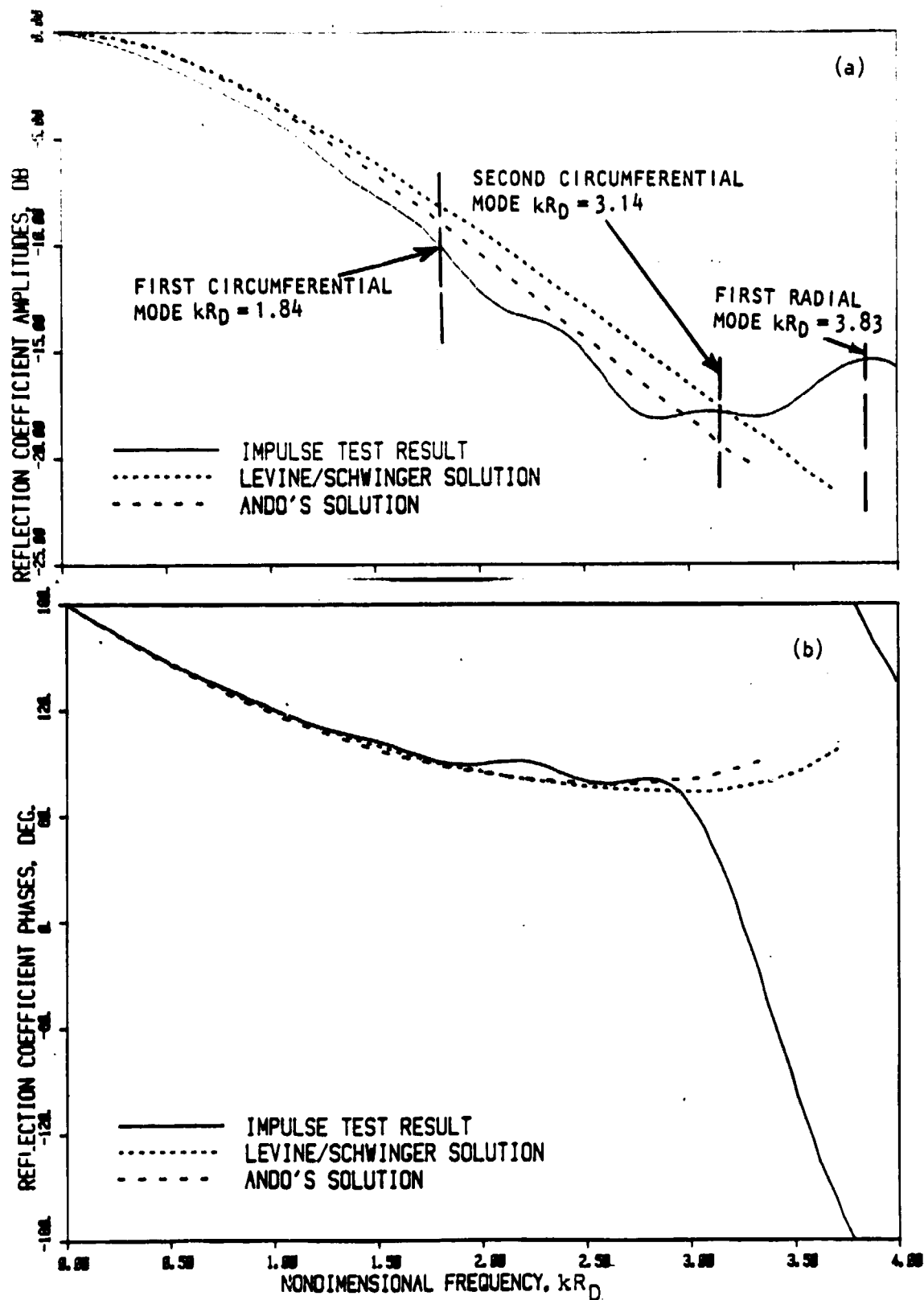


Figure 2.16 Reflection coefficient comparison between impulse and Levine-Schwinger theory and Ando's results for 10 cm diameter unflanged duct.

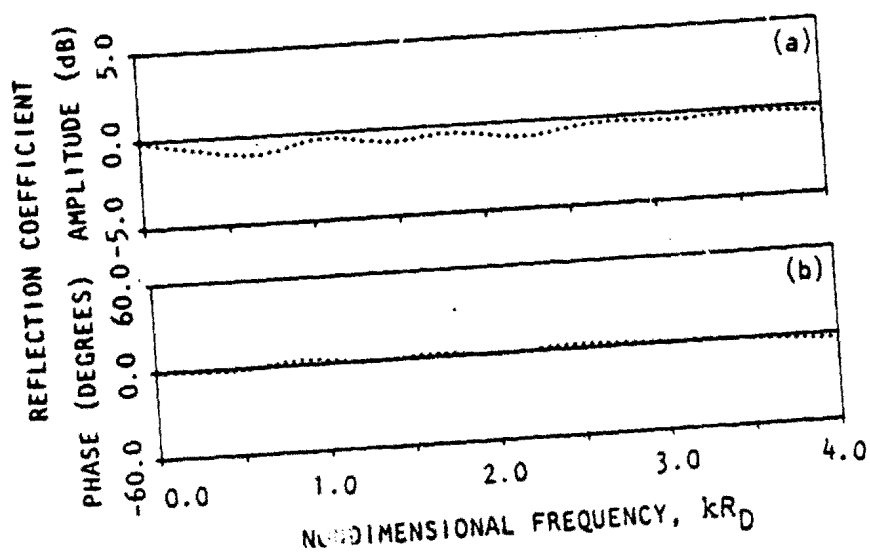


Figure 2.17 Reflection coefficient amplitude and phase of a rigid surface.

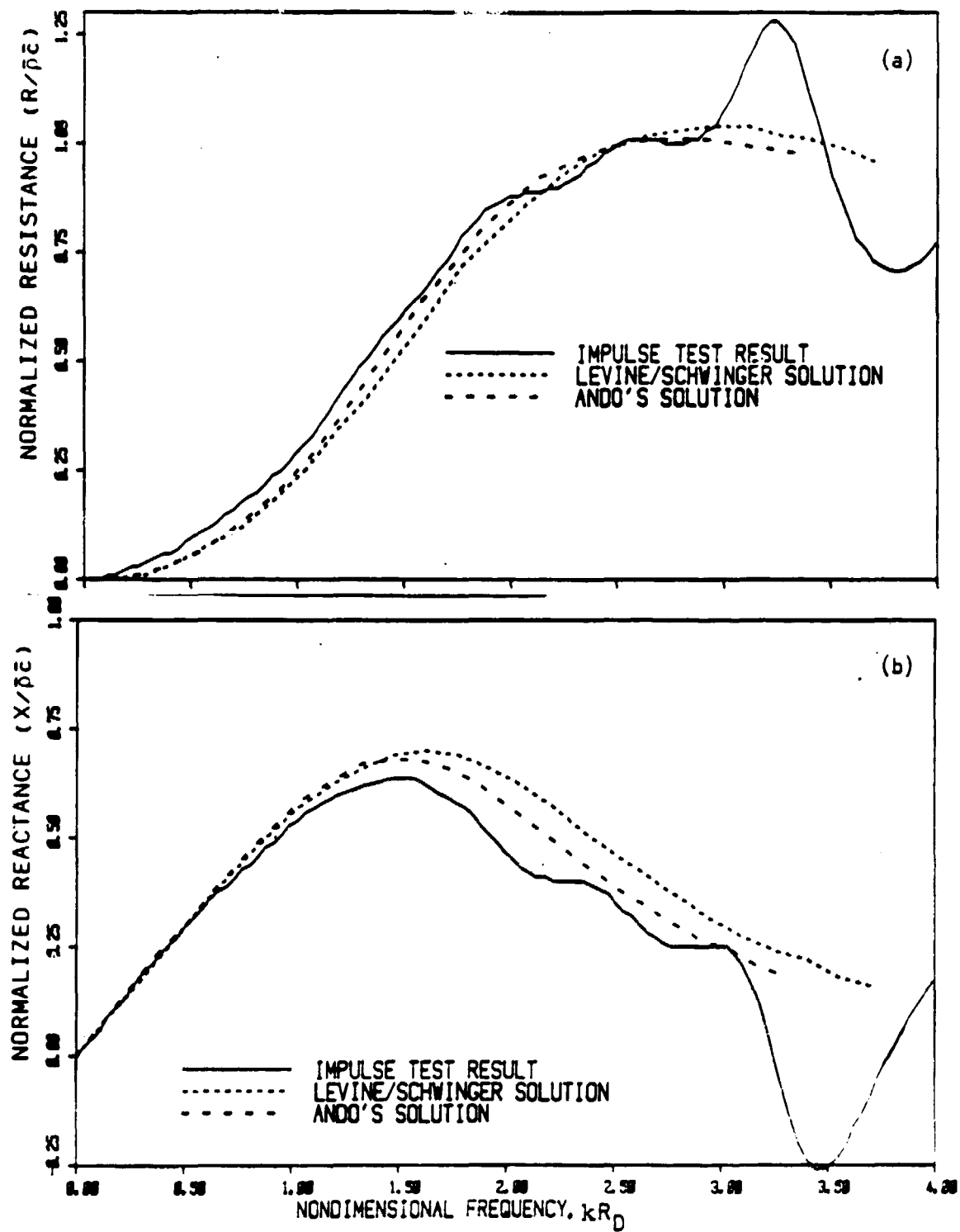


Figure 2.18 Radiation impedance comparison between impulse method and Levine-Schwinger theory and Ando's results for 10 cm diameter unflanged duct.

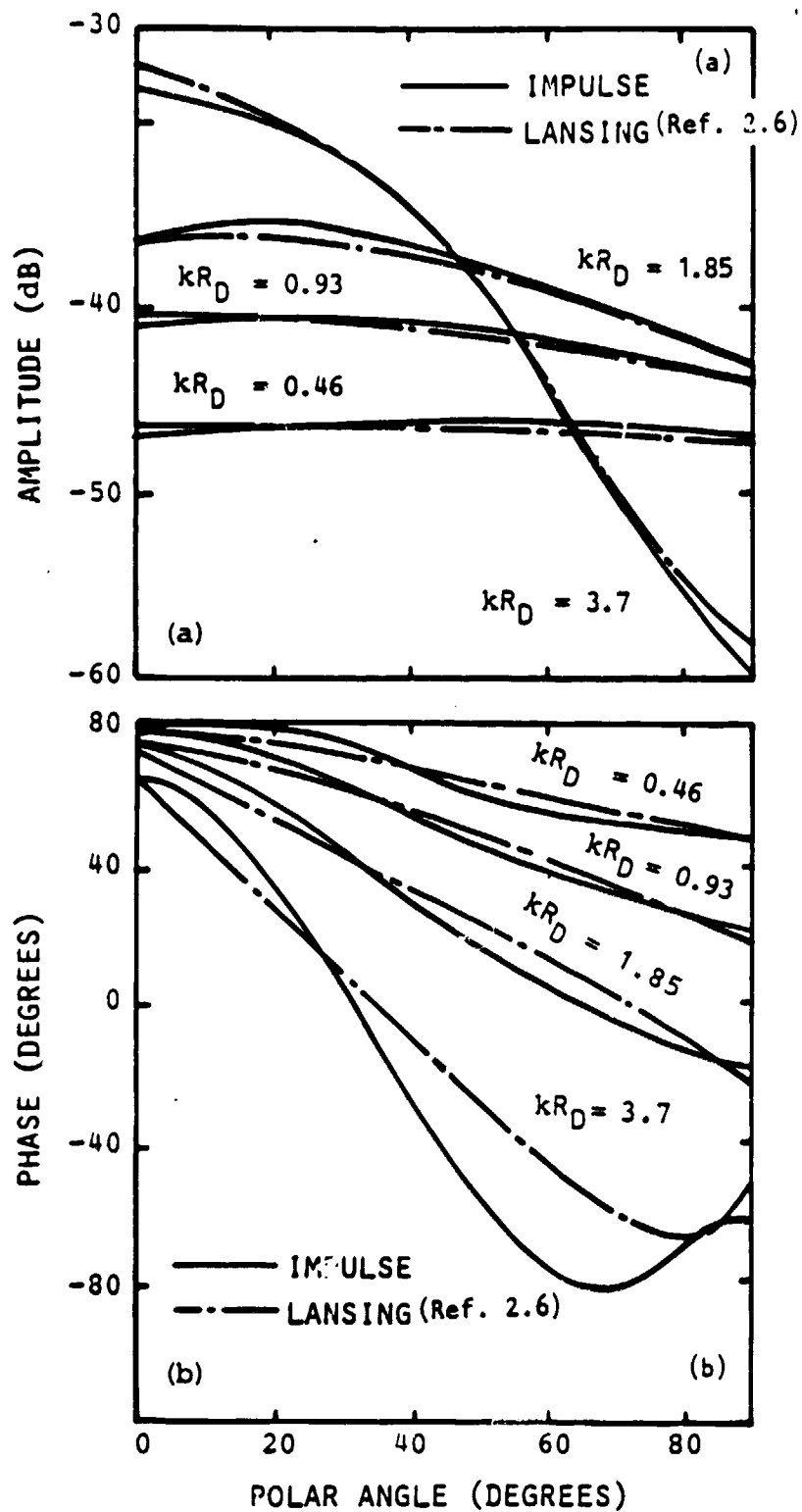


Figure 2.19 Directivity comparison between impulse method and Lansing's solution for 10 cm unflanged duct.



## 2.4 APPLICATIONS: ACOUSTIC PROPERTIES OF CONICAL NOZZLES

Having established that the acoustic impulse technique is a valid experimental tool, a series of tests similar to that described for the unflanged straight pipe was conducted for two conical nozzles. Two tests were conducted: *First*, without jet flow to establish the effects of nozzle geometry, and *second* with (unheated) jet flow, over a range of Mach numbers varying from 0.38 to 0.81. Three types of acoustic data are presented under each test. These are: (1) the nozzle reflection coefficient, (2) the radiation impedance, and (3) radiation directivity.

From the measurements of incident and reflected pulses in the duct-nozzle system the complex reflection coefficient spectrum is evaluated. The phase of the reflection coefficient depends on the time translation between the reflected and incident pulses. From such a reflection coefficient spectrum, it is possible to evaluate the impedance spectrum at the location corresponding to the rotation. Thus, if a rotation is used that corresponds to the nozzle exit, then the nozzle exit impedance can in principle be evaluated in terms of the corresponding reflection coefficient. In the absence of the mean flow, exact expressions for exit impedance in terms of reflection coefficients are available only for the straight duct or the conical nozzle in isolation and only for the straight duct in presence of mean flow. However, an exact expression for nozzle exit impedance for a duct-nozzle system in combination is not possible to formulate with and without the mean flow. A numerical method was, therefore, developed by Mungur (ref. 2.8) to determine the exit impedance of the duct-nozzle system including flow effects. The impedance at the shoulder of the duct-nozzle system is evaluated in terms of the complex reflection coefficient. This impedance is then transferred to the nozzle exit using a solution of the wave equation appropriate for the nozzle, taking axial flow gradients into account. The mathematical details of this method are given in Appendix A.

### 2.4.1 Effect of Nozzle Geometry

Two conical nozzles of 5 cm and 2.5 cm exit diameter with corresponding convergence angles of  $5.7^\circ$  and  $6.0^\circ$ , respectively, were used in these tests. The 10 cm unflanged pipe data are used as the basis for comparison.

Some useful information about the physical phenomenon can be deduced by examining the basic pressure time histories, shown in figure 2.20, for each nozzle. For the 10 cm straight duct case, all the reflection occurs at the termination, with the rounding of the sharp edges showing loss of high frequencies. For the 5 cm nozzle the reflected wave has a positive pressure pulse, followed by a negative pressure pulse resulting from the reflection at the termination. The positive reflection is characteristic of the signal obtained when a pulse reflects from a solid wall and represents the reflection from the nozzle contraction upstream of the exit plane. This portion of the signal is thus closer in time to the incident pulse. In addition, the reflected pulse "tail" is elongated due to the propagation of the open

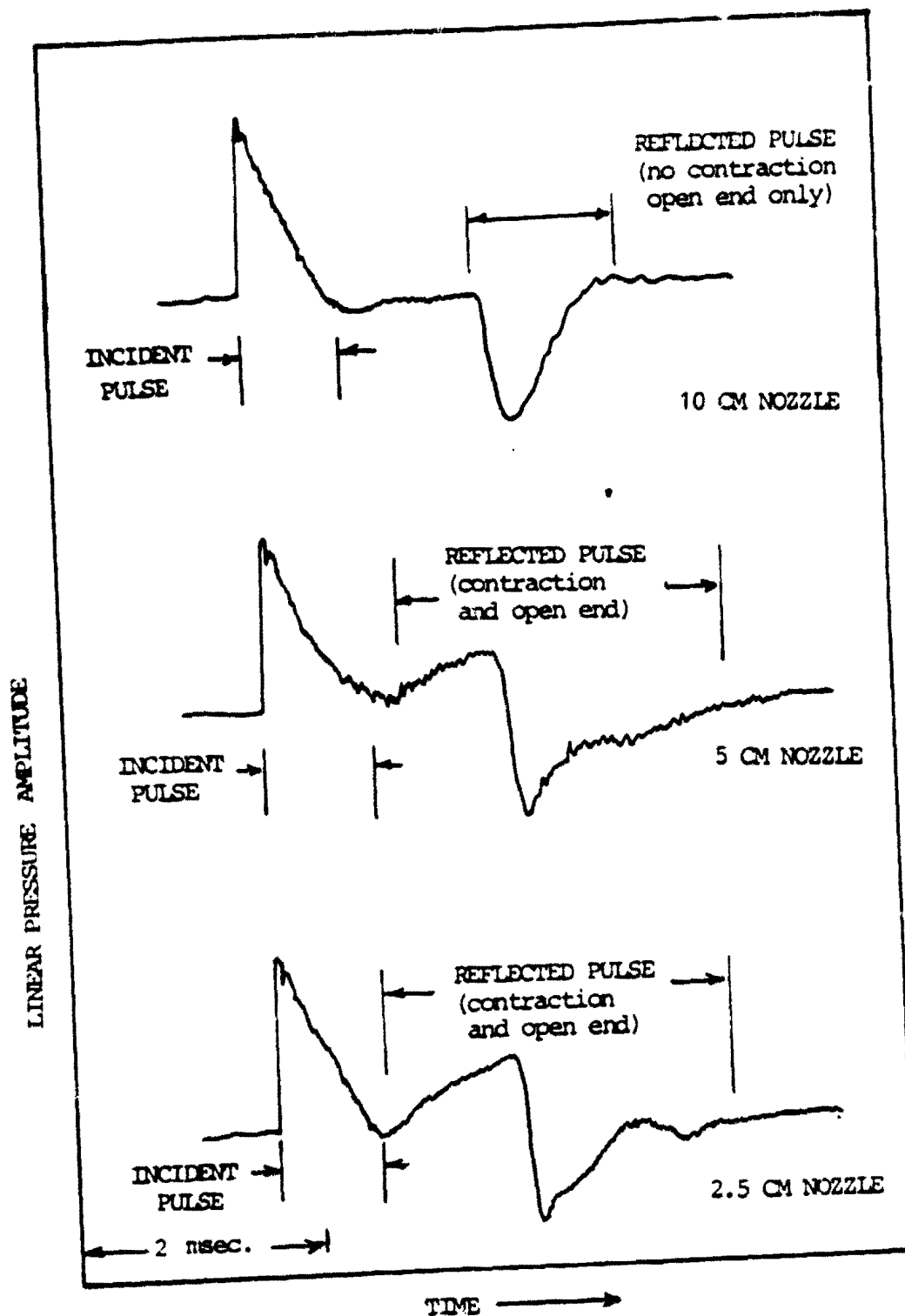


Figure 2.20 In-duct time histories for 10 cm, 5 cm and 2.5 cm diameter nozzles at zero flow velocity.

end reflection back up the nozzle contraction. Since these pressure-time history segments are the effects of nozzle geometry they cannot be edited out. The 2.5 cm nozzle pressure-time history behaves similarly to that of the 5 cm nozzle, with increased positive reflected amplitudes from the nozzle shoulder.

The reflection coefficients at the exit plane were obtained using a reflected pulse time rotation equal to the pulse propagation time from the upstream transducer to the exit plane and back to the transducer, whereas the radiation impedance was computed using the method described in Appendix A.

The reflection coefficient amplitudes and phases are shown in figure 2.21 for three nozzle configurations. The 10 cm pipe reflection coefficient is zero dB at zero frequency, indicating very inefficient low frequency radiation. For the 5 cm and 2.5 cm nozzles, two types of reflection are involved. The reflection of the nozzle contraction is in the form of a compression wave, in phase with the incident wave, whereas the reflection from the open termination is out of phase with the incident wave. These reflections tend to cancel at very low frequencies, giving a small reflection coefficient.

The termination impedance is shown in figure 2.22. Considerable differences are observed in the impedance values between the different nozzle configurations. There are two competing effects contributing to the nozzle impedance. First, the nozzle termination can be assumed to have a contribution that scales on nozzle exit diameter and is virtually unaffected by upstream conditions. Therefore, if the data are scaled on exit diameter, then some similarity should be observed. Second, there would be another component of nozzle impedance, due to nozzle contraction shape, that is, independent of the exit diameter. The reactance values collapse when the nondimensional frequency is scaled based on nozzle exit radius, up to a value  $kR_j \approx 0.8$ . However, no such trend was observed with the resistance values indicating that the nozzle contraction effect is more dominant on resistance.

In figure 2.23, the radiation directivity for the three nozzles is shown for two frequencies, scaled on  $kR_j$ , and it is seen that the radiation field directivity shapes do indeed collapse uniformly. The amplitude of the data shown in figure 2.23 is the transfer function amplitude (measured at a constant radius) between the pulse at a far-field location, and the upstream incident pressure pulse. For constant source strength at the nozzle exit, the level at the far-field location should decrease by 6 dB for each halving of nozzle diameter. However, the constant source strength in the duct is also being amplified at the nozzle exit plane by the duct-to-exit-area ratio, thereby offsetting the nozzle diameter change. The data here indicate conservation of energy as a function of nozzle diameter change.

#### 2.4.2 Theory vs. Measurements

An analytical model is developed in Appendix C to predict the acoustic behavior of conical nozzles with no mean flow. It is shown that for nozzles with small angles of convergence the acoustic properties will not differ markedly from those of a straight pipe which have been studied initially by Levine and Schwinger (ref. 2.5) and Ando (ref. 2.7). The analysis described in Appendix C makes use of an extension of the method of spherical

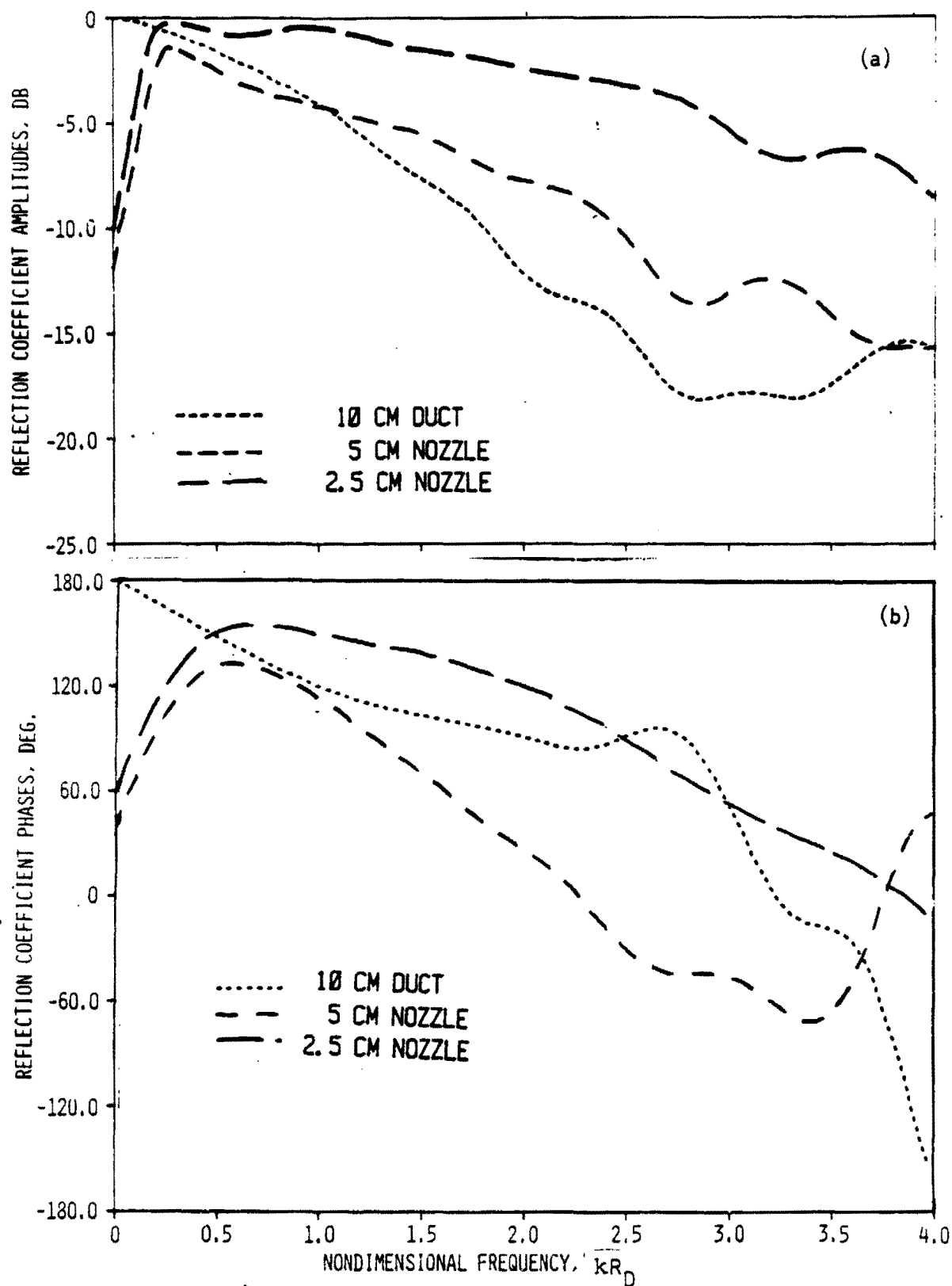


Figure 2.21 Reflection coefficients for 10 cm, 5 cm and 2.5 cm diameter nozzles at zero flow velocity.

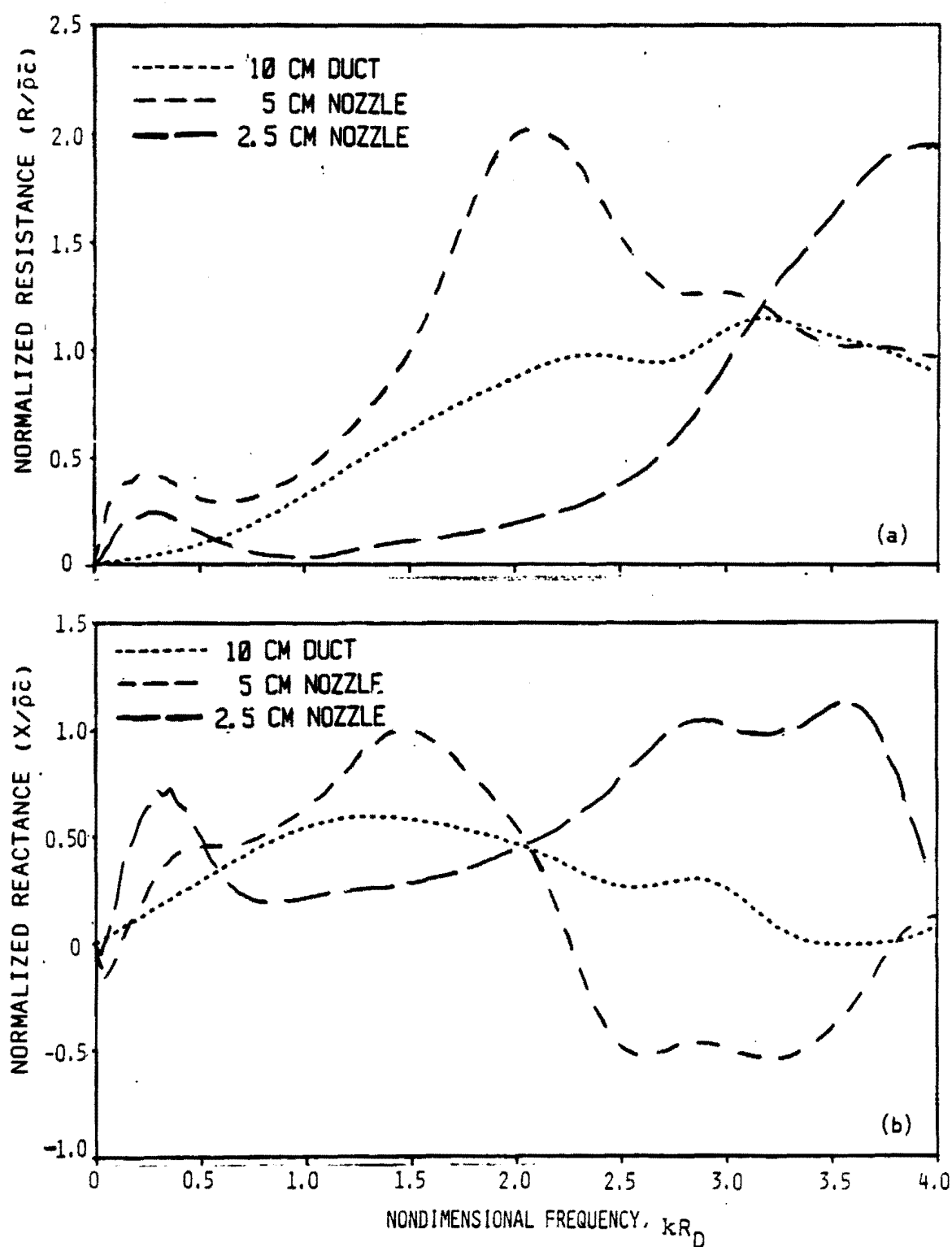


Figure 2.22 Radiation impedance for 10 cm, 5 cm and 2.5 cm diameter nozzles at zero flow velocity.

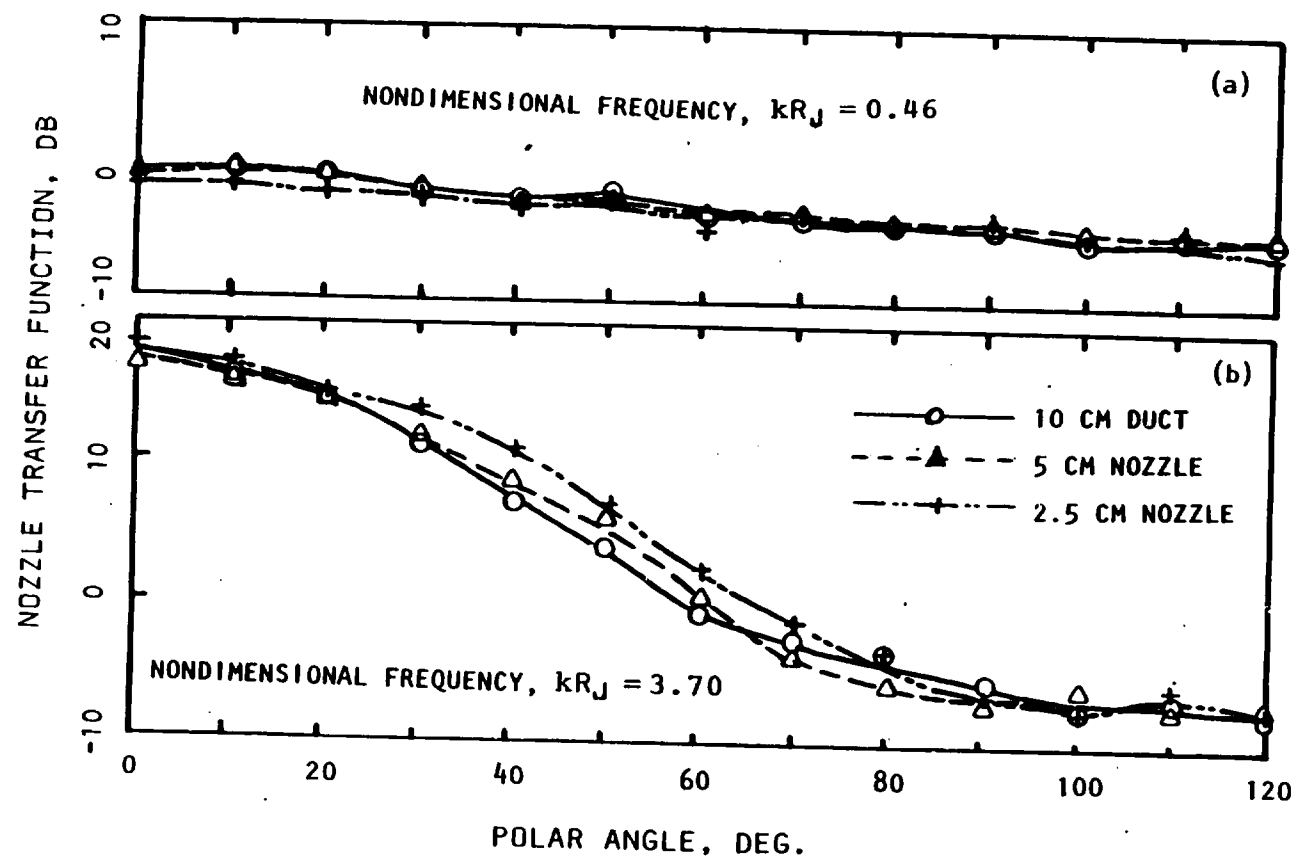


Figure 2.23 Far-field directivities for 10 cm, 5 cm and 2.5 cm diameter nozzles at zero flow for (a)  $kr_J = 0.46$  and (b) 3.70.

harmonics. This is then used to study the effects of nozzle angle of convergence on the radiated acoustic near- and far-fields, by comparing the far-field directivity, the acoustic radiation impedance and the reflection coefficient for three nozzles with angles of convergence equal to  $6^\circ$ ,  $10^\circ$  and  $20^\circ$ . These results are also compared with data derived from the measurements described above.

2.4.2.1 Directivity. - The three nozzles used in the numerical study have the following geometric properties. The length-to-nozzle-exit ratio is assumed infinite in each case; that is, there is no junction with a straight pipe. The half angles of convergence are  $6^\circ$ ,  $10^\circ$  and  $20^\circ$ . The far field is computed at  $r = 6 R_j / \sin \theta_0$ , where  $r$  is the spherical radial coordinate measured from the virtual origin, and  $R_j$  is the nozzle exit radius.

Although the analysis does not account for the effect of a shoulder (junction with a straight pipe) on the acoustic far-field, a comparison with a set of measured directivities for nozzles of finite lengths may not be too inappropriate. Figure 2.24 shows two sets of data corresponding to radiation from a straight pipe and a  $6^\circ$  convergent conical nozzle (radii 5 cm and 2.54 cm, and length 26 cm).

Clearly the comparison is rather good and further confirms the validity of the impulse technique.

2.4.2.2 Radiated Acoustic Power. - In the absence of mean flow the acoustic power radiated by a nozzle is governed by terms similar to those from a straight pipe. This power is proportional to the acoustic radiation impedance, the square of the velocity fluctuation at the nozzle exit and the surface area of the source.

For nozzles with small angles of convergence, the nozzle exit surface area is very nearly the same as that of a straight pipe if the exit radius is the same. Thus, the ratio of the acoustic power radiated by a nozzle to that radiated by a straight un baffled pipe is directly proportional to the ratio of the respective radiation resistance spectra. By making use of figure 2.24, the acoustic power ratio is plotted in figure 2.25 and a comparison is made with a corresponding set of measurements for two  $6^\circ$  nozzles.

The first observation is that in the low frequency range, the convergent conical nozzle radiates acoustic power more efficiently than an un baffled straight pipe. This is somewhat surprising, for one would have expected a greater mismatch between the convergent nozzle and the outer acoustic fields in comparison to divergent nozzles or acoustic horns. In this range the relative acoustic efficiency increases with nozzle angle of convergence.

The second observation is that above a critical frequency (which depends on the nozzle convergence angle) the acoustic radiation efficiency is lower than that of a straight pipe.

Finally, the two sets of measurements for the two nozzles correspond to an angle of convergence of approximately  $6^\circ$  (actually  $5.7^\circ$  and  $6.1^\circ$ ) and seem to confirm the trends predicted by the numerical analysis.

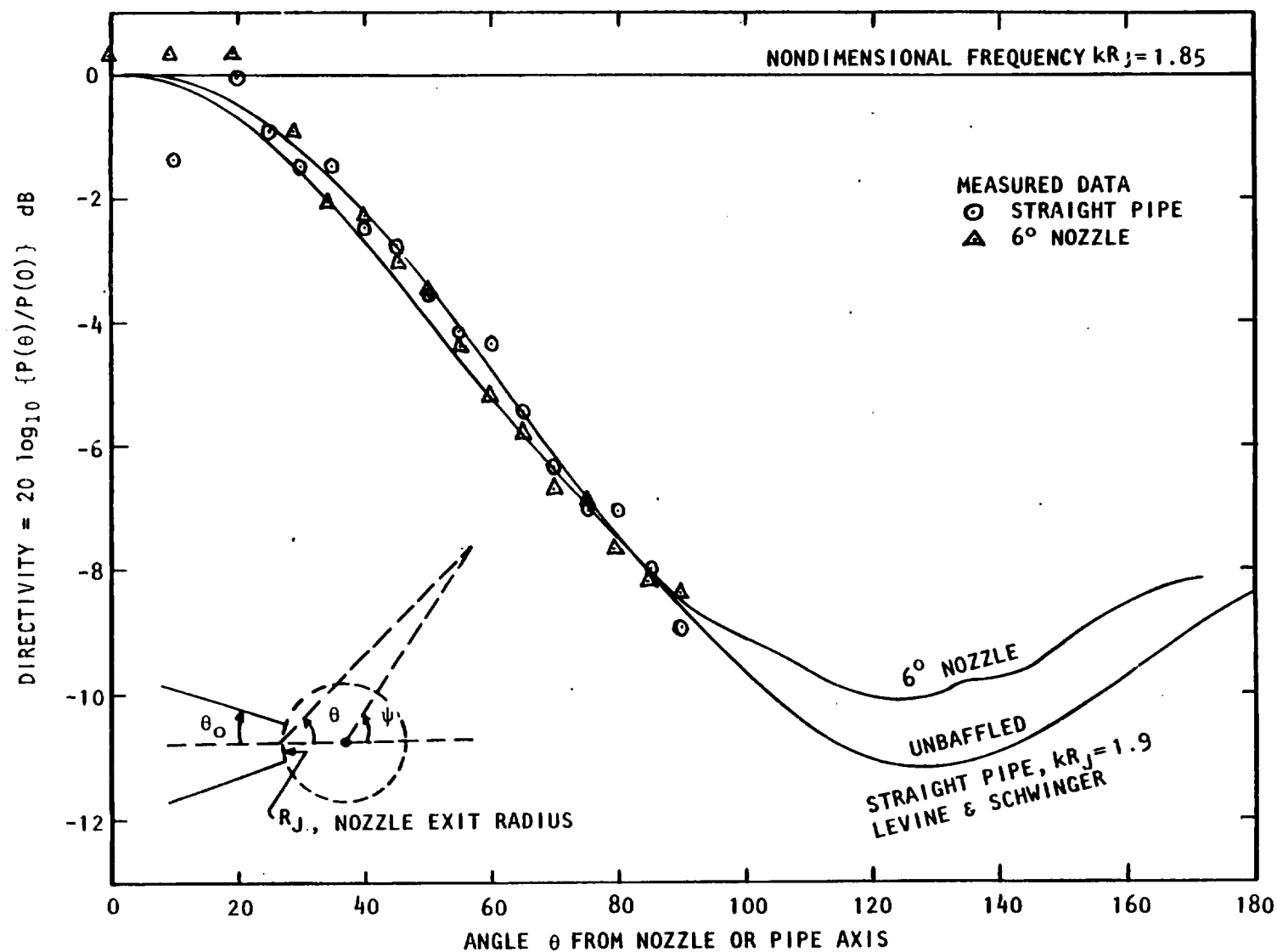


Figure 2.24 Comparison of measured directivity for a straight pipe and a 6° nozzle with present analysis (for 0° and 6° nozzles) and that of Levine and Schwinger for straight pipe.



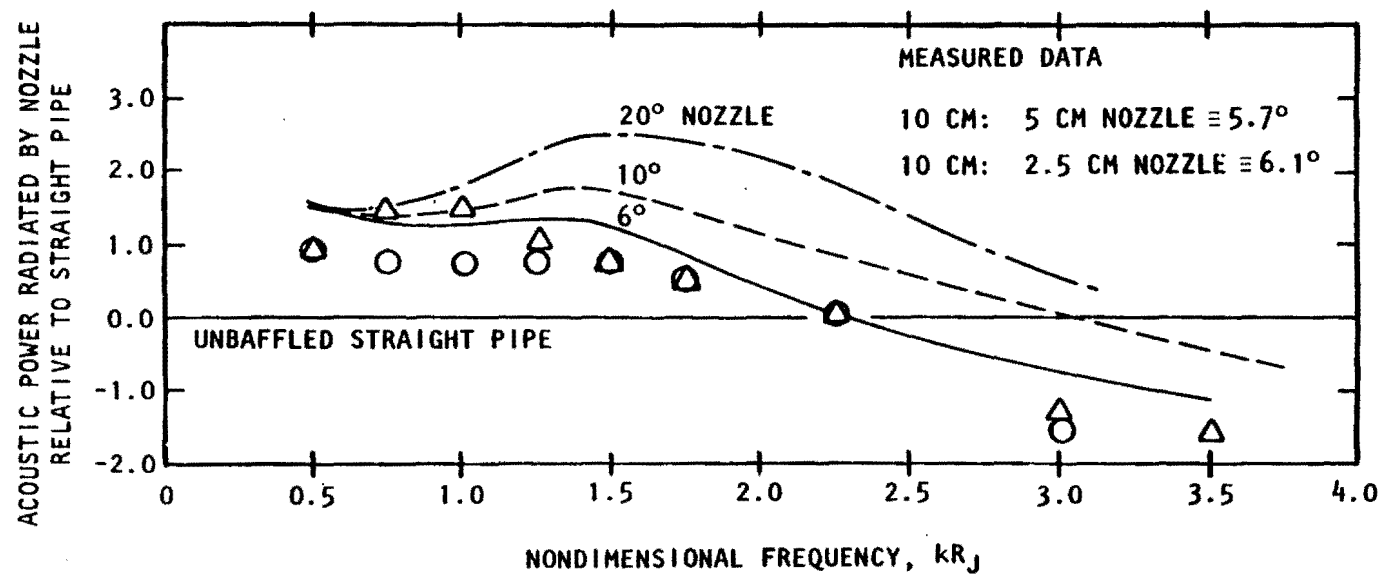


Figure 2.25 The efficiency of acoustic power radiation by 6, 10 and 20 degree nozzles relative to acoustic power radiated by an unbauffed straight pipe.

### 2.4.3 Effect of Flow

The impulse technique promises to be a useful method for testing the acoustic behavior of nozzle systems in the presence of flow. The primary advantage is that the intense pressure level of the peak can be detected above the flow-generated noise. If the major features of the impulse can be visually discerned, then the superfluous background noise can be eliminated by editing the time history.

In the following subsection, the test results of a 2.5 cm conical nozzle with exit flow velocities up to a Mach number of 0.81 are described. The in-duct pressure time histories are shown in figure 2.26. The analyzer display always shows the pulse leading edge at the same location because of its built-in triggering mechanism. Thus, no effect of convection can be seen there. However, by careful observation, it can be seen that the reflected pulse does stretch in time, indicating the slight increased propagation time required to make the round trip from the measurement point to the nozzle termination and back. Close examination of the reflected pulse shapes of figure 2.26 show that, as Mach number increases, the reflected pulse leading edge flattens, indicating more high-frequency sound transmitted outside.

Radiation impedance results calculated (using the method described in Appendix A) for these cases are shown in figure 2.27. It is observed that the reactance remains almost constant up to a nondimensional frequency of 0.3 for all Mach numbers and then decreases with increasing values of Mach number up to a nondimensional frequency of 1.0, except for  $M_j = 0.38$ , for which a sudden rise is observed between the nondimensional frequency of 0.65 and 1.0. Similarly, the resistance values decrease with increasing Mach number up to a nondimensional frequency of 0.3 and the peak values occur at a nondimensional frequency of 1.0. At higher frequencies, however, the trend is not very consistent.

The far-field pulse time histories are shown in figure 2.28 for polar angles of 20 degrees and 90 degrees. It is difficult to observe the direct consequence of the increase of high frequency transmitted energy as the jet Mach number increases because the refraction effect of the jet redistributes this energy to other polar angles away from the axis. This effect can be seen in the 20° case as a broadening of the pulse shape with increasing Mach number, indicating a depletion of high-frequency energy at this angle due to refraction. The time histories shown in figure 2.28 were Fourier transformed to obtain the radiation levels and directivity, based upon an analysis similar to that used in the discussion of nozzle diameter variations.  $kR_j$  of 0.6 has been chosen for this representative figure, as a particularly clear example of the physical phenomena involved.

It can be seen that as the jet exit velocity increases, the refractive effect near the axis grows rapidly, while the level in the region from 30° to 60° increases with increasing flow velocity. This off-axis increase is a result of energy being refracted from the cone-of-silence region. It should be noted also that levels in the forward arc decrease with velocity.

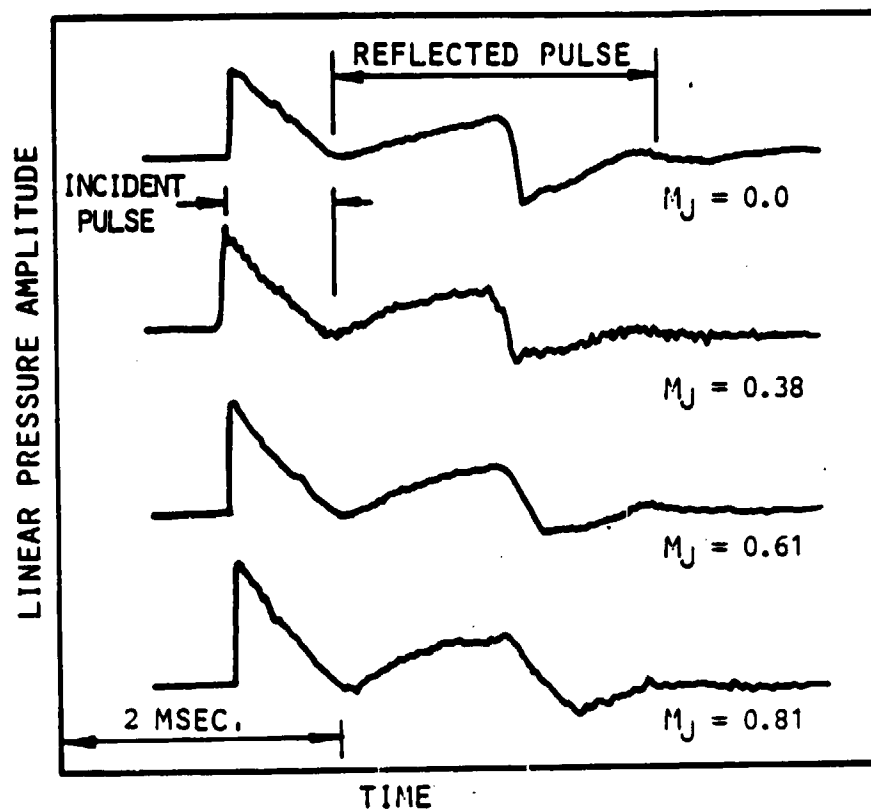


Figure 2.26 Effect of flow on in-duct time histories of 2.5 cm diameter nozzle.

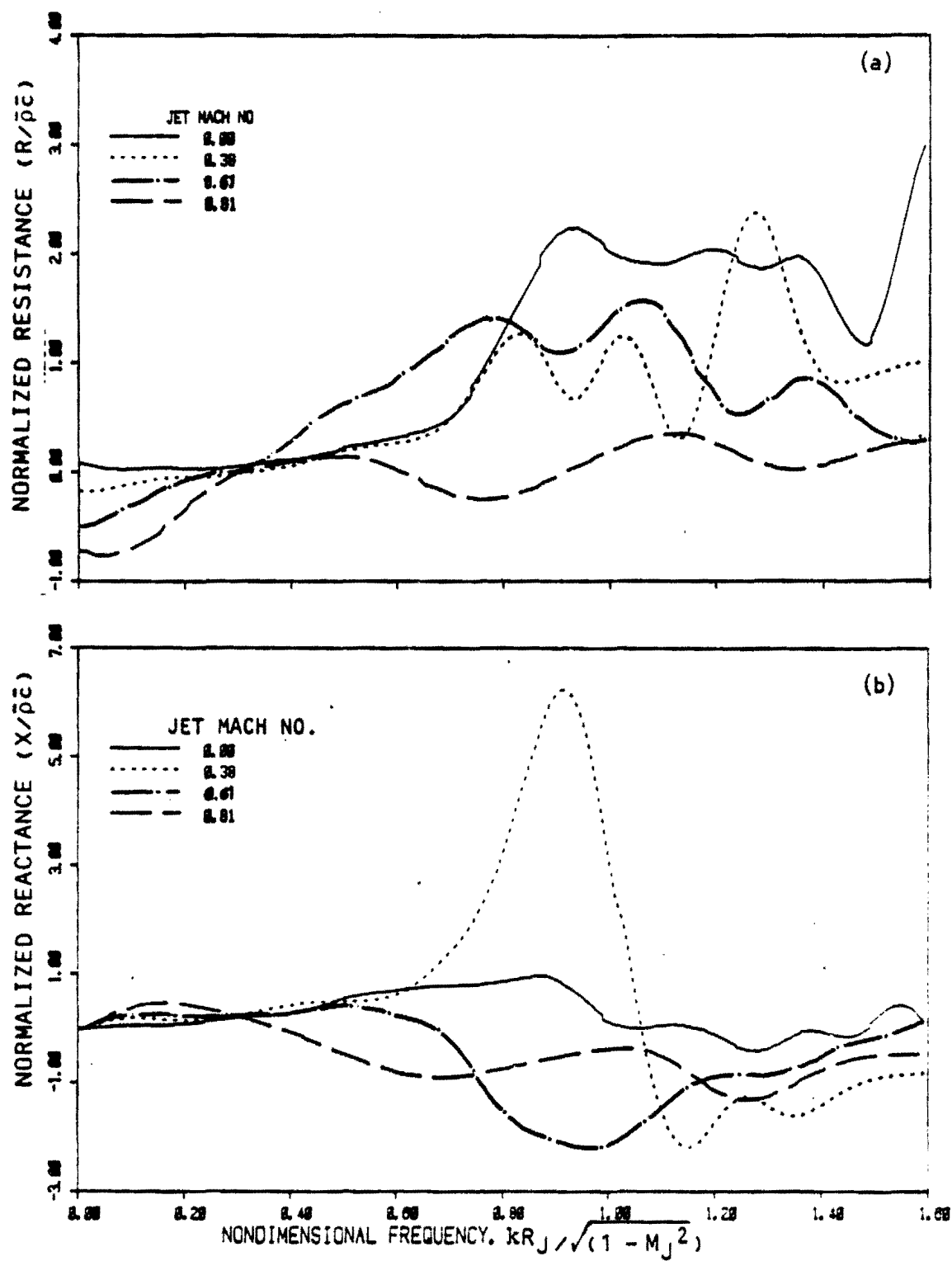


Figure 2.27 Effect of flow on radiation impedance of 2.5 cm diameter nozzle.

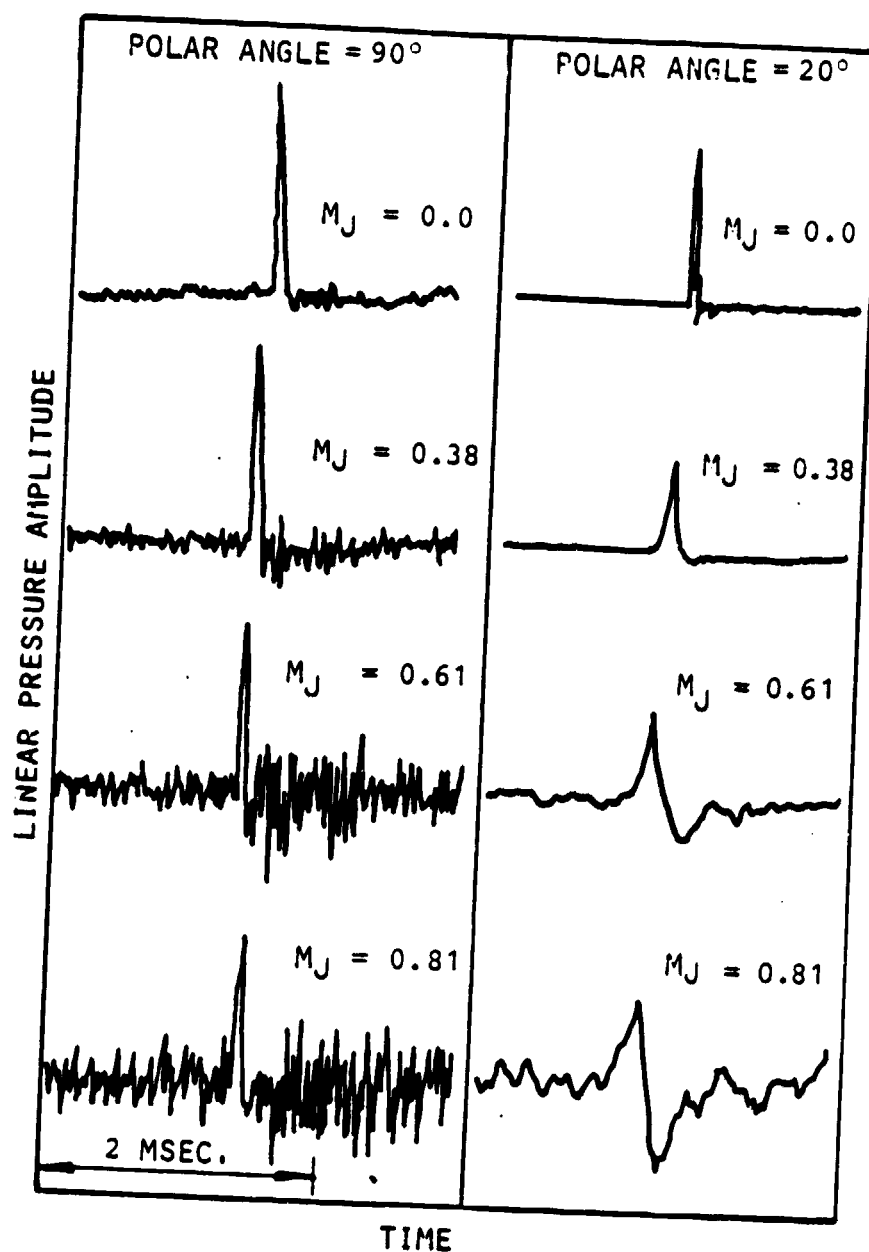


Figure 2.28 Effect of flow on far-field time histories of 2.5 cm diameter nozzle at 20° and 90° polar angles.

These general observations are corroborated by a superposition on this plot of the data by Pinker and Bryce (ref. 2.9) who performed a similar experiment. They used discrete frequency plane wave excitation in the jet pipe and measured the radiation directivity. This data, when compared with the results measured by the impulse technique, show excellent correlation (fig. 2.29). This lends further credence to the impulse technique and also validates the noise editing procedure using single impulses, rather than multiple impulse averaging (the traditional method of random background noise reduction).

Finally, the effect of jet velocity on spectrum levels is shown at two polar angles in figure 2.30. At  $30^\circ$ , an increase of jet velocity is shown to enhance low frequency radiation, but gives a substantial reduction at higher frequencies (due to refraction) observed before. At  $90^\circ$ , however, an increase of jet velocity tends to decrease levels at all frequencies. The high-frequency decrease, at both  $30^\circ$  and  $90^\circ$ , is compensated for by an increase in level from  $40^\circ$  to  $60^\circ$ , as shown in figure 2.29.

## 2.5 CONCLUSIONS FROM PRELIMINARY INVESTIGATION

The preliminary investigation had as its basic objective the determination of a valid test procedure. The three aspects investigated were: (1) the type of in-duct source, (2) the measurement technique, and (3) the appropriate signal analysis procedure.

Within this framework, the conclusions were:

(1) The impulse acoustic source was to be utilized for all tests. It would be produced by a spark discharge across an air gap resulting in a close approximation to a point source.

(2) The in-duct measurements would be performed by a single point transducer placed in such a way that the pulse reflected from the nozzle can be separated in time from the incident pulse. This single measurement point is an approximate indicator of the total incident in-duct energy.

(3) The appropriate nozzle transmission coefficient was defined to be identical to the magnitude of the transfer function between the far-field mean square pressures of the pulse and the in-duct mean square pressures. The in-duct mean square pressure was normalized to represent the far-field pressure produced by a point source of equivalent in-duct power. This transfer function was computed from the Fourier transform of the appropriate in-duct and far-field transient time histories after appropriate editing to reduce extraneous noise.

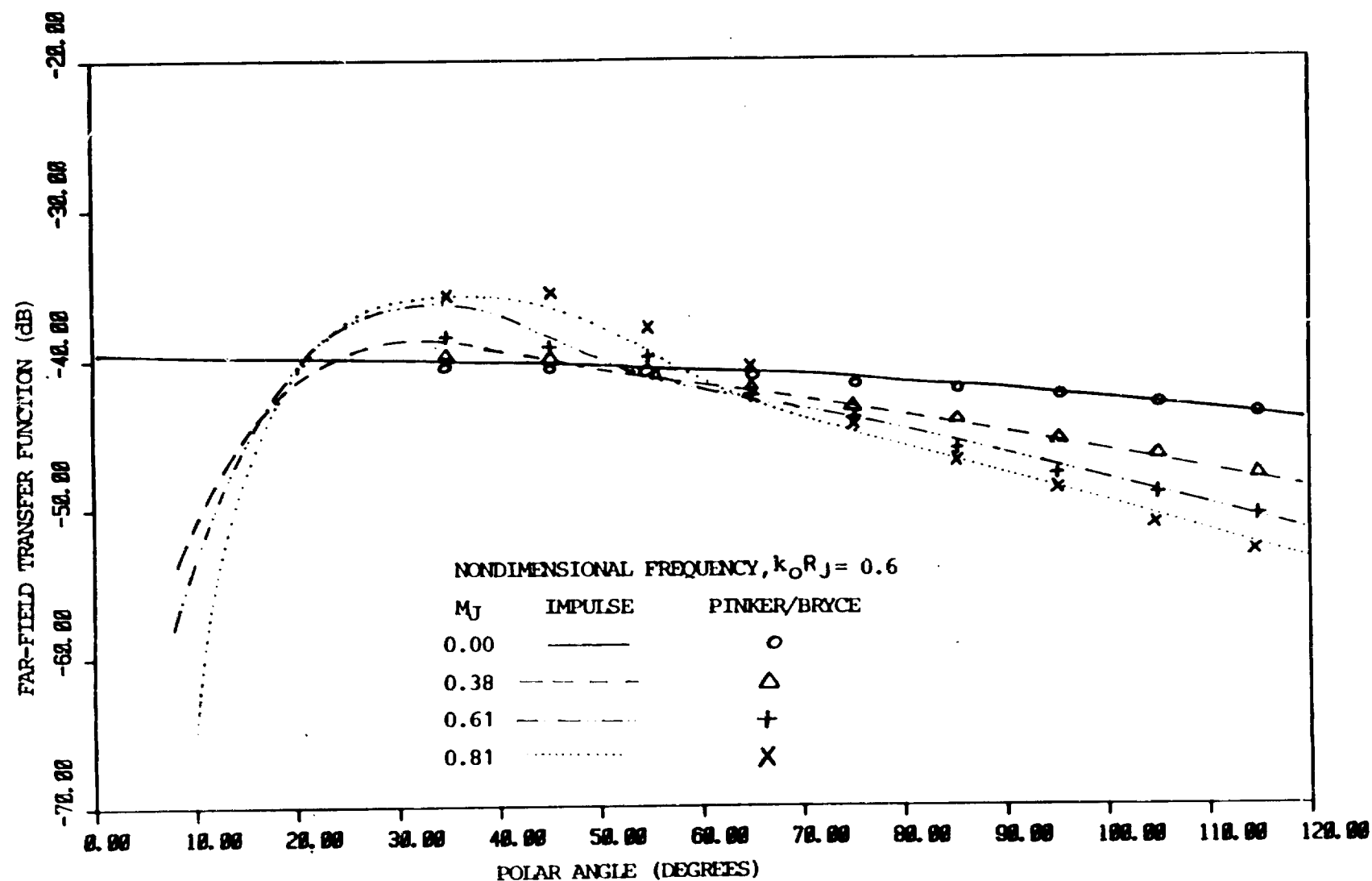


Figure 2.29 Far-field directivity comparisons between impulse method and Pinker and Bryce data for 2.5 cm diameter nozzle for flow Mach numbers of 0.0, 0.38, 0.61 and 0.81 at  $k_0 R_J = 0.60$ .

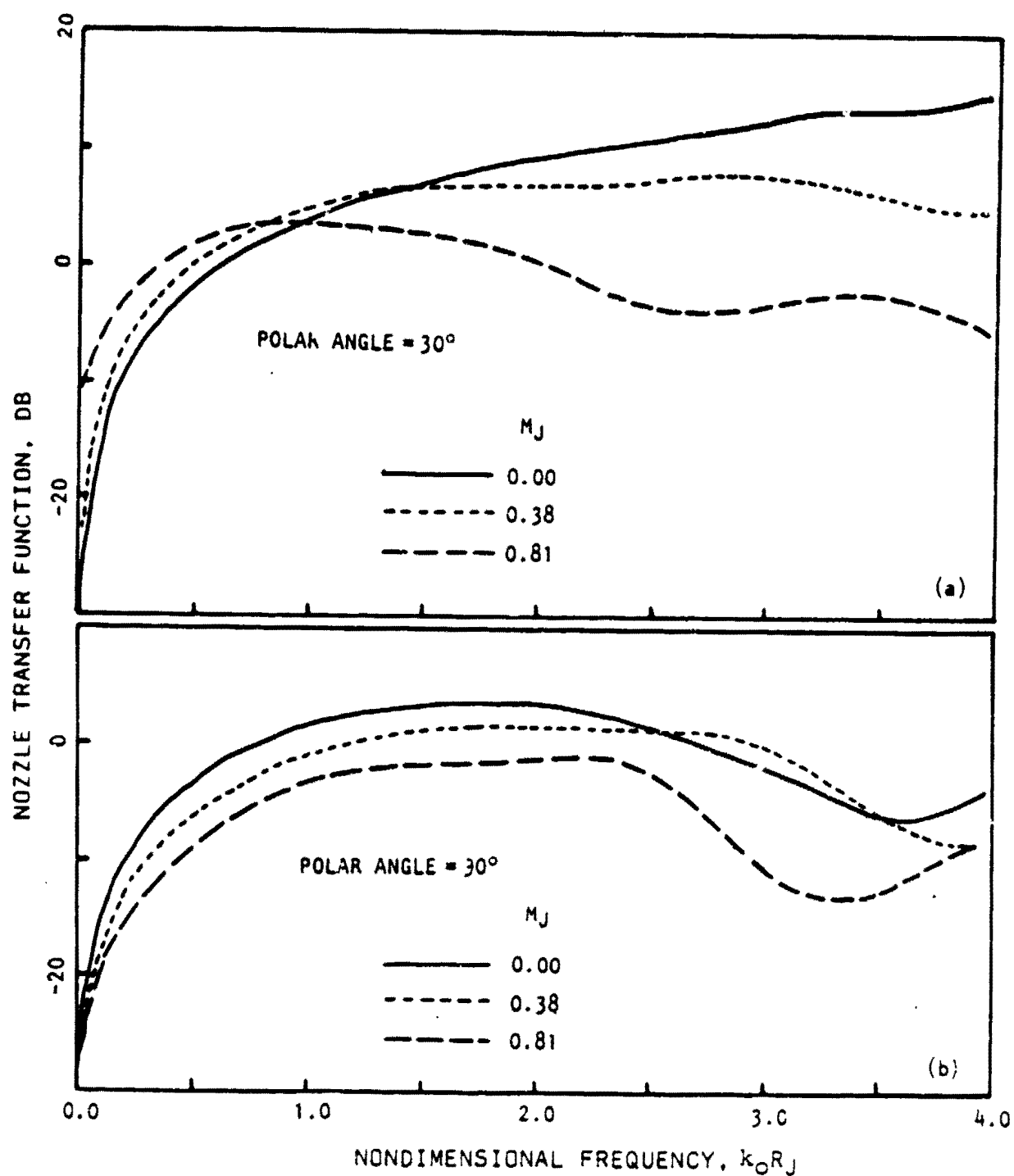


Figure 2.30 Effect of flow on nozzle transfer function spectra of 2.5 cm diameter nozzle at  $30^\circ$  and  $90^\circ$  polar angles.



### 3. TEST CONFIGURATIONS AND PROCEDURE

#### 3.1 FACILITY DESCRIPTION

The acoustic measurements for determining the nozzle transmission coefficient of the coaxial nozzle system were conducted in the Lockheed anechoic facility. This facility has been used extensively in the past to make measurements of noise from single jets. In 1977, the existing single jet rig was modified to enable measurements of noise from dual-flow jets. This modified facility, and the calibration tests conducted to check both the acoustic and aerodynamic cleanliness of the facility are described in detail in reference 3.1.

The anechoic chamber provides a free-field environment for all frequencies above 200 Hz, and incorporates a specially-designed exhaust collector/muffler which (1) provides adequate quantities of jet entrainment air, (2) distributes this entrainment air symmetrically around the jet axis, and (3) keeps the air flow circulation velocities in the room to a minimum.

The air for the primary and secondary jets is supplied by the main compressor which provides up to 9 Kg/sec. of clean dry air at  $2.07 \times 10^6$  Pa. The air is heated by a propane burner to approximately 1100K. The primary and secondary air supplies are controlled independently downstream of the burner. Each supply has a hot and cold valve such that the desired operating conditions can be obtained within the pressure and temperature limitations of the system. Each air stream is then directed through a set of diffuser/muffler systems to minimize internal noise levels. The primary flow then passes through banks of electric heaters so that the primary plenum temperature may be further raised to ~1350K. The two streams finally enter their respective plenums which are located upstream of the coannular nozzle section.

In order to insure that the relative axial positions of the exit planes of the two nozzles do not vary, a special expansion coupling has been incorporated in the primary duct work, with a corresponding spacer in the secondary duct work. It provides for expansion or contraction of the inner duct relative to the outer duct of  $\pm 4$  mm from center which is adequate for the thermal expansion associated with the likely temperature differentials between primary and secondary flows.

##### 3.1.1 Nozzle Description

The test nozzle configuration is shown schematically in figure 3.1. In all, six secondary nozzles were used in conjunction with one fixed primary nozzle of diameter 7.62 cm (3 in.) and conical half-angle of  $15^\circ$ . The outer nozzles were constructed from 321 stainless steel in order to satisfy the temperature limits. These outer nozzles are defined in Table 3.1 by means of convergence angle and an axial-to-annulus-width ratio ( $L/h$ ). The length,  $L$ , is the difference between the primary and the fan exit planes.

Table 3.1  
Outer Nozzle Designations

Nozzle No.	Angle, Deg.	L/h	L, Cm
1	20	1	1.373
2	20	3	5.124
3	20	5	11.295
4	40	1	1.373
5	40	3	5.124
6	40	5	11.295

These nozzles are shown in figures 3.1 and 3.2. The complete facility with the nozzles in place is shown in figure 3.3.

### 3.1.2 Source Section

Internal noise was generated by inducing sparks across two electrodes separated by 0.1 cm to 0.2 cm wide air gaps. The spark source for the primary plenum is shown in figure 3.4. As shown in this figure the spark source was used in conjunction with a parabolic reflector. The spark source (electrode gap) itself was placed at the focus of the paraboloid. The effect of the reflector was to both increase the impulse energy travelling in the axial direction and to modify the wave front from spherical to essentially plane in nature.

To minimize the flow disturbances around the reflector, the inner surface of the primary plenum in the vicinity surrounding the reflector was suitably contoured such that the flow velocities did not increase significantly due to the presence of the reflector. Furthermore, specially designed cruciforms facing downstream were attached to the periphery of the paraboloid reflectors, to reduce the separation farther downstream. This cruciform arrangement is not shown in the photographic view (fig. 3.4) for the sake of clarity but is shown schematically in figure 3.5(a). Measurements with and without the cruciforms showed that they had no significant effect on the acoustic behavior of the reflector.

Figure 3.5(b) shows a schematic of the source section for the secondary plenum. For the secondary plenum, six spark sources, equi-spaced in the secondary annulus, were used. Three of these spark sources are visible in the photographic view in figure 3.6. Here also, paraboloid reflectors fitted with cruciforms were used. Each of the spark gaps in this case was connected in series through high voltage cables such that all of them fired simultaneously. Unlike the electrodes for the primary plenum, where the two electrodes faced each other, the secondary-plenum electrodes had an included angle of about 20°.

Each electrode was removable through a threaded connection and entered the paraboloid through narrow openings drilled on the side of the paraboloids. Except for its tip, the entire length of the electrode was surrounded by a ceramic sleeve. This prevented cross-firing between the electrode and the grounded metal parts in the vicinity.

Nozzle #	L/h	$r_i$ (cm)	$h = r_i/3$	$r_o$	L	$A_2$	$A_2/A_1$
1,4	1	4.118	1.373	5.491	1.373	41.45	0.91
2,5	3	5.123	1.708	6.831	5.124	64.14	1.41
3,6	5	6.776	2.259	9.035	11.295	112.21	2.46

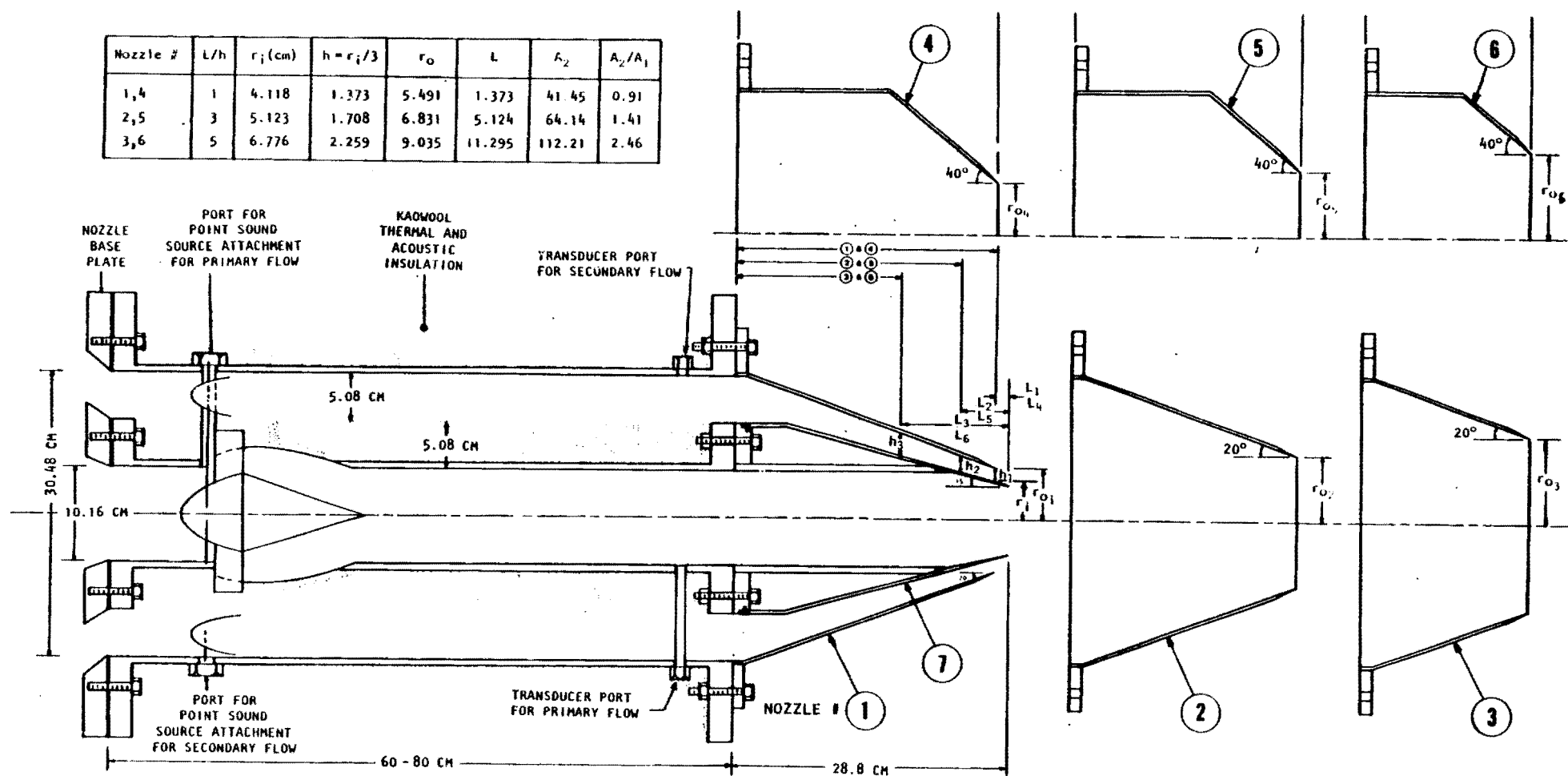


Figure 3.1 Test nozzle configuration.

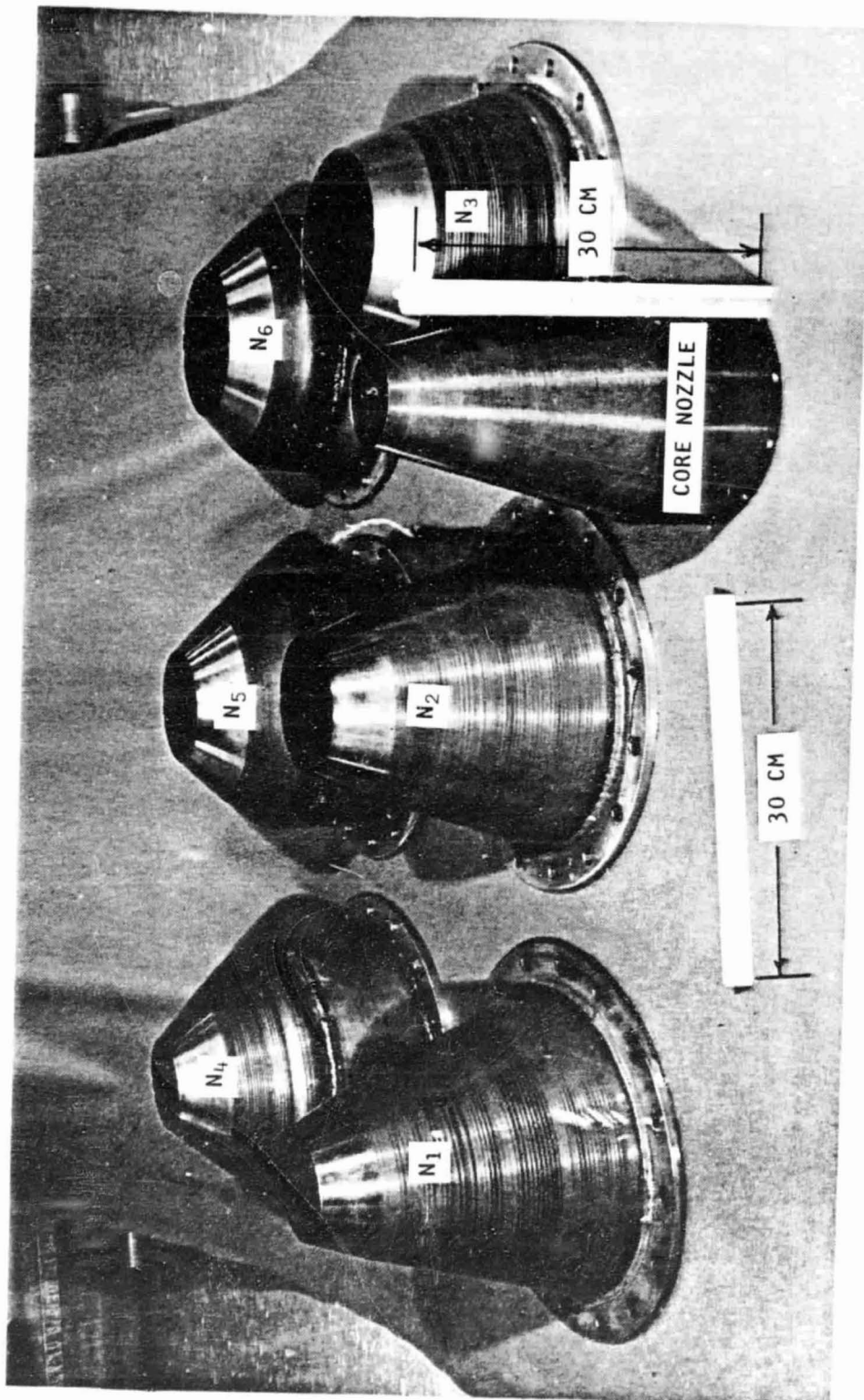


Figure 3.2 Illustration of core and fan nozzles  $N_1$  to  $N_6$ .

REPRODUCIBILITY OF THE  
ORIGINAL PAGE IS POOR

56  
INTENTIONALLY BLANK

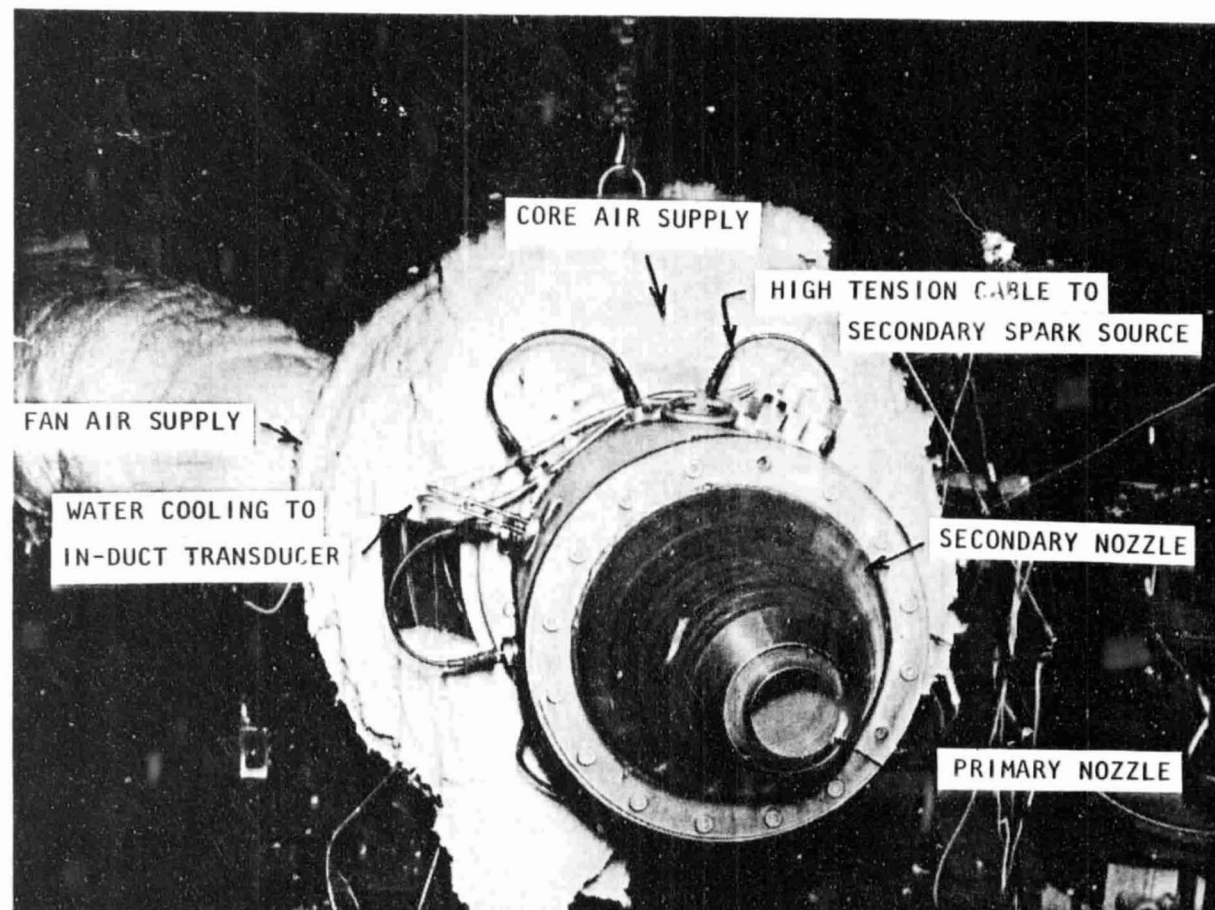


Figure 3.3 Illustration of coaxial jet facility.

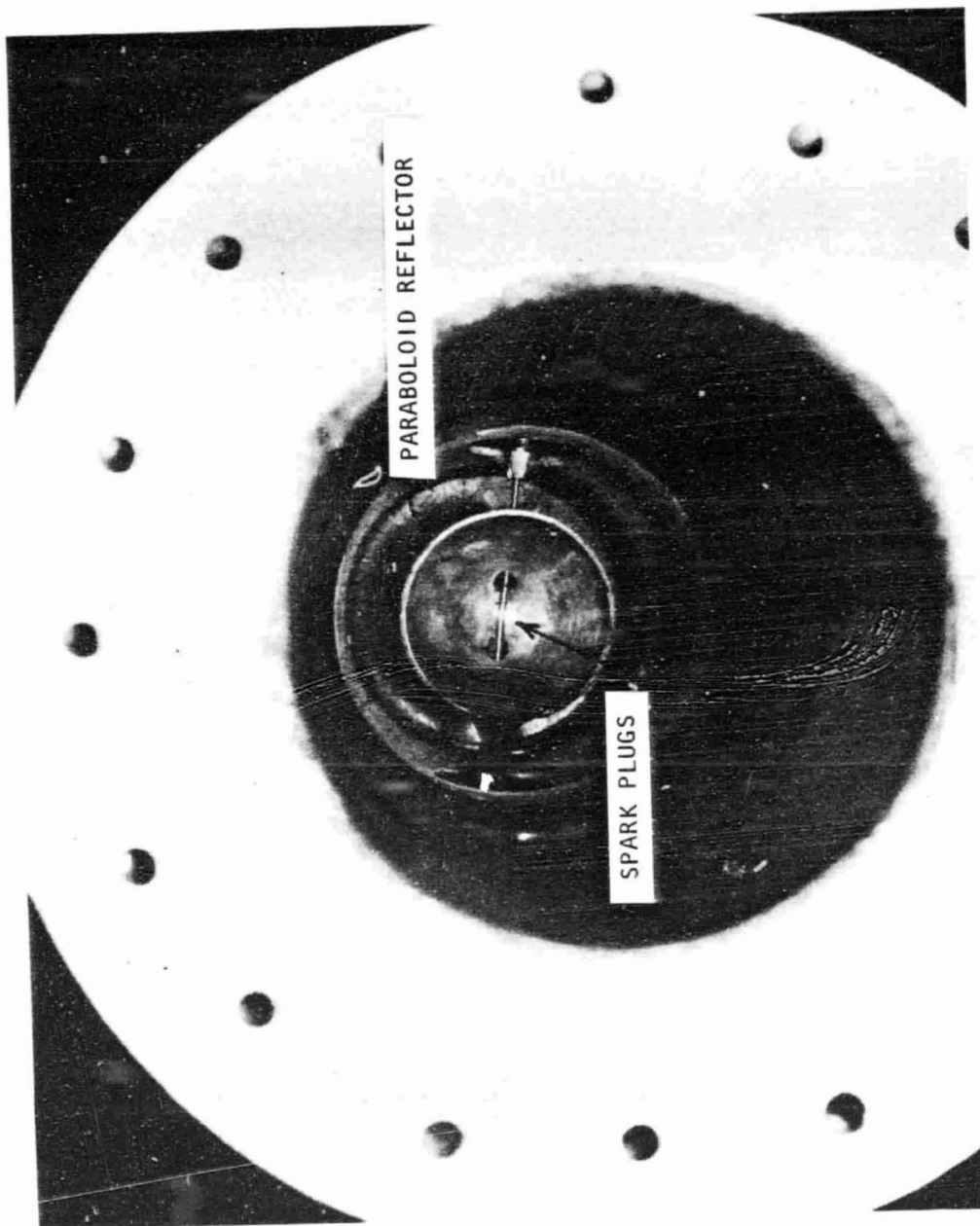


Figure 3.4 Source section of core nozzle plenum.

REPRODUCTION OF THE  
ORIGINAL PAGE IS POOR

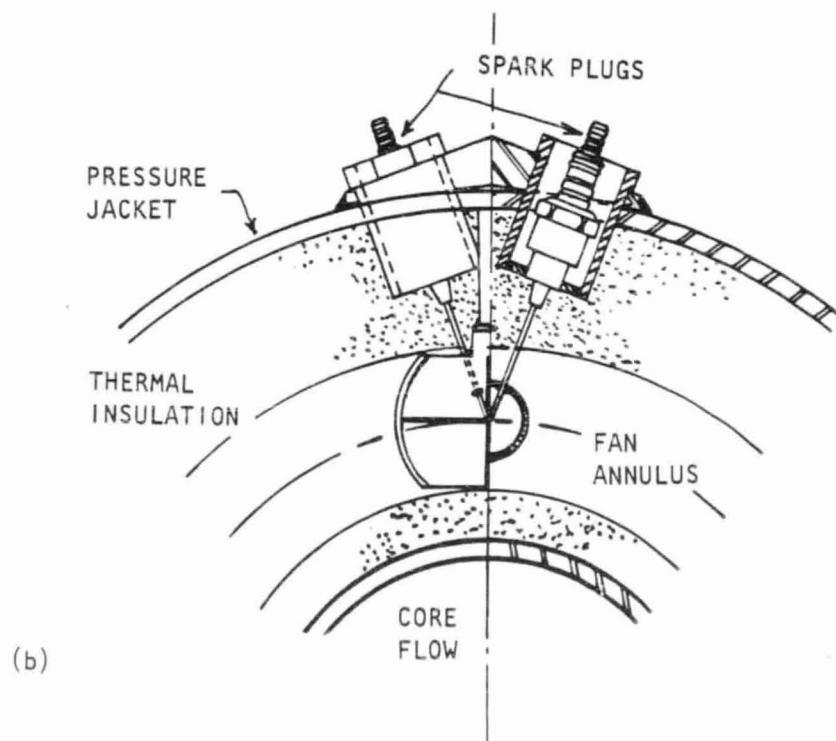
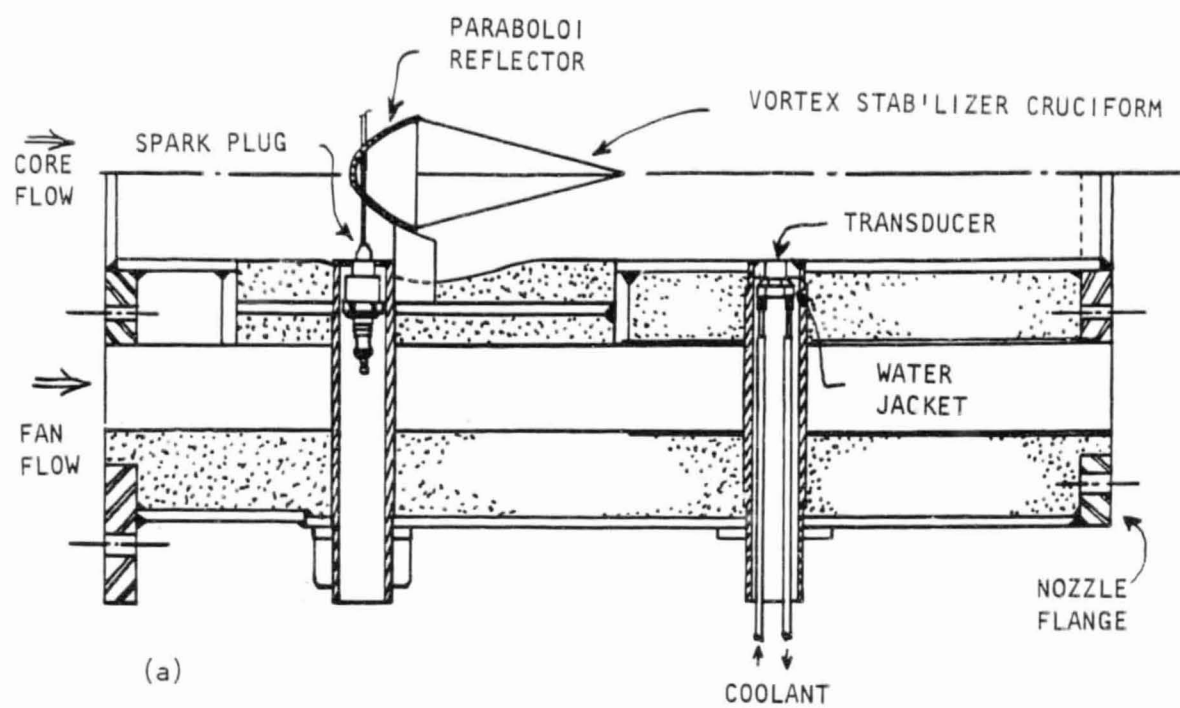


Figure 3.5 Schematic of the source sections for the (a) primary plenum and (b) secondary plenum.



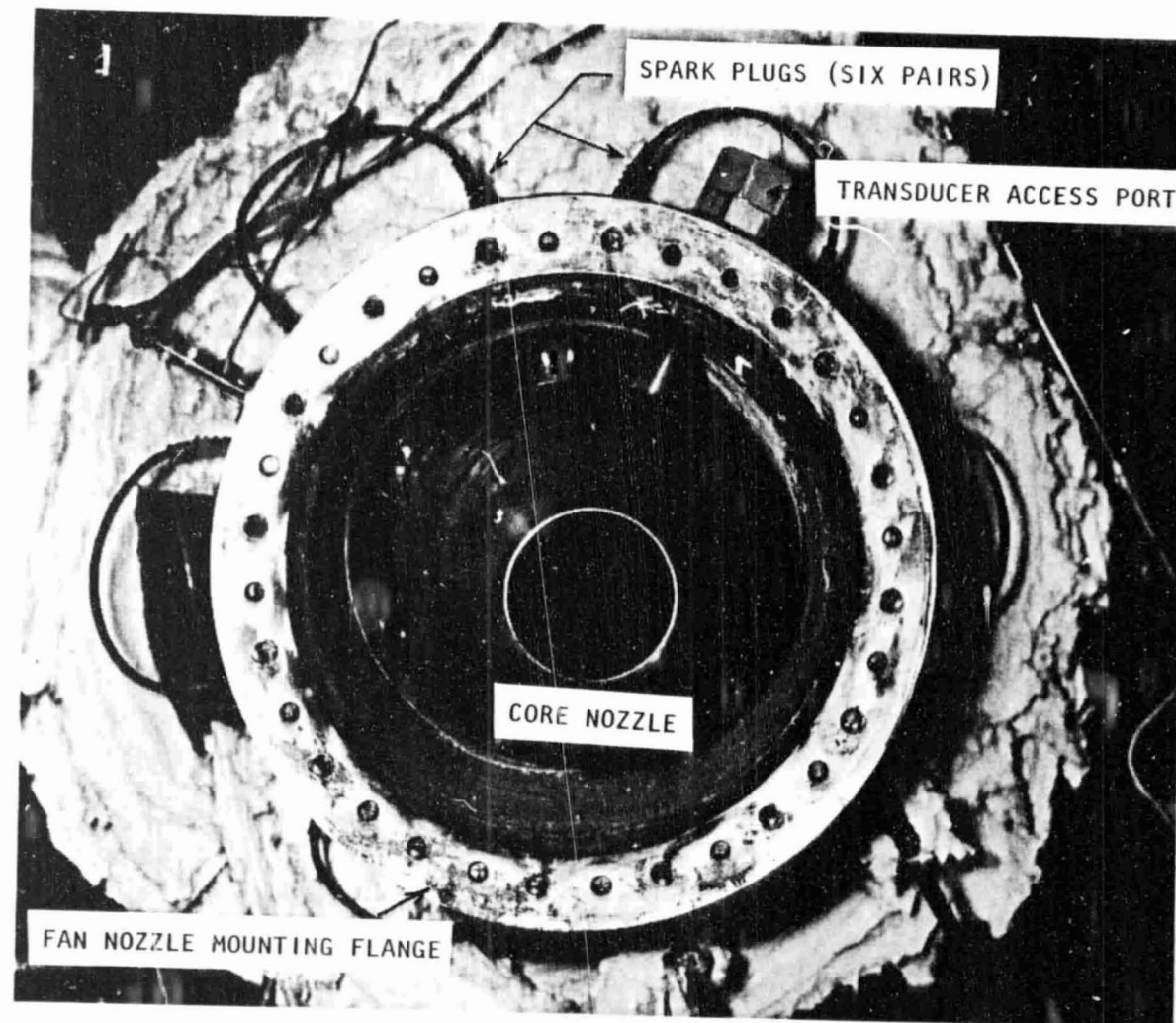


Figure 3.6 Source section of fan nozzle plenum.



To determine the effect of the presence of the source-section upon far-field jet noise, a short facility validation exercise was carried out. Without firing the spark but with the jet operating, far-field spectra were measured and compared with those predicted by the SAE method. Typical comparison for  $V_j/\bar{c} = 0.9$  and  $\theta = 90^\circ$  is shown in figure 3.7 for flow only through the primary nozzle. Excellent agreement with the measured data and the predicted jet mixing noise indicates that the presence of the paraboloidal reflector in the pipe upstream had little effect on the far-field jet noise.

To determine the effect of the secondary source section, both jets were operated simultaneously at the same Mach number. At this condition, the coaxial jet is equivalent to a single jet of diameter equal to that of the secondary jet. This condition is best met when the two coaxial nozzles are coplanar and the lip thickness of the primary nozzle approaches zero. In the present nozzle combination,  $L/h=1$  configuration (outer nozzle diameter = 10.98 cm) was closest to being coplanar. The corresponding far-field spectra measured with both jets operated at  $M_j = 0.9$  is compared in figure 3.8 with that predicted for the equivalent single jet by SAE method. Once again, except for frequencies below 200 Hz, the secondary source section also has negligible effect on the far-field jet noise.

### 3.1.3 Spark Circuit

The essential elements of the spark discharge circuit are shown in figure 3.9. A high voltage power supply charges a storage capacitor (70  $\mu\text{F}$ ) to 5 to 10 KV. The discharge of the capacitor occurred through the air gap between the electrodes, thus producing a powerful, but physically small, acoustic pulse.

To fire the spark, special vacuum switches were used to prevent current surges back through the power supply. It was found essential to "float" the capacitor from all ground circuits as the discharge currents (~2,000 amp) induced local ground potential shifts, with resultant digital equipment malfunctions.

## 3.2 TEST PLAN

The nozzle system consists of a primary and secondary (fan) nozzle, each with its own nozzle transmission coefficient. Two sets of measurements were thus required for primary and fan nozzle, respectively. As shown in Table 3.2, each of the outer nozzles was tested for the unheated conditions with the source located in the fan. With the source located in the primary (or core), only the outer nozzles designated 1, 2 and 3 were used.

The heated-jet tests were, however, limited to the measurement of the fan nozzle transmission coefficient only. Only two nozzles (#1 and #2) were tested.

Seven unheated-jet test conditions were employed and are given in Table 3.3.

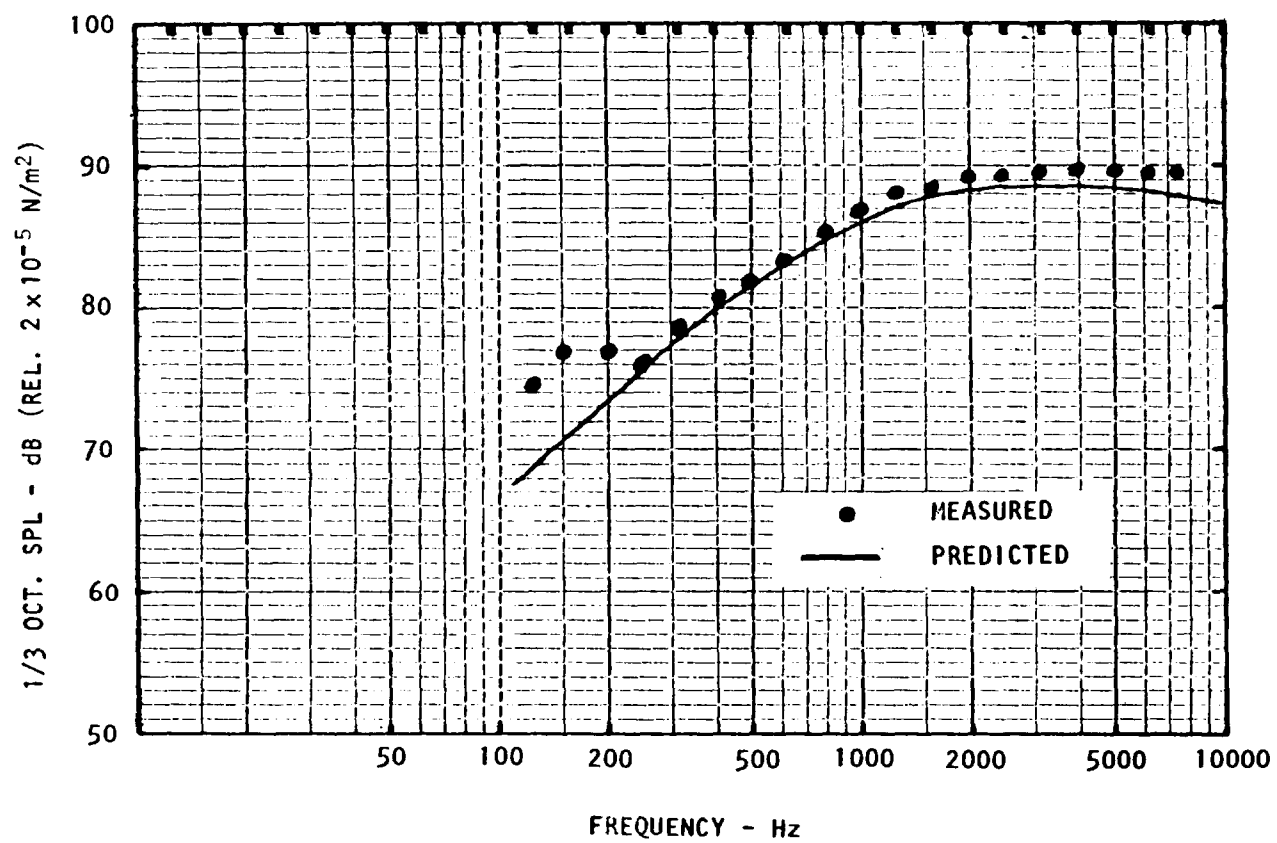


Figure 3.7 Comparison of measured far-field noise spectrum with SAE prediction for primary jet.  $M_{J1} = 0.9$ ;  $M_{J2} = 0$ ;  $\theta = 90^\circ$ ;  $R_m = 3m$ .

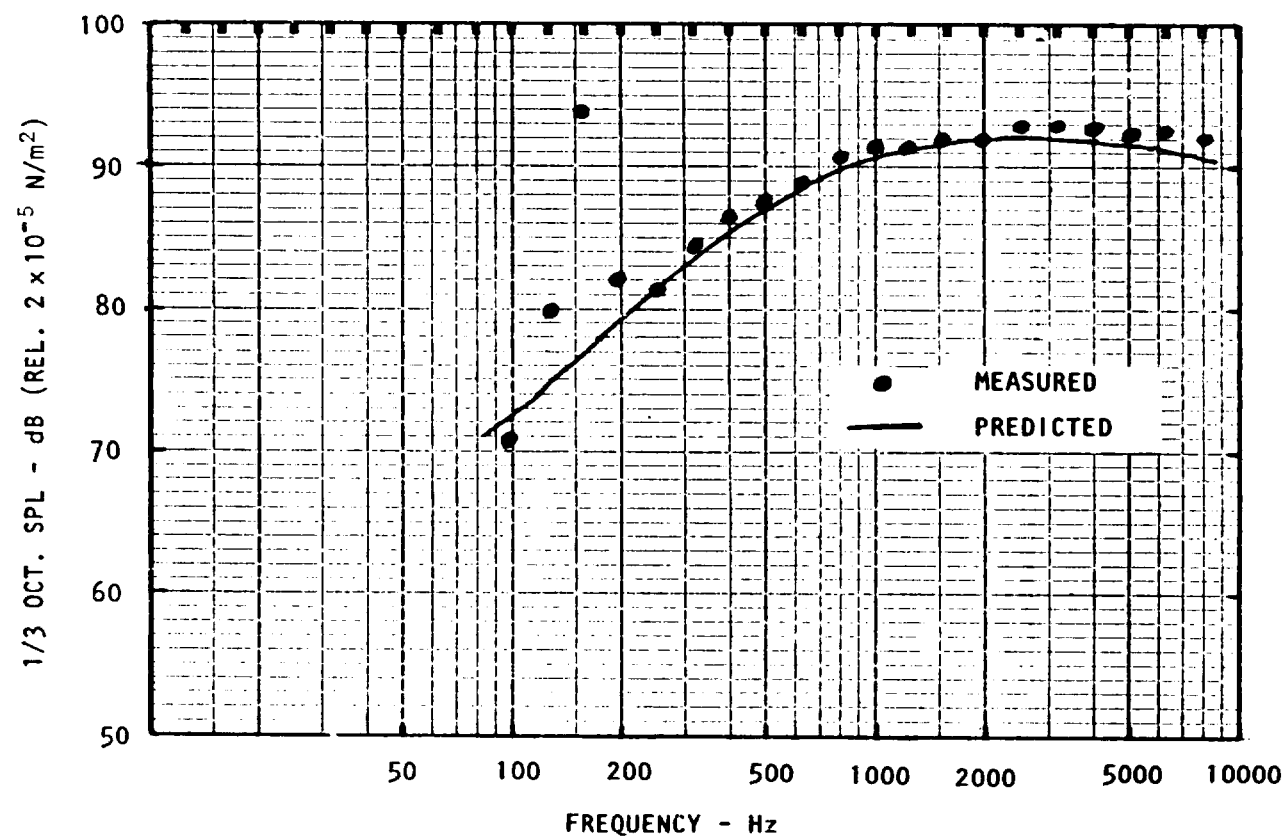


Figure 3.8 Comparison of measured far-field noise spectrum of coaxial jet with SAE prediction for equivalent single jet.  $M_{J1} = M_{J2} = 0.9$ ;  $\theta = 90^\circ$ ;  $R_m = 3m$ .

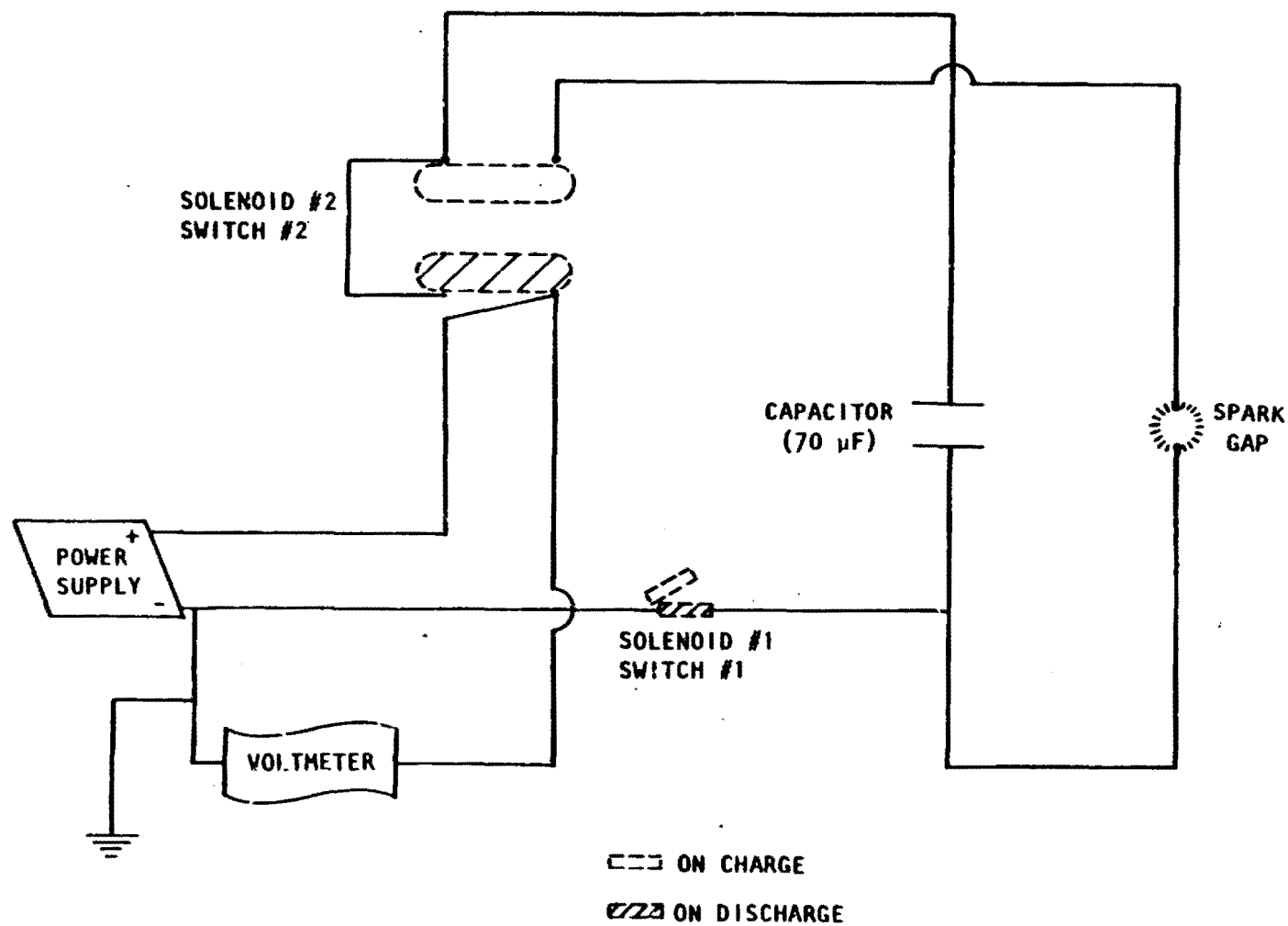


Figure 3.9 The spark discharge circuit.

Table 3.2  
Nozzle Test Summary

Outer Nozzle No.	Location of Source	Jet Condition
1,2,3,4,5 and 6	Fan	Unheated
1,2 and 3	Primary	Unheated
1 and 2	Fan	Heated

Table 3.3  
Unheated Nozzle Test Conditions\*

Run No.	$M_{J1}$	$P_{R1}$ (KPa)	$M_{J2}$	$P_{R2}$ (KPa)
1	0.0	0.0	0.0	0.0
2	0.4	11.5	0.6	27.1
3	0.8	51.5	0.9	68.0
4	0.8	51.5	1.2	140.2
5	0.8	51.5	1.4	214.5
6	1.2	140.1	1.4	140.1
7	0.0	0.0	1.2	140.1

\*Since Mach number is the only specified parameter, the stagnation temperatures and pressures may vary slightly from those given due to air supply temperature and atmospheric pressure variations of a day-to-day nature.

The heated jets were tested over 12 operating conditions which are given in Table 3.4. It should be noted that the total pressure values given in Tables 3.3 and 3.4 are calculated assuming that the ambient temperature was 294K and the ambient pressure was 98 KPa. Variation of  $\gamma$  with temperature has been taken into account in calculating the operating pressures for heated jets.

The heated jets were tested over twelve operating conditions and are given in Table 3.4.

Table 3.4  
Heated Nozzle Test Conditions\*

Run No.	Primary Nozzle			Fan		
	$M_{J_1}$	$T_{R_1}$ (K)	$P_{R_1}$ (KPag)	$M_{J_2}$	$T_{R_2}$ (K)	$P_{R_2}$ (KPag)
1	0.8	294	51.5	0.9	600	67.3
2	0.8	294	51.5	0.9	759	66.5
3	0.8	294	51.5	0.9	900	66.0
4	0.8	450	51.5	0.9	600	67.3
5	0.8	562	51.1	0.9	759	66.5
6	0.8	675	50.7	0.9	900	66.0
7	0.8	294	51.5	1.2	600	139.4
8	0.8	294	51.5	1.2	759	138.0
9	0.8	294	51.5	1.2	900	136.9
10	0.8	450	51.5	1.2	600	139.4
11	0.8	562	51.1	1.2	759	138.0
12	0.8	675	50.7	1.2	900	136.9

\*Since Mach number is the only specified parameter, the stagnation temperature and pressures may vary slightly from those given due to air supply temperature and atmospheric pressure variations of a day-to-day nature.

### 3.3 DATA ACQUISITION AND ANALYSIS

#### 3.3.1 Facility Instrumentation

The in-duct signals were measured by a Model 202 Series Piezotron pressure transducer made by a Sunstrand Data Control, Inc. This transducer has a rugged stainless steel mounting with provision for water cooling. The transducer was located 28 cm downstream of the spark source and 48 cm upstream of the primary nozzle exit plane. The transducer was mounted in an electrically isolated bushing (nylon for cold tests and ceramic for hot) to avoid ground-induced voltage spikes from the spark discharge E.M. radiation (see figs. 3.3 and 3.5).

Far-field signals were measured on an arc of 3.05 m radius with 0.635 cm diameter B&K microphones (Type B&K 4135) in conjunction with B&K cathode followers (B&K 2619). Measurements in the far-field were made in the polar angle range  $0^\circ$  to  $120^\circ$  at intervals of  $10^\circ$ .

The basic test procedures consisted of firing the spark at the desired operating flow conditions and simultaneously recording the signals, both in-duct and the far-fields, on a 14-channel tape recorder. Subsequent analysis of each pulse was achieved conveniently on a dual-channel transfer function analyzer, while maintaining accurate time interrelationships between impulse signals. The system schematic is shown in figure 3.10.

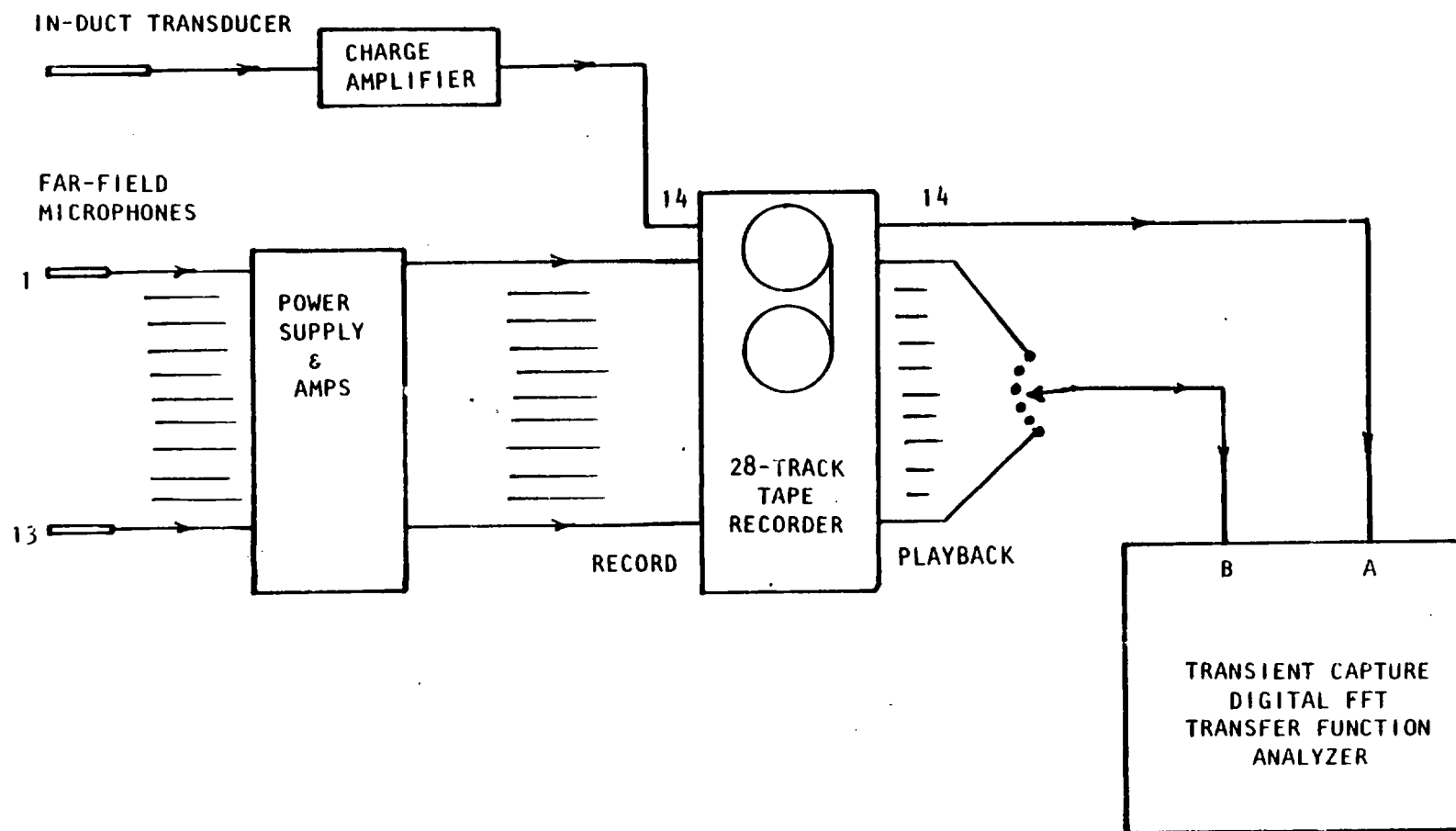


Figure 3.10 Instrumentation layout.

### 3.3.2 Transient Capture and Editing

The method of capturing the in-duct pulse and that in the far-field was similar to that described under the results of the preliminary investigation. For this part of the program, primary interest was in the in-duct incident pulse and the corresponding far-field pulse. Little attention was paid to the pulse reflected back from the nozzle exit plane.

Using the transient capture capability of the digital FFT signal analyzer (Spectral Dynamics SD360), the in-duct and the far-field signals were first captured on channels A and B. The analyzer has the ability not only of capturing the time histories, but also of data editing and relative time translation (rotation). With the exception of the two highest Mach numbers (1.2 and 1.4) where jet noise levels are quite high, the far-field pulse was easily detectable. The in-duct pulse, however, was always strong. Having located the in-duct pulse and the corresponding far-field pulse, all components of the two time histories except these two pulses were edited out. An example of this procedure is shown in figure 3.11. The two pulses were then Fourier transformed to produce their respective power spectra. The ratio of far-field to in-duct power spectra was then taken to be the transfer function as discussed in section 3.3.1. This procedure was repeated for each measurement angle.

The above transfer functions were obtained up to a frequency of 100 KHz. Since atmospheric absorption becomes important at these frequencies, appropriate corrections were made to the far-field data in accordance with the data of reference 3.2.

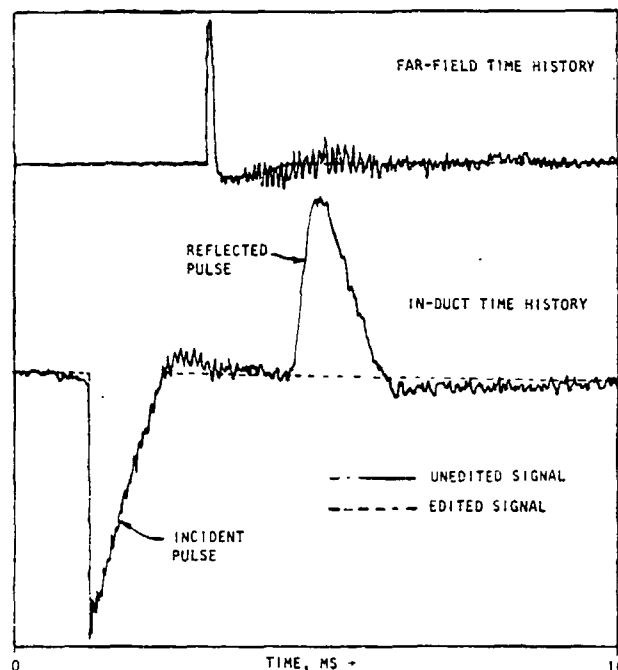


Figure 3.11 An example of the editing process used in the evaluation of incident and transmitted power spectra.



### 3.3.3 Calibrations of Far-Field Microphones with Respect to the In-Duct Transducer

In order to obtain a true measure of the transfer function  $B/A$ , it was essential to account for the frequency responses of each microphone and the in-duct transducer. This was accomplished by mounting the transducer next to a given microphone as shown in figure 3.12 and measuring the noise of a pulse generated by a spark source mounted at a location directly in front of the transducer and the microphone. The spark source produced a pulse with high spectral energy up to a frequency of 100 KHz. Since the signals captured by the microphone and the transducer were the same, a transfer function between the two was the calibration of one with respect to the other. Using the in-duct transducer as the reference, the calibration of each microphone was thus obtained and incorporated as a frequency response correction. A typical frequency response is shown in figure 3.13.

### 3.3.4 Transformation and Smoothing

The power spectra of edited in-duct and far-field signals are obtained by the Fourier transform of each pulse using the digital FFT signal analyzer. These data (some 512 spectral points of constant bandwidth) are recorded on cassettes and then transferred to a mini-computer for frequency response and atmospheric corrections. Each corrected record is then individually smoothed to remove fine detail of little practical interest. The transfer function spectra between the far-field and in-duct signals is then computed from these smoothed in-duct and far-field spectra.

The transfer function spectra between in-duct and far-field signals are also noisy in nature, particularly in the higher frequency range. With this situation it is difficult to distinguish between the effect of any nozzle operating parameter, such as flow velocity, flow temperature, nozzle shape, etc. on the transfer functions. Therefore, to obtain a more meaningful comparison, an averaging procedure has also been used to smooth the transfer function spectra which are computed from the smoothed power spectra of individual signals. The smoothing technique (a standard derivative of Simpson's rule) used in this study can be illustrated as follows. The smoothed value of the function (or power spectra),  $F$ , at the  $l^{\text{th}}$  frequency point is given by

$$\bar{F}(l) = \frac{F_1(l)}{X_{l+m} - X_{l-m}} \quad (3-1)$$

where

$$F_1(l) = \frac{H}{3} \left\{ F(l-m) + 4F(l-m+1) + 2F(l-m+2) + 4F(l-m+3) + \dots + 2F(l+m-2) + 4F(l+m-1) + F(l+m) \right\}, \quad (3-2)$$

$X_l$  = coordinate of  $l^{\text{th}}$  point,

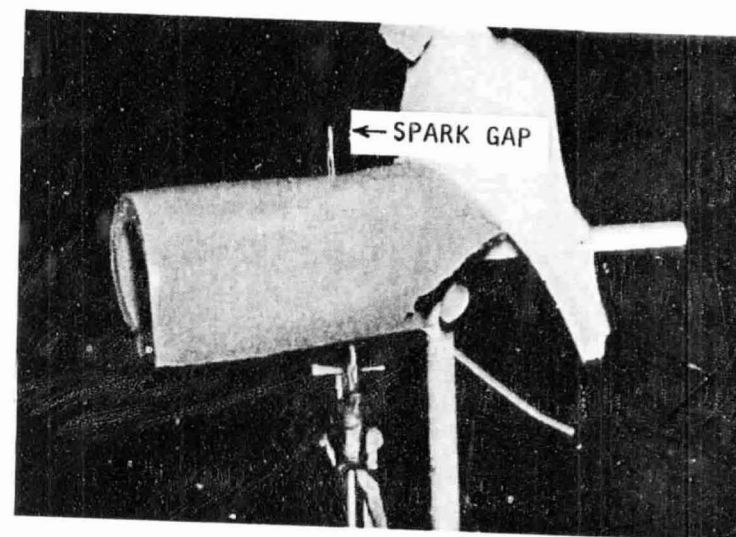
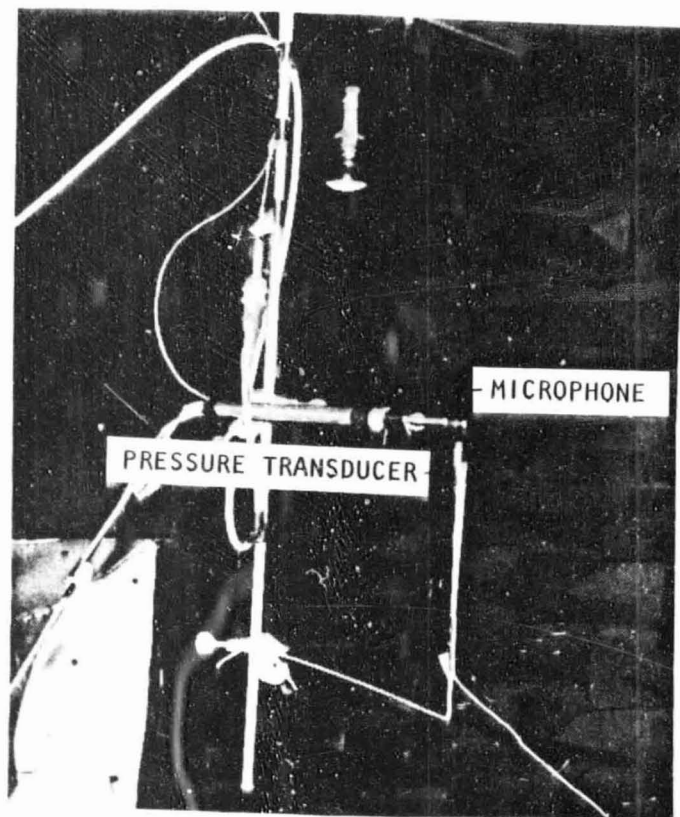


Figure 3.12 Illustration of microphone/pressure transducer calibration using the spark source.

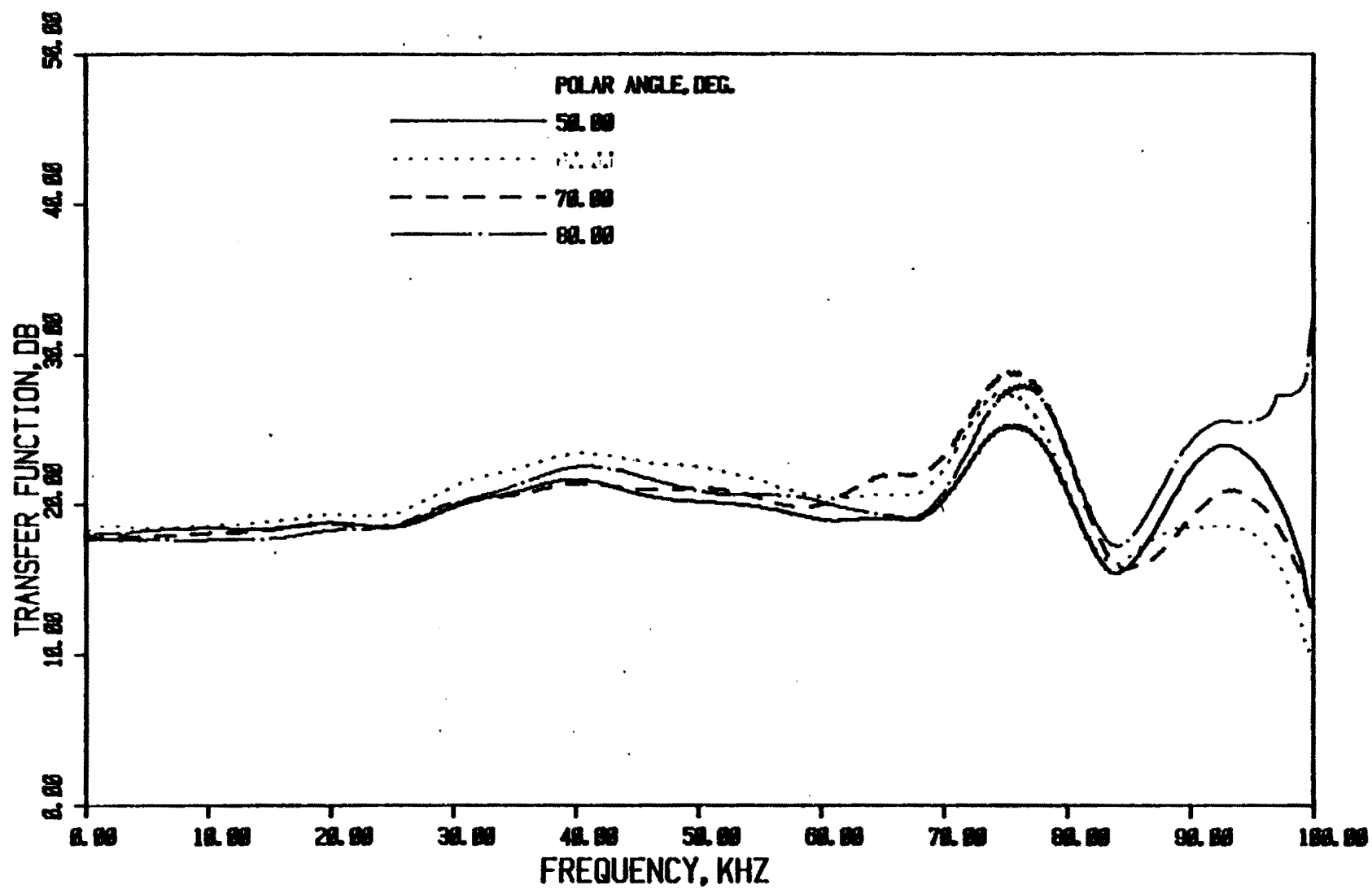


Figure 3-13 Typical frequency response calibrations between the in-duct transducer and the microphone used in the far field.

$H$  = difference between the coordinates of two successive points,

$2m+1$  = number of points used for averaging,

and  $n = 2m+1$ .

In the smoothing procedure, the number of points  $n$  has been varied with respect to frequency. The number  $n$  is chosen such that it becomes equal to the octave band for a given frequency, up to a maximum of 31 points. (The difference between two successive points is the bandwidth which is 200 Hz in this case.) The smoothing process is repeated three times to obtain a more uniform variation. The number of points,  $n$  used in smoothing is given by

$$n = 1/\sqrt{2} \quad (\text{rounded up}) \leq 31.$$

(If  $n$  comes out to be even, then it is increased by one.)

Typical in-duct and far-field power spectra before and after smoothing are shown in figures 3.14(a) and 3.14(b), respectively. The corresponding spectra of the transfer function calculated from the values in figures 3.14(a), and (b) are plotted in figure 3.14(c).

The average value of the transfer function at the  $j$ th frequency point is obtained by summing the smoothed transfer function data  $\bar{F}$  between the frequency points  $1/\sqrt{2}$  to  $1 \times \sqrt{2}$  and dividing the sum by the corresponding number of frequency points, as described below.

$$\text{Let } n_1 = 1/\sqrt{2} \quad (\text{rounded})$$

$$n_2 = 1 \times \sqrt{2} \quad (\text{rounded})$$

$$\bar{\bar{F}}(j) = \left[ \sum_{J=n_1}^{J=n_2} (\bar{F}(J)^2 / (n_2 - n_1 + 1)) \right]^{1/2}. \quad (3-3)$$

where  $\bar{\bar{F}}(j)$  = Average transfer function at  $j$ th frequency point.

This procedure is repeated for each polar angle to provide a basic directivity at the far-field measurement point.

### 3.3.5 Data Normalization

Based on the corrected smoothed individual data, two normalization procedures were undertaken for the purposes of comparison between operating and geometrical parameters. The first simply transforms the absolute frequency to nondimensional frequency based on the parameter  $2\pi\ell/\lambda$ , where  $\ell$  is a characteristic length and  $\lambda$  is the wavelength. For the core,  $\ell$  is

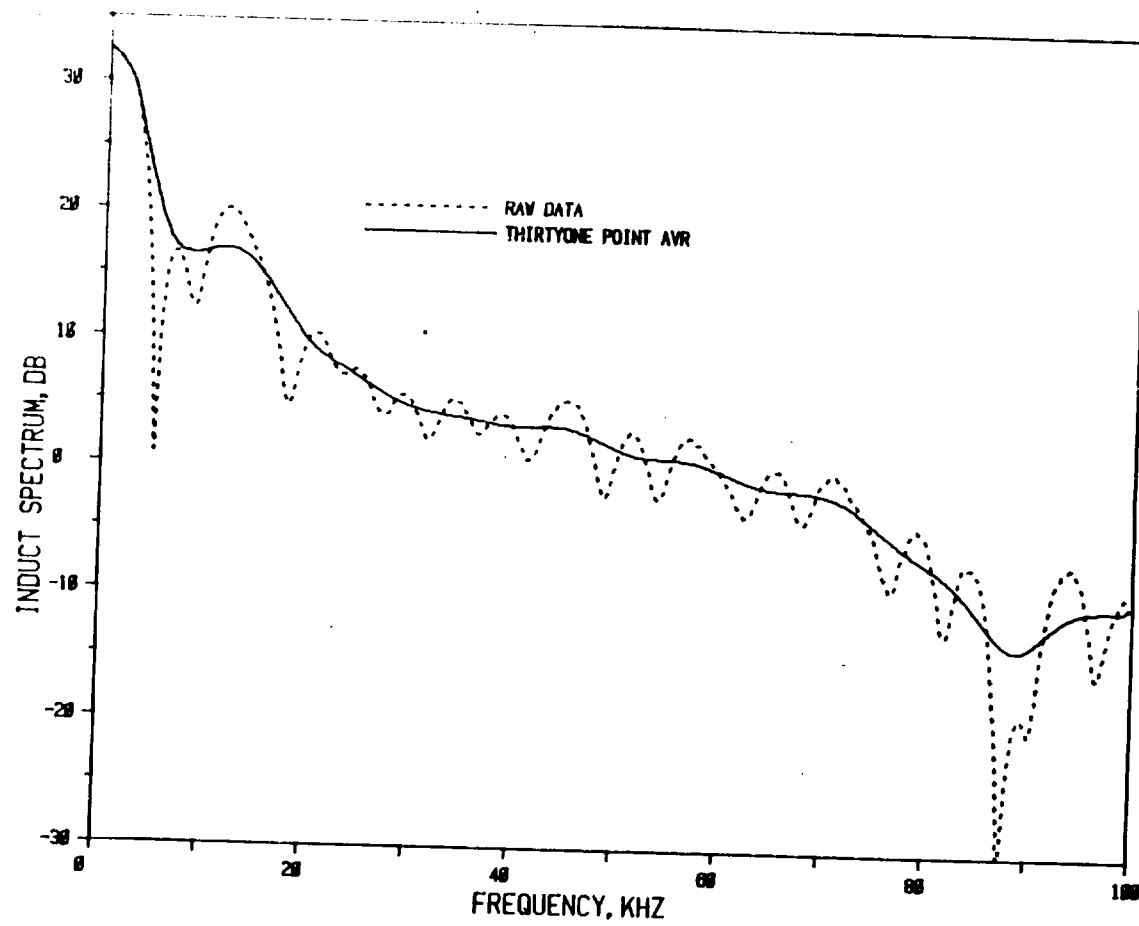


Figure 3-14(a) Typical in-duct power spectrum before and after smoothing.

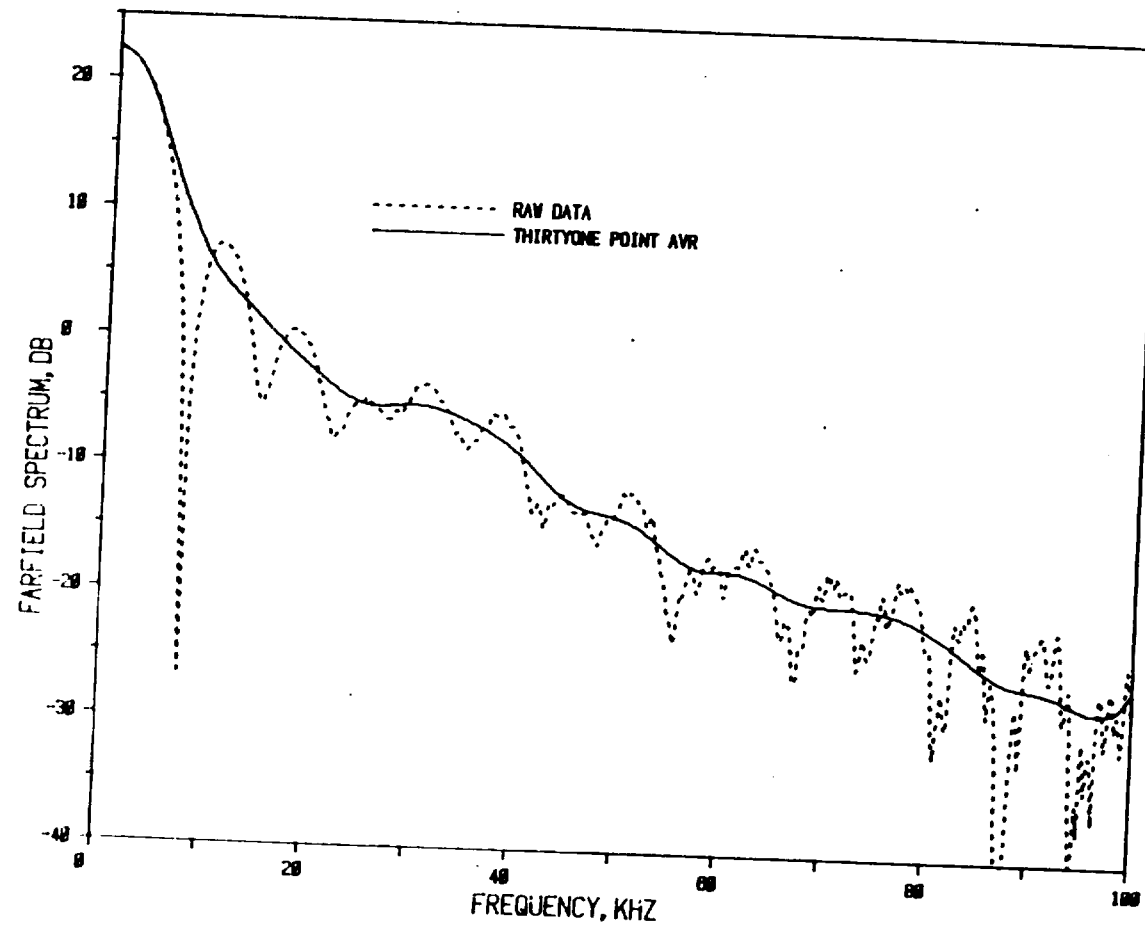


Figure 3-14(b) Typical far-field power spectrum before and after smoothing.

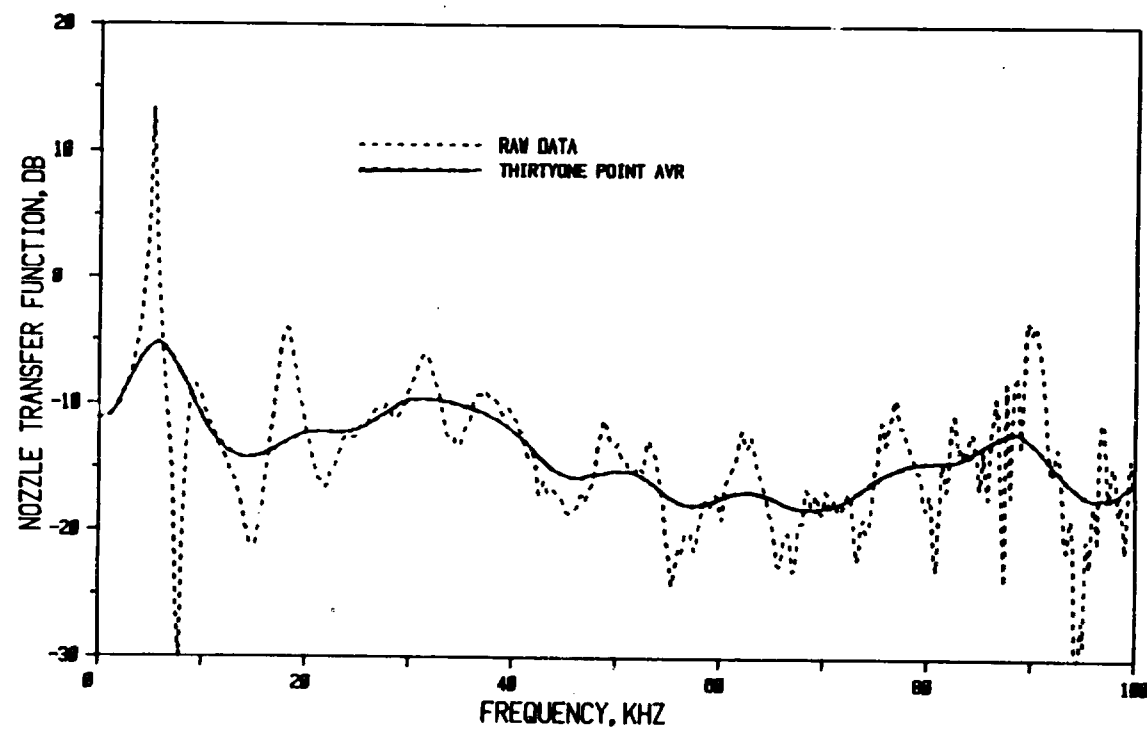


Figure 3.13(c) Typical nozzle transfer function (NTF) before and after smoothing.

defined as the jet radius ( $r$ ), while for the fan the characteristic length is the fan exit plane annulus height ( $h$ ). The wavelength is a function of the speed of sound ( $\lambda \propto 1/\bar{c}$ ), which is a function of temperature ( $\bar{c} \propto \sqrt{T}$ ). Thus, for the heated tests the nondimensional frequency transformation will reduce as the temperature increases. Therefore, the comparisons between nozzle geometries and temperatures described in Section 4 are based not on an absolute frequency basis, but on a nondimensional frequency basis.

The second normalization procedure for directivity data was the transformation of the transfer functions to the standard directivity index or N.T.F. presentation. This, in essence, is a procedure which relates the measured sound pressures at any fixed polar angle to that which would be given from a point source of equivalent power in free space. The standard normalization distance is 1 meter.

The basic assumption is that the measured incident pressure spectrum in the duct is uniform over the cross-section.

The in-duct power is then given by  $(1 + M_D)^2 \bar{p}_i^2 \cdot A_D / (\bar{\rho} \bar{c})_{duct}$  where  $A_D$  is duct cross-section and  $(\bar{\rho} \bar{c})_{duct}$  is the characteristic in-duct acoustic impedance.

The intensity at one meter from the equivalent in-duct source is

$$I_D = \frac{\bar{p}_i^2 A_D (1 + M_D)^2}{4\pi (\bar{\rho} \bar{c})_{duct}} \quad (3-4)$$

and the intensity at one meter transformed from far-field measurements at radius  $R_m$  meters is given by

$$I_{rad} = \frac{\bar{p}_{rad}^2(\theta) R_m^2}{(\bar{\rho} \bar{c})_{amb}} \quad (3-5)$$

The ratio of the far-field intensity to the in-duct intensity is the nozzle transfer function (NTF) and that can be written as

$$NTF = \frac{\bar{p}_{rad}^2(\theta)}{\bar{p}_i^2} \cdot \frac{4\pi R_m^2}{A_D} \cdot \frac{(\bar{\rho} \bar{c})_{duct}}{(\bar{\rho} \bar{c})_{amb}} \cdot \frac{1}{(1 + M_D)^2}.$$

This further simplifies to

$$NTF = \frac{\bar{p}_{rad}^2(\theta)}{\bar{p}_i^2} \frac{4\pi R_m^2}{A_D} \sqrt{\frac{T_{amb}}{T_{duct}}} \frac{1}{(1 + M_D)^2} \quad (3-6)$$

The NTF in dB terms is

$$(NTF)_{dB} = 10 \log_{10} \left\{ \frac{\bar{p}_{rad}^2(\theta)}{\bar{p}_i^2} \right\} + 10 \log_{10} \left\{ \frac{4\pi R_m^2}{A_D} \sqrt{\frac{T_{amb}}{T_{duct}}} \frac{1}{(1 + M_D)^2} \right\}.$$



## 4. TEST RESULTS

The test results presented in this section are the outcome of the test plan specified by NASA which represents proposed realistic engine configurations. Subsequent analysis of the data revealed that in the many cases no consistent trends were discovered. Thus, these results should be interpreted with the precaution that they are applicable only to similar geometric configurations and flow conditions. The possible reasons for observed inconsistencies are outlined in section 4.5.

The outcome of the data analysis and normalization procedures described earlier took the form of two basic plots for each test configuration. The first was the transfer function frequency spectrum for fixed polar angles for various Mach number conditions. The second basic plot was the transfer function frequency spectrum for fixed Mach number for various polar angles.

Neither of these types of plots proved particularly illuminating in the general sense, thus the emphasis in this section for comparison and discussion purposes is placed on a third type of plot, namely a directivity plot. This consists of the transfer function at a particular non-dimensional frequency versus polar angle for various combinations of jet conditions and nozzle/source configurations as appropriate to describe relevant features. Only the data relevant to the parametric comparisons is presented. A complete set of all data is presented in a companion volume (ref. 4.1).

It should also be noted that for some flow conditions, data points at small angles\* to the exhaust axis (typically less than 30 to 50 degrees) are missing. This is due to the fact that no detectable signal was present as a result of refraction out of the cone of silence. An estimate of this angle is given in Table B-5 of Appendix B, based on a simple ray theory analysis.

In all discussions that follow a convention for jet flow conditions has been used. In this convention, a jet flow condition with the core Mach number of 0.8 and the fan Mach number of 0.9 is written as (0.8, 0.9).

---

\*The zero and 10 degree polar angles were not measured for all flow conditions above  $M_J = 0.8$  due to excessive microphone flow noise.

#### 4.1 SOURCE IN CORE FLOW

Three nozzle configurations were tested. The core nozzle was common to all configurations, with the changes occurring in the fan geometry only. The fan nozzles were identified by their L/h ratios, namely 1, 3 and 5, with the convergence angle for each being 20 degrees. The configurations were identified as N1, N2, and N3, respectively.

For the source in the core, the nondimensional frequency parameter is  $kR_j$  ( $k$  being wavenumber and  $R_j$  the nozzle exit radius), the conversions to absolute frequency being shown in Table 4.1. Three representative  $kR_j$  values are used for discussion: 1, 8 and 32 corresponding to absolute frequencies of about 1.4, 11.4 and 45.6 KHz, respectively. For reference purposes, all directivity plots show the zero flow case.

##### 4.1.1 Mach Number Effects

Figures 4.1 and 4.2 show the effect of cold jet flow on measured directivities for nozzle configuration N1. Data for the inverted flow profile configurations of most practical interest [core and fan conditions of (0.8, 0.9); (0.8, 1.2) and (0.8, 1.4)] are shown in figure 4.1. Two characteristics are immediately obvious. The first is the effect of refraction, at angles less than 40 degrees, as evidenced by the reduction of the transfer function with respect to the zero flow case. The second effect is an amplitude increase above the zero flow case at all angles greater than 40 degrees.

Table 4.1 Non-dimensional frequency conversion to real frequency for source in core ( $R_j = 7.62$  CM, Temperature 295K)

NON-DIMENSIONAL FREQUENCY ( $kR_j$ )	REAL FREQUENCY (f, Hz)
0.5	713
1.0	1,426
2.0	2,852
4.0	5,704
8.0	11,408
16.0	22,816
32.0	45,633

At  $kR_j = 1.0$  [figure 4.1(a)] the effect of increasing the fan Mach number from 0.9 to 1.2 raises the amplitude by about 2 dB at 50 and 60 degrees while

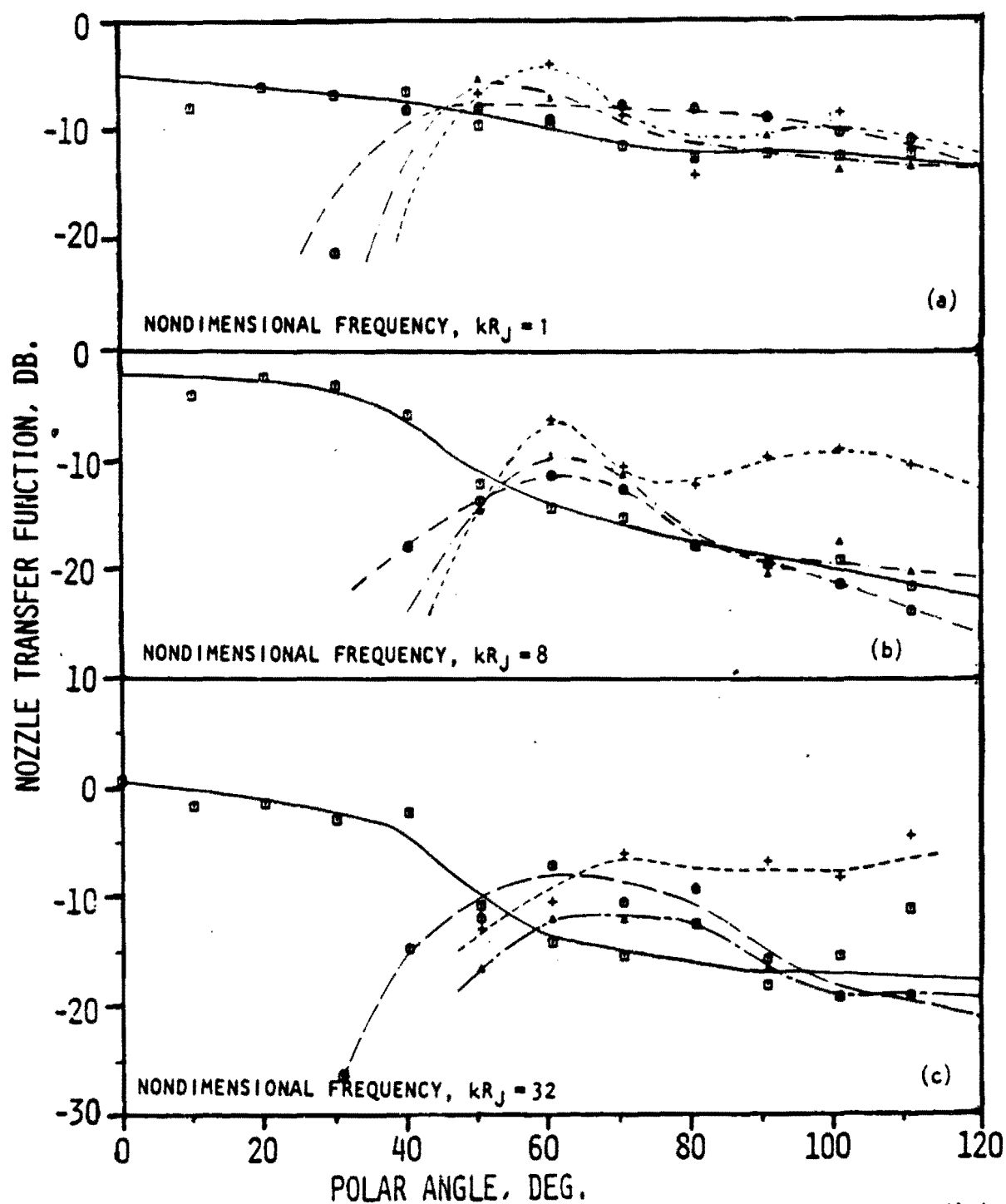


Figure 4.1 Nozzle transfer function directivity for various flow conditions. Source at core, Nozzle  $N_1$  ( $\alpha = 20$  Deg.,  $L/h = 1$ ).

CODE:  $M_{J1}$ ,  $M_{J2}$

—○—	1.00	0.90
—●—	1.00	0.98
—△—	0.90	1.20
—+—	0.90	1.40

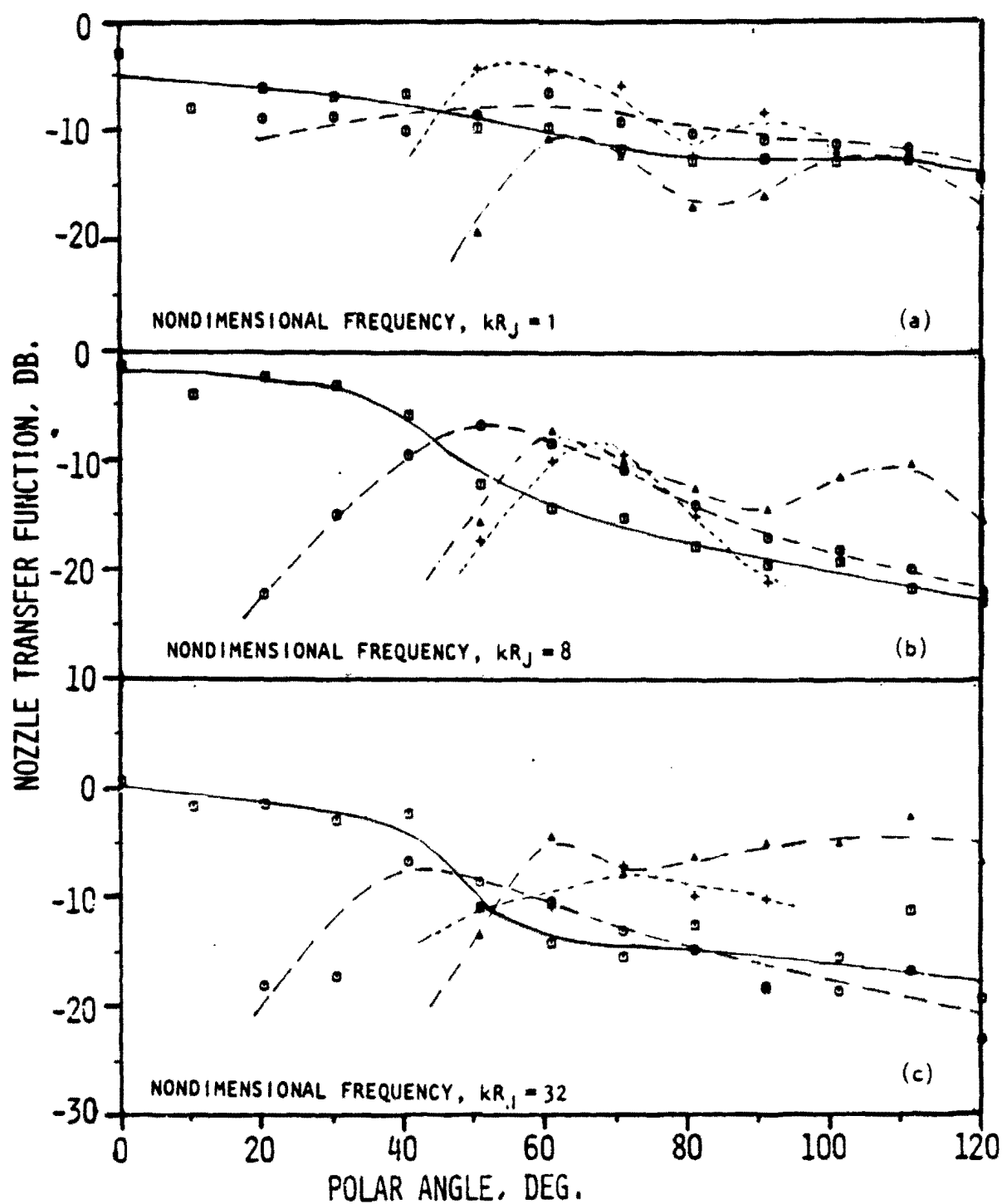


Figure 4.2 Nozzle transfer function directivity for various flow conditions. Source at core, Nozzle  $N_1$  ( $\alpha = 20$  Deg.,  $L/h = 1$ ).

CODE:  $M_{J1}$ ,  $M_{J2}$

—○—	1.00	1.00
—●—	1.48	1.63
- - -▲-	1.00	1.28
- - -+---	1.28	1.48

evoking little change at higher angles. This is a consequence of a deeper and wider refraction valley below 50 degrees, redistributing energy to the  $60^\circ$  region. Similar behavior is observed at  $kR_j = 8$  [figure 4.1(b)] and 32 [figure 4.1(c)]. The effect of increasing the fan flow to 1.4 (at  $kR_j = 1.0$ ) causes the  $60^\circ$  peak to increase some 2 dB more, with little change at larger angles compared to the (0.8, 1.2) case. Similarly at  $kR_j = 8.0$ , a 3 dB increase is noted. In addition, however, for the (0.8, 1.4) case a marked secondary lobe occurs between  $90^\circ$  and  $120^\circ$ . Through the use of a highly idealized model described in Appendix B it can be shown that it is possible to obtain a secondary lobe at high angles of incidence. It is attributable to diffraction from the core nozzle lip.

When the core stream Mach number is increased from 0.8 to 1.2 (fan remaining at 1.4), the transfer function directivities remain similar in shape but are raised by about 2 dB as can be seen in figure 4.2. Also shown on these figures are two special cases (0, 1.2) and (0.4, 0.6) flow conditions. For the first case (0, 1.2), refraction can be seen at all frequencies, however, as  $kR_j$  increases, the transfer function values which are always lower than the zero flow case at  $kR_j = 1.0$  increase to values always greater than the zero flow case (above  $60^\circ$  polar angle) at  $kR_j = 8.0$ . At  $kR_j = 32.0$ , these values increase by some 10 dB above the zero flow case.

The second special case of (0.4, 0.6) reveals behavior intermediate to the (0.8, 0.9) case. Refraction is reduced as is the higher angle lift.

It is interesting to consider the spectra at the peak angle of  $60^\circ$  and the flyover angle of  $90^\circ$  in figure 4.3. It can be seen that at  $60^\circ$ , peak levels will occur in a narrow region around  $kR_j = 3.0$ , while at  $90^\circ$  the peak level occurs in a broad band centered around  $kR_j = 24$ . For nozzle configuration  $N_2$  ( $L/h = 3$ ), the directivity trends, as shown in figure 4.4 is similar to that of configuration  $N_1$ . Physically, the difference between the two configurations is an increase in annulus height, with this annulus being further upstream from the core exit plane. Thus, the fan jet flow surrounding the core at the exit plane will be both thicker and slower. An increase in thickness would enhance refraction, while a reduction in velocity would reduce it. Thus, little change in refraction characteristics would be expected: which, in fact, is observed.

Spectral behaviour at polar angles of  $60^\circ$  and  $90^\circ$  was similar to that of the  $N_1$  configuration. For all velocity combinations the peaks in the spectra occurred at  $kR_j = 3.0$  for  $60^\circ$  and around  $kR_j = 24$  for  $90^\circ$ .

With nozzle configuration  $N_3$  ( $L/h = 5$ ) (fig. 4.5) it proved impossible to run the high flow cases of (0.8, 1.2) and (0.8, 1.4) as the increase in annulus area created air supply demands greater than the system capability. However, for all other cases tested, refraction effects with increasing velocity showed trends similar to those for nozzle  $N_1$ . A notable exception can be seen in figure 4.5(a) for  $kR_j = 1.0$ . The small angle roll-off (below  $40^\circ$ ) appears to be almost as steep for the (0.4, 0.6) flow configuration as for the (0.8, 0.9), a situation which is not seen in the  $N_1$ ,  $N_2$  nozzle data.

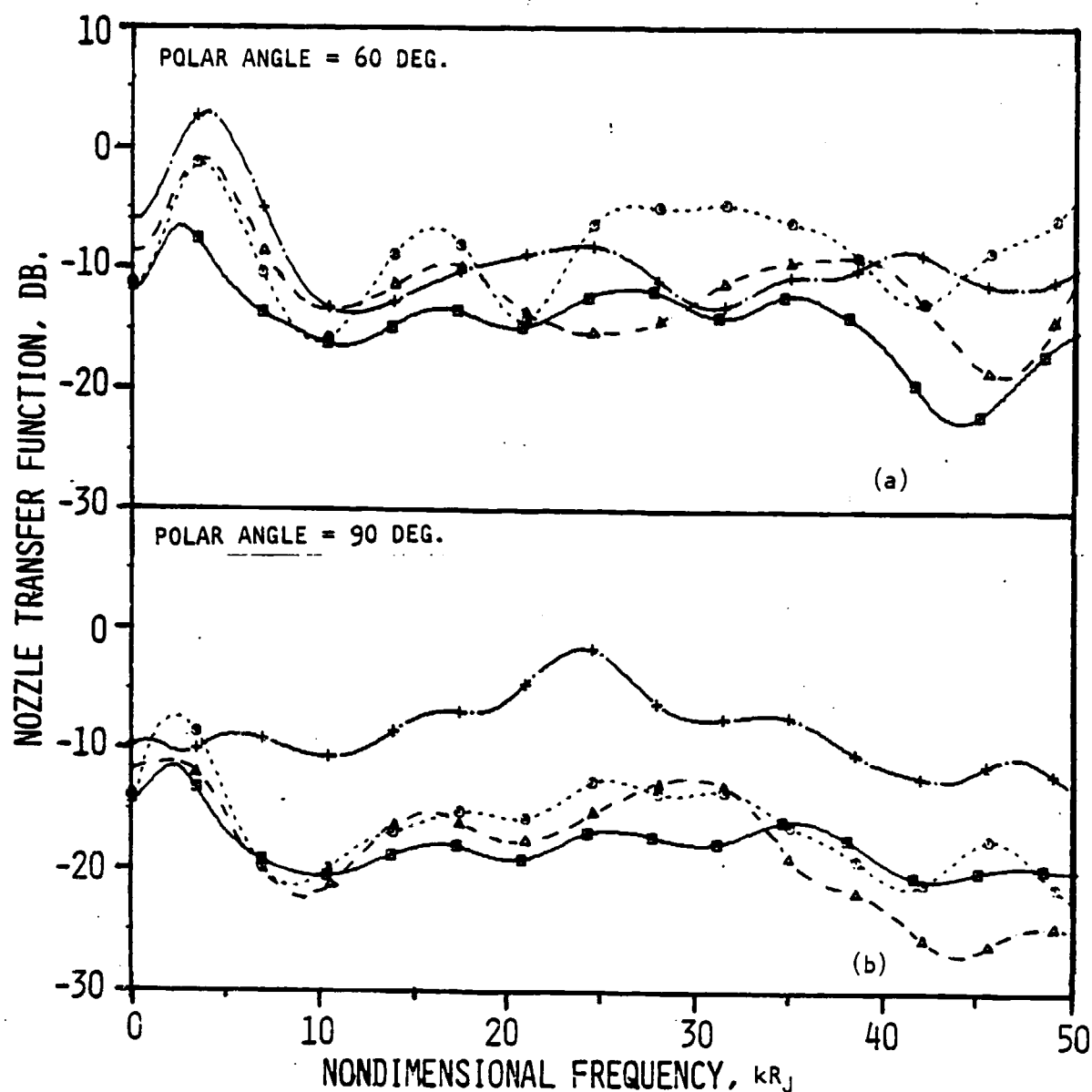


Figure 4.3 Nozzle transfer function spectrum for various flow conditions.  
 Source at core, nozzle  $N_1$  ( $\alpha = 20$  Deg.,  $L/h = 1$ )  
 CODE:  $M_{j1}$  —  $M_{j2}$

—●—	0.80	0.80
-○-	0.80	0.90
-△-	0.80	1.20
-+—	0.80	1.40
—	1.00	1.00

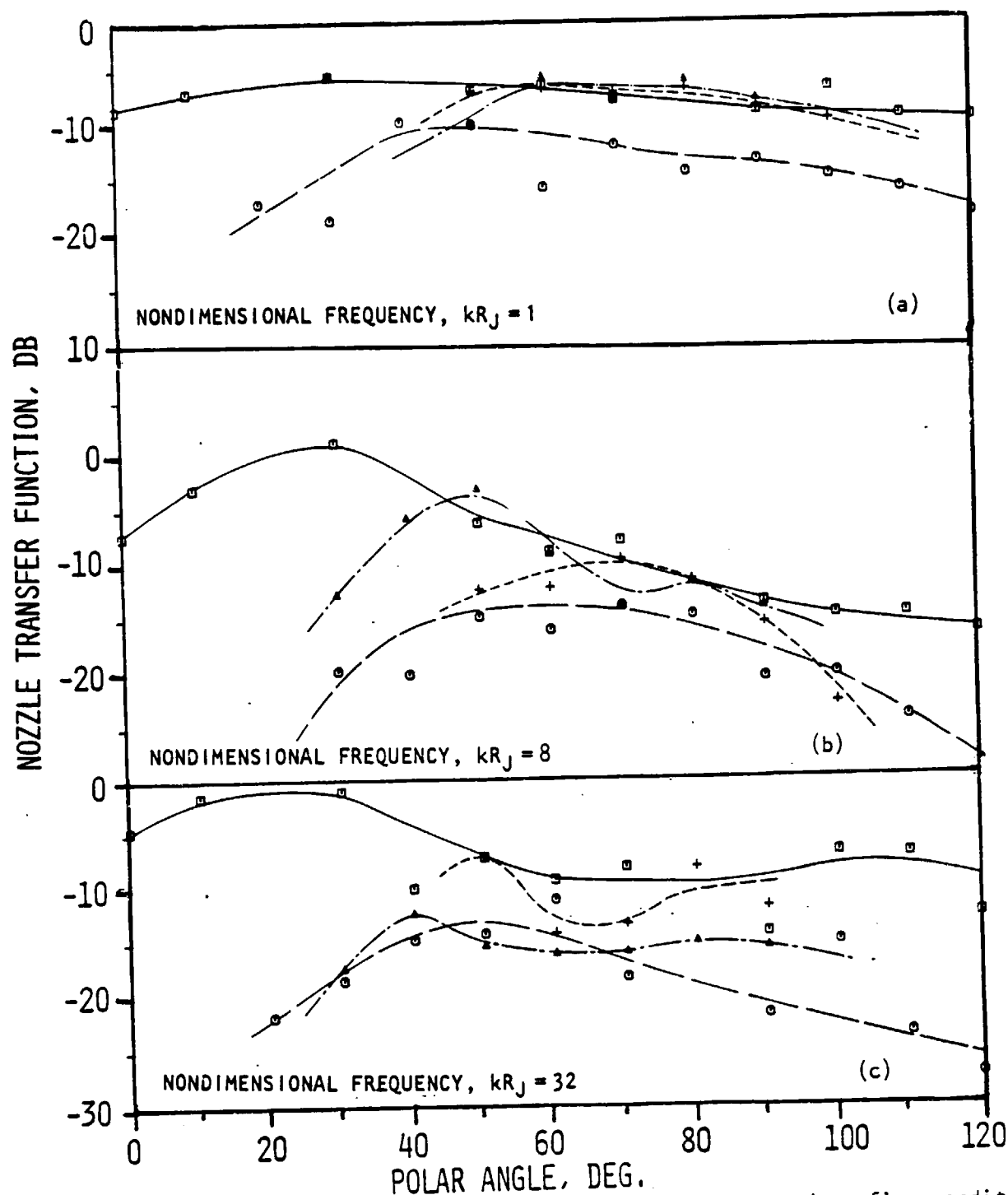


Figure 4.4 Nozzle transfer function directivity for various flow conditions. Source at core, nozzle  $N_2$  ( $\alpha = 20$  Deg.,  $L/h = 3$ )

CODE:	$M_{J_1}$	$M_{J_2}$
—□—	0.80	0.80
—○—	0.80	0.90
—△—	0.80	1.20
- - + - -	0.80	1.40

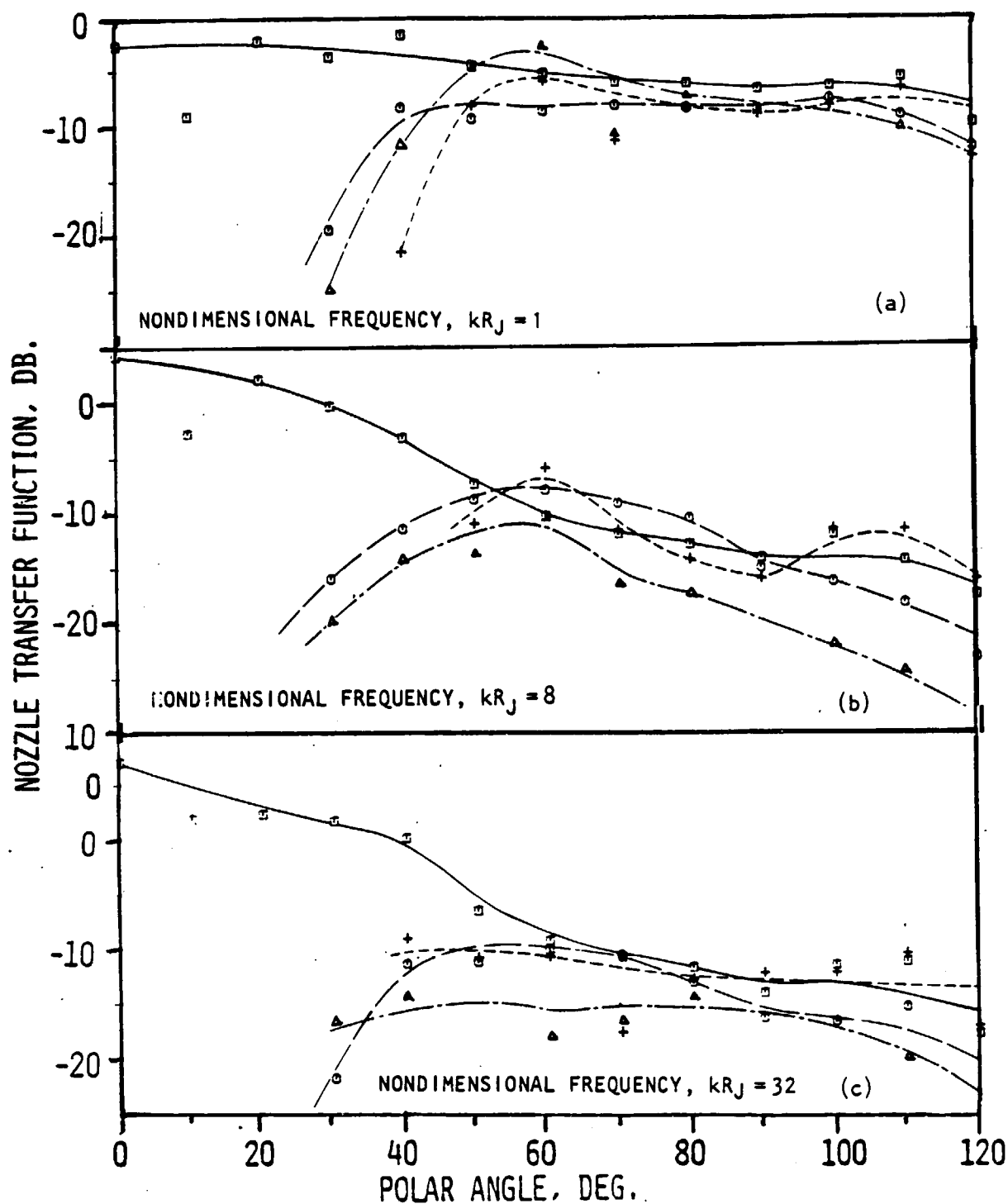


Figure 4.5 Nozzle transfer function directivity for various flow conditions.

Source at core, nozzle  $N_3$  ( $\alpha = 20$  Deg.,  $L/h = 5$ ).

CORE:  $M_{J1}$ ,  $M_{J2}$

—○—	1.00	1.00
—○—	1.43	1.00
—●—	1.88	1.00
—+—	1.00	1.20



#### 4.1.2 Effect of L/h Ratio

At any one velocity combination the effect of L/h variations (i.e. differences between nozzles  $N_1$ ,  $N_2$  and  $N_3$ ) is essentially a "plume" effect (i.e. the source characteristics and the core flow are unchanged).

Figure 4.6 shows the  $kR_j = 1.0$  directivities for a range of flow conditions. The zero flow case [fig. 4.6(a)] is almost omnidirectional with a weak peak at  $30^\circ$ . As L/h is increased the transfer function increases uniformly by 1 or 2 dB for each L/h change, for all angles above  $40^\circ$ . As the velocity is increased to (0.4, 0.6), the refraction valley can be clearly seen in figure 4.6(b) to be a marked function of L/h. From L/h = 1 to L/h = 3, at  $20^\circ$ , the transfer function reduces 5 dB, while from L/h = 3 to L/h = 5 the reduction is in excess of 15 dB.

A further increase in the velocity condition to (0.8, 0.9) [see figure 4.6(c)] has the effect of deepening the refraction valley and lifting the NTF at the higher angles, particularly in the L/h = 5 case. The slight drop in the L/h = 3 case should be treated with caution as it appears to go against the trend for no apparent physical reason and is possibly due to an analysis error (the same nozzle at (0.8, 1.2) does not show this effect). The special flow case of (0.0, 1.2) [fig. 4.6(d)] is interesting in that the fan shear layer appears to have induced a refraction effect in the forward arc as evidenced by a marked lift at  $110^\circ$ . Such conditions are theoretically possible as outlined in Appendix B.

In the mid-frequency region ( $kR_j = 8$ ) the zero flow case [fig. 4.7(a)] shows a marked on-axis beaming effect, with 2 to 3 dB increases in the transfer function as L/h is increased. As flow is increased to (0.4, 0.6) [fig. 4.7(b)] and (0.8, 0.9) [fig. 4.7(c)], the expected refraction effects occur. The most notable point is the remarkable uniformity of collapse of the directivity patterns for each L/h condition. The observed scatter of  $\pm 2$  dB about the mean line is within experimental error. Again, similar to the  $kR = 1.0$  case, the flow condition (0, 1.2) [fig. 4.7(d)] exhibits a high angle lift which appears to be more dominant for the L/h = 1.0 case.

In the high frequency region ( $kR_j = 32$  for zero flow [fig. 4.8(a)], and the (0.4, 0.6) flow case [fig. 4.8(b)], the directivity is similar in both shape and level to that at  $kR_j = 8.0$ . However, at (0.8, 0.9) [fig. 4.8(c)] L/h = 5 now appears to transmit minimum energy at polar angles less than  $80^\circ$ , in sharp contrast to the uniform collapse shown at lower frequencies [see fig. 4.7(b) for example]. This trend is continued in figure 4.8(d) [the (0, 1.2) flow case] where at angles about  $60^\circ$  the L/h = 5 case radiates levels some 5 to 7 dB below those of the L/h = 1 nozzle.

#### 4.1.3 Summary

The effects of velocity and nozzle geometry for the case of the source in the core can be summarized as follows:

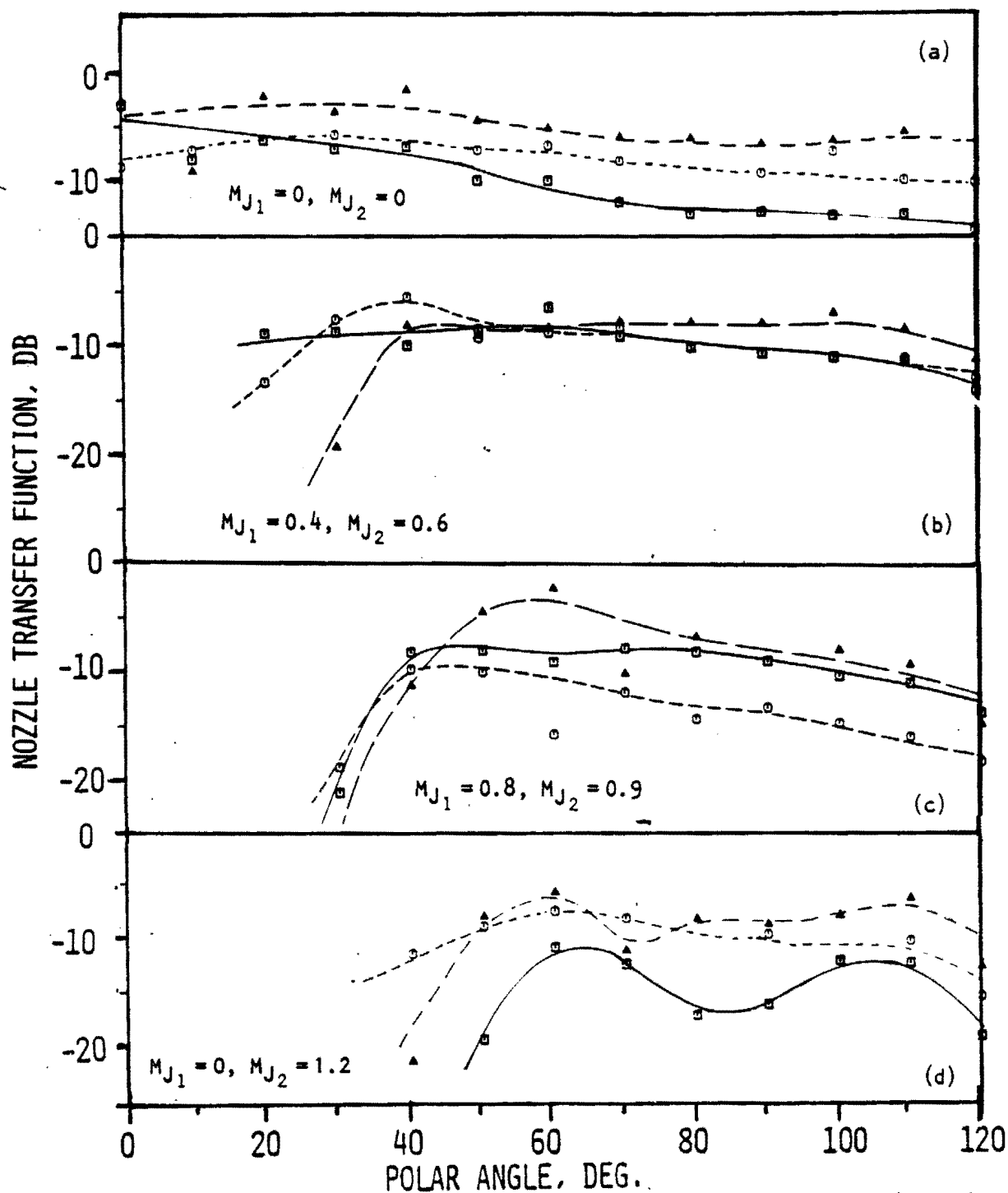


Figure 4.6 Nozzle transfer function directivity for various  $L/h$  ratios.  
Source at core,  $\alpha = 20$  Deg.,  $kR_J = 1$   
CODE:  $L/h$ .

—■—	1
- - -○- -	3
- · -△- ·	5

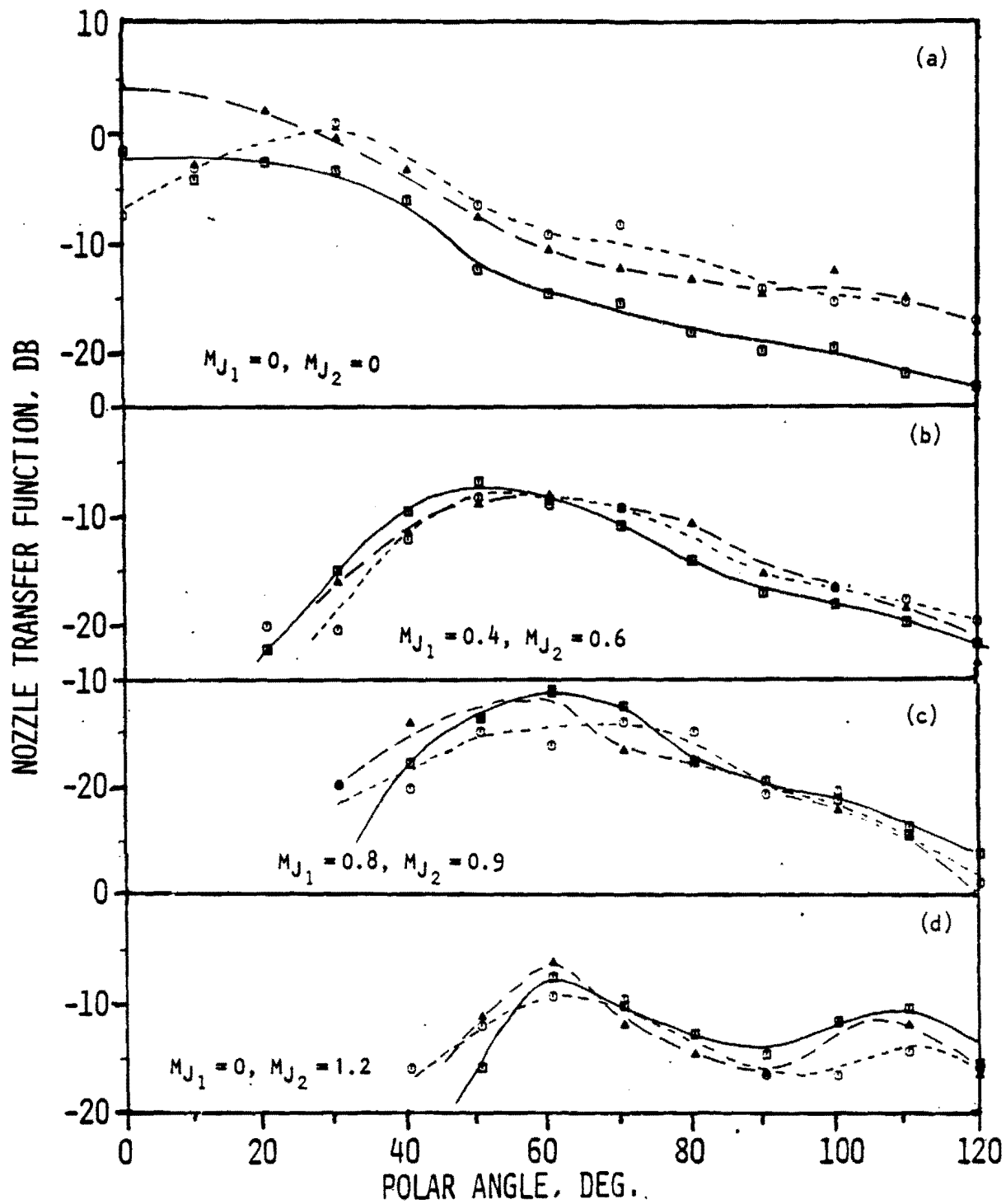


Figure 4.7 Nozzle transfer function directivity for various L/h ratios.  
 Source at core,  $\alpha = 20$  Deg.,  $kR_J = 8$   
 CODE: L/h.  
 —■— 1  
 - - -○- - 3  
 - · -△- · 5

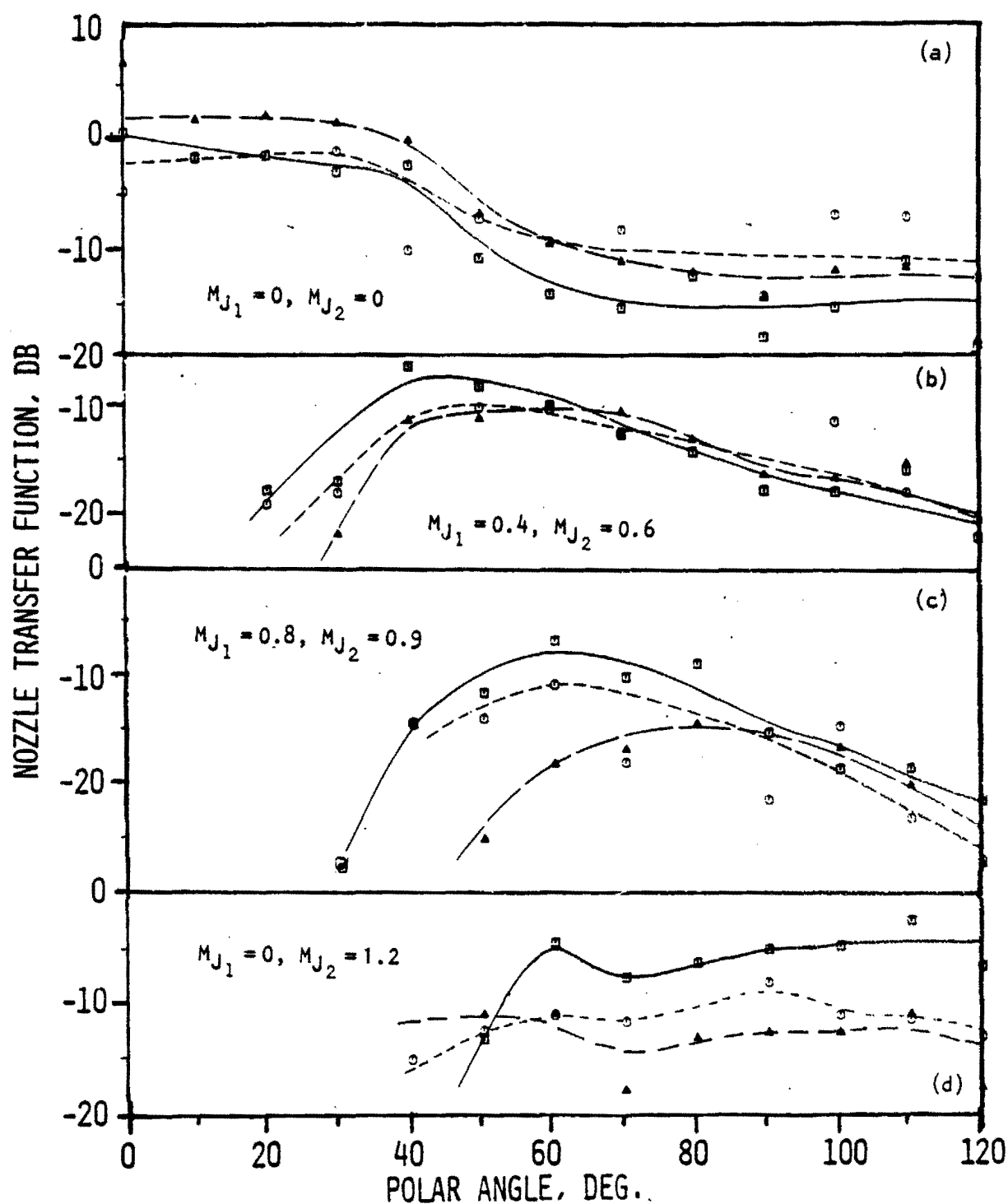


Figure 4.8 Nozzle transfer function directivity for various  $L/h$  ratios.  
Source at core,  $\alpha = 20$  Deg.,  $kR_J = 32$

CODE:  $L/h$ .

—■—	1
- - -○- - -	3
- · -△- · -	5

- o Refraction of the pulse is strongly evident and shows both velocity and frequency dependence.
- o As flow is increased at polar angles outside the refraction valley, high frequency energy is transmitted more strongly.
- o At the flow condition of (0.0, 1.2) all frequencies exhibit greatly increased NTF over the zero flow case at all angles outside the cone of silence.
- o For different nozzle geometries (defined by  $L/h$  ratios) NTF directivities are globally similar with little change for all dual flow conditions except that:
  - (1) At zero flow or at low frequencies  $L/h=5$  show highest NTF's.
  - (2) At the flow condition of (0.0, 1.2) a frequency dependence is observed in that  $L/h=1$  shows the highest NTF's at high frequencies while  $L/h=5$  shows the maximum NTF's at low frequencies.

## 4.2 SOURCE IN FAN

The frequency parameter used for these tests is  $kh$  where  $h$  is the annulus height. Thus, nozzle configurations  $N_1$ ,  $N_2$ , and  $N_3$  each have different nondimensional frequencies for the same absolute frequency. Table 4.2 lists a range of absolute frequencies for representative  $kh$  values in order to provide a feel for the nondimensional frequency presentations and data comparisons which follow. It should be noted also that nozzle configurations  $N_4$ ,  $N_5$  and  $N_6$  are identical to  $N_1$ ,  $N_2$  and  $N_3$  with the exception that fan nozzle outer wall convergence angle is  $40^\circ$  for  $N_4$ ,  $N_5$  and  $N_6$  rather than  $20^\circ$ . Thus in the discussion below the representative frequencies will be limited to  $kh$  values of 0.5, 2, and 8. These are considered as typical low, mid and high-frequency regimes of operation.

### 4.2.1 Mach Number Effects

**4.2.1.1 Twenty-Degree Convergence Angle.** - Figure 4.9 shows the effect of Mach number for  $kh$  values of 0.5, 2, and 8 for nozzle configuration  $N_1$ . The primary points are: (1) As flow increases from zero to (0.4, 0.6) to (0.8, 0.9), the effect of refraction is smaller than for the source in the core case, and the entire directivity pattern is lifted; (2) the peak angle of radiation in all cases is 40 to 50 degrees and (3) the effect of increasing the fan Mach number from 0.9 to 1.2 (the core remains at 0.8) only slightly increases the refraction valley at large  $kh$  values. Otherwise, little change occurs.

The special flow case of (0.0, 1.2) shows some interesting features. At  $kh=0.5$  [fig. 4.10(a)] NTF is always less than that for the zero flow case (except for one point at  $60^\circ$ ) and the (0.8, 1.2) flow case. As the frequency

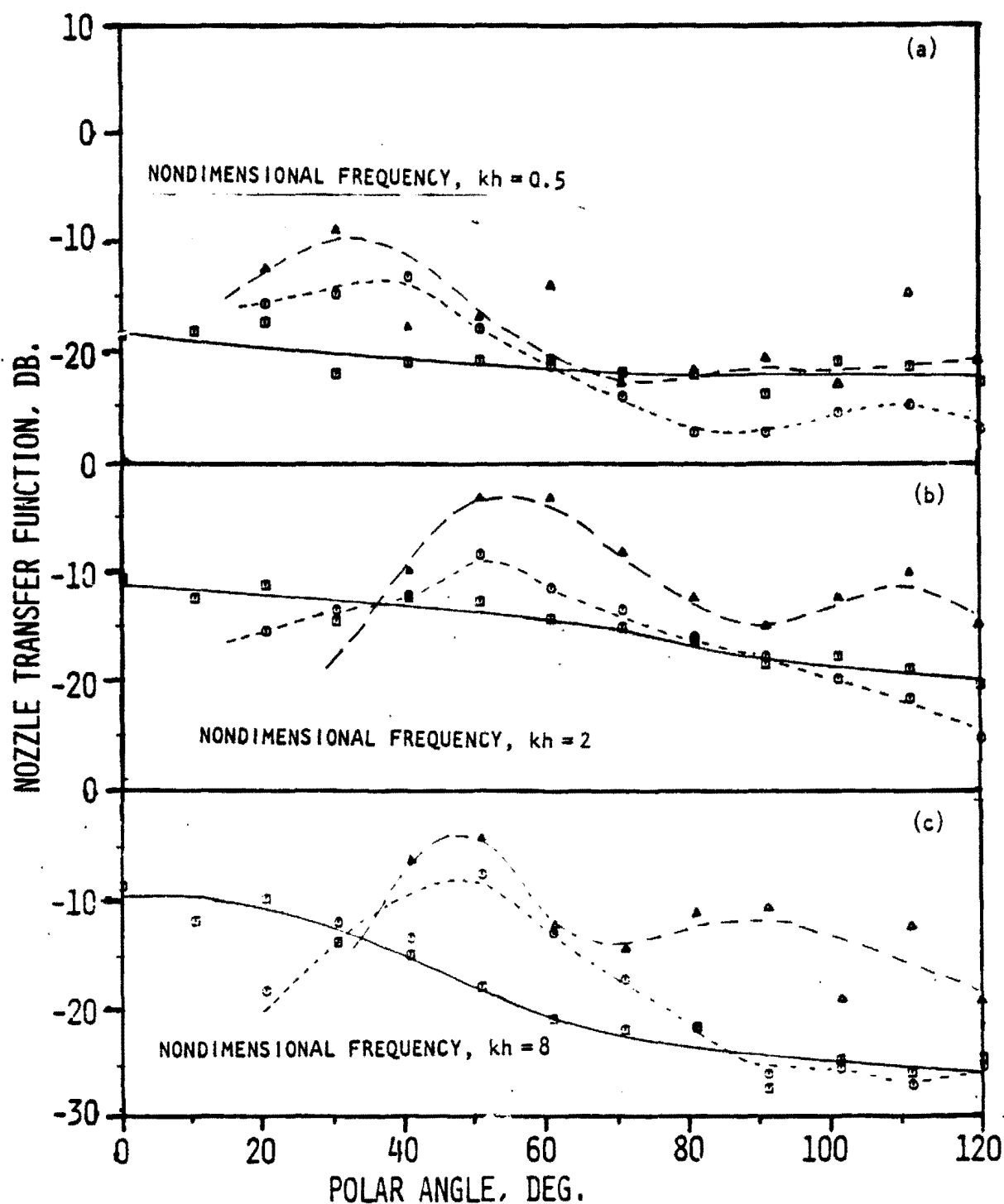


Figure 4.9 Nozzle transfer function directivity for various flow conditions. Source at fan, Nozzle  $N_1$  ( $\alpha = 20$  Deg.,  $L/h = 1$ ).

CODE:  $MJ_1$ ,  $MJ_2$

—□—	1.20	1.20
-○-	1.40	1.60
-△-	0.80	0.90

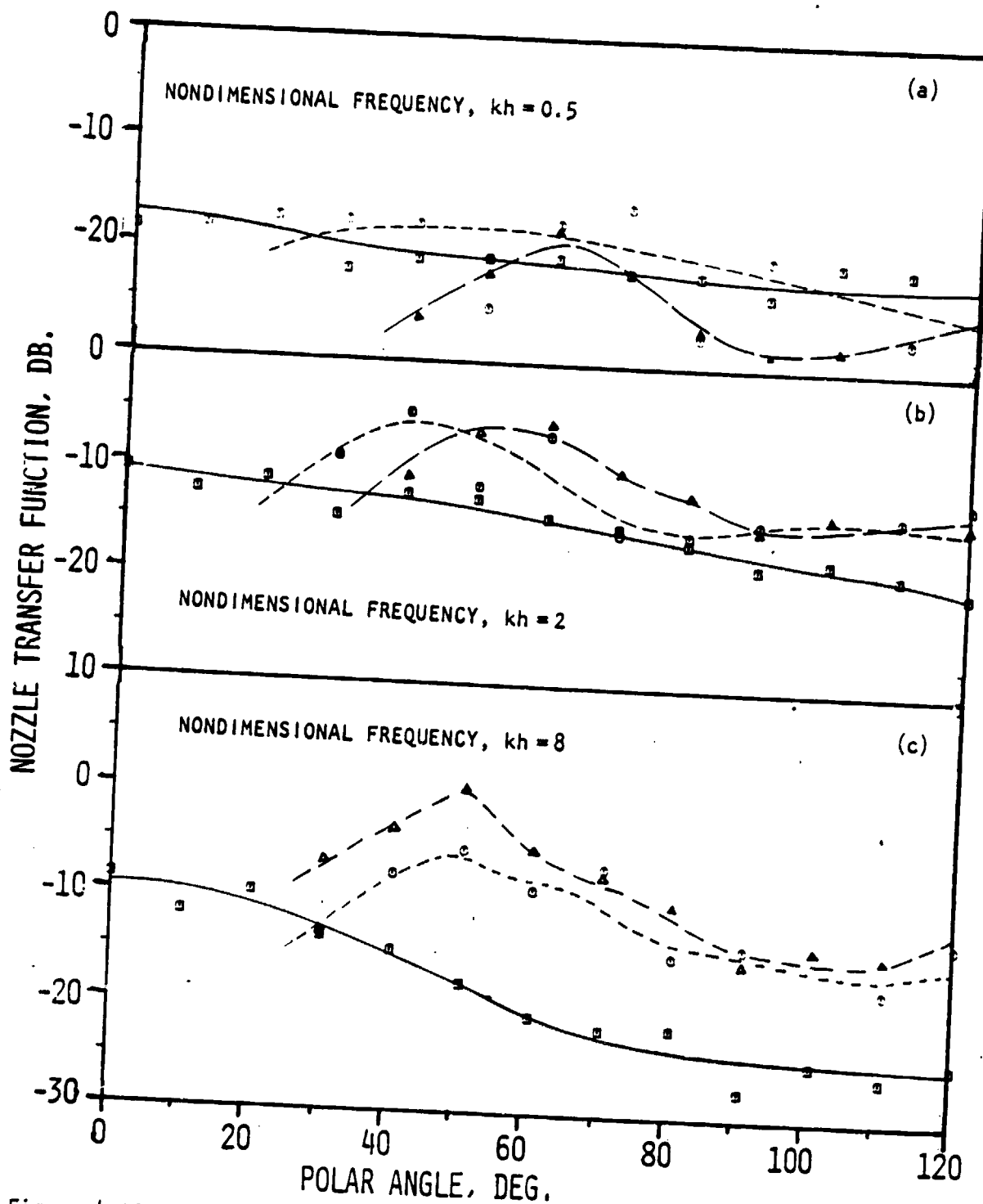


Figure 4.10 Nozzle transfer function directivity for various flow conditions. Source at fan, Nozzle  $N_1$  ( $\alpha = 20$  Deg.,  $L/h = 1$ ).

CODE:  $M_{J1}$ ,  $M_{J2}$

—○—	1.20	1.20
- - -○-	0.80	1.20
- - -△-	0.80	1.20

Table 4.2 Real frequency conversions for nondimensional frequencies for source in fan for each nozzle configuration

NONDIMENSIONAL FREQUENCY, $kh$	REAL FREQUENCY, $f$ Hz			
	295K (AMB)	600K	750K	900K
<b>L/h=1 (<math>h=1.373</math> cm)</b>				
0.25	990	1,419	1,587	1,738
0.5	1,980	2,838	3,173	3,476
1.0	3,961	5,677	6,347	6,953
2.0	7,922	11,354	12,693	13,905
4.0	15,844	22,708	25,386	27,811
8.0	31,688	45,416	50,772	55,621
16.0	63,376	90,832	101,545	111,242
<b>L/h=3 (<math>h=1.708</math> cm)</b>				
0.25	793	1,141	1,275	1,397
0.5	1,586	2,282	2,551	2,794
1.0	3,173	4,564	5,102	5,589
2.0	6,345	9,127	10,204	11,178
4.0	12,691	18,254	20,407	22,356
8.0	25,381	36,508	40,814	44,712
16.0	50,763	73,017	81,628	89,424
<b>L/h=5 (<math>h=2.259</math> cm)</b>				
0.25	600			
0.5	1,199			
1.0	2,399			
2.0	4,798			
4.0	9,595			
8.0	19,190			
16.0	38,381			

is increased to  $kh=2.0$  [fig. 4.10(b)], however, the transfer function rises above the zero flow case and is of the same order of magnitude as the (0.8, 1.2) flow case.

Further, at  $kh=8.0$  [fig. 4.10(c)] for angles less than 70 degrees the transfer function exceeds the (0.8, 1.2) flow case results. The inference here is that some sort of frequency dependent refraction (or reflection) mechanism at the core to fan interface is responsible for this high frequency enhancement at small angles to the exhaust axis.

For nozzle configuration N<sub>2</sub> the only discernable effect of velocity at  $kh=0.5$  [fig. 4.11(a)] is the unexpected small refraction valley. Otherwise, the directivities are remarkably uniform, in fact, almost omnidirectional. At  $kh=2.0$  [fig. 4.11(b)] the effect of refraction is clearer and stronger,



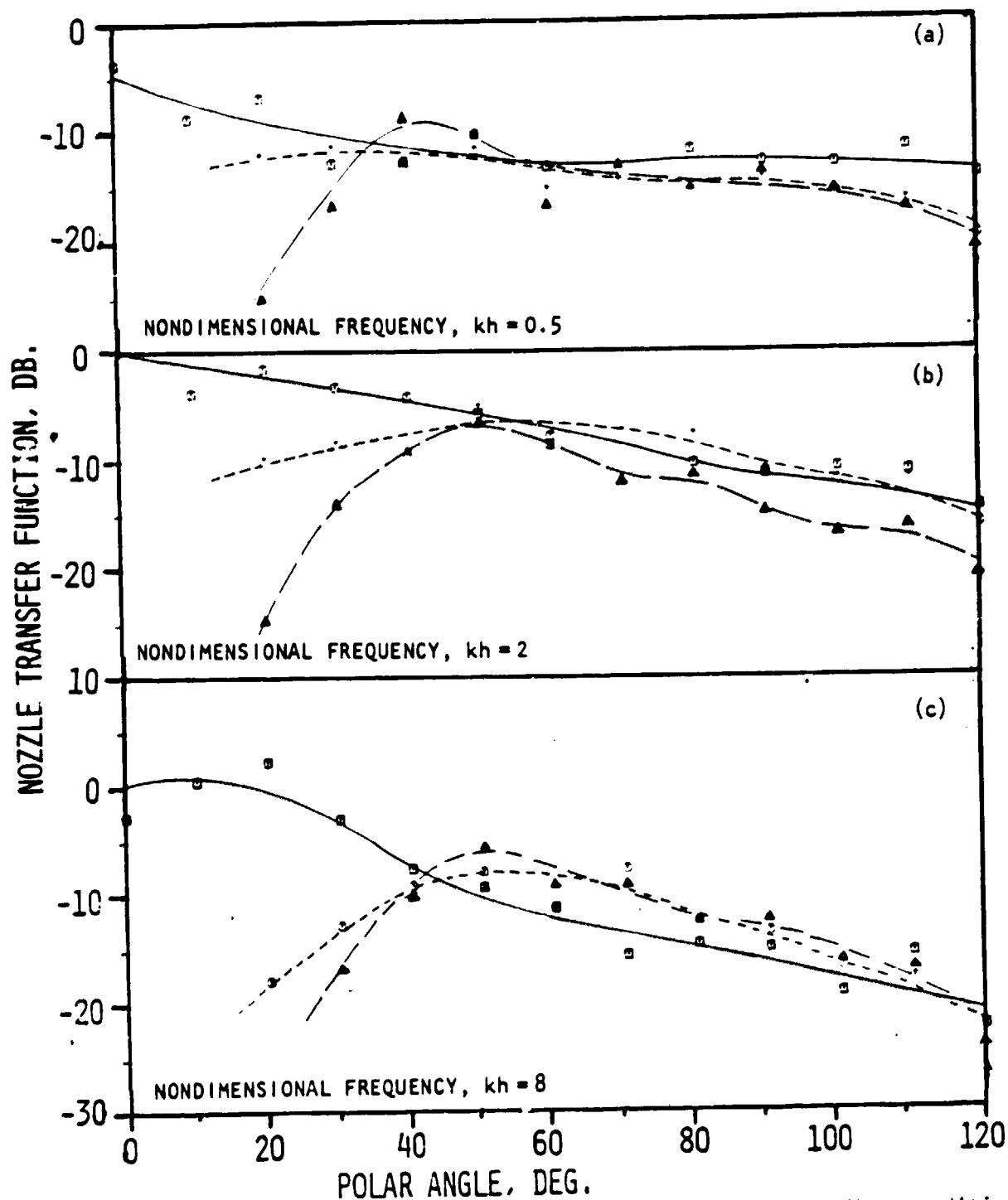


Figure 4.11 Nozzle transfer function directivity for various flow conditions. Source at fan, Nozzle N<sub>2</sub> ( $\alpha = 20$  Deg.,  $L/h = 3$ ).

CODE:  $M_{J1}$ ,  $M_{J2}$   
 —○— 1.00 2.00  
 - - -○- 0.40 0.00  
 - - -△- 0.00 0.90

with an apparent transfer of energy from small angles to about  $50^\circ$ . For the high frequency case [ $kh=8$ , fig. 4.11(c)] the characteristic beaming down the axis can be seen at the zero flow condition. Again, as expected\*, refraction effects (i.e. a small angle valley and mid-to-high angle lift) can be easily discerned as both fan and core velocities increase.

Nozzle configuration  $N_3$  directivities are shown in figures 4.12 to 4.14. At  $kh=5$  [fig. 4.12(a) and 4.12(b)] for all velocities tested, the radiation outside the refraction valley is largely omnidirectional, the major point of interest being the rise in NTF as velocity conditions increase (thus implying a more efficient transfer of energy from the nozzle).

For  $kh=2.0$  (fig. 4.13) an anomaly can be seen in that the measured transfer function for zero flow is always greater than the (0.4, 0.6) case. The data reduction has been verified and no obvious physical explanation is readily available. For the flow condition of (0.8, 0.9), the directivity returns to higher levels (except for the refraction valley), again consistent with all other nozzle configurations. At  $110^\circ$  a second peak becomes pronounced at the (0.8, 0.9) flow condition and dominates as the fan velocity is increased to 1.2.

At  $kh=8$  (fig. 4.14) all physical trends are similar to the  $kh=2.0$  case with the only major difference being a more pronounced high frequency beaming effect on the jet exhaust axis. Figures 4.15(a) and 4.15(b) show the measured NTF spectrum at the peak flow radiation angle of  $60^\circ$  for zero and (0.8, 0.9) flow cases for both  $N_1$  and  $N_3$  nozzles, respectively. It is interesting to note that the  $kh$  values of the spectral peaks (viz.  $kh=2.2, 12.5$ ) correspond closely for equivalent flow conditions. This lends credence to the use of annulus height as the characteristic length dimension for normalization purposes.

4.2.1.2 Forty-Degree Convergence Angle. - It is apparent from the discussion of nozzles  $N_1$ ,  $N_2$  and  $N_3$  in the previous section that a trend exists. Figure 4.16(a) shows the effect of velocity for nozzle  $N_3$  at a  $kh$  of 0.5, which fits in quite well with this established trend. Small angle reductions and mid-angle lifts due to refraction are clearly defined, as are also generalized increases with velocity in the transfer function at high angles (above  $60^\circ$ ). This latter behavior is indicative of an overall radiated energy increase as velocity increases. The special flow case of (0, 1.2) is characterized by an omni-directional field above  $40^\circ$  and a NTF some 10 dB greater than that of the zero flow case.

As the frequency is increased to  $kh=2$  [fig. 4.16(b)] the nozzle becomes a more efficient radiator, and the on-axis beaming phenomenon becomes more apparent. The now familiar refraction trends appear more marked as the velocity increases with peak amplitude being 50 degrees for (0.4, 0.6) and (0.8, 0.9) flow conditions. Again, the flow condition of (0.0, 1.2) has a

---

\*Refraction is a frequency dependent phenomenon. For a given velocity gradient, the higher the frequency the greater the refractive effects.

**"Page missing from available version"**

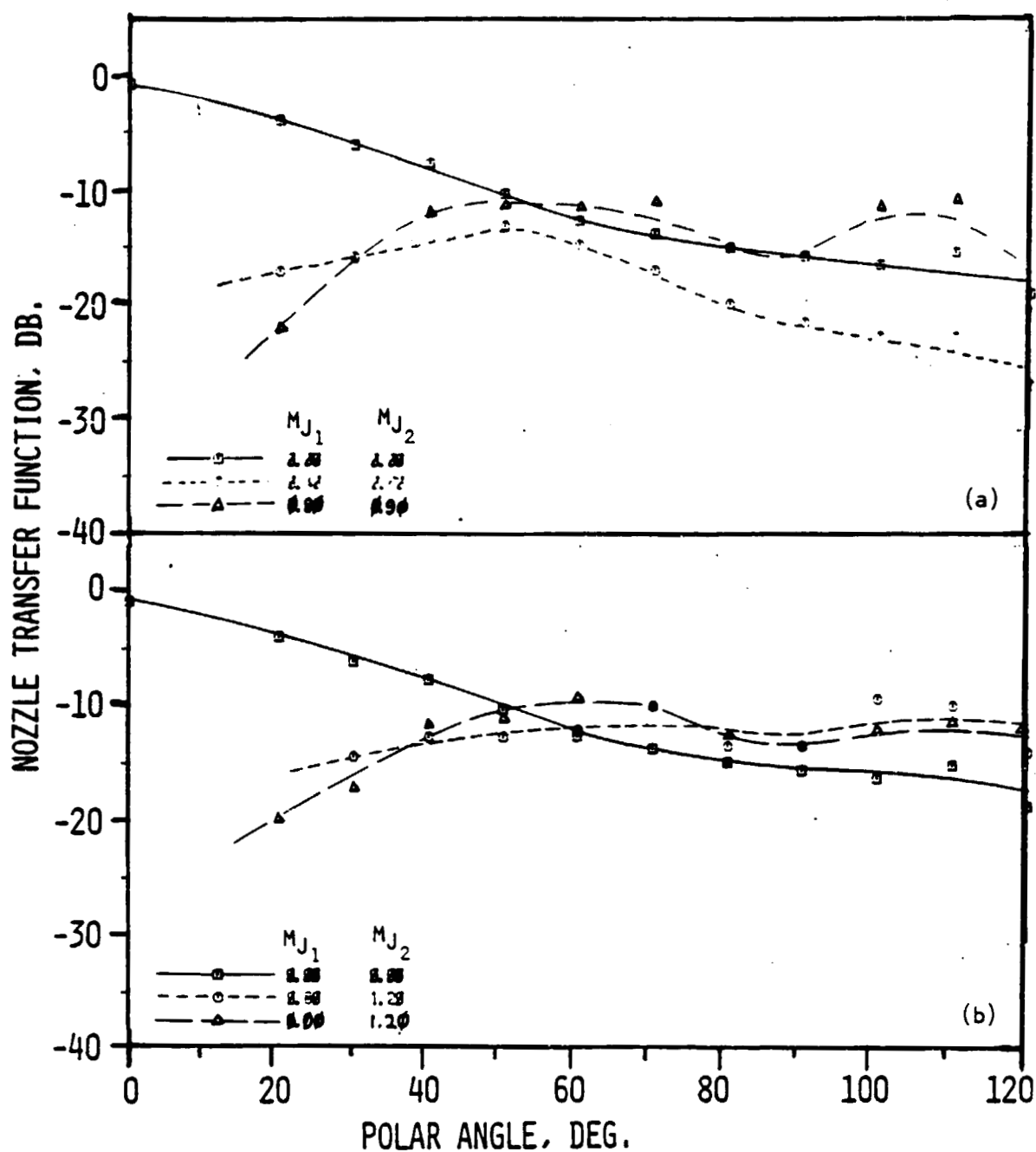


Figure 4.13 Nozzle transfer function directivity for various flow conditions. Source at fan, nozzle  $N_3$  ( $\alpha = 20$  Deg.,  $L/h = 5$ ),  $kh = 2$ .

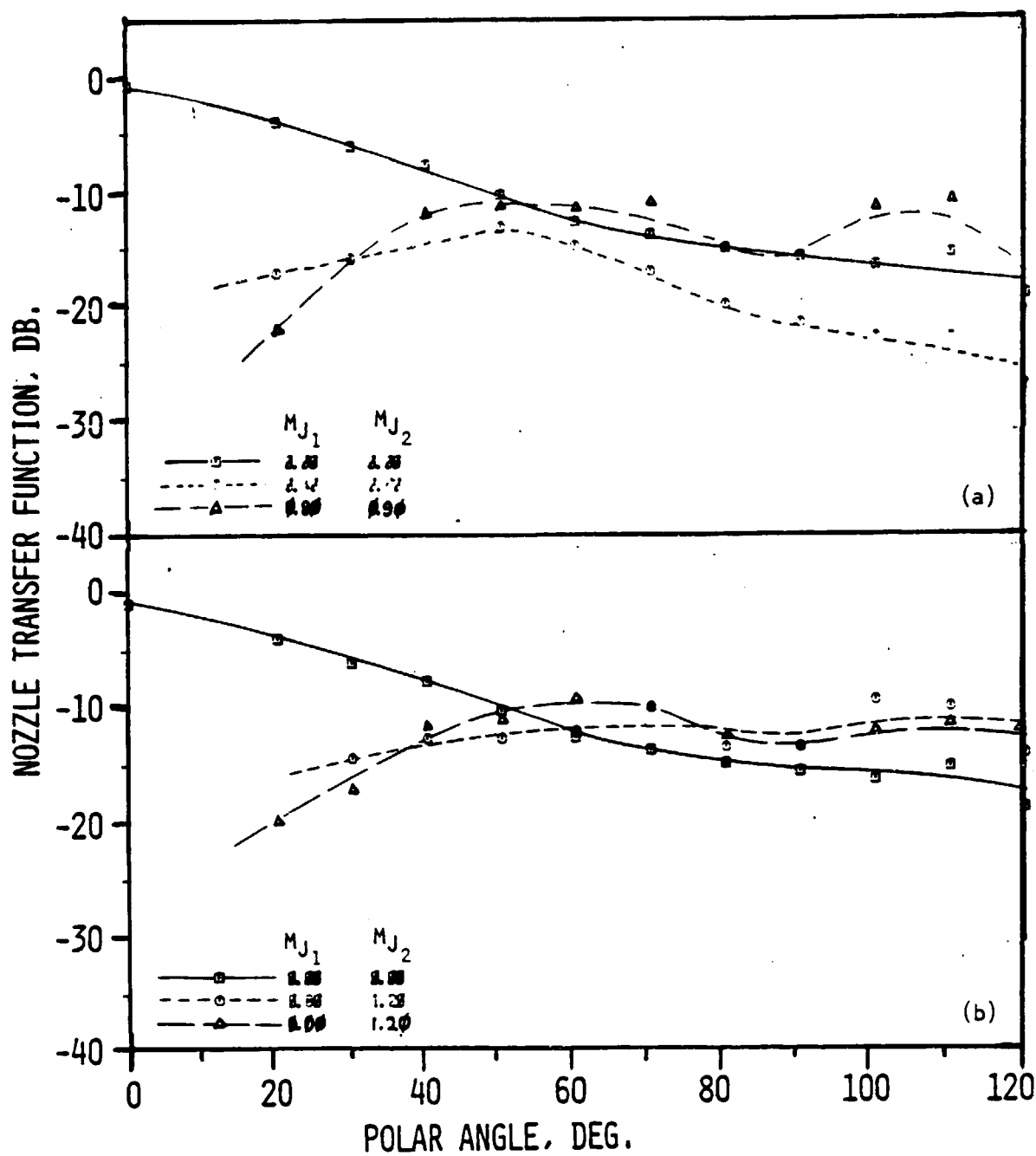


Figure 4.13 Nozzle transfer function directivity for various flow conditions. Source at fan, nozzle  $N_3$  ( $\alpha = 20$  Deg.,  $L/h = 5$ ),  $kh = 2$ .

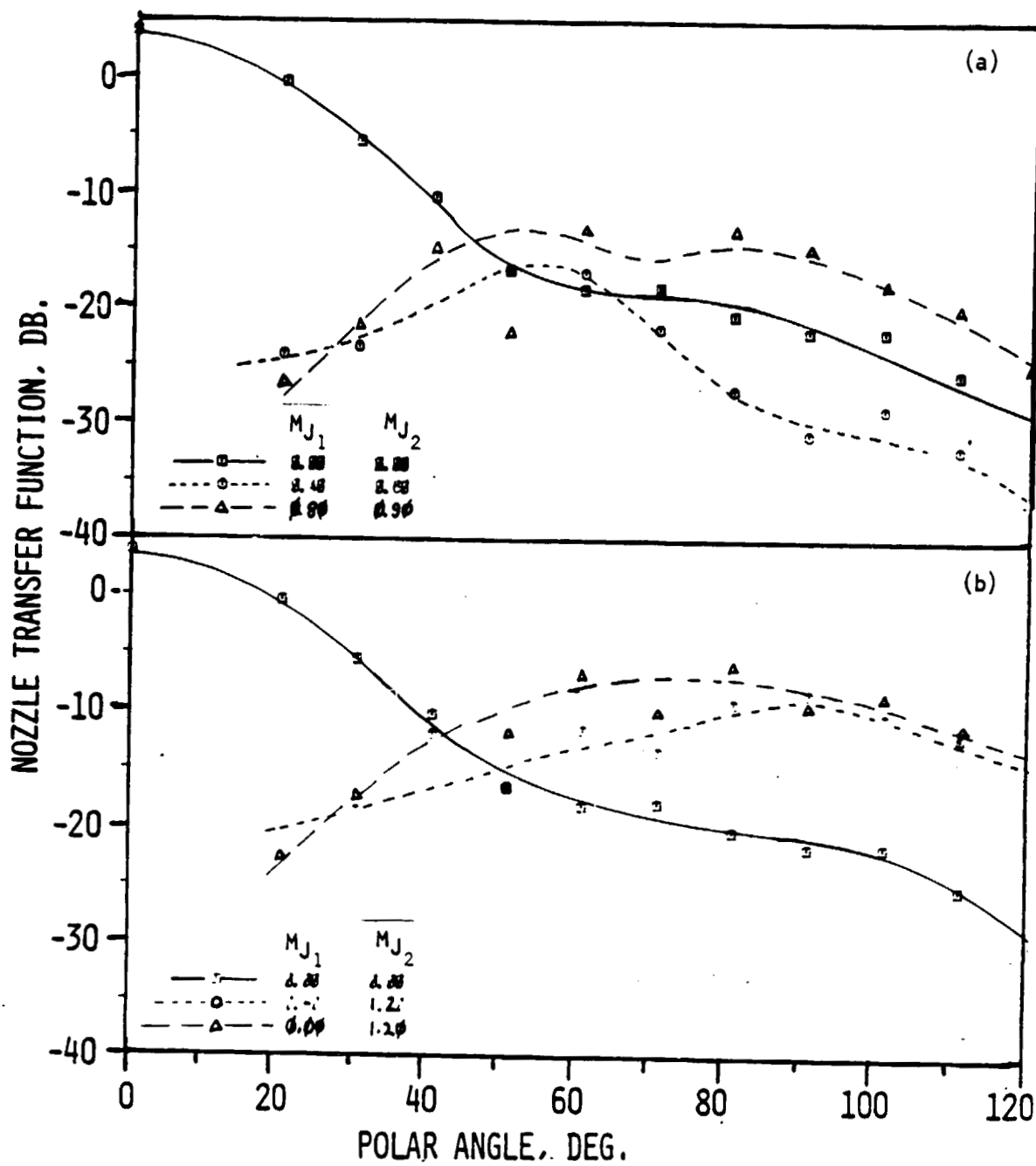


Figure 4.14 Nozzle transfer function directivity for various flow conditions. Source at fan, nozzle  $N_3$  ( $\alpha = 20$  Deg.,  $L/h = 5$ ),  $kh = 8$ .

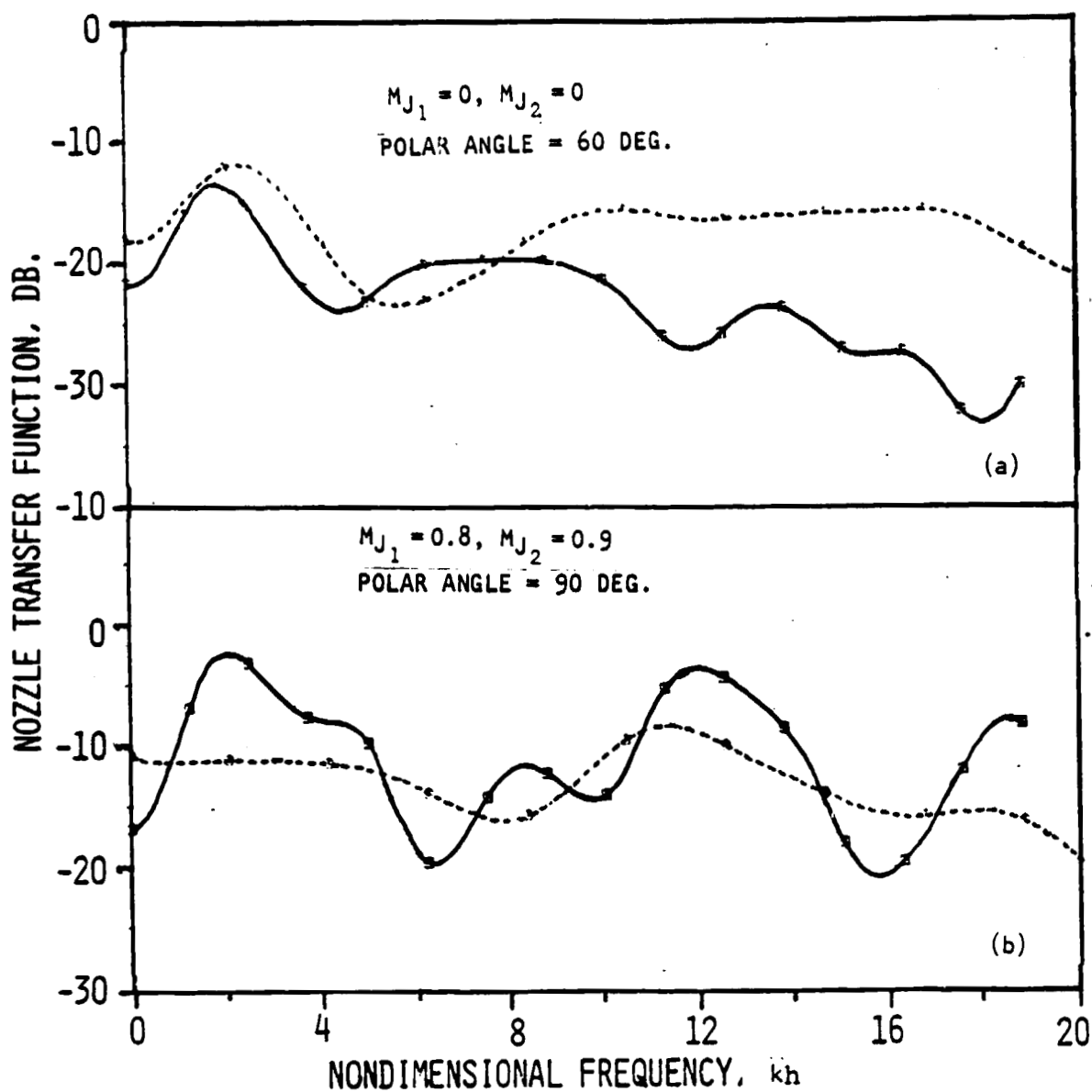


Figure 4.15 Nozzle transfer function spectrum for various  $L/h$  ratios. Source at fan,  $\alpha = 20$  Deg.

CODE:  $L/h$ .

—■—	1
- - -●- - -	5

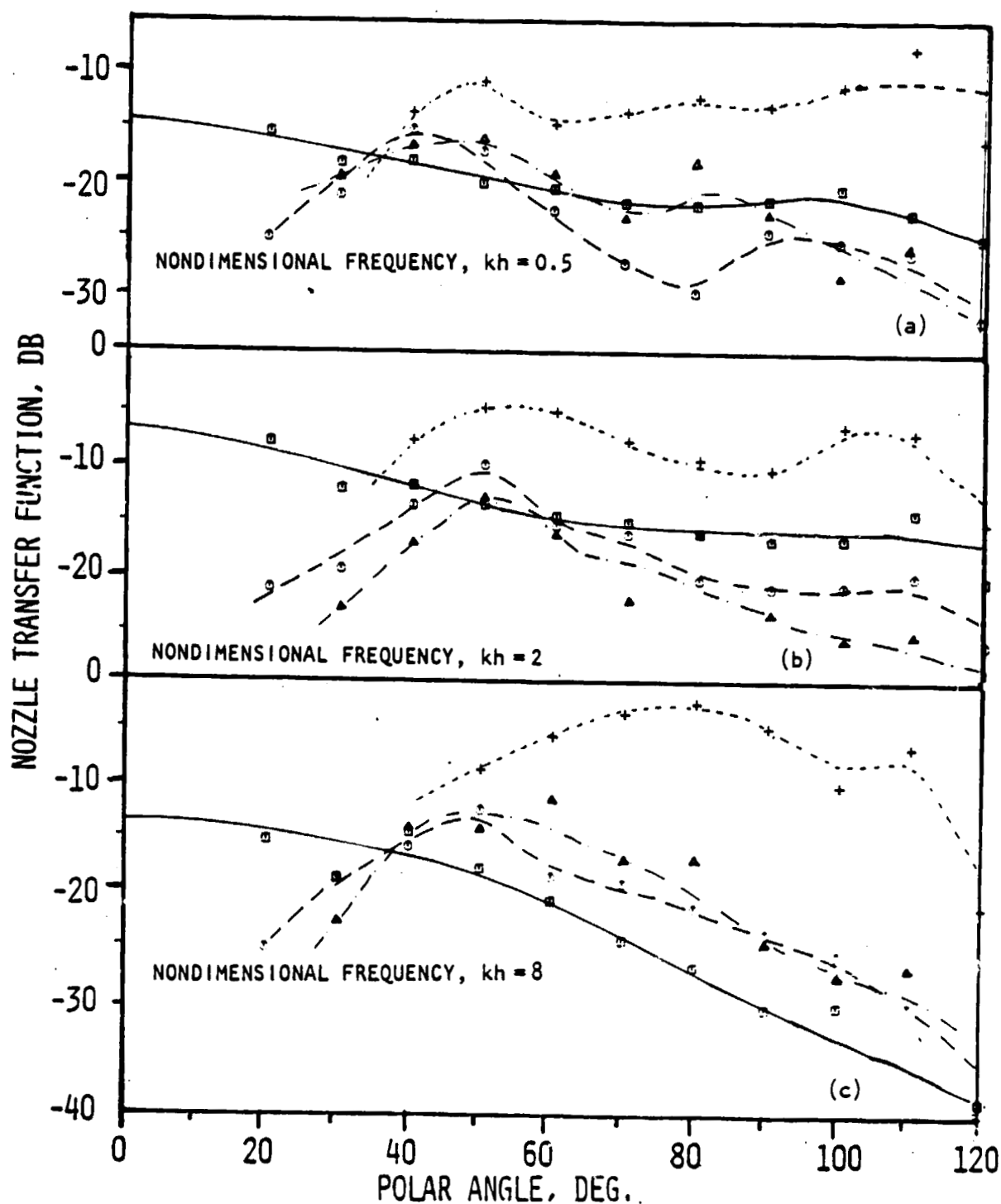


Figure 4.16 Nozzle transfer function directivity for various flow conditions. Source at fan, nozzle  $N_4$  ( $\alpha = 40$  Deg.,  $L/h = 1$ ).

CODE:  $M_{J1}$ ,  $M_{J2}$

—○—	0.80	0.80
—□—	0.40	2.00
—△—	0.80	1.90
---+---	0.80	1.20



much higher, almost omnidirectional, NTF with some evidence of a second peak near  $100^\circ$ .

Figure 4.16(c) shows the velocity effects at  $kh=8$ . It is evident that above  $40^\circ$  any increase in velocity increases the radiated level with the special case of (0, 1.2) showing dramatic level increases (some 25 dB at  $90^\circ$ ). The cause of this behavior is not clear, but the possibility exists that the pulse is somehow reflected off the core/fan flow interface. For nozzle configuration  $N_5$  at  $kh=5, 2.0$  and  $8.0$  (fig. 4.17) all trends with increasing velocity are consistent with configuration  $N_4$  with the exception of the (0.8, 1.2) and (0.0, 1.2) flow conditions. With all previous nozzles the (0.0, 1.2) flow condition, NTF has been measured to be essentially omnidirectional with levels of about 10 dB higher than the zero flow case at the same frequency. However, in figures 4.17(a) and 4.17(b) the (0.0, 1.2) levels at  $kh=0.5$  and  $2.0$  are comparable to the zero flow case, while at  $kh=8.0$  [fig. 4.17(c)] the levels above  $60^\circ$  are 10 dB or more higher for no apparent physical reason.

Nozzle configuration  $N_6$  behaves quite rationally at all frequencies as jet velocity increases. The significant points in figure 4.18 are (1) the apparent high angle reduction in low frequency radiation efficiency of the (0.4, 0.6) flow case over the zero and (0.8, 0.9) flow cases and (2) the marked increase in high frequency transmission at mid angles (some 10 dB at  $60$  degrees).

4.2.1.3 Summary. - The effects of velocity on the NTF can be summarized as follows:

(1) For the  $20^\circ$  nozzle series:

- o Strong refraction effects are observed.
- o For nozzle configurations  $N_1$  and  $N_2$  ( $L/h=1, 3$ ) as velocity and frequency increases the NTF increases at angles above  $30$  to  $40$  degrees.
- o For nozzle configuration  $N_3$  ( $L/h=5$ )
  - o As velocity increases a low frequency increase in NTF is observed.
  - o At high frequencies an increase in NTF is seen only above  $60^\circ$  at high velocities.

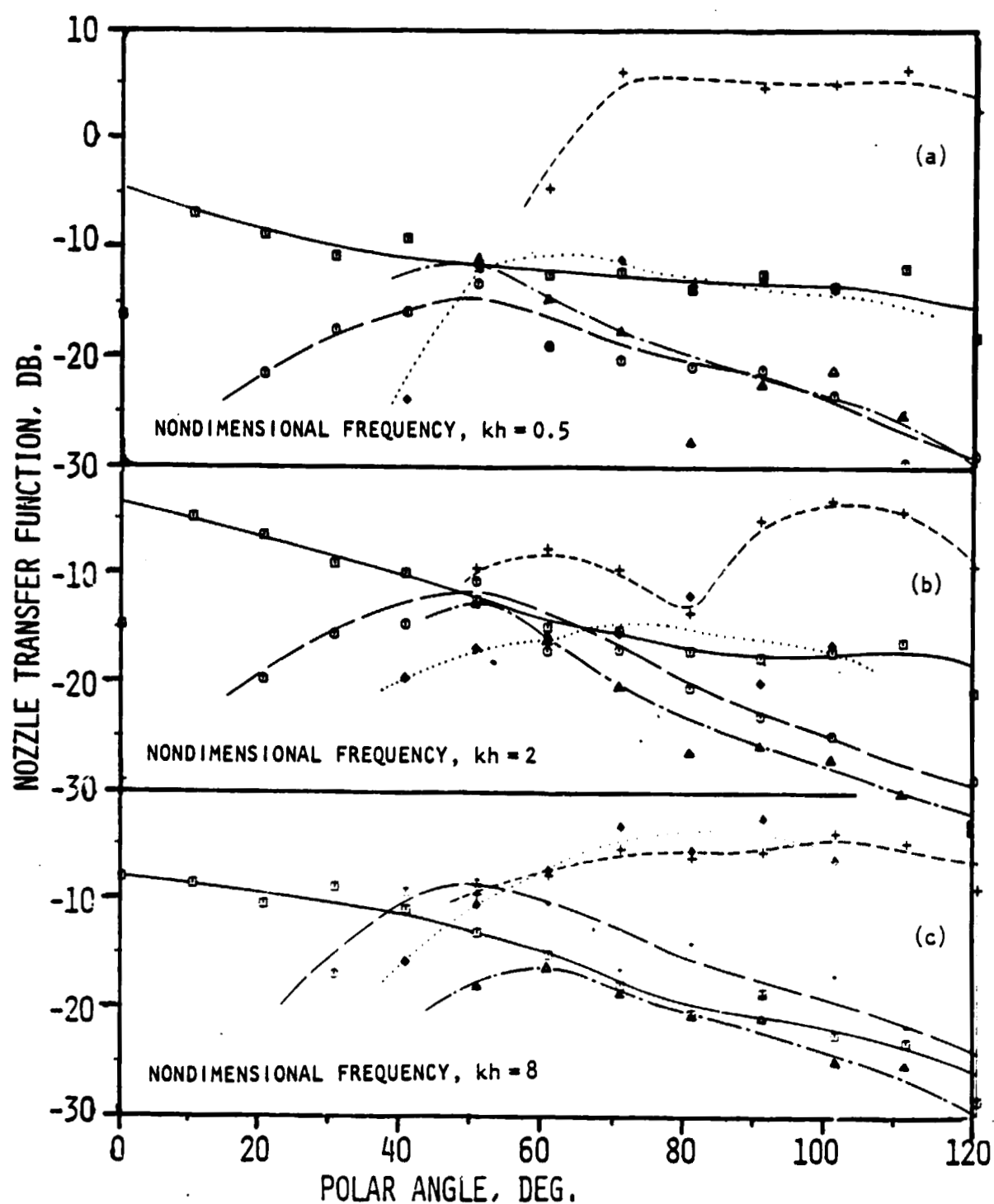


Figure 4.17 Nozzle transfer function directivity for various flow conditions.  
Source at fan, Nozzle  $N_5$  ( $\alpha = 40$  Deg.,  $L/h = 3$ ).  
CODE:  $MJ_1$ ,  $MJ_2$

—○—	0.00	0.00
—○—	0.40	0.00
—△—	0.60	0.90
—+—	0.80	1.20
—◇—	0.00	1.20

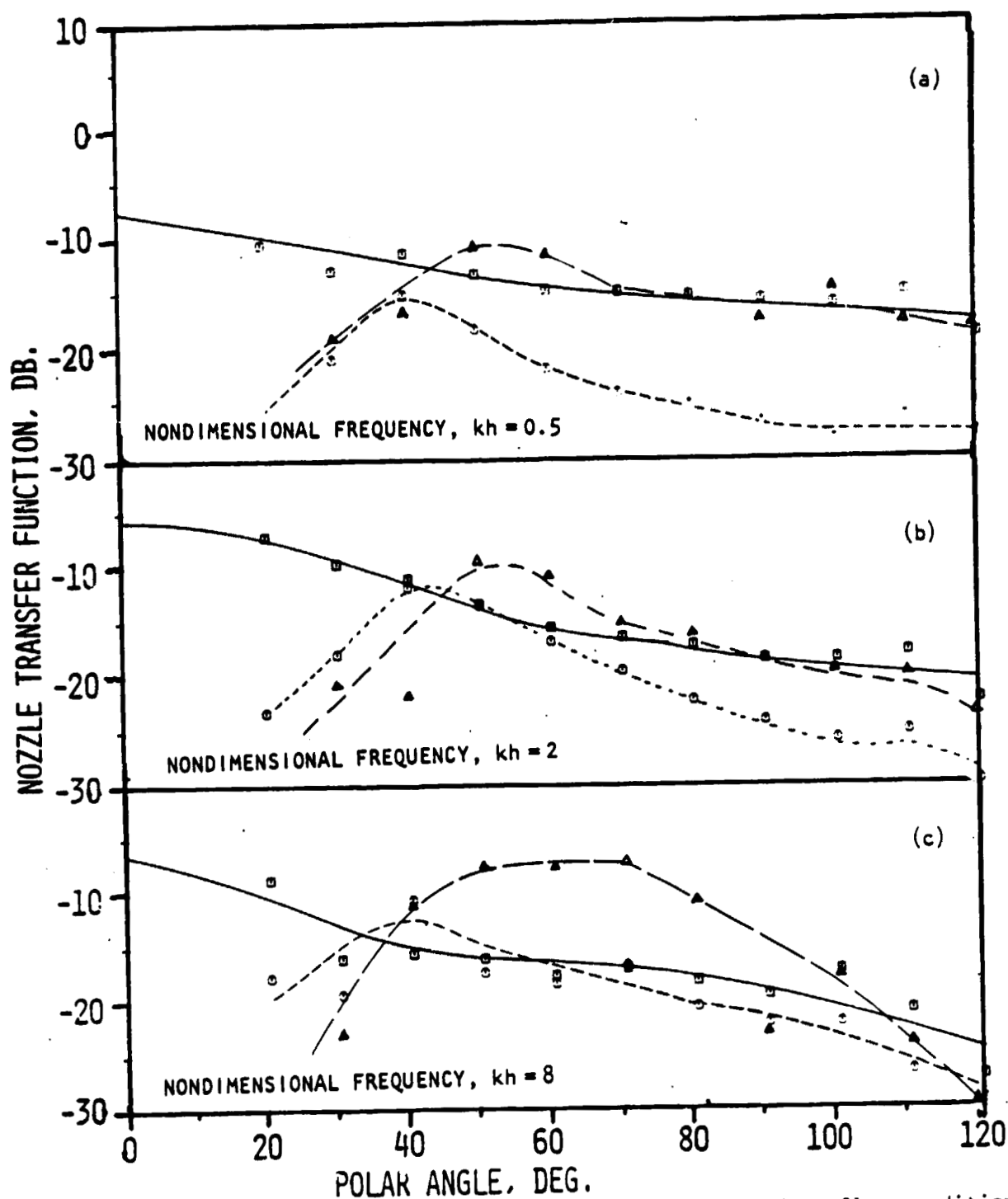


Figure 4.18 Nozzle transfer function directivity for various flow conditions.  
Source at fan, Nozzle  $N_6$  ( $\alpha = 40$  Deg.,  $L/h = 5$ ).  
CODE:  $M_{J1}$ ,  $M_{J2}$

—□—	1.20	1.20
- - -○- -	0.40	0.60
- · -△- ·	0.80	0.90

(2) For the 40° nozzle series:

- o Refraction effects are observed.
- o For all nozzle configurations ( $N_4$ ,  $N_5$ ,  $N_6$  corresponding to  $L/h=1, 3, 5$ ).
  - o At low and mid frequencies velocity effects are negligible.
  - o At high frequencies a small increase in NTF is observed above 40°.
- o The flow case of (0.0, 1.2) is characterized by much higher output than other velocity combinations at all angles above 40°.

#### 4.2.2 Effect of L/h Ratio

4.2.2.1 Twenty-Degree Convergence Angle. - Figures 4.19 and 4.20 show the effect on the NTF of nozzle configurations  $N_1$ ,  $N_2$  and  $N_3$  at  $kh=0.5$  for increasing flow conditions. At zero flow, the  $L/h=3$  ( $N_2$  configuration) is almost 10 dB higher than for  $L/h=1$ . However, a further increase of  $L/h$  to 5 shows a 3 to 5 dB increase, the inference being, that the  $N_3$  configuration is less efficient than  $N_2$ . At the (0.4, 0.6) velocity condition, this difference vanishes as the  $L/h=3$  and  $L/h=5$  directivities [in fig. 4.19(b)] are identical. The next velocity condition (0.8, 0.9) reveals that an orderly trend of increasing NTF with  $L/h$  exists with some 8 dB difference between  $N_1$  and  $N_3$ . Figure 4.20 shows the high velocity (0.8, 1.2) and (0, 1.4) comparisons for  $L/h=1$  and 5 (the data for  $L/h=3$  proved, on analysis, to be irrecoverable due to a spark pulse system malfunction). In spite of the data scatter, it is obvious that  $L/h=1$  is the least efficient transmitter of sound at this frequency.

As  $kh$  is increased to 2.0, the zero flow directivities [fig. 4.21(a)] are similar to those observed at  $kh=0.5$ , but with reduced amplitude differences between each  $L/h$  case. At the velocity condition of (0.4, 0.6) [fig. 4.21(b)], the  $L/h=3$  nozzle still dominates above both  $L/h=1$  and 5, the most interesting feature being the fact that  $L/h=5$  is apparently slightly less efficient at all angles than the  $L/h=1$  case. The high velocity condition of (0.8, 0.9) [fig. 4.21(c)] shows a reverse trend from the  $kh=0.5$  case in that for all angles up to 80° the  $L/h=1$  configuration dominates with little difference noted between  $N_2$  ( $L/h=3$ ) and  $N_3$  ( $L/h=5$ ). For the two highest flow conditions (0, 1.2) and (0.8, 1.2) in figure 4.22, little difference between the two nozzles is observed at all angles.

For  $kh=8$ , at zero flow [fig. 4.23(a)] again nozzle  $N_2$  dominates with  $N_1$  being the least efficient. At (0.4, 0.6) [fig. 4.23(b)]  $N_1$  remains dominant, however now  $N_3$  is the least efficient in this case by a dramatic 10-12 dB below the  $N_3$  nozzle configuration. Figure 4.23(c) [flow condition of (0.8, 0.9)] shows that  $L/h=1$  now dominates over all angles. This effect is a combination of a reduction in  $L/h=3$  directivity in conjunction with an

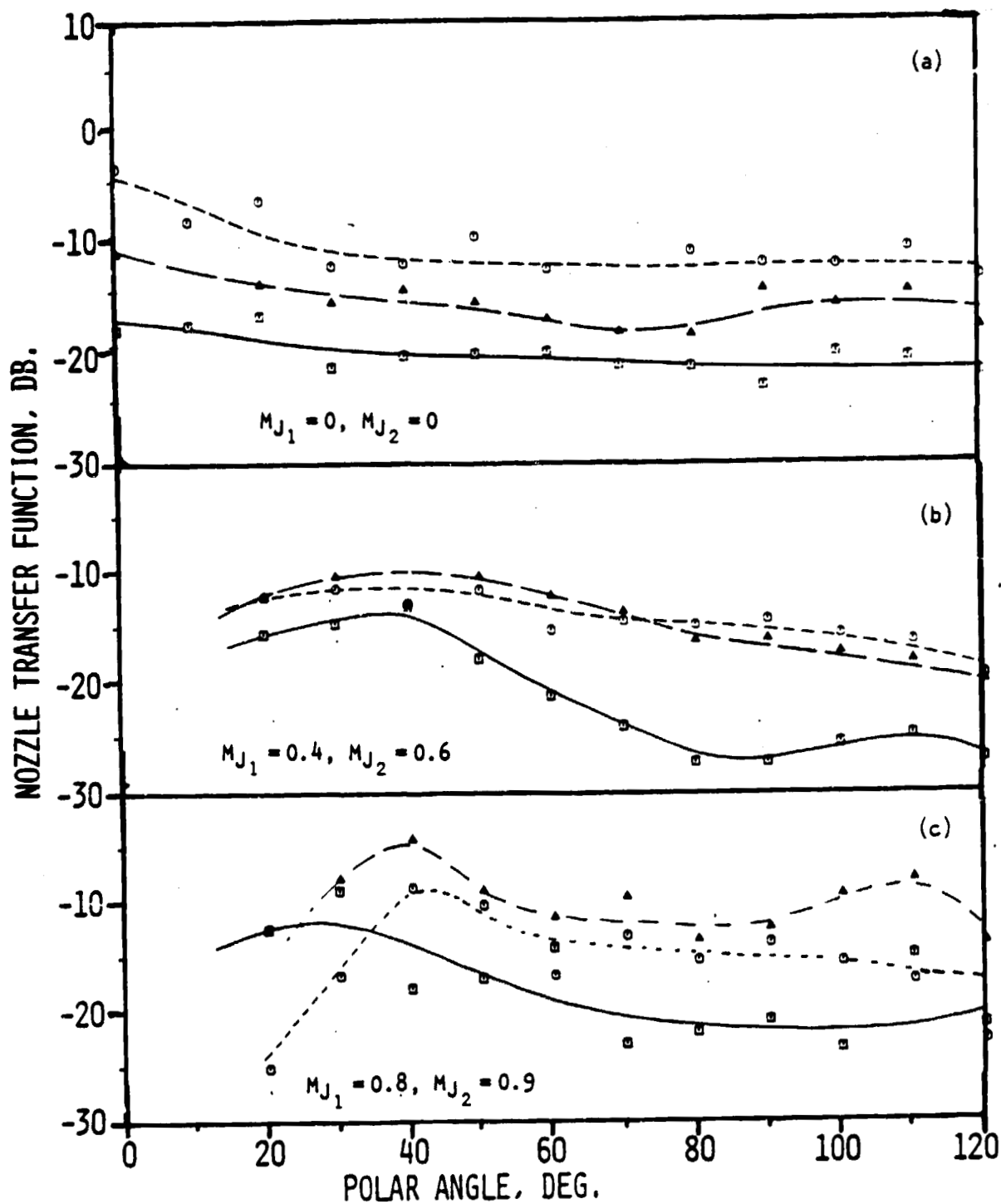


Figure 4.19 Nozzle transfer function directivity for various  $L/h$  ratios  
Source at fan,  $\alpha = 20$  Deg.,  $kh = 0.5$ .  
CODE:  $L/h$

—○— 1  
- -○- - 3  
- -△- - 5

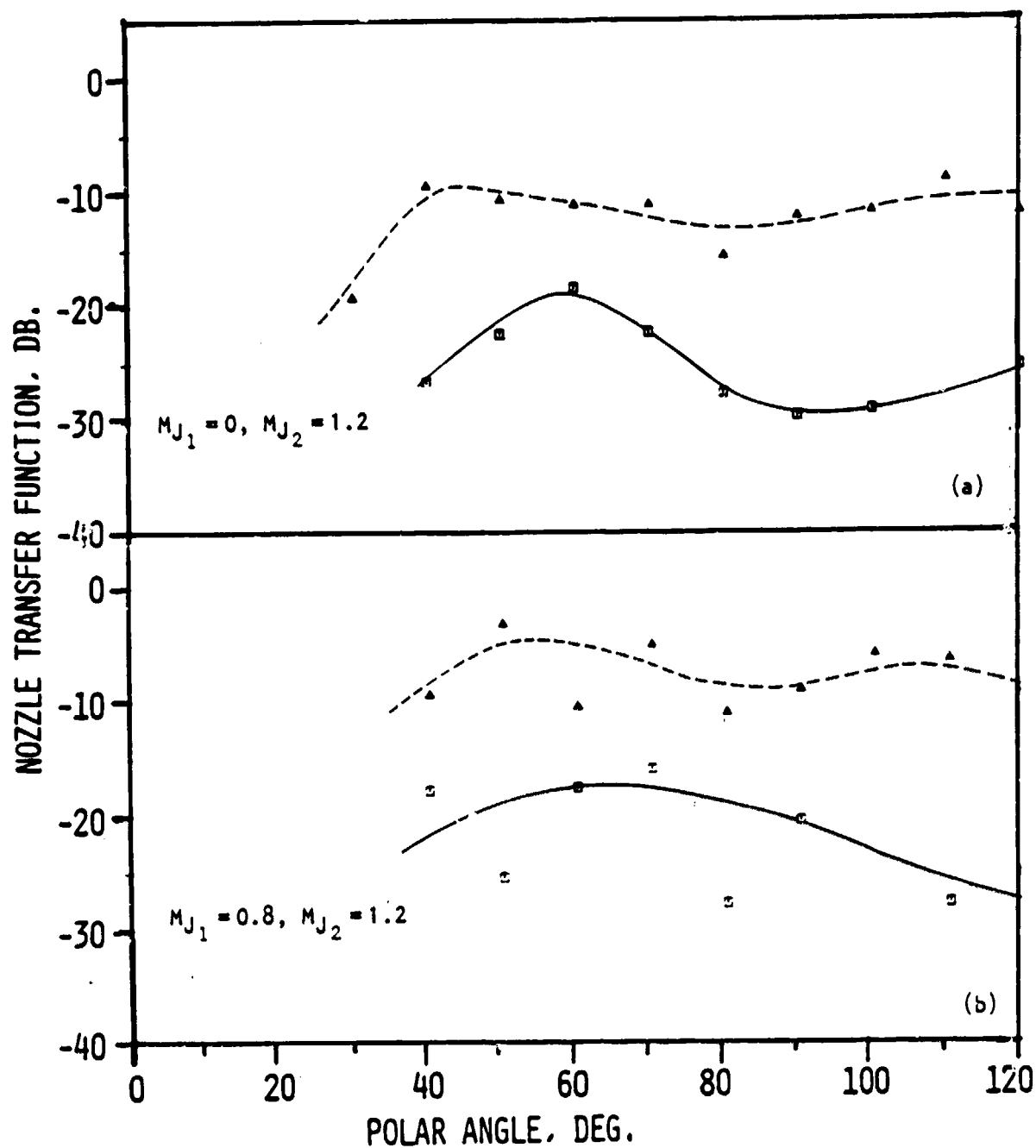


Figure 4.20 Nozzle transfer function directivity for various  $L/h$  ratios. Source at fan,  $\alpha = 20$  Deg.,  $kh = 0.5$ . CODE:  $L/h$ .

—□— 1  
- - -△- - - 5

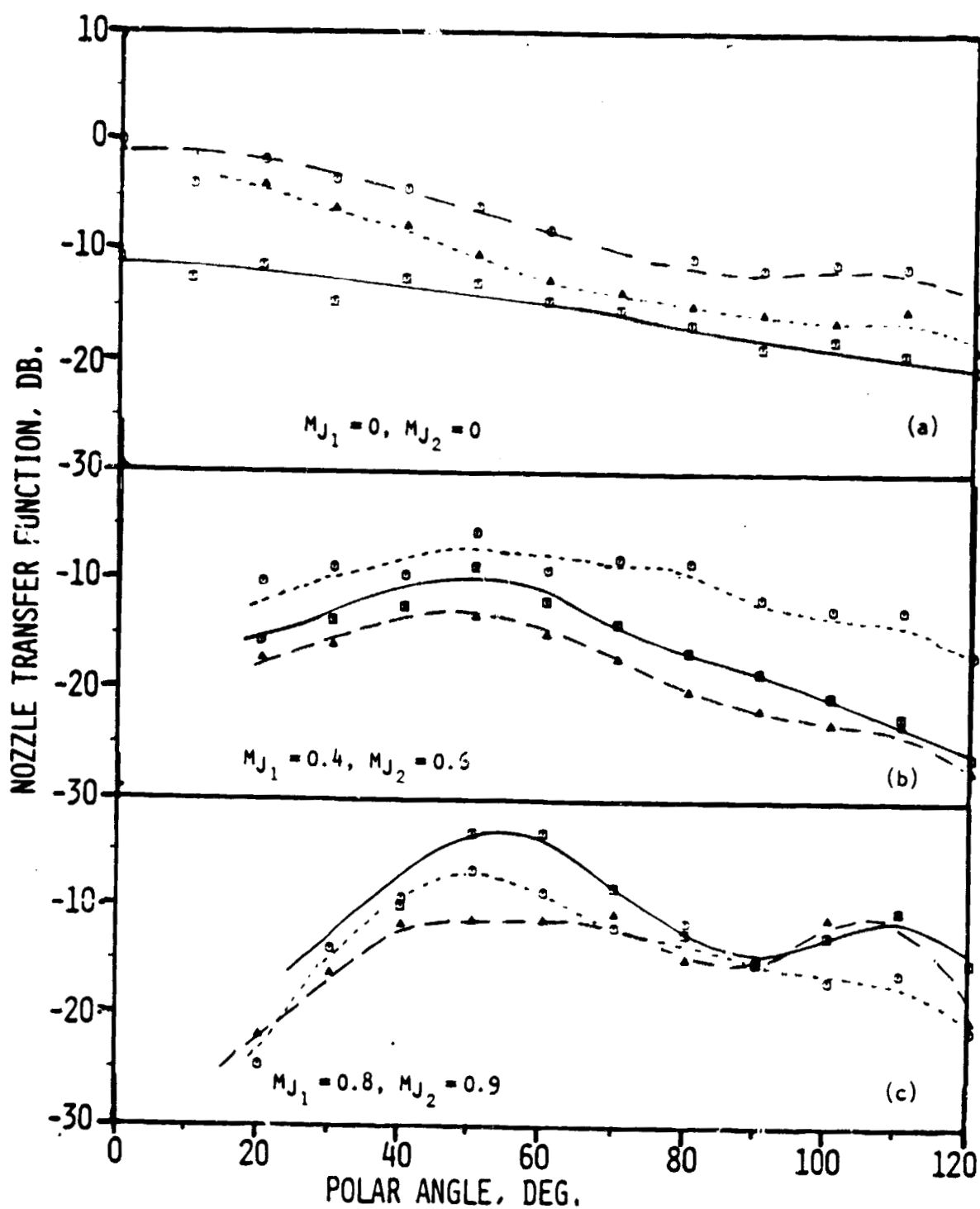


Figure 4.21 Nozzle transfer function directivity for various  $L/h$  ratios  
 Source at fan,  $\alpha = 20^\circ$  deg.,  $kh = 2$ .  
 CODE:  $L/h$

—○— :  
 - - - □ - - :  
 ···· △ ···· :

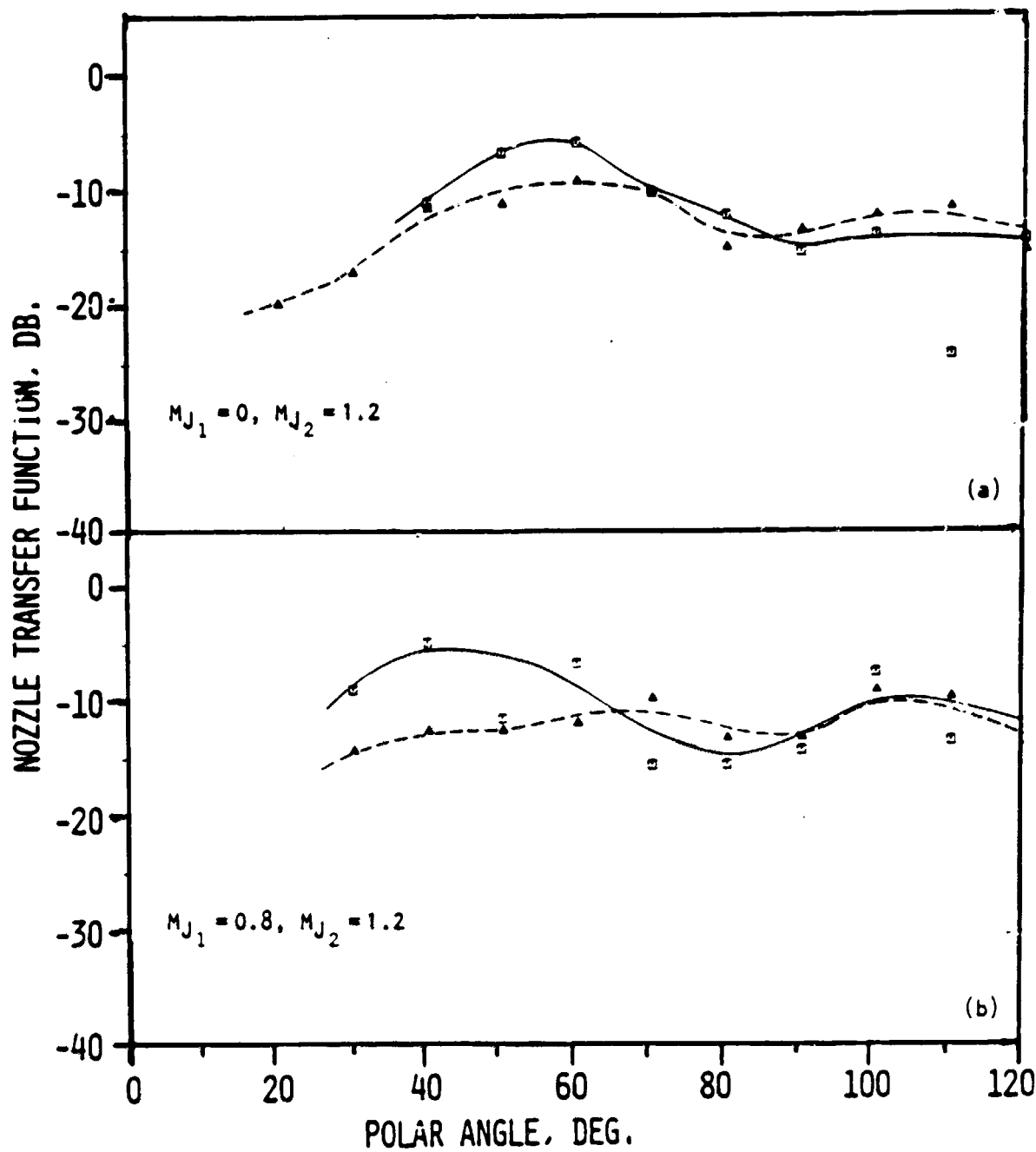


Figure 4.22 Nozzle transfer function directivity for various  $L/h$  ratios.  
Source at fan,  $\alpha = 20$  Deg,  $kh = 2$ .  
CODE:  $L/h$ .

—○—  
- - -△- - -



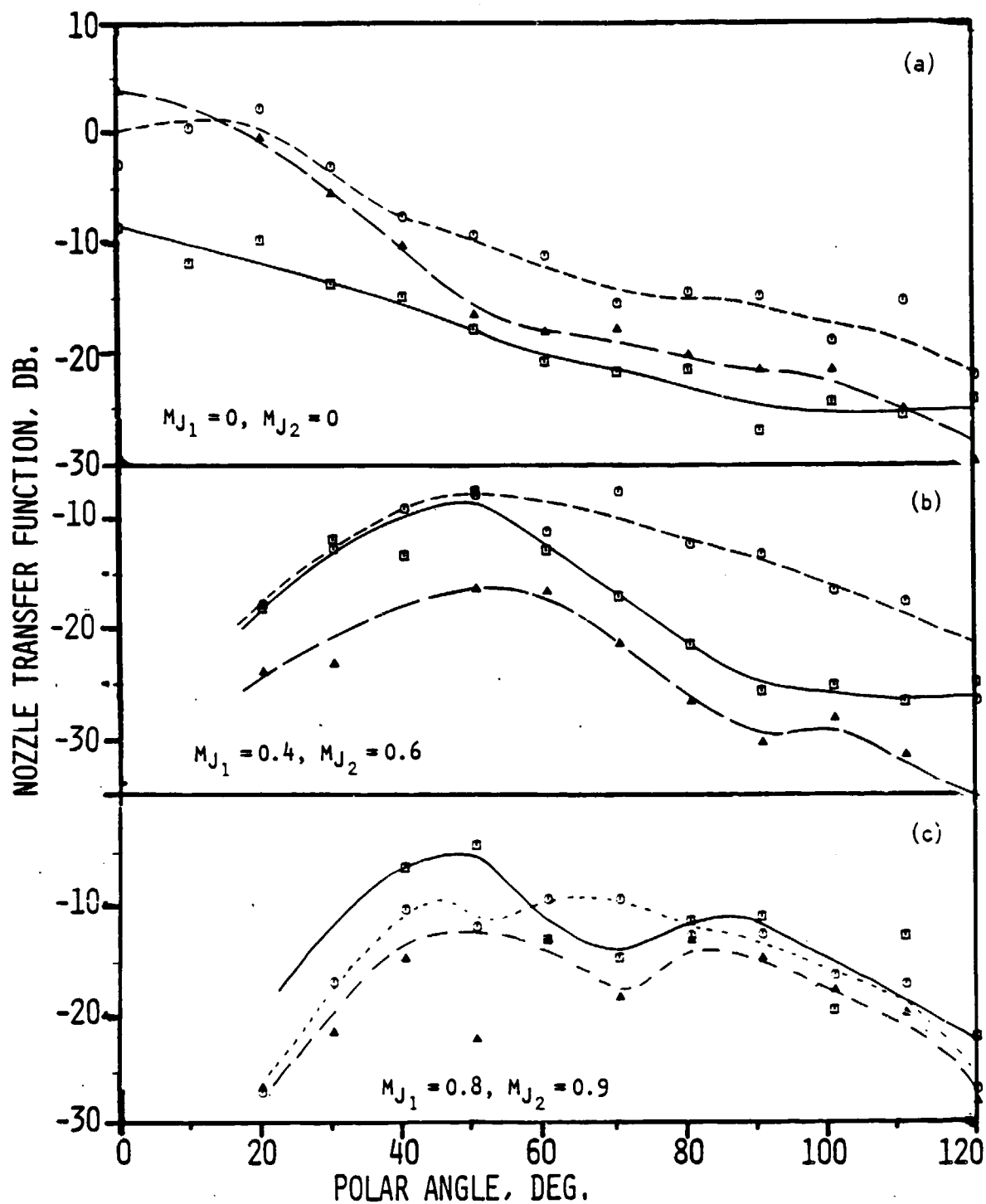


Figure 4.23 Nozzle transfer function directivity for various  $L/h$  ratios  
Source at fan,  $\alpha = 20$  Deg.,  $kh = 8$ .  
CODE:  $L/h$

—○— 1  
- -○- - 3  
- · -△- 5

increase in  $L/h=1$  directivities. The high flow conditions in figure 4.24 show considerable scatter, however, a trend is discernable in that below  $60^\circ$   $L/h=5$  is the minimum radiation condition whereas above this angle  $L/h=1$  is the minimum condition.

4.2.2.2 Forty-Degree Convergence Angle. - At  $kh=0.5$ , the zero flow comparison [fig. 4.25(a)] shows the  $L/h=3$  NTF dominating by about 10 dB above  $L/h=1$  and about 2 dB above the  $L/h=5$  nozzle configuration. An increase in flow velocity to (0.4, 0.6) reduces this difference markedly such that in figure 4.25(b), the  $L/h=1$  and 5 directivities are almost identical with the  $L/h=3$  case.

The next velocity condition of (0.8, 0.9) [fig. 4.25(c)] shows a more orderly directivity in that for all angles above  $50^\circ$ , the NTF increases with  $L/h$ ; that is, the higher the  $L/h$ , the more energy out. For the special flow condition of (0, 1.2) [fig. 4.25(d)], little difference is seen between  $L/h=1$  and 3 (the  $L/h=5$  data for this case was invalid due to a spark pulse cable defect).

As  $kh$  is increased to 2, figure 4.25(a) shows that at zero flow, little difference between each  $L/h$  directivity exists. Similarly at the flow condition of (0.4, 0.6) [fig. 4.26(b)] although the experimental scatter is greater, the basic directivity shapes are identical. At (0.8, 0.9) [fig. 4.26(c)] nozzle configurations  $N_4$  and  $N_5$  (i.e.  $L/h=1$  and 3) remain identical but the  $N_6$  ( $L/h=5$ ) configuration now shows increased transmission of energy of about 3-6 dB at polar angles larger than  $50^\circ$ . For the special flow case of (0.0, 1.2) [fig. 4.26(d)] the minimum radiation condition is for  $L/h=3$ , some 8 dB difference on average being observed over all angles. The interesting point to note is the second directivity peak in the 100 to 110 degree region.

Figure 4.27 shows the  $L/h$  comparisons for  $kh=8$ . At zero flow [fig. 4.27(a)],  $L/h=1$  is the minimum radiation configuration with  $L/h=3$  the maximum. As velocity is increased to (0.4, 0.6) [fig. 4.27(b)] the difference between  $L/h=1$  and 5 appears minimal with  $L/h=3$  dominating the directivity by 2 or 3 dB at all angles above  $50^\circ$ . At (0.8, 0.9) velocity condition [fig. 4.27(c)]  $L/h=5$  now dominates the radiation with  $L/h=3$  the minimum radiation condition at the peak angles of 50 and 60 degrees. The flow condition of (0.0, 1.2) [fig. 4-27(d)] shows little difference between  $L/h=1$  and 3, the apparent lower values of  $L/h=3$  at mid angles being within experimental error and thus the trend is questionable.

4.2.2.3 Summary. - The effects of  $L/h$  variations on the NTF can be summarized as follows:

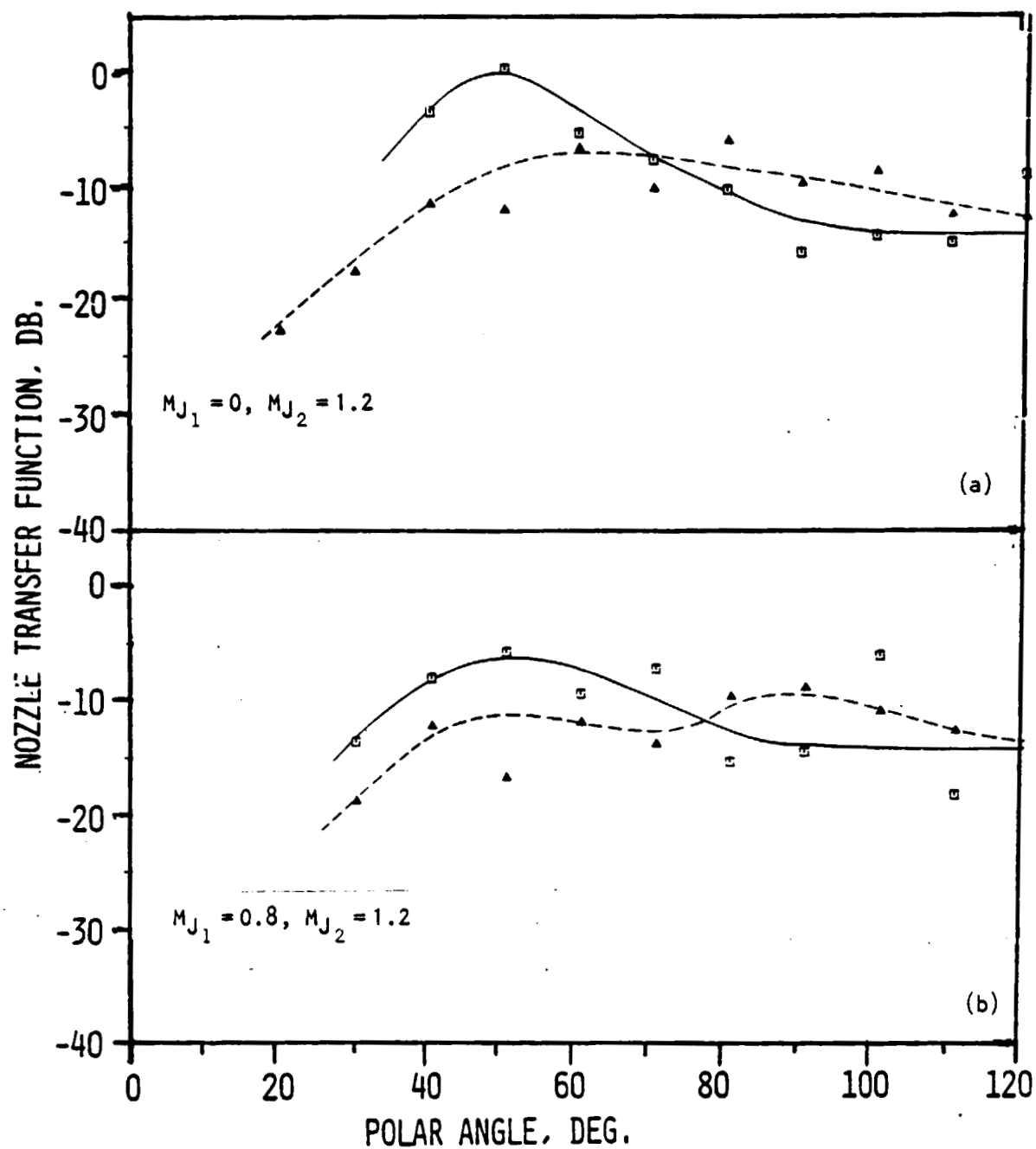


Figure 4.24 Nozzle transfer function directivity for various  $L/h$  ratios.  
Source at fan,  $\alpha = 20$  Deg,  $kh = 8$ .  
CODE:  $L/h$ .

—□— 1  
- - -△- - 5

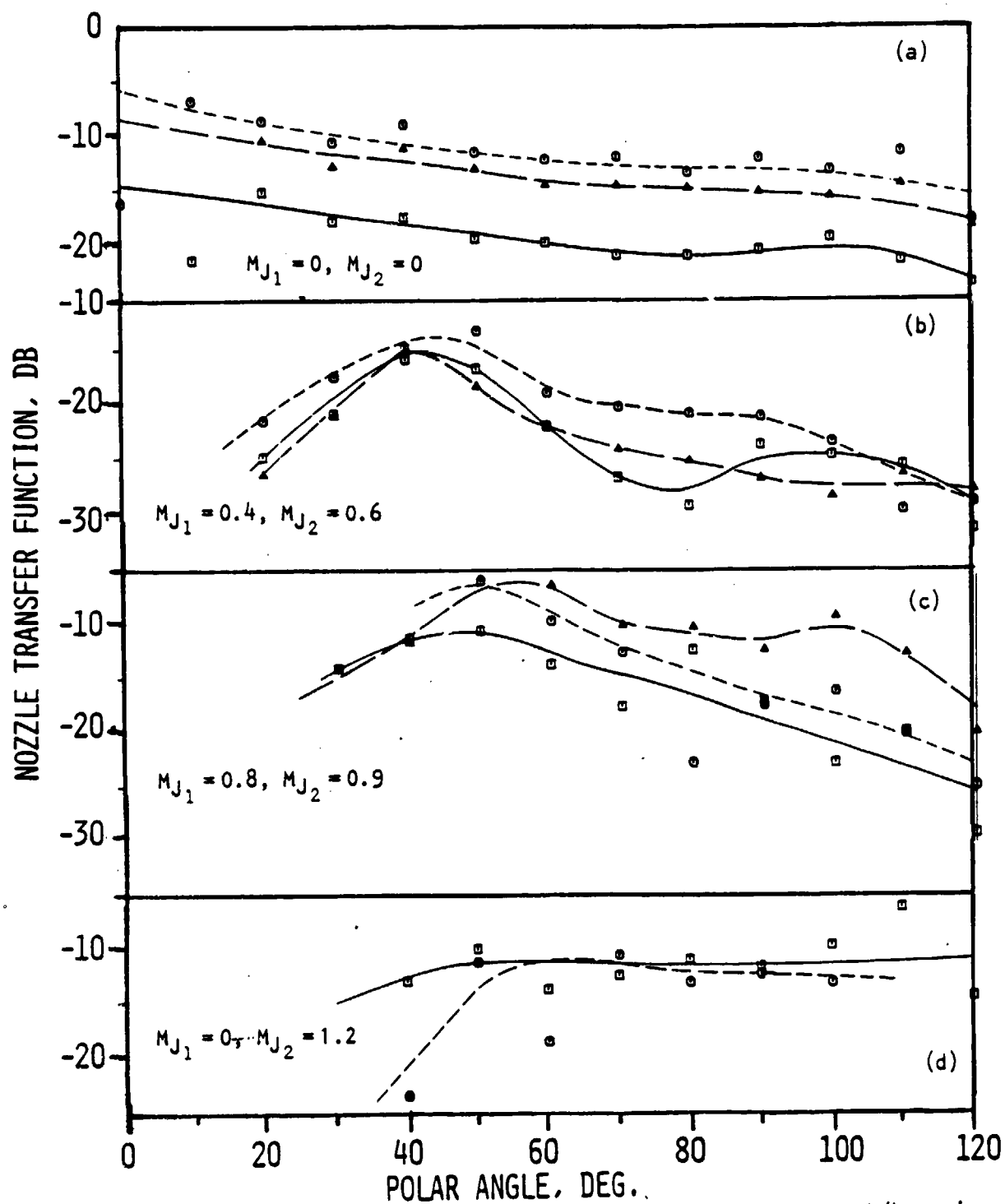


Figure 4.25 Nozzle transfer function directivity for various  $L/h$  ratios.  
Source at fan,  $\alpha = 40$  Deg.,  $kh = 0.5$   
CODE:  $L/h$ .

—○— 1  
- -○- - 3  
—△— 5

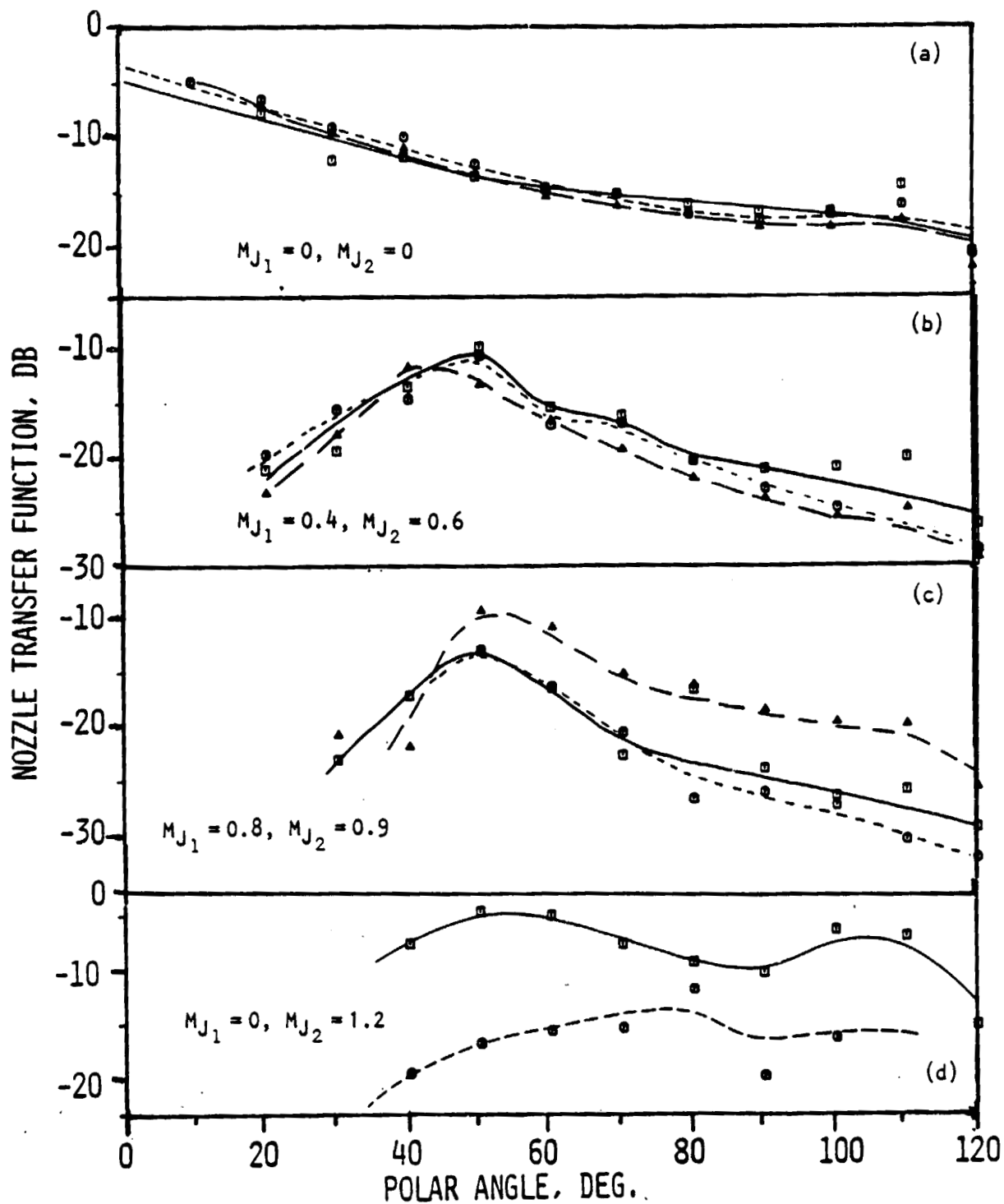


Figure 4.26 Nozzle transfer function directivity for various L/h ratios. Source at fan,  $\alpha = 40$  Deg,  $kh = 2$ . CODE: L/h.

—□— 1  
- - -○- - 3  
- · - · - 5

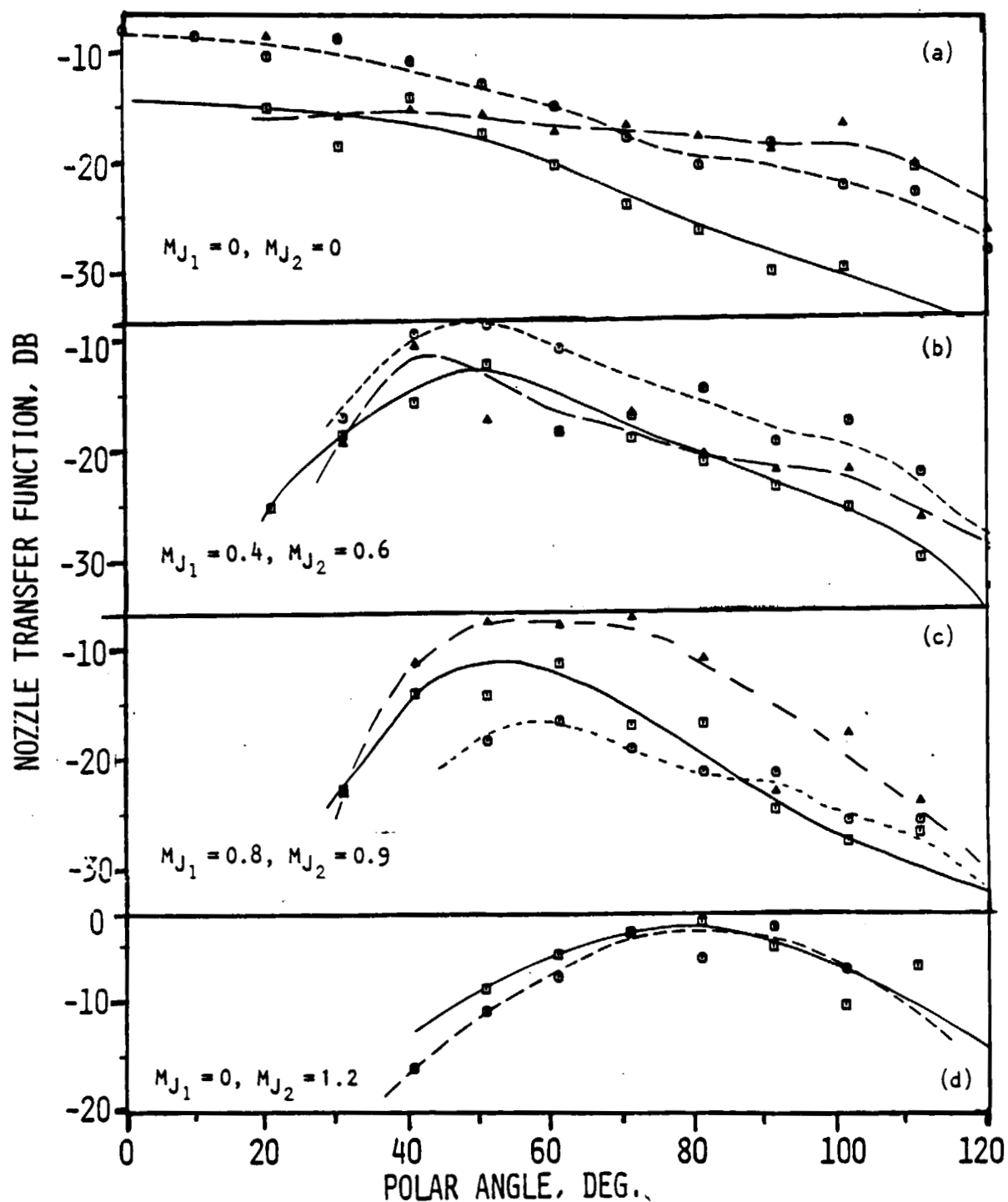


Figure 4.27 Nozzle transfer function directivity for various  $L/h$  ratios. Source at Fan,  $\alpha = 40$  Deg.,  $kh = 8$ .  
CODE:  $L/h$

—○— 1  
- - -○- - 3  
—△— 5

(1) For the 20° nozzle series:

- o Nondimensional frequency comparisons on  $kh$  appear valid.
- o The nozzle configuration for minimum level conditions of NTF are defined by both frequency and velocity conditions.
  - o At low frequencies, low velocities, the minimum-observed NTF occurs with  $L/h=1$  nozzle.
  - o At mid frequencies, for all velocities  $L/h=5$  is the minimum NTF configuration
  - o At high frequencies, high velocities, NTF is minimum for  $L/h=5$  configuration and maximum for  $L/h=1$ .

(2) For the 40° nozzle series:

- o At low- and mid-frequencies and low velocities little difference in NTF is observed between  $L/h=1$  and 3.
- o At low and mid frequencies and high velocities the maximum NTF is observed for  $L/h=5$  nozzle configuration.
- o At high frequencies and velocities the minimum NTF configuration is  $L/h=3$ .

#### 4.2.3 Convergence Angle Effects

For the purposes of this discussion, only  $L/h=1$  nozzles will be considered. However, the trends are similar for  $L/h=3$  and  $L/h=5$ , and the basic data for these nozzle configurations are given in the accompanying data report. At zero flow for  $kh=0.5$ , little visible change between 20 and 40 degree fan convergence angle tests was observed. Figure 4.28(a) shows a comparison at  $kh=0.5$  which illustrates the typical scatter of the directivities, which is well within experimental error. As the velocity condition is increased to (0.4, 0.6) [fig. 4.28(b)], some divergence can be seen in the refraction valley at 20 and 30 degrees (the  $N_1$  nozzle being more efficient) with all other angles comparing excellently. As the velocity condition is increased to (0.8, 0.9), the measurement scatter has increased but the trends are clearly similar. The special flow case of (0.0, 1.2) [fig. 4.28(d)] shows marked differences of some 10 dB or more between the directivities with 20° convergence angle being the minimum condition.

At  $kh=2.0$  for zero flow [fig. 4.29(a)] the directivities are virtually identical. As flow increases to (0.4, 0.6) [fig. 4.29(b)] the 40° convergent nozzle is clearly a less efficient transmission system. This trend continues until at (0.8, 0.9) [fig. 4.29(c)] the 20° convergence angle nozzle stands out higher by almost 10 dB. The parallel nature of the two curves was such that a plotting error was suspected. However, the data was verified as correct, and the cause for such large amplitudes is not yet understood. In figure 4.29(d) [the special flow case of (0.0, 1.2)], it can be seen that the

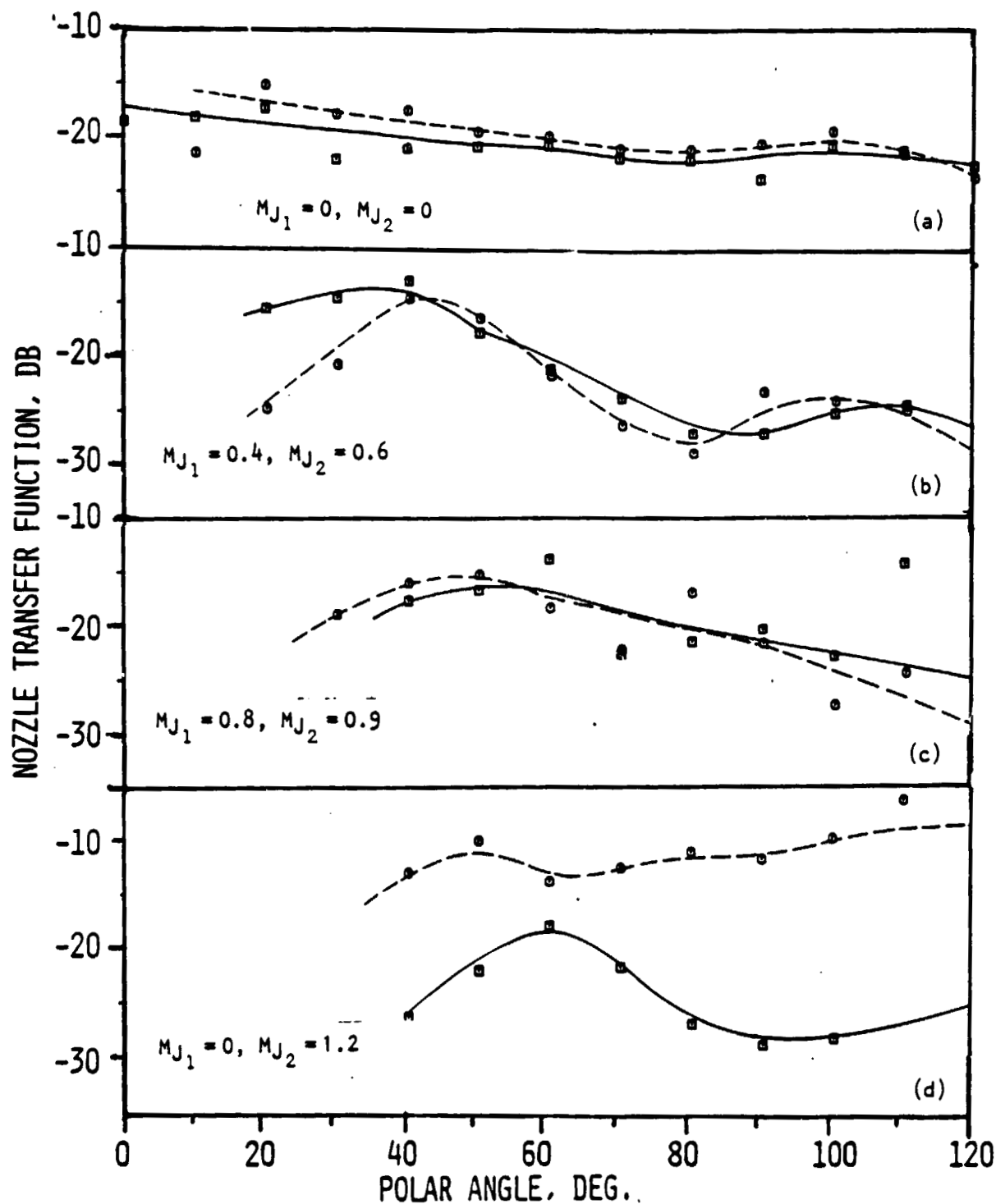


Figure 4.28 Nozzle transfer function directivity for various convergence angles,  $\alpha$ . Source at fan,  $L/h=1$ ,  $kh=0.5$ .

CODE: CONVERGENCE ANGLE, DEG



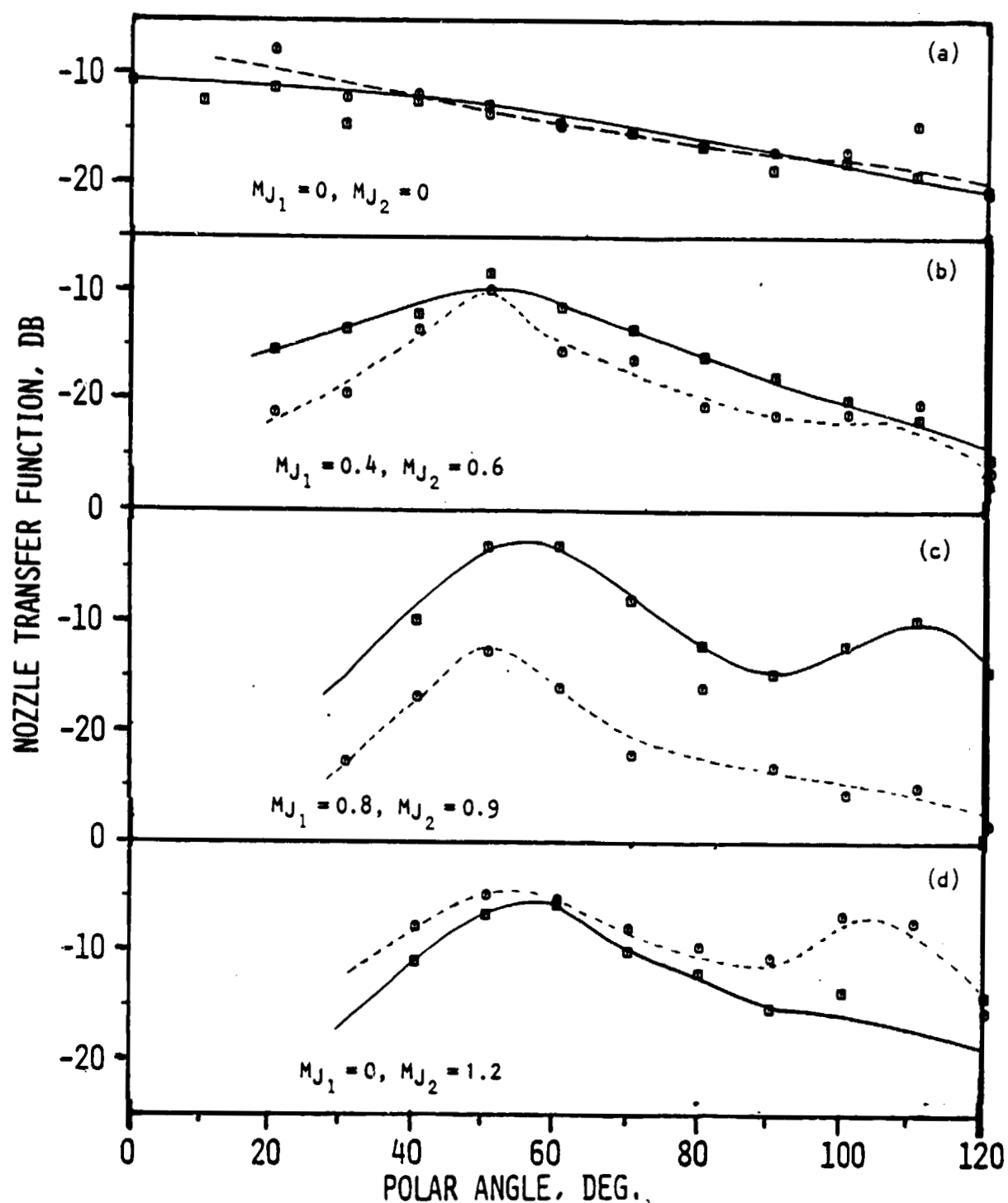


Figure 4.29 Nozzle transfer function directivity for various convergence angles,  $\alpha$ . Source at fan,  $L/h=1$ ,  $kh=2$ .

CODE: CONVERGENCE ANGLE, DEG  
 —○— 28  
 - - -○- - 48

40° convergence angle now dominates. This does not imply that the 20° nozzle NTF has reduced but that for the 40° nozzle has increased in level. This flow situation is the only one at low and mid frequencies for which the 40° nozzle dominates.

In the high-frequency regime ( $kh=8.0$ , fig. 4.30) the trends are similar to  $kh=2.0$  with the exception that at the flow condition of (0.0, 1.2) the 40° nozzle dominates only above 60° polar angle, unlike the lower frequencies which showed dominance at all angles.

For the  $L/h$  ratios of 3 and 5, similar trends were observed, although some individual features are worthy of comment. For example, for  $L/h=3$  at  $kh=2.0$  in figure 4.31, the directivity plots for each nozzle angle are almost parallel being separated by 7 to 10 dB. Similarly, for  $L/h=5$  (fig. 4.32) the directivity plots are also parallel but separated now by no more than 2 or 3 dB. (Thus, the inference is clearly that for this frequency, directivity collapse could be achieved by inclusion of an  $L/h$  efficiency parameter.)

4.2.3.1 Summary. - The effects of convergence angle on the NTF are summarized as follows:

- o At low velocities a frequency dependence is observed such that the 40° convergence angle shows slightly higher NTF at low frequencies while the 20° nozzle configuration shows the maximum NTF at high frequencies.
- o As the velocity conditions increase the 20° nozzle configuration dominance of NTF increases at mid and high frequencies.
- o At the special flow case of (0.0, 1.2) the minimum NTF configuration is the 20° convergence angle.
- o No significant trend differences are observed between  $L/h$  configurations of 1, 3 and 5.

### 4.3 COMPARISON OF SOURCES IN CORE AND FAN

This directivity comparison will be restricted to the 20° nozzle series only, that is,  $N_1$ ,  $N_2$  and  $N_3$ . For nozzle configuration  $N_1$ , figure 4.33 shows the comparison at  $kR=kh=0.5$  for three velocity configurations: zero, (0.4, 0.6) and (0.8, 0.9). The zero flow case shows the fan NTF to be some 10 dB less than that of the core but still having the same angular distribution. As the velocity increases to (0.4, 0.6) [fig. 4.33(b)], the fan NTF lifts considerably at polar angles less than 50° and reduces at high angles, with the peak reduction occurring at 80°.

For  $kR_j=kh=2.0$ , the trends are similar to the low frequency case, but the absolute differences are considerably less. Figures 4.34(a) and 4.34(b)

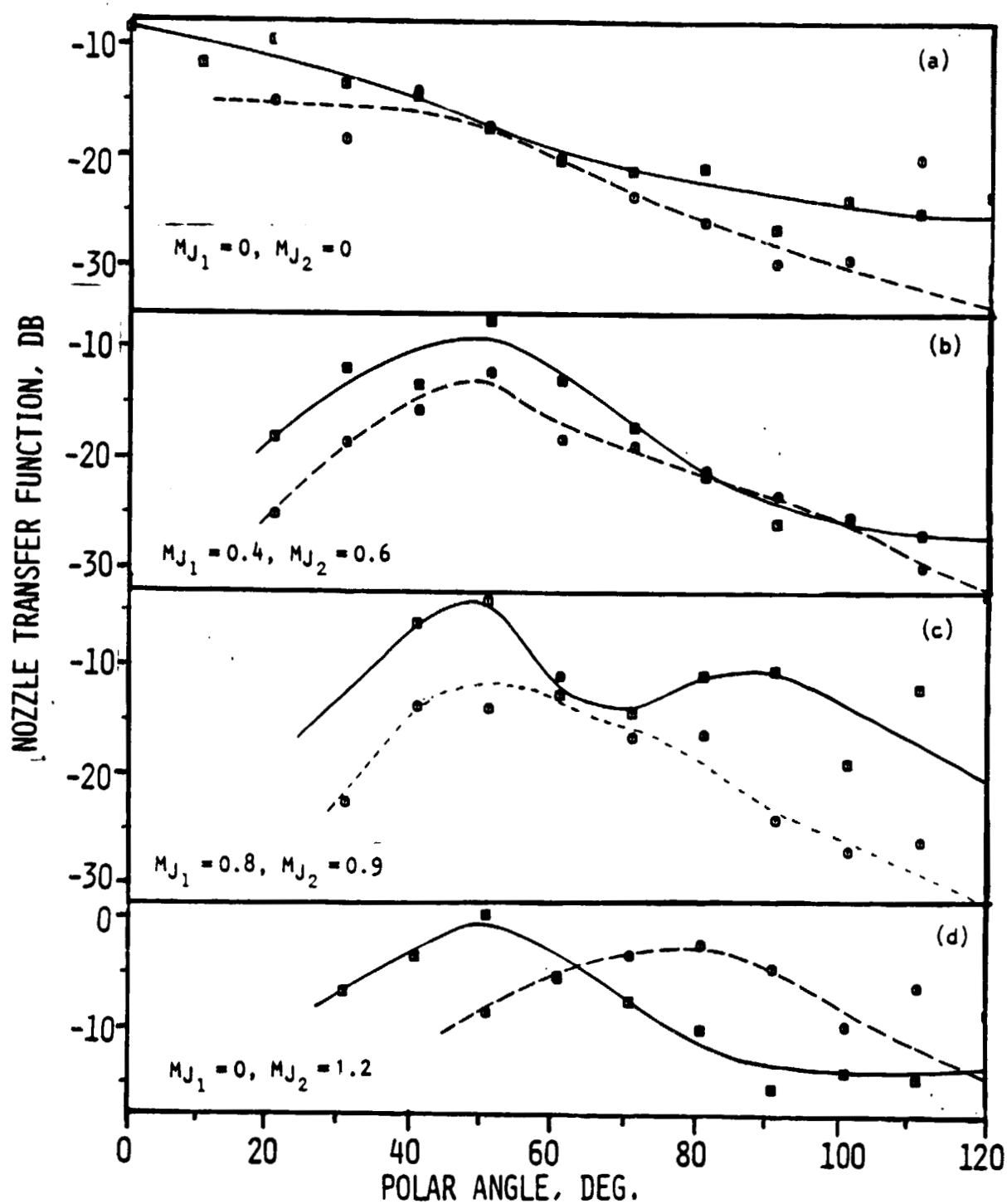


Figure 4.30 Nozzle transfer function directivity for various convergence angles,  $\alpha$ .  
 Source at Fan,  $L/h=1$ ,  $kh=8$ .  
 CODE: CONVERGENCE ANGLE, DEG  
 —●— 28  
 - - -○- - 48

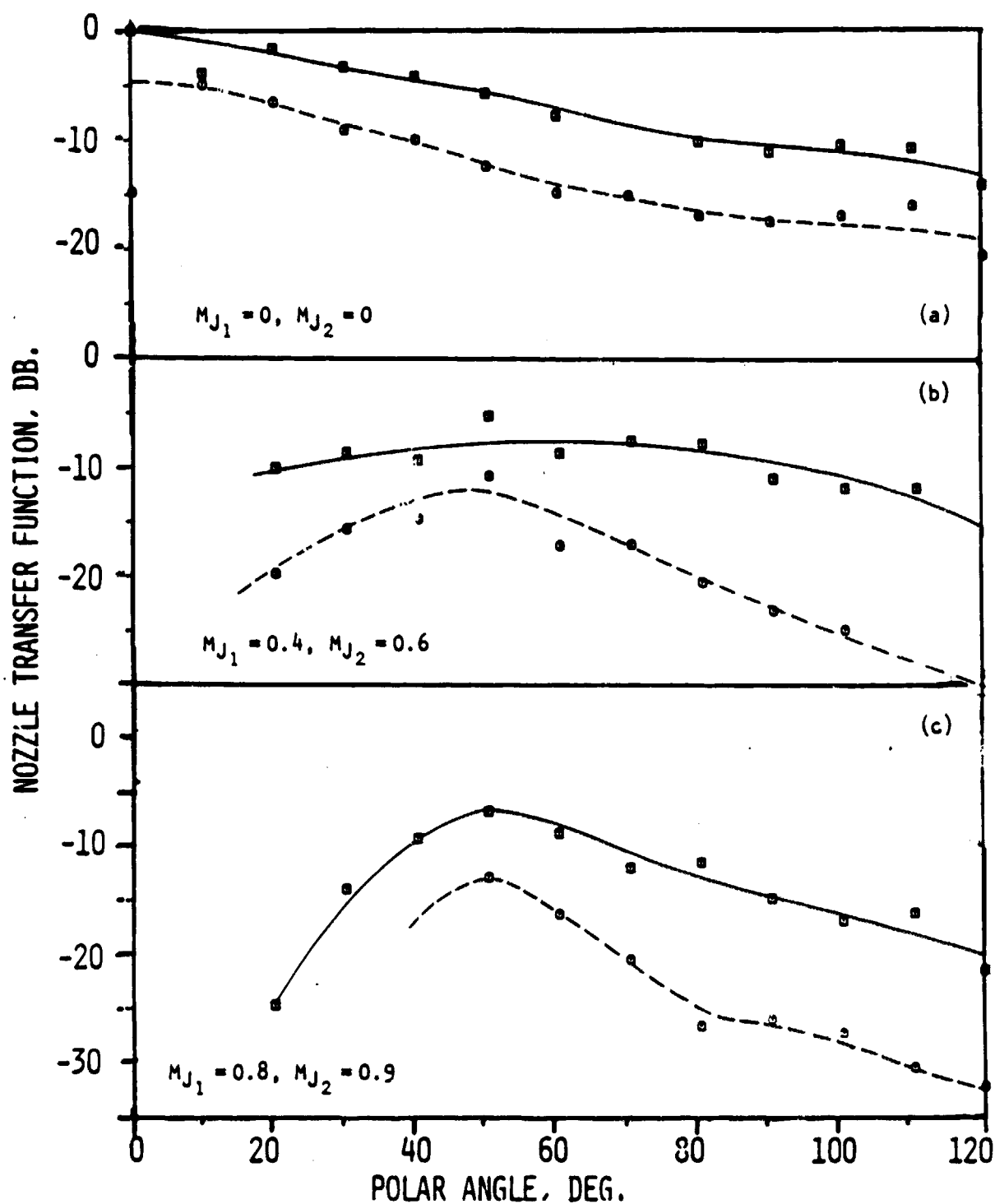


Figure 4.31 Nozzle transfer function directivity for various convergence angles,  $\alpha$ . Source at fan,  $L/h=3$ ,  $kh=2$ .

CODE: CONVERGENCE ANGLE, DEG  
 —■— 28  
 - - -○- - 48

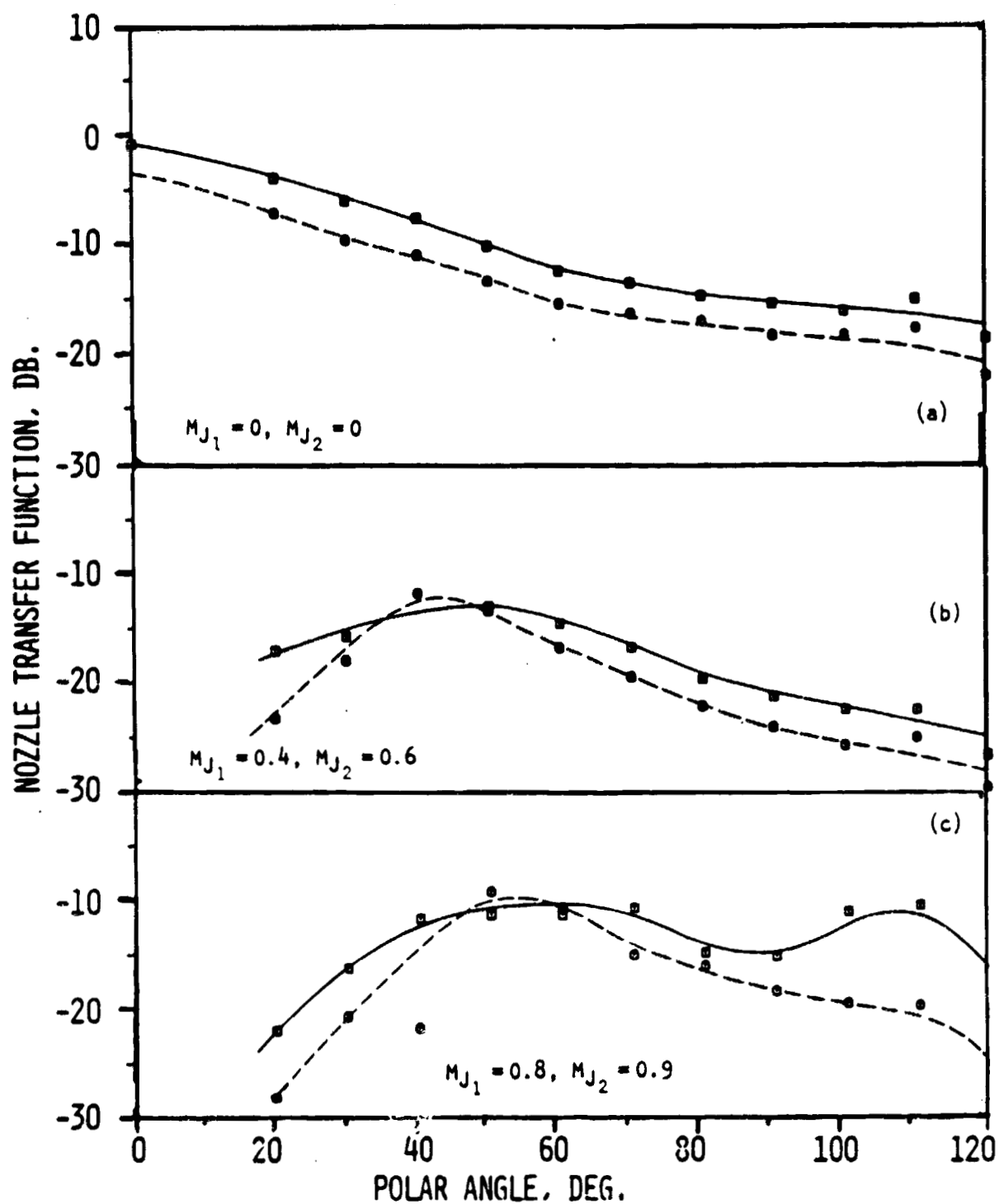


Figure 4.32 Nozzle transfer function directivity for various convergence angles,  $\alpha$ . Source at fan,  $L/h=5$ ,  $kh=2$ .

CODE: CONVERGENCE ANGLE, DEG  
 —■— 20  
 -○- 40

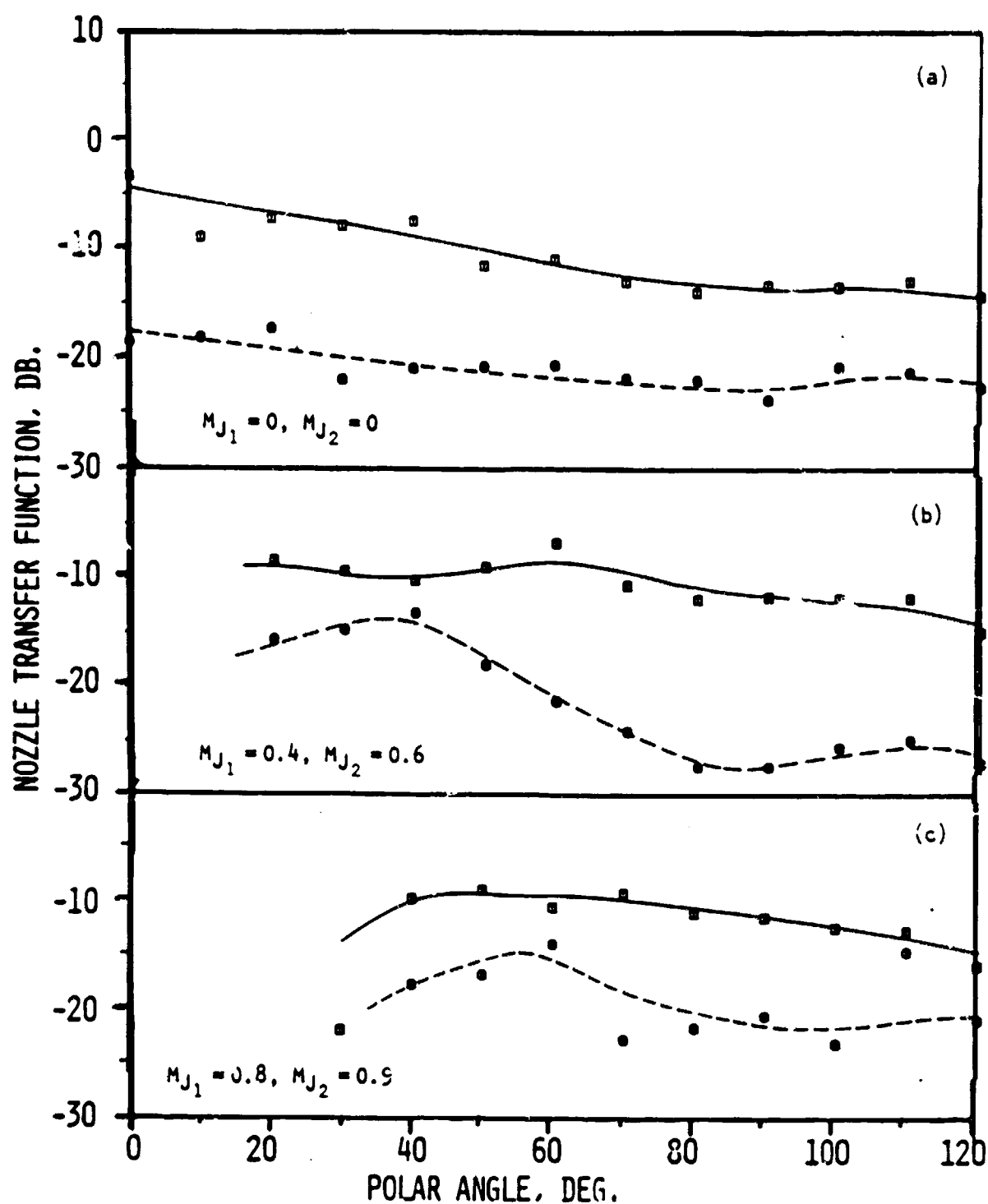


Figure 4.33 Nozzle transfer function directivity for various source locations. Nozzle  $N_1$  ( $\alpha = 20$  Deg.,  $L/h = 1$ ),  $kR_J = kh = 0.5$ .

CODE: SOURCE LOCATION  
 —■— CORE  
 - - -○- - FAN

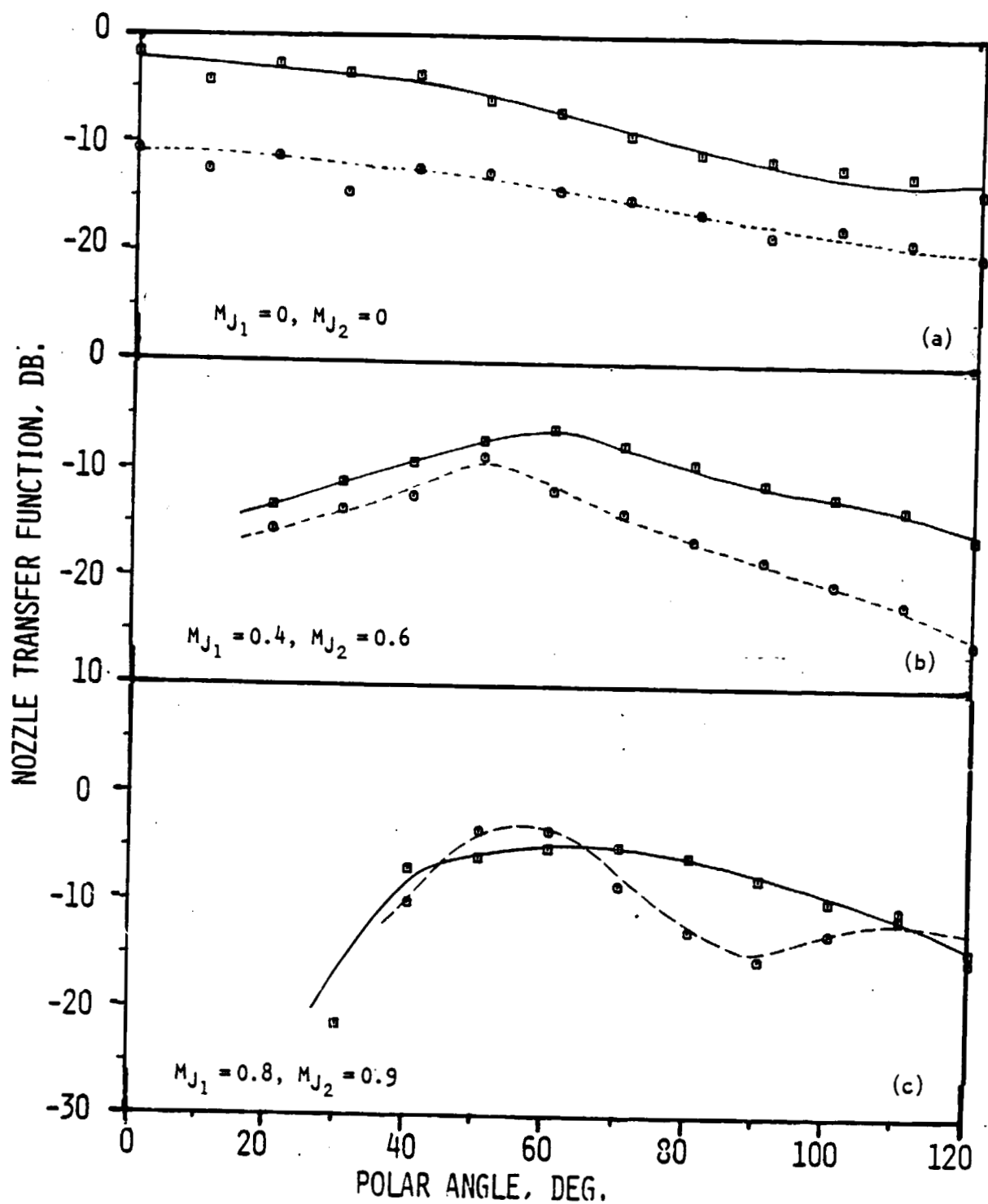


Figure 4.34 Nozzle transfer function directivity for various source locations. Nozzle  $N_1$  ( $\alpha = 20$  Deg.,  $L/h = 1$ ),  $kR_J = kh = 2$ .

CODE: SOURCE LOCATION

—○— CORE  
 - -○- - FAN

show the similarities of shape for the two lowest velocity conditions. At the velocity condition of (0.8, 0.9) [fig. 4.34(c)], the fan directivity now tends to collapse everywhere except in the  $80^\circ$  region.

As frequency is increased to  $kr_j = kh = 8.0$  in figures 4.35(a) and 4.35(b) consistent trends similar to the lower frequency data can be seen with high angle divergence again observed in the (0.4, 0.6) flow case. The high flow case of (0.8, 0.9) [fig. 4.35(c)] shows the situation of the fan NTF now exceeding the core NTF over both low and high angles by almost 10 dB, with the 60 and 70 degree angle values of core and fan NTF being almost identical.

From the above observations a pattern emerges. The similar shape of the directivities is indicative of a potential data collapse as well as a positive indicator of the validity of comparison of  $kr$  and  $kh$  as nondimensional frequency parameters. A fan velocity dependence is also indicated in that its NTF increases from below that of the core at zero velocity, to a reasonable collapse at (0.4, 0.6), to exceeding the core NTF at (0.8, 0.9). This trend is observed at all frequencies.

The probable cause of these amplitude differences lies in the basic definition of the NTF which considers only *incident* energy. If the fan reflects more energy than the core, then the transmitted sound is correspondingly lower. Collapse would only then be expected if the NTF was defined as transmitted sound to far-field measured sound directivity ratio.

Nozzle configuration  $N_2$  ( $L/h=3$ ) shows the best example of similarity of NTF for all nozzle configurations. The trends with velocity still exist but are so subdued that they appear to be of the same order of magnitude as the data scatter. For  $kh = kr_j = 0.5$ , figure 4.36 shows remarkable similarity at all angles. Similarly for  $kh = kr_j = 2.0$  (fig. 4.37) a good data collapse is evident. These data also show a trend of a relative fan NTF amplitudes increase with increasing flow velocity. The high frequency regime (fig. 4.38) shows this trend to be even more accentuated with the fan NTF exceeding the core NTF by some 3 to 5 dB.

The  $L/h=5$  nozzle configuration ( $N_3$ ) reverts to the relative amplitude trends noted for  $L/h=1$ . For  $kh = kr_j = 0.5$  at zero flow [fig. 4.39(a)] the fan NTF is now 12 dB below the core NTF. However, as the velocity is increased to (0.4, 0.6), not only does the fan NTF rise relative to that of the core, but the shape changes slightly such that the refraction valley is less than that of the core, while the high angle drop-off is more severe. This characteristic is retained at the flow condition of (0.8, 0.9) [fig. 4.39(c)] with the additional modification of high angle lift above  $80$  degrees.

At  $kh = kr_j = 2.0$  (fig. 4.40) the trends observed for the low frequency case are more accentuated. Figure 4.40(b) is a clear example of the refraction effect. Here, it is obvious that the core source is refracted much more than the fan source. This is expected, since the core source sound pressure must propagate through a much thicker shear layer than that of the fan source. The high frequency regime ( $kh = kr_j = 8.0$ ) in figure 4.41 exhibits similar characteristics to those observed for the ( $kh = kr_j = 2.0$ ) case.



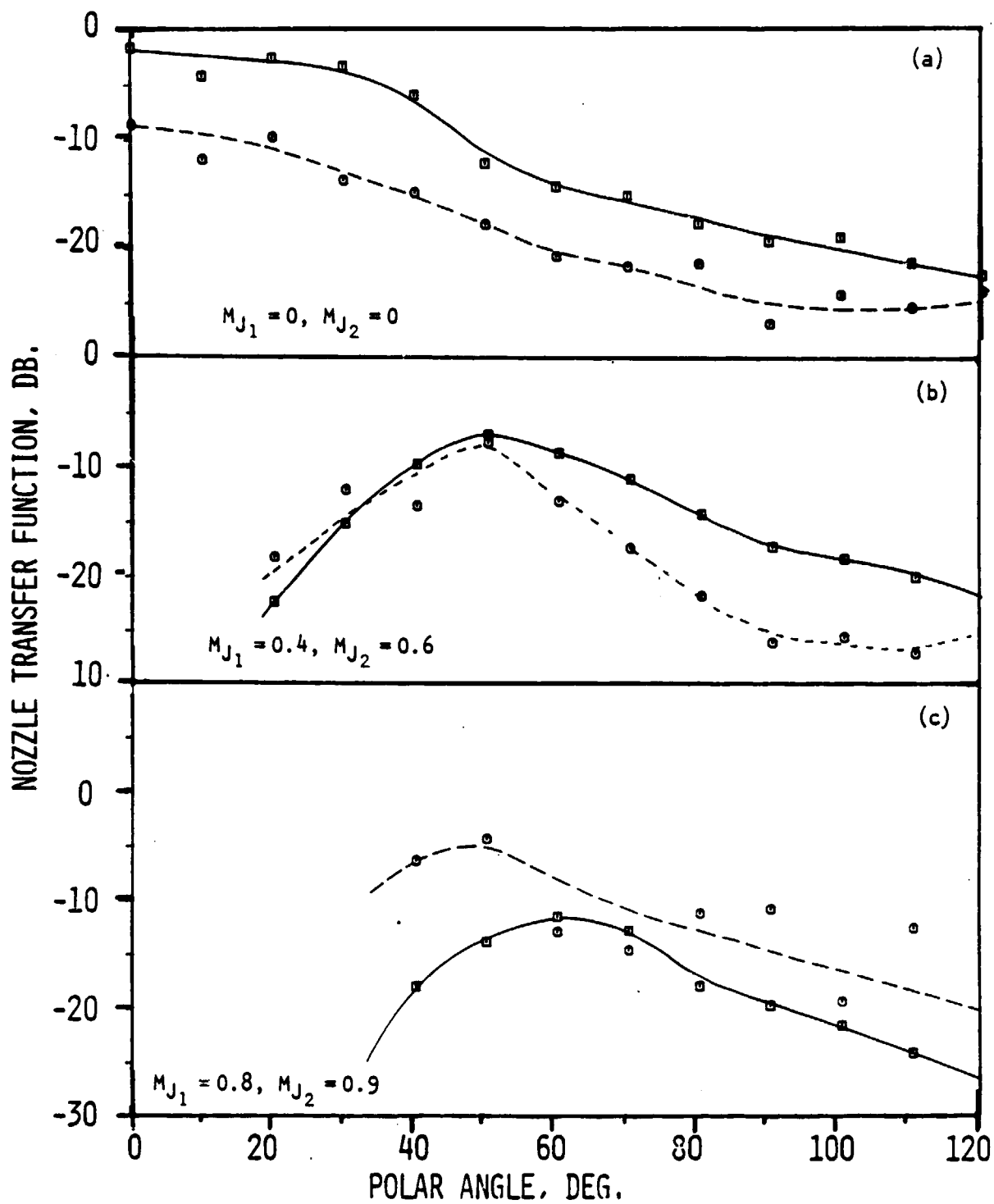


Figure 4.35 Nozzle transfer function directivity for various source locations.  
Nozzle  $N_1$  ( $\alpha = 20$  Deg.,  $L/h = 1$ ),  $kR_J = kh = 8$

CODE: SOURCE LOCATION  
 —○— CORE  
 - - -○- FAN

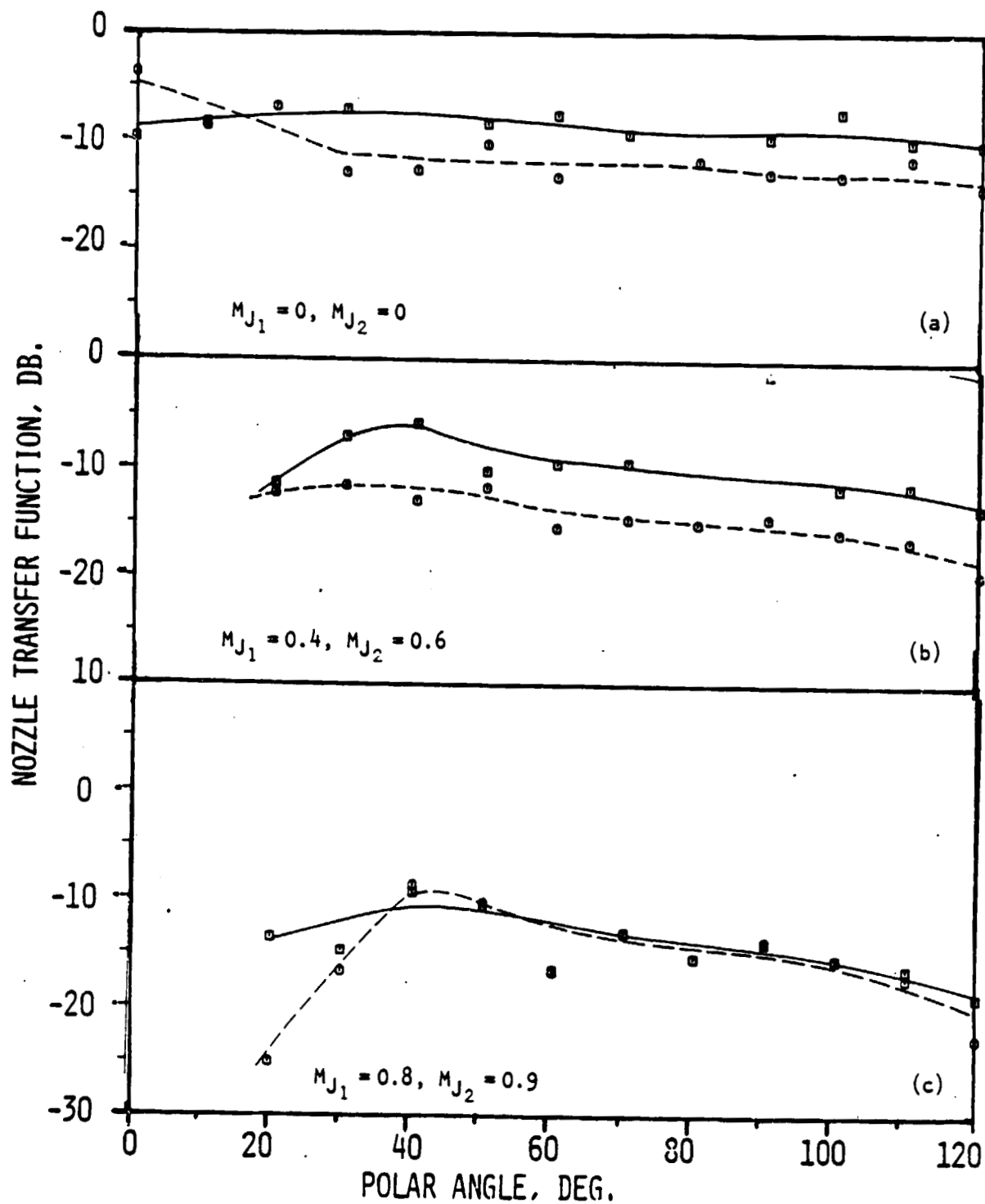


Figure 4.36 Nozzle transfer function directivity for various source locations. Nozzle N<sub>2</sub> ( $\alpha = 20$  Deg.,  $L/h = 3$ ),  $kr_J = kh = 0.5$ .

CODE: SOURCE LOCATION  
 —□— CORE  
 - -○- - FAN

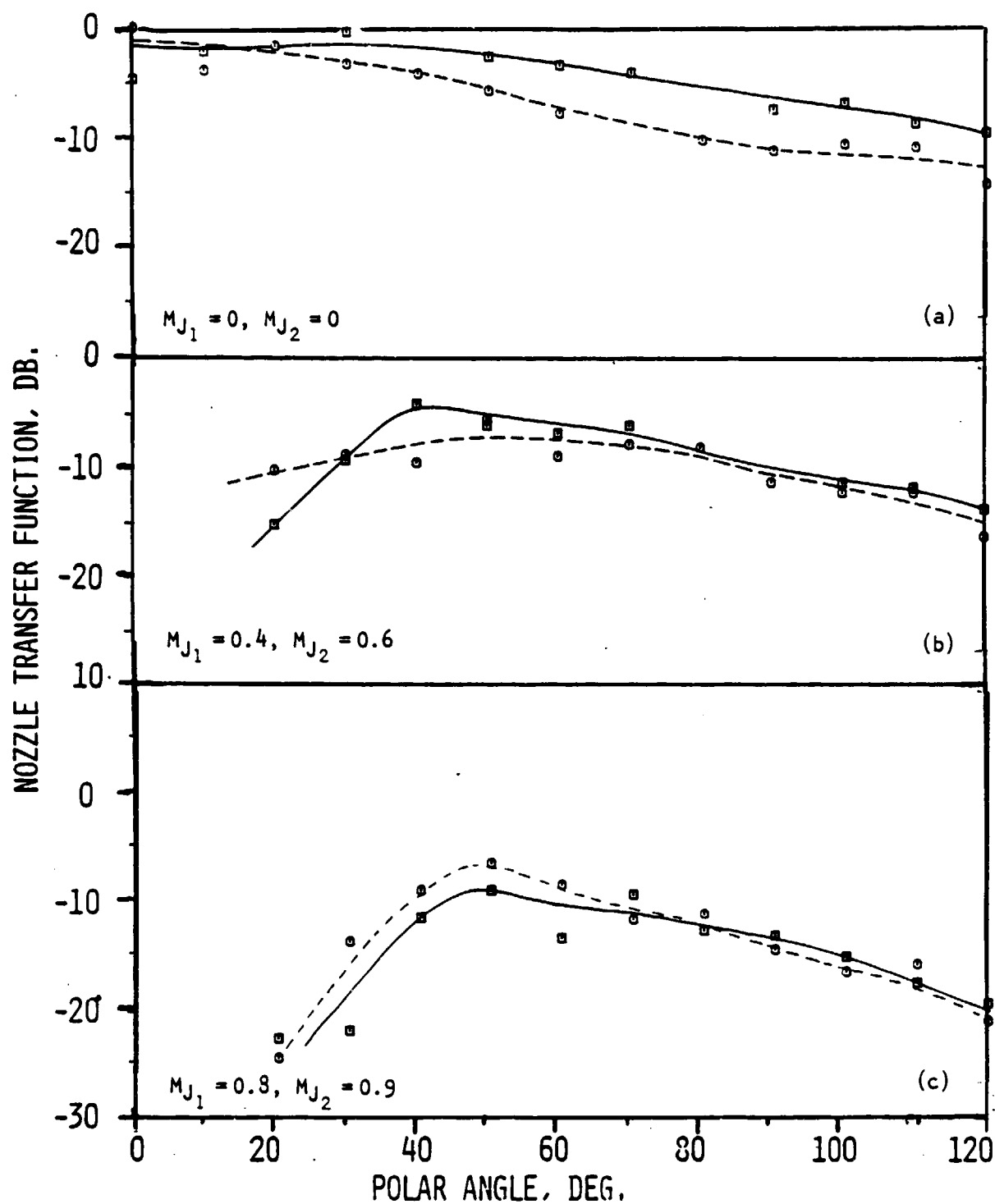


Figure 4.37 Nozzle transfer function directivity for various source locations. Nozzle N<sub>2</sub> ( $\alpha = 20$  Deg.,  $L/h = 3$ ),  $kR_J = kh = 2$ .

CODE: SOURCE LOCATION  
 —○— CORE  
 - - -○- - FAN

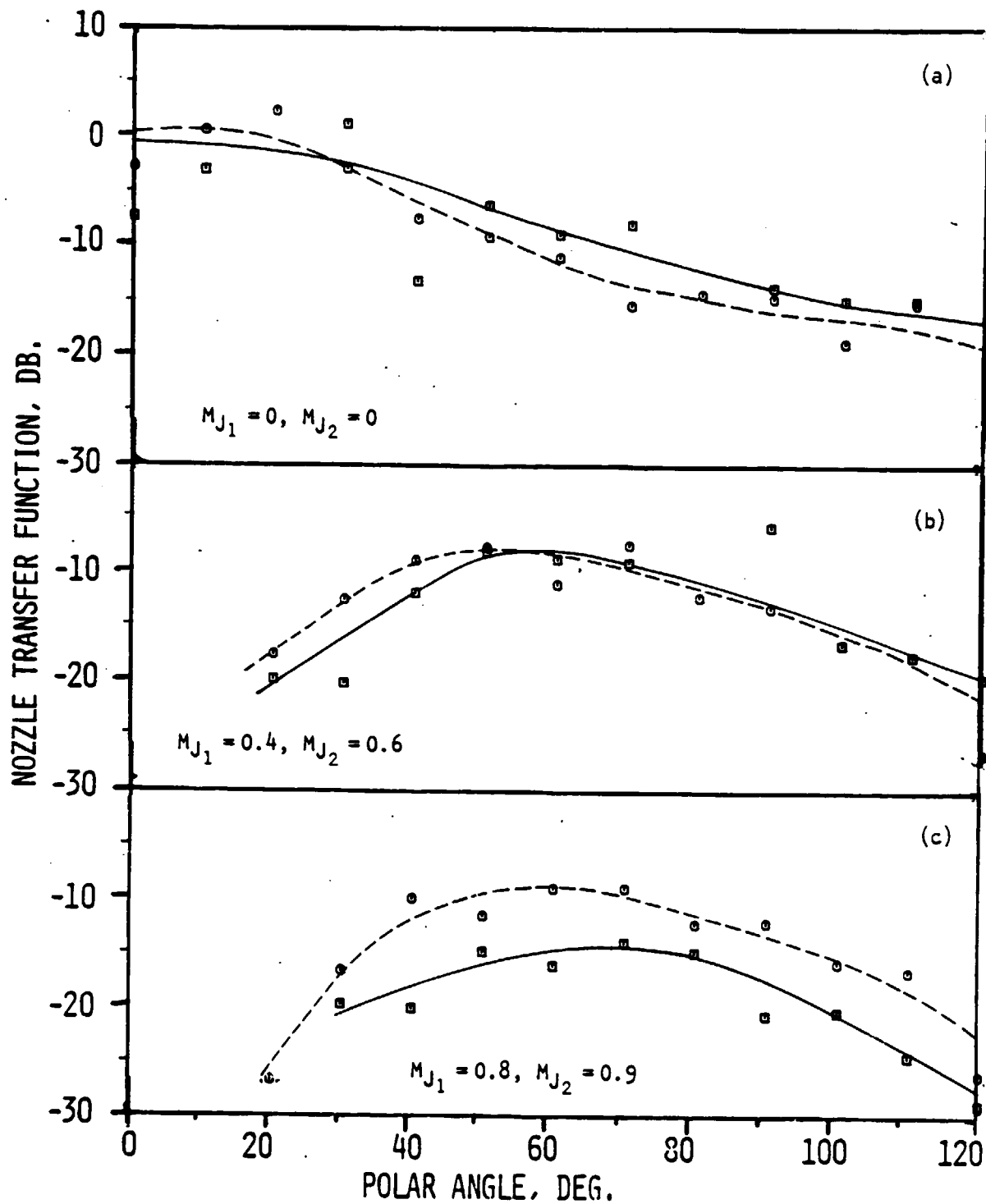


Figure 4.38 Nozzle transfer function directivity for various source locations. Nozzle  $N_2$  ( $\alpha = 20$  Deg.,  $L/h = 3$ ),  $kR_J = kh = 8$ .

CODE: SOURCE LOCATION

—○— CORE

- - -○- - FAN

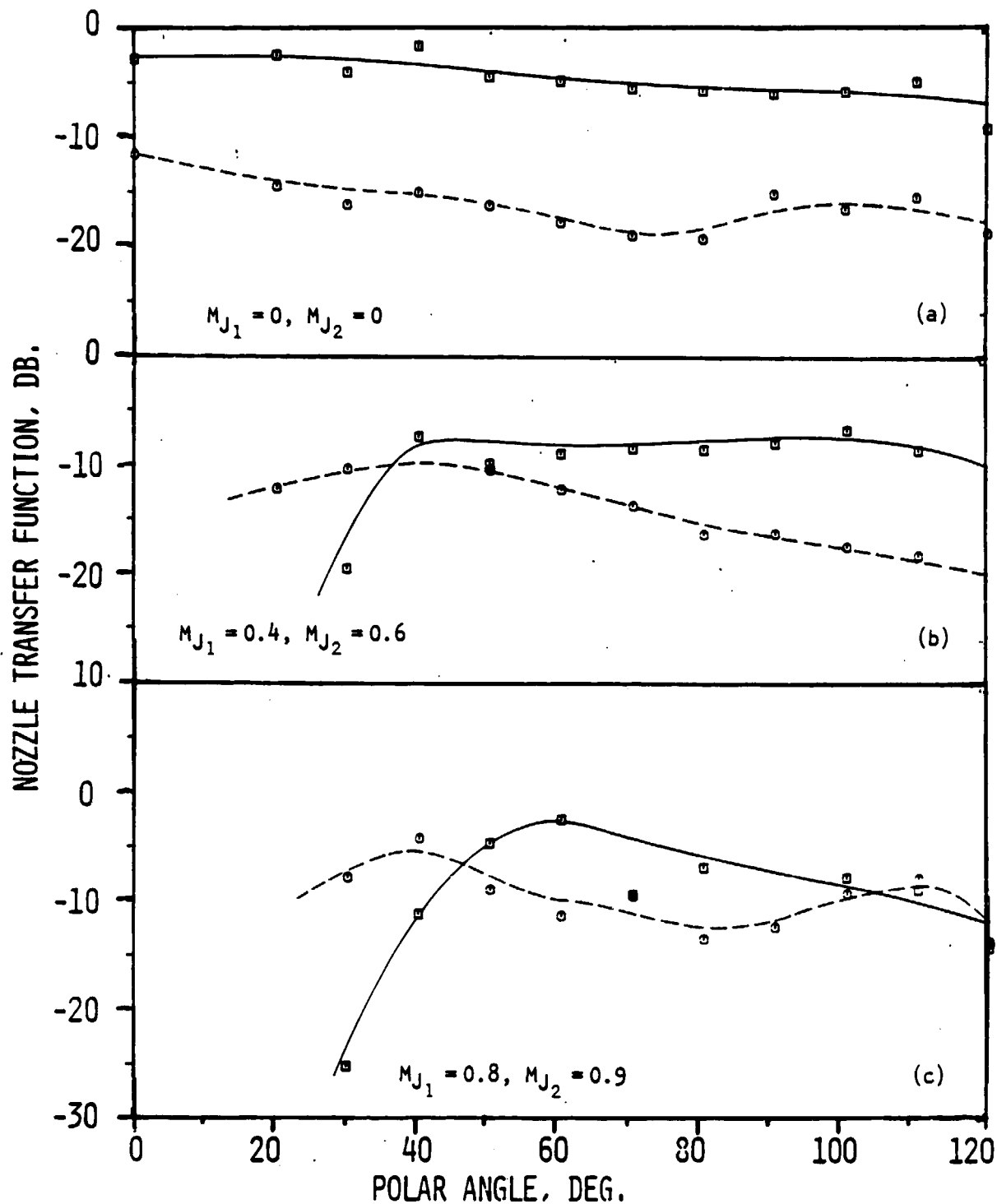


Figure 4.39 Nozzle transfer function directivity for various source locations. Nozzle  $N_3$  ( $\alpha = 20$  Deg.,  $L/h = 5$ ),  $kR_J = kh = 0.5$ .

CODE: SOURCE LOCATION

—□— CORE

- - -○- - FAN

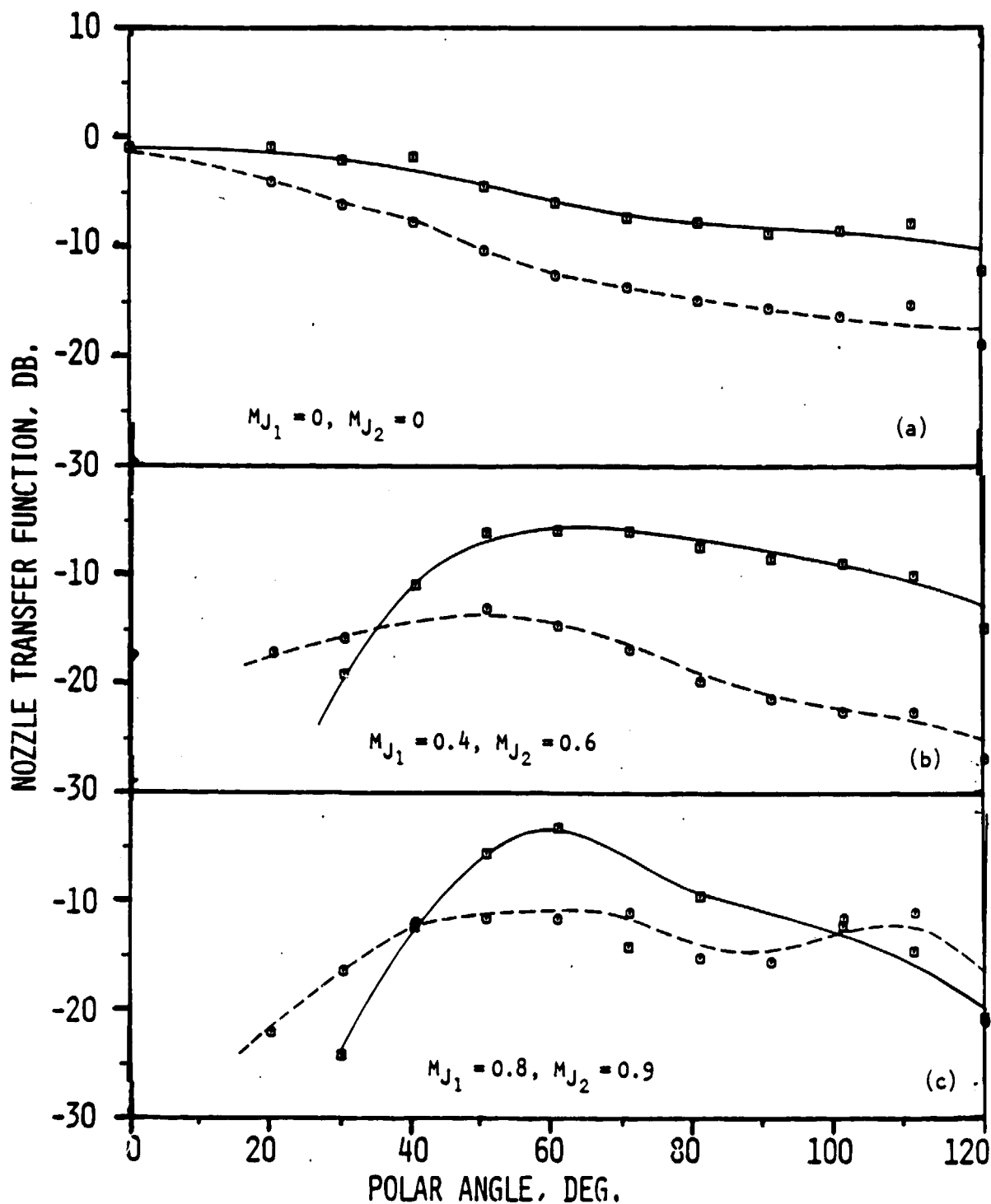


Figure 4.40 Nozzle transfer function directivity for various source locations. Nozzle  $N_3$  ( $\alpha = 20$  Deg.,  $L/h = 5$ ),  $kR_J = kh = 2$ .

CODE: SOURCE LOCATION  
 —●— CORE  
 - - -○- - - FAN

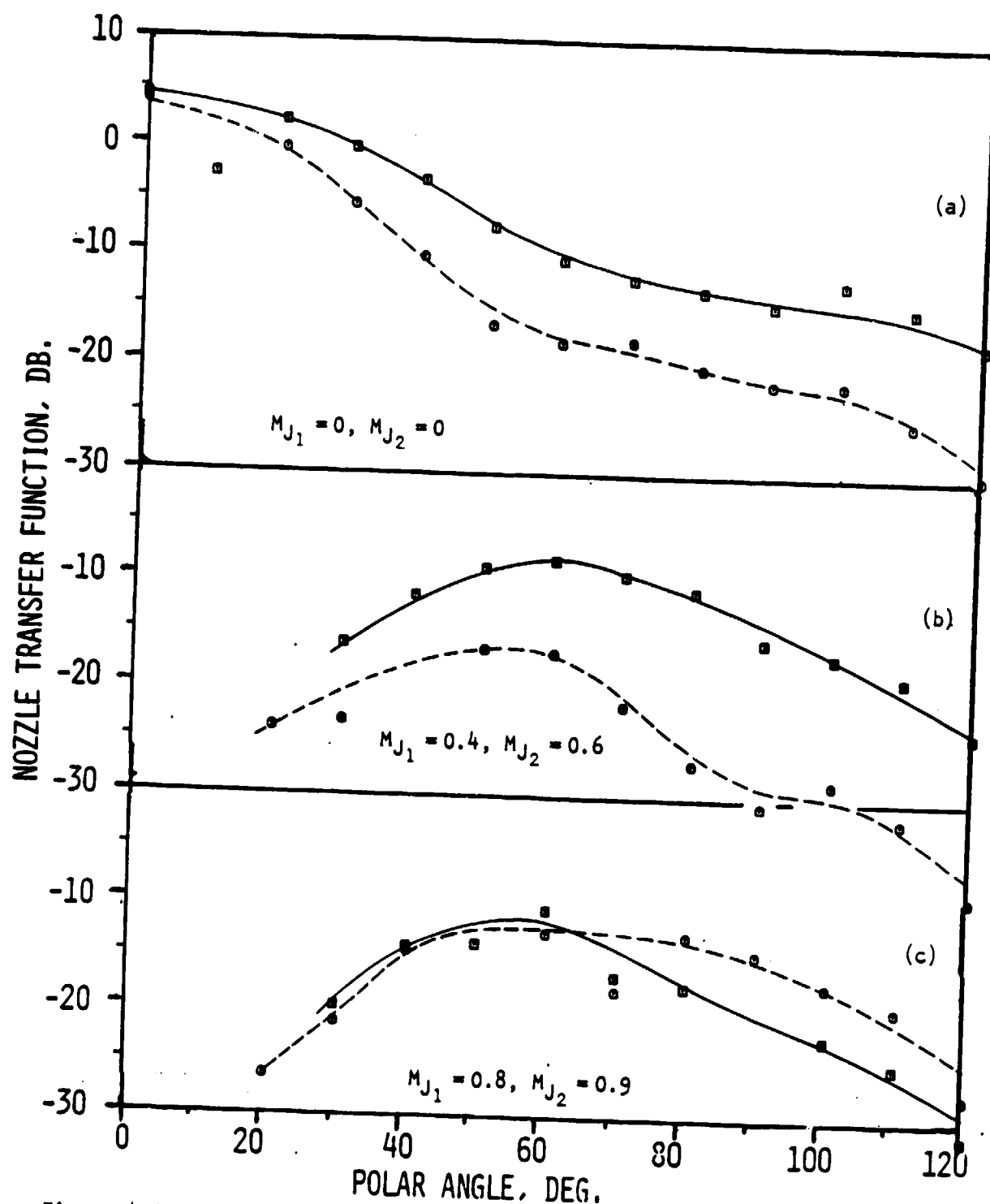


Figure 4.41 Nozzle transfer function directivity for various source locations. Nozzle  $N_3$  ( $\alpha = 20$  Deg.,  $L/h = 5$ ),  $kR_J = kh = 8$ .

CODE: SOURCE LOCATION  
 —■— CORE  
 - - -○- - FAN

#### 4.3.1 Summary

The comparison of NTF effects between the source in the core and fan ducts can be summarized as follows:

- o Nondimensional frequency scaling comparisons on  $kR$  (for core) and  $kh$  (for fan) appear to be valid.
- o As velocity increases, the collapse between core and fan improves at low and mid frequencies. At high frequencies the fan NTF is lower than the core at zero flow but exceeds the core at high velocities.
- o Little difference between NTF directivities is observed with changes in  $L/h$ .

#### 4.4 EFFECTS OF HEATING IN CORE AND FAN

These tests were conducted on two nozzle configurations only,  $N_1$  ( $L/h=1$ ) and  $N_2$  ( $L/h=3$ ). The source was located in the fan annulus and the test velocities were restricted to two flow conditions, namely Mach number combinations of core and fan of (0.8, 0.9) and (0.8, 1.2).

Two major difficulties were encountered in these tests. The first was a signal-to-noise problem in the far-field microphones due to the high jet noise levels arising from the high jet velocities as a result of jet heating. The time history of jet noise showed amplitude spikes of a similar nature to that of the pulse which made its detection and editing difficult. Thus, in the NTF directivity, when no data point is shown (particularly at small angles to the jet axis), it should be assumed that no reliable signal could be detected.

The second difficulty encountered was far-field signal contamination due to undetected (at that time of the test) external firing of the spark at the cable connection points to the source section. This condition appeared to occur only at elevated temperatures. As a consequence, the 600K data points for nozzle  $N_1$  with the source in the fan were invalid. For nozzle  $N_2$  the 900K fan condition could not be reached due to mass flow limitations of the air supply system.

In the next two subsections, the effect of heating the core for a fixed Mach number combination ( $M_{J_1}$ ,  $M_{J_2}$ ) and for a fixed fan temperature are presented first. It should be noted that in this mode of operation, even though the core Mach number  $M_{J_1}$  is fixed, the core velocity changes because of heating the core. NTF's as a function of constant core-to-fan temperature ratio are presented. Wherever possible, the ambient temperature no-flow case is shown for reference.



#### 4.4.1 Fan Temperature 750K

Figure 4.42 shows the effect of increasing core temperature on nozzle configuration  $N_1$  at fixed Mach number flow conditions of (0.8, 0.9) for three nondimensional frequencies ( $kh=0.5$ , 2, and 8) representing low, medium, and high frequency regimes, respectively. At  $kh=0.5$  [fig. 4.42(a)] two points are immediately obvious. First, as the core temperature increases, the transmission coefficient increases, i.e. more sound energy is escaping. Second, refraction is minimized as the core temperature increases, moving the radiation peak inward from  $70^\circ$  to  $60^\circ$  from the exhaust axis. In addition, at the highest core temperature case (563K) a significant high-angle NTF increase is observed, such that radiation at angles greater than  $50^\circ$  appears almost omni-directional.

For  $kh=2.0$  [fig. 4.42(b)] similar directivity trends can be seen except that now the highest core temperature case (563K) does not rise as much in the mid-angle region. In fact, at  $60^\circ$ , the radiation level at 450K exceeds that of the 563K case. In terms of defining a peak radiation angle, the high temperature case is indeterminate due to the flat directivity above  $70^\circ$ . At both lower temperatures (ambient and 450K), however, the radiation peaks are well defined, being  $70^\circ$  for the ambient and  $60^\circ$  for the 450K cases.

Mid-angle dominance of the 450K core temperature case is also observed in a more marked manner in figure 4.42(c) ( $kh=8.0$ ) where in fact the level exceeds the 563K level by at least 5 dB. Again the trend at polar angles greater than  $80^\circ$  is such that the increase in NTF level due to heating from ambient (about 290K) to 450K is far less than that observed in heating from 450K to 563K. It is evident that the whole character of sound radiation has undergone a significant change in the highest temperature regime.

For the case of nozzle configuration  $N_2$  ( $L/h=3.0$ ) at the flow condition of (0.8, 0.9), data at angles less than  $60^\circ$  could not be obtained for two basic reasons: (1) this larger area nozzle produced higher jet noise levels than configuration  $N_1$  and (2) the pulse signal levels reduced sharply due to refraction which made detection difficult. However, it is possible to say from figure 4.43 that an increase in core temperature from ambient to 450K reduces the radiation. This reduction is small at  $kh=0.5$  but increases to some 5 or 8 dB at the higher frequencies. In addition, the relationship of these levels to the no-flow cases shows that at low and mid frequencies, the levels are of the same order and only in the high frequency regime of  $kh=8.0$  [fig. 4.43(c)] do the NTF directivity levels exceed those of the no-flow ambient case.

An increase in fan velocity to a Mach number of 1.2 for nozzle configuration  $N_1$  has the effect that core temperature changes do not induce major changes in directivity. Signal-to-noise problems are most severe and definitive data points at small angles are lacking (particularly for the 450K core temperature case). Figure 4.44 shows the measured directivities at  $kh=0.50$ , 2.00 and 8.00, respectively. The major point to note is the relative omni-directionality at high angles with correspondingly less sharp refraction valleys. One significant trend, however, does emerge. At  $kh=0.5$  the ambient core temperature directivity dominates the directivity over

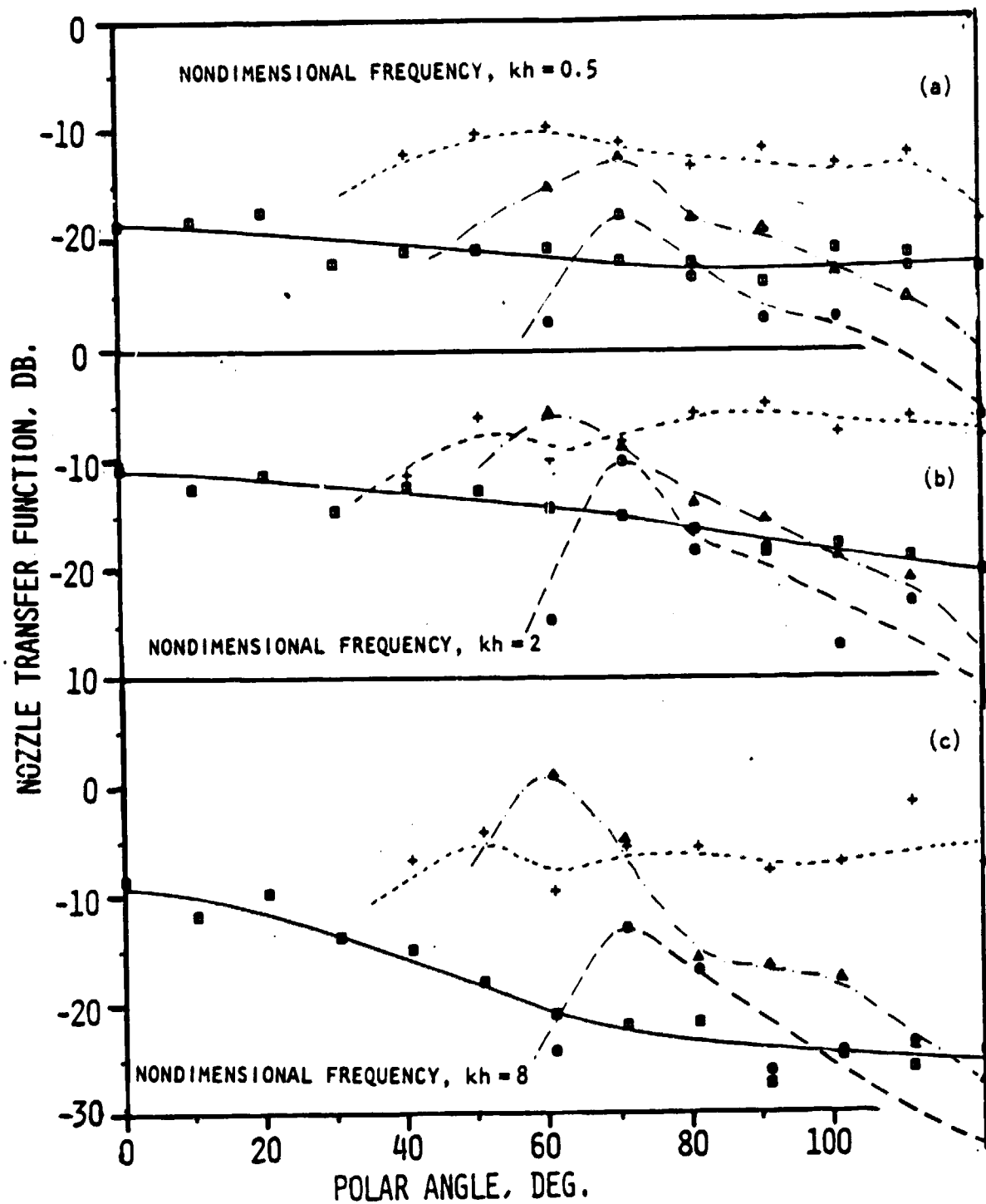


Figure 4.42 Nozzle transfer function directivity for various temperature conditions. Source at fan, Nozzle  $N_1$  ( $\alpha = 20$  Deg.,  $L/h = 1$ ),  $M_{J1} = 0.8$ ,  $M_{J2} = 0.9$ ,  $T_{R2} = 750K$ . CODE:  $T_{R1}$ .

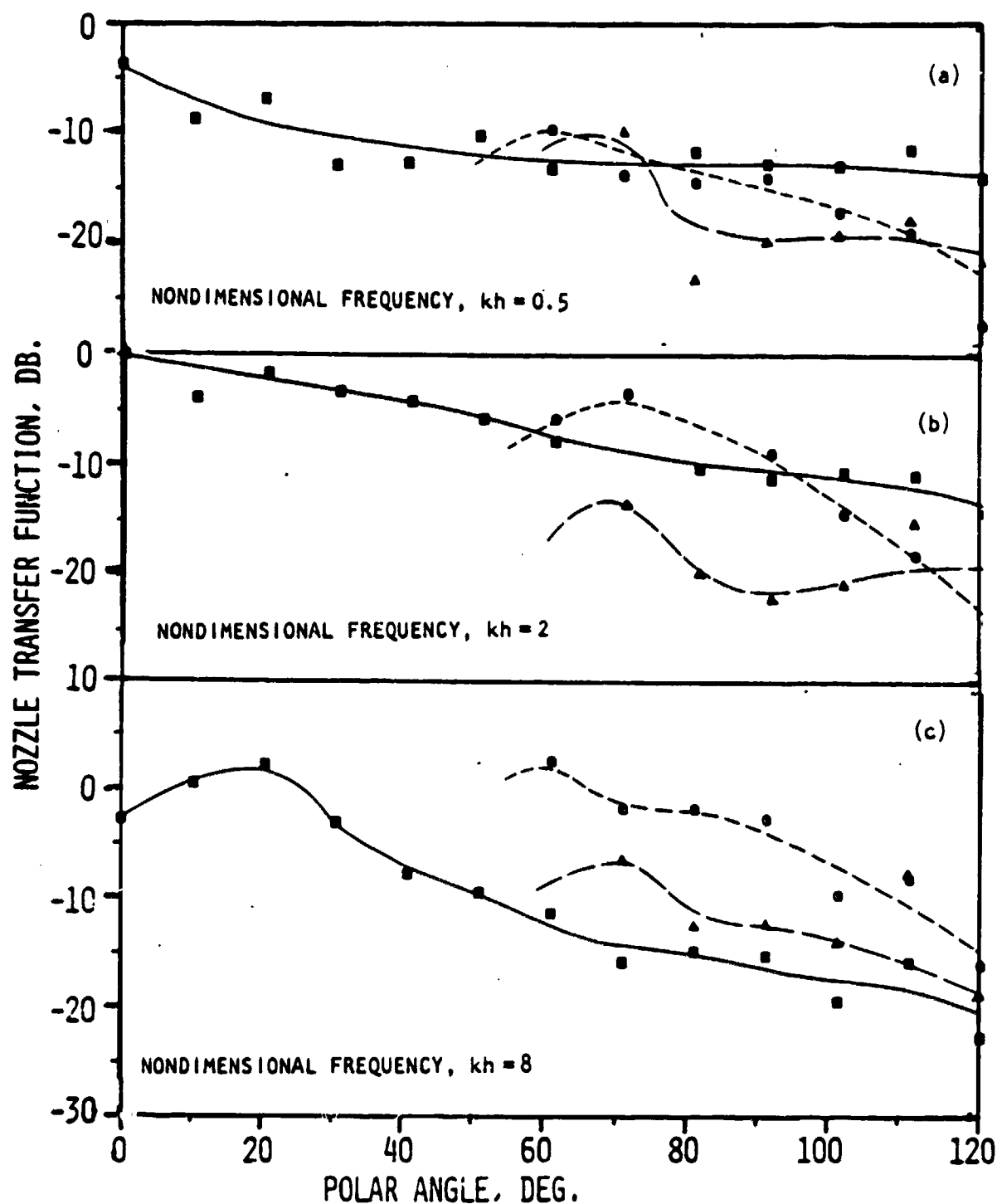


Figure 4.43 Nozzle transfer function directivity for various temperature conditions. Source at fan, nozzle  $N_2$  ( $\alpha = 20$  Deg.,  $L/h = 3$ ),  $M_{J1} = 0.8$ ,  $M_{J2} = 0.9$ ,  $T_{R2} = 750K$ . CODE:  $T_{R1}$ .

—●— AMBIENT GAS FLOW  
 - - -●- - - AMBIENT  
 - - -▲- - - 450 K

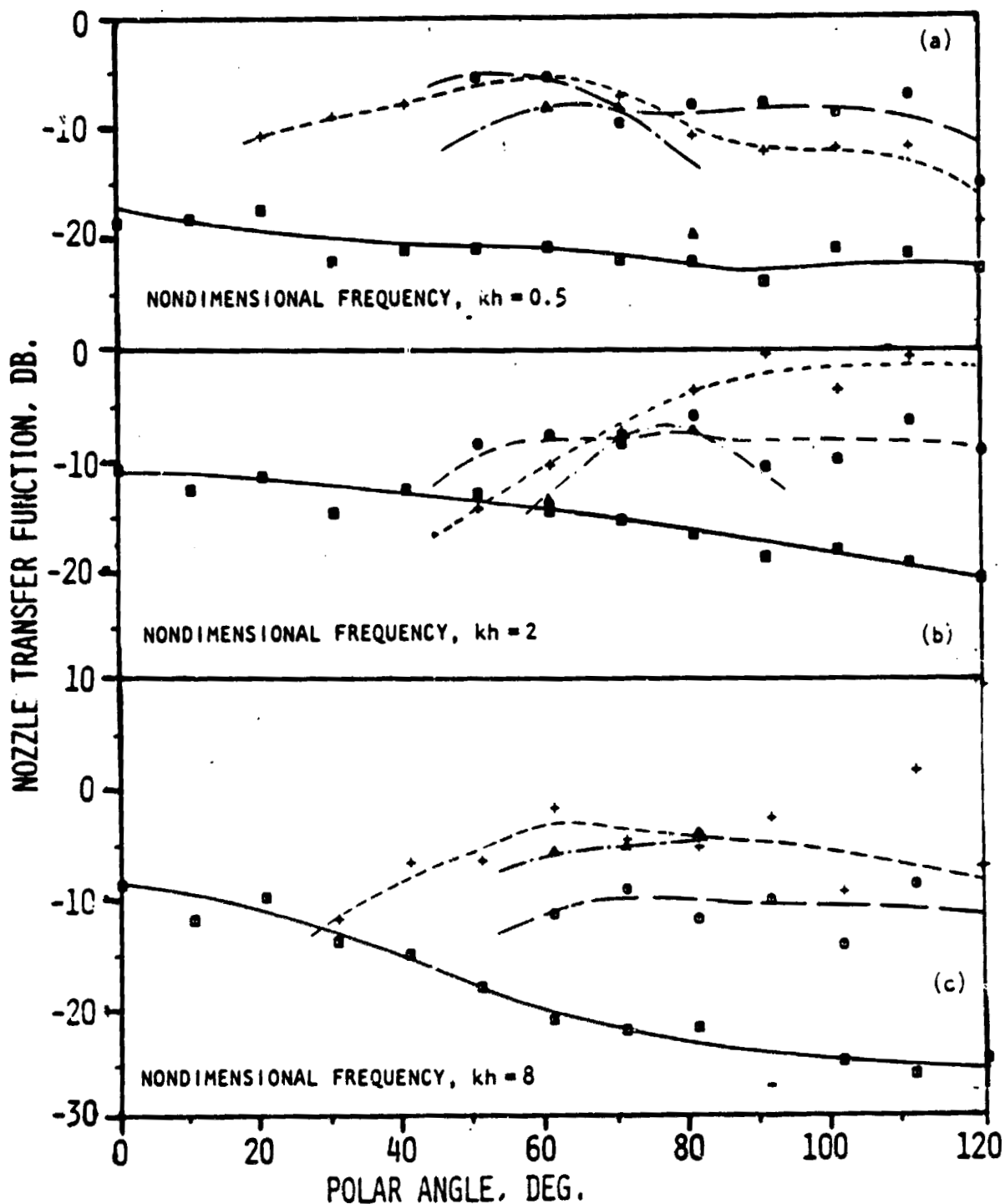


Figure 4.44 Nozzle transfer function directivity for various temperature conditions. Source at fan, nozzle  $N_1$  ( $\alpha = 20$  Deg.,  $L/h = 1$ ),  $M_{J1} = 0.8$ ,  $M_{J2} = 1.2$ ,  $T_{R2} = 750K$ . CODE:  $T_{R1}$ .

—■— AMBIENT ON FLOW  
 —●— AMBIENT  
 - - -▲- - - 400 K  
 - · - · - 500 K

almost all angles, while at  $kh=8.0$  [fig. 4.44(c)] the ambient core temperature case is the minimum energy radiator.

Nozzle configuration  $N_2$  ( $L/h=3.0$ ) at the flow condition (0.8, 1.2) shows some significant differences from the  $N_1$  case. The first observation from figure 4.45 is the frequency dependence of core heating with respect to the ambient no-flow directivity. At  $kh=0.5$ , heating the core to 450K results in little level change over all angles, while at  $kh=2.0$  a marked hump of 10 dB at  $80^\circ$  can be seen which then falls to the ambient no-flow levels some  $20^\circ$  to either side. This hump persists at  $kh=8.0$  [fig. 4.45(c)] but the peakiness is now more diffused, such that omni-directionality is almost achieved. The behavior of the ambient core temperature case also shows frequency dependence in that it represents the minimum radiation condition at  $kh=0.5$  and the maximum radiation condition at  $kh=8.0$ .

#### 4.4.2 Fan Temperature 900K

The flow condition of (0.8, 0.9) for nozzle configuration  $N_1$  is shown in figure 4.46. At  $kh=0.5$  the peak radiation occurs at  $60^\circ$ . Above this angle the effect of core temperature appears minimal with data collapse within  $\pm 2$  dB. Below this angle, data is limited due to a rapid drop in signal amplitude, however the 450K directivity appears to be the minimum radiation condition. As frequency is increased to  $kh=2.0$ , the data shows remarkable collapse, i.e. little core temperature dependence, with peak radiation now at  $70^\circ$ . The high frequency regime [ $kh=8.0$ , fig. 4.46(c)] shows the radiation peak now to be between 70 and 80 degrees. In addition, the ambient core temperature directivity shows considerably reduced radiation (by almost 10 dB) at all angles greater than the peak.

An increase in fan Mach number to 1.2 (fig. 4.47) can be seen to produce a general broadening of directivity at all frequencies. Data scatter is considerable, being a direct consequence of poor signal-to-noise ratios due to contamination by radiated noise from the very high velocity jets at these operating conditions. Peak radiation for 450K and 675K core temperatures can be positively identified to be in the 60 to 70 degree region with the ambient core temperature case far less clear due to the existence of similar levels over the 50 to 80 degree polar angles. The 675K case is particularly interesting in that it radiates less efficiently than the ambient or 450K case at larger angles at all frequencies.

#### 4.4.3 Constant Temperature Ratio Comparisons

This comparison was made in order to determine what, if any, collapse could be expected based on constant temperature ratios between core and fan but with differing fan (or core) temperatures. The directivities plotted are for three cases, two of which are for the design temperature ratio of 0.75 for core to fan. These temperature values for core and fan, respectively, are (563K, 750K) and (675K, 900K). The third case shown is for a temperature ratio of 0.6 (core to fan of 450K, 750K) as the data for the 0.75 ratio case (450K, 600K) proved invalid due to external pulse firing problems on that run.

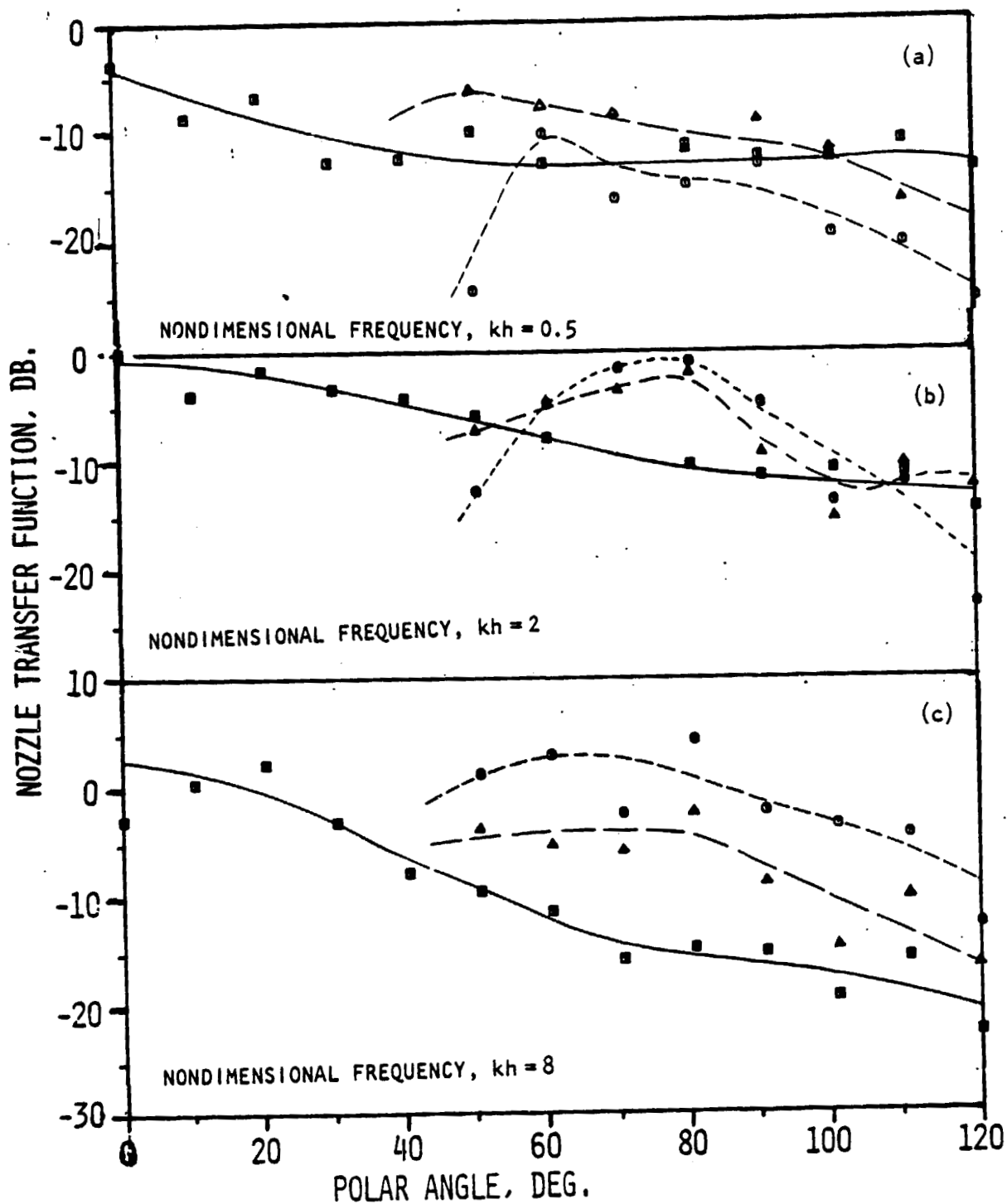


Figure 4.45 Nozzle transfer function directivity for various temperature conditions. Source at fan, nozzle  $N_2$  ( $\alpha = 20$  Deg.,  $L/h = 3$ ),  $M_{J1} = 0.8$ ,  $M_{J2} = 1.2$ ,  $T_{R2} = 750K$ . CODE:  $T_{R1}$ .

—■— AMBIENT NO FLOW  
 - - - ○ - - - AMBIENT  
 - · - · - △ - 450 K

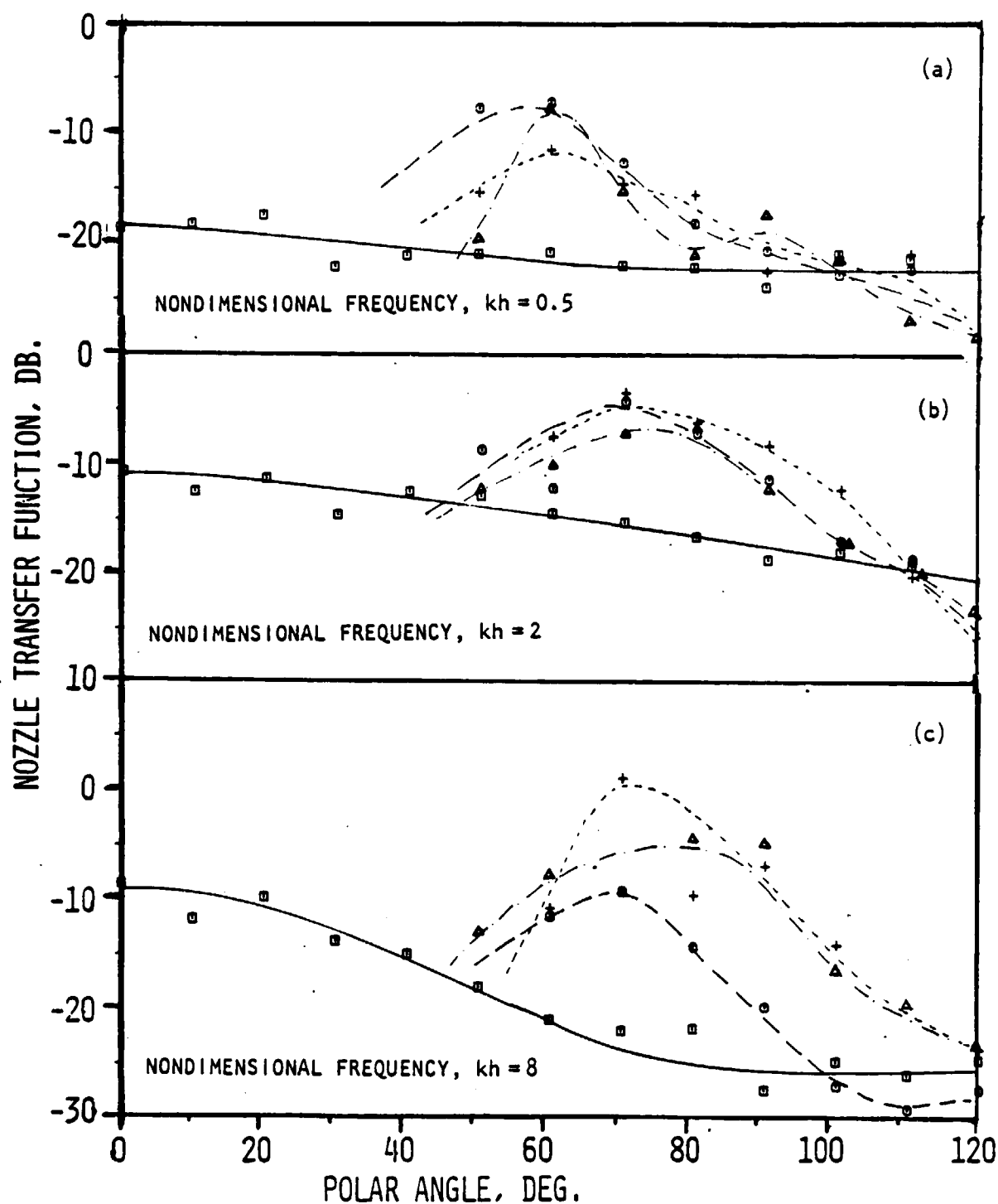


Figure 4.46 Nozzle transfer function directivity for various temperature conditions. Source at fan, nozzle  $N_1$  ( $\alpha = 20$  Deg.,  $L/h = 1$ ),  $M_{J1} = 0.8$ ,  $M_{J2} = 0.9$ ,  $T_{R2} = 900K$ . CODE:  $T_{R1}$ .

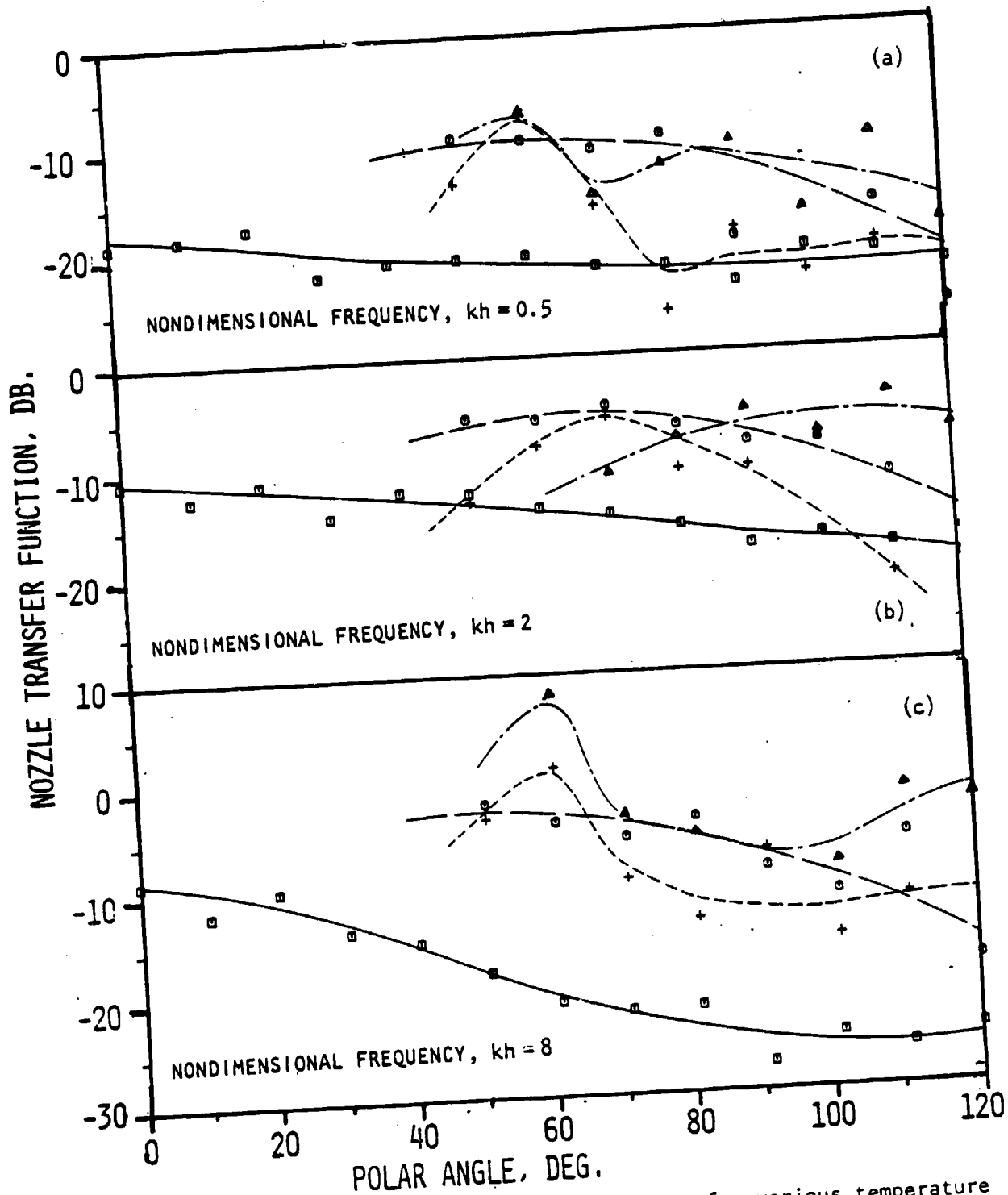


Figure 4.47 Nozzle transfer function directivity for various temperature conditions. Source at fan, nozzle  $N_1$  ( $\alpha = 20$  Deg.,  $L/h = 1$ ),  $M_{J1} = 0.8$ ,  $M_{J2} = 1.2$ ,  $TR_2 = 900K$ . CODE:  $TR_1$ .



Figure 4.48 shows the directivities for nozzle configuration  $N_1$  for a flow condition of (0.8, 0.9) for the three representative frequencies  $kh=0.5, 2$  and  $8$ , respectively. It can be seen that except in the peak radiation region of 60 to 70 degrees polar angle, little evidence of a collapse can be seen. The only positive indication of a parameter normalization is the similarity in the  $kh=0.5$  case [fig. 4.43(a)] between the directivities of core and fan temperature combinations of (450K, 750K) (ratio=0.6) and (675K, 900K) (ratio=0.75).

Figure 4.49 shows the same comparisons for a velocity condition of (0.8, 1.2). Again, data collapse is observed in the 60 to 70 degree region. This high velocity test condition produced such poor signal-to-noise ratios that positive pulse identification in the far field could only be achieved over a limited range of polar angles. Thus, the test data points shown represent confirmed, not inferred data.

One feature of both velocity conditions is the dominance of the core, fan temperature case of (563K, 750K) at high angles above 80 degrees for all frequency regimes. There appears to be no physical explanation as yet for this effect.

#### 4.4.4 Summary

The effects of heating both core and fan streams on the fan NTF can be summarized as follows:

- (1) For fan temperature at 750K:
  - o As core temperature increases, the NTF increases.
  - o As frequency increases, the NTF increases.
  - o As core temperature increases, the peak radiation angles reduce for the (0.8, 0.9) flow condition and increase for the (0.8, 1.2) flow condition.
  - o Variations of NTF with  $L/h$  are minimal.
- (2) For fan temperature at 900K:
  - o As core temperature increases, the peak radiation angles increase.
  - o At low and mid frequencies the increase in NTF with core temperature is minimal above  $70^\circ$  degrees polar angle.
  - o Variations of NTF with  $L/h$  are minimal.

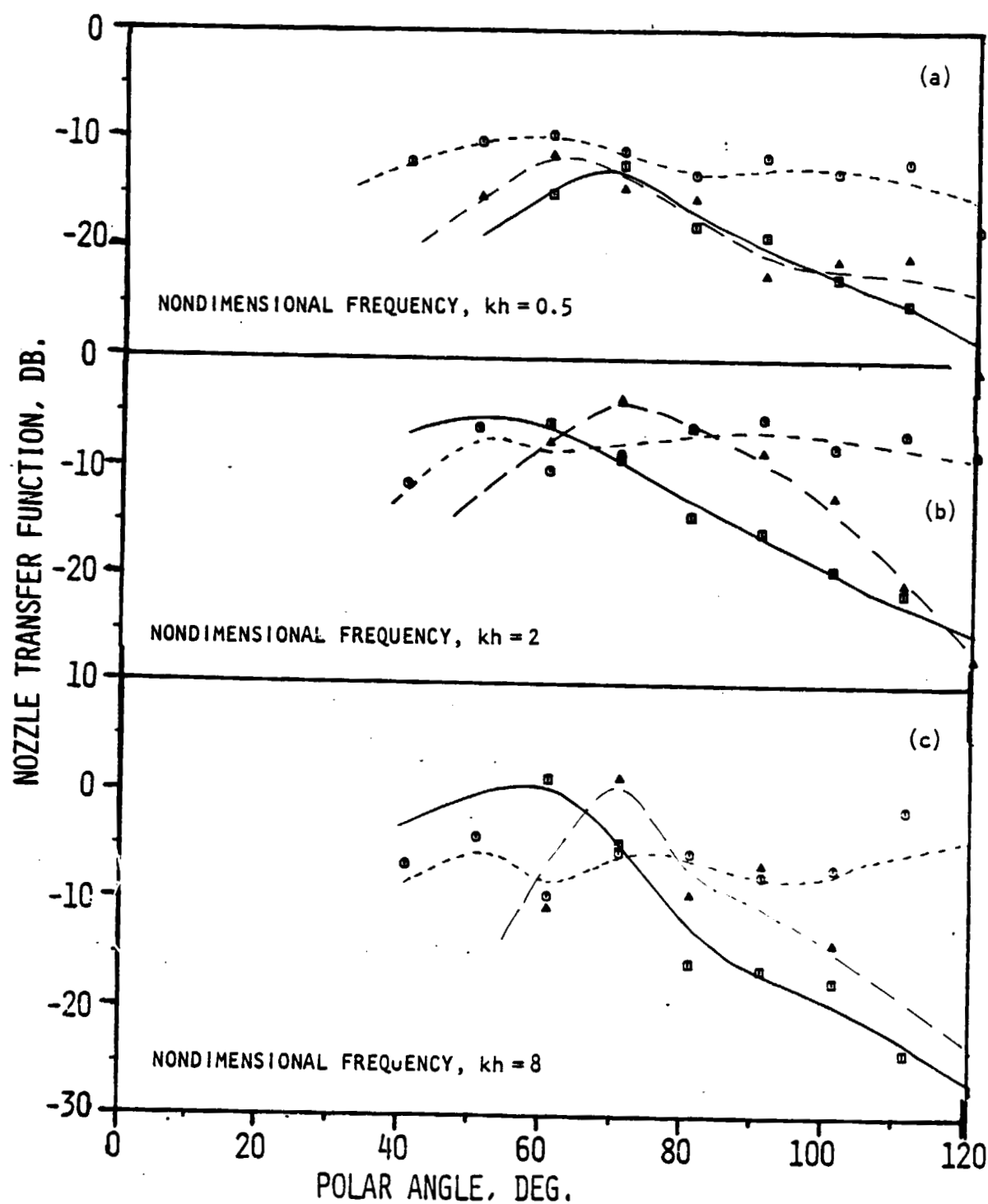


Figure 4.48 Nozzle transfer function directivity for various temperature conditions. Source at fan, nozzle  $N_1$  ( $\alpha = 20$  Deg.,  $L/h = 1$ ),  $M_{J1} = 0.8$ ,  $M_{J2} = 0.9$ . CODE:  $T_{R1}$ ,  $T_{R2}$ .

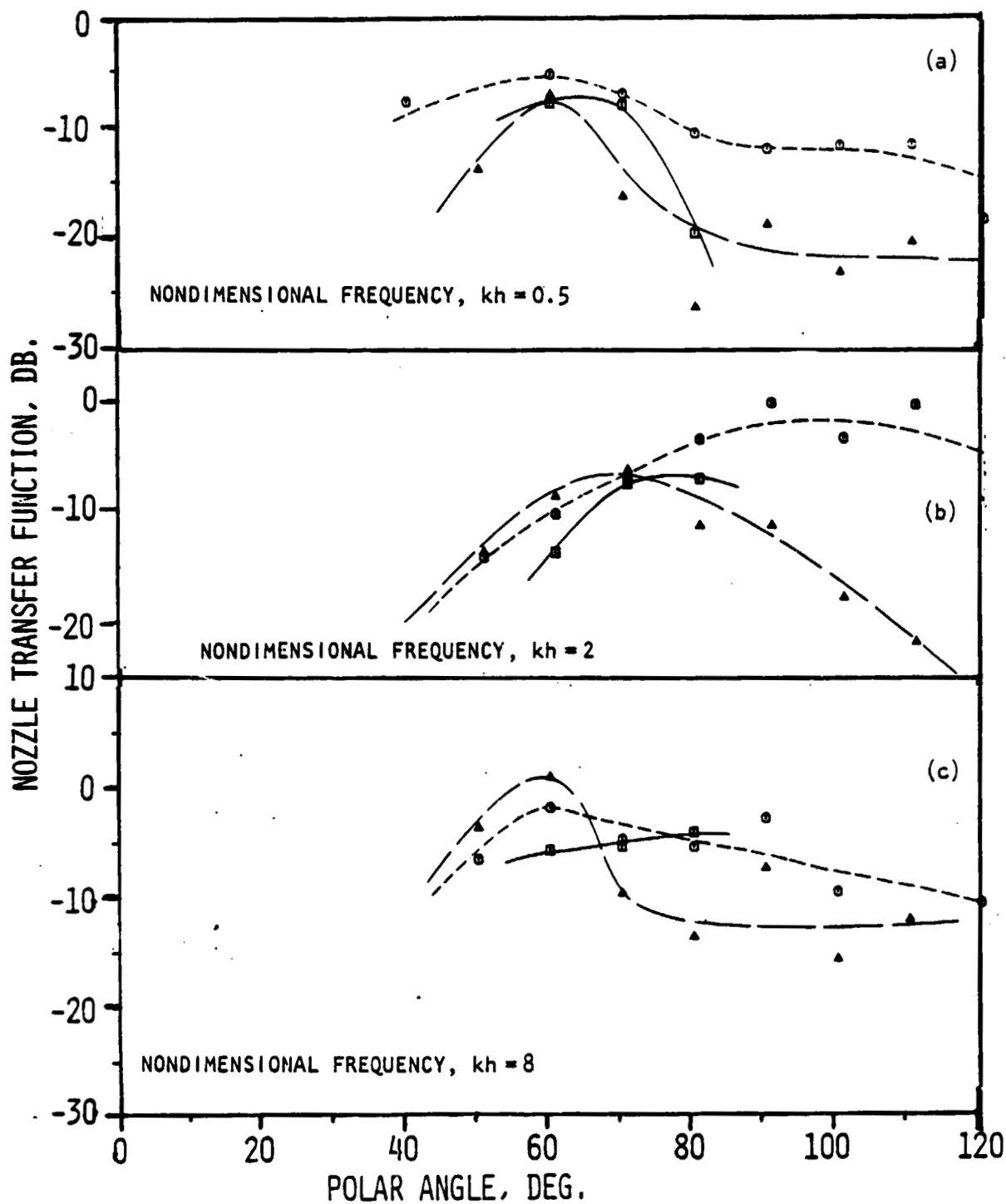


Figure 4.49 Nozzle transfer function directivity for various temperature conditions. Source at fan, nozzle  $N_1$  ( $\alpha = 20$  Deg.,  $L/h = 1$ ),  $M_{J1} = 0.8$ ,  $M_{J2} = 1.2$ . CODE:  $TR_1$ ,  $TR_2$ .

—○—	458. K	758. K
- -○- -	583. K	758. K
—△—	673. K	988. K

(3) Temperature ratio comparisons:

- o For all frequencies, the NTF above  $70^\circ$  polar angle is minimized for (450K, 750K) temperature condition.
- o For all frequencies, the NTF below  $60^\circ$  polar angle is minimized for (675K, 900K) temperature conditions.
- o The peak radiation angles are observed in  $60$ - $70^\circ$  polar angle region for all conditions.

#### 4.5 CONCLUSIONS

The various aspects studied in this program have already been summarized at the end of each subsection and will, therefore, not be repeated here. It is considered necessary, however, to point out that within the constraints of the contract requirement the data could be studied only in a global sense.

By this point, the reader has probably become quite aware of the fact that the NTF directivities by themselves in the present plotted form do not necessarily show a consistent trend. One of the major reasons for this is that the test plan did not adequately reflect the complexity of the problem. This realization is due to the lack of past fundamental work in this field. For example, there is a lack of sufficient information about a proper normalizing frequency parameter. In the absence of sufficient guidelines, the data has been plotted as a function of normalized frequency represented by  $kh$  or  $kR_j$ .  $kR_j$  is probably a correct parameter for source in the core because of its use in other studies in the past on single nozzles, and as also established in our primary investigation. Use of  $kh$  as a proper parameter for normalized frequency is, however, subject to debate and further confirmation.

It is worth pointing out here that in all cases where either of the coaxial streams was operated at supercritical pressure ratios, the results followed a trend completely different from that obtained at subcritical pressure ratios. At these conditions the jets were underexpanded and, therefore, were characterized by Prandtl-Meyer expansions at the nozzle exit, followed by a complex shock structure within the coaxial jet. The present results certainly indicate the need for fundamental research on the interaction of sound with shocks and propagation of sound through flow containing shocks.

At all high jet velocity conditions, particularly at small angles to the exhaust axis, jet noise was found to dominate internal noise radiation. This was despite the fact that the internal noise levels at the exit plane were of the order of 140 dB. The implications are therefore that in the full scale, engine internal noise radiation will not make a significant contribution to far-field noise levels.

As a final note, the NTF as used may not be the best measure of the transmission characteristics of the inverted velocity profile coaxial

nozzles. NTF was taken to be the ratio of the measured far-field intensity and that from a monopole acoustic source located at the nozzle exit with total power equal to the incident power. *First*, the incident power is realistically not equal to the total transmitted power and *second*, it does not radiate as a monopole.

In short, the engineering approach taken in this work is inappropriate from the standpoint of a fundamental research investigation in that individual effects could not be investigated in a rigorous manner. The present results should, therefore, be interpreted with the caution that they are applicable only to similar nozzle configurations and flow conditions.

## APPENDIX A

### RADIATION IMPEDANCE OF CONICAL NOZZLES WITH MEAN FLOW

In this section, a method to evaluate the radiation impedance of a conical nozzle exit with and without mean flow using the complex reflection coefficient at the shoulder of the duct-nozzle system is presented. The situation considered here is that where acoustic waves, in the fundamental mode, are generated by an "impulse source" in a conical rigid-walled flow nozzle (see fig. A-1) where the axial mean flow may vary. The acoustic processes in the nozzle are assumed to be one-dimensional and isentropic even though small radial flow gradients are present in this system.

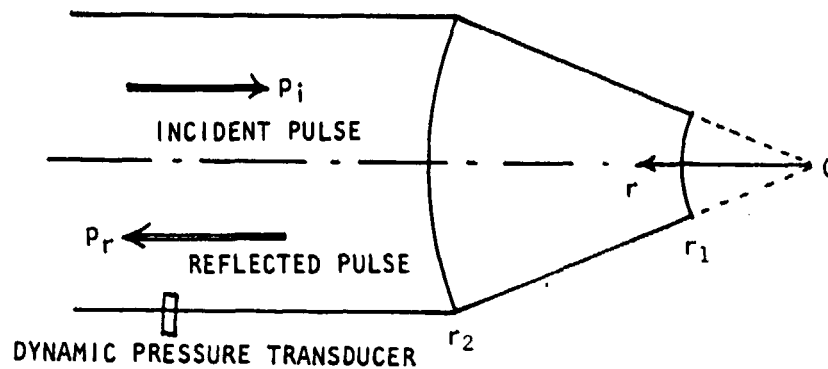


Figure A-1 A Duct Nozzle System

The linearized conservation equations for axisymmetric flow field can be written as follows:

Continuity:

$$\frac{D\bar{\rho}}{Dt} + \bar{\rho} \left( \frac{\partial u_r}{\partial r} + \frac{2u_r}{r} \right) + \rho \left( \frac{d\bar{U}}{dr} + \frac{2\bar{U}}{r} \right) = 0 \quad (A-1)$$

Momentum:

$$\frac{Du_r}{Dt} + u_r \frac{d\bar{U}}{dr} + \bar{U} \frac{d\bar{U}}{dr} \frac{\rho}{\bar{\rho}} = - \frac{1}{\bar{\rho}} \frac{\partial p}{\partial r} \quad (A-2)$$

Energy:

$$\frac{D\rho}{Dt} = \frac{1}{\bar{c}^2} \frac{Dp}{Dt} \quad (A-3)$$

The barred and unbarred quantities describe the steady and unsteady state variables, respectively. It can be shown that equations (A-1) through (A-3)

reduce to the following equations for time harmonic perturbations:

$$p'' + a(r)p' + b(r)p = 0 \quad (A-4)$$

$$\text{and } \bar{\rho} \bar{c} u_r = \alpha(r)p' + \beta(r)p \quad (A-5)$$

$$\text{where } a(r) = \frac{2}{r} + f_1(M, M', M'', \frac{\bar{\rho}'}{\bar{\rho}}, \frac{\bar{c}'}{\bar{c}}, \frac{\bar{c}''}{\bar{c}}, k) \quad (A-6)$$

$$b(r) = K^2 + f_2(M, M', M'', \frac{\bar{\rho}'}{\bar{\rho}}, \frac{\bar{c}'}{\bar{c}}, \frac{\bar{c}''}{\bar{c}}, k) \quad (A-7)$$

$$\alpha(r) = f_3(M, M', \frac{\bar{c}'}{\bar{c}}, k) \quad (A-8)$$

$$\beta(r) = f_4(M, M', \frac{\bar{c}'}{\bar{c}}, k) \quad (A-9)$$

For a constant area duct all the derivatives of mean flow variables, with respect to  $r$  vanish and since the virtual origin "0" shifts to infinity, all  $1/r$  terms vanish (see fig. A-1). Therefore, equations (A-4) and (A-5) become:

$$\frac{d^2 p}{dx^2} - \frac{2jkM}{(1-M^2)} \frac{dp}{dx} + \frac{k^2 p}{(1-M^2)} = 0 \quad (A-10)$$

and

$$\bar{\rho} \bar{c} u_r = Mp - \frac{(1-M^2)}{jk} \frac{dp}{dx} \quad (A-11)$$

Solution of Eq. (A-10) is given by

$$p = Ae^{jkx/(1-M)} + Be^{-jkx/(1+M)} \quad (A-12)$$

$$\text{and } \bar{\rho} \bar{c} u_r = -Ae^{jkx/(1-M)} + Be^{-jkx/(1+M)}$$

where  $x$  is an arbitrary coordinate in the same direction of  $r$ . Therefore, the transfer impedance at any location inside the duct is given by

$$Z = \frac{p}{\bar{\rho} \bar{c} u_r} = - \frac{1 + \sigma}{1 - \sigma} \quad (A-13)$$



where  $\sigma = (B/A)e^{-2jkx/(1-M^2)}$ , the complex reflection coefficient. Assigning a coordinate  $r_2$  to the shoulder of the duct-nozzle system (see fig. A-1) and applying equation (A-13), the transfer impedance at the shoulder can be rewritten as follows:

$$Z(r_2) = -\frac{1 + \sigma}{1 - \sigma} \quad (A-14)$$

Equation (A-4) can be expressed in the following form:

$$\begin{bmatrix} p \\ p' \end{bmatrix}_r = \begin{bmatrix} 0 & 1 \\ -b(r) & -a(r) \end{bmatrix} \begin{bmatrix} p \\ p' \end{bmatrix}_{r_2} \quad (A-15)$$

and a solution can be written using the transmission matrix in the following form

$$\begin{bmatrix} p \\ p' \end{bmatrix}_r = \begin{bmatrix} T(r) \end{bmatrix}_r \begin{bmatrix} p \\ p' \end{bmatrix}_{r_2} \quad (A-16)$$

The transmission matrix can be expressed as follows:

$$\begin{bmatrix} T(r) \end{bmatrix}_r = \begin{bmatrix} 0 & 1 \\ -b(r) & -a(r) \end{bmatrix}_r \begin{bmatrix} T(r) \end{bmatrix}_r \quad (A-17)$$

The matrix  $[T(r)]_r$  can be determined integrating equation (A-17) numerically. Letting  $r_1$  to be the radial coordinate of nozzle exit and using equation (A-16), the oscillatory pressure and its derivative at  $r_1$  can be expressed in terms of oscillatory pressure and its derivative at  $r_2$  as follows:

$$p(r_1) = T_{11} p(r_2) + T_{12} p'(r_2) \quad (A-18)$$

$$p'(r_1) = T_{21} p(r_2) + T_{22} p'(r_2) \quad (A-19)$$

Using Equations (A-13) and (A-5),  $p'(r)$  can be expressed as

$$p'(r) = \frac{1}{B(r)} \left\{ \frac{1}{Z(r)} - a(r) \right\} p(r) \quad (A-20)$$

$$\therefore p'(r_2) = \frac{1}{B(r_2)} \left\{ \frac{1}{Z(r_2)} - a(r_2) \right\} p(r_2) \quad (A-21)$$

Using equation (A-21), equations (A-18) and (A-19) can be written as:

$$p(r_1) = \left[ T_{11} + \frac{T_{12}}{\beta(r_2)} \left\{ \frac{1}{Z(r_2)} - \alpha(r_2) \right\} \right] p(r_2) \quad (\text{A-22})$$

and

$$p'(r_1) = \left[ T_{21} + \frac{T_{22}}{\beta(r_2)} \left\{ \frac{1}{Z(r_2)} - \alpha(r_2) \right\} \right] p(r_2) \quad (\text{A-23})$$

$$\therefore Z(r_1) = \frac{p(r_1)}{\bar{\rho} \bar{c} u_r(r_1)} = \frac{1}{\alpha(r_1) + \beta(r_1) \frac{p'(r_1)}{p(r_1)}}$$

or

$$Z(r_1) = -Z_R = \frac{1}{\alpha(r_1) + \beta(r_1) \cdot \psi(r_1)} \quad (\text{A-24})$$

where

$Z_R$  = radiation impedance at the nozzle exit, and

$$\psi(r_1) = \frac{p'(r_1)}{p(r_1)} = \frac{T_{21} + \frac{T_{22}}{\beta(r_2)} \left\{ \frac{1}{Z(r_2)} - \alpha(r_2) \right\}}{T_{11} + \frac{T_{12}}{\beta(r_2)} \left\{ \frac{1}{Z(r_2)} - \alpha(r_2) \right\}} \quad (\text{A-25})$$

## APPENDIX B

### ACOUSTIC TRANSMISSION ACROSS A SYSTEM OF PLANE PARALLEL MULTI-LAYER FLOW FIELDS

PAGE 169 INTERNAL SECURITY

## B.1 INTRODUCTION

In determining the transmission and reflection of sound from a multi-layer media, two relevant quantities are the transmitted-to-incident-amplitude ratio and the angle of emergence of the sound field as a function of the angle of incidence of the beam and the mean aerodynamic and thermodynamic parameters of the different layers.

The angles of emergent sound field are first evaluated in terms of the angles of incidence field. This is described in Section B.2. Transmitted to incident amplitude ratios are then evaluated in Section B.3. This involves matching of the fluctuating pressure and displacement fields at the interfaces. The continuity of displacement field must be imposed because of the relative motion on either side of each interface.

## B.2 ANGLE CHANGES ACROSS MULTI-LAYER FLOW FIELDS

A necessary requirement for acoustic transmission across a system of plane parallel interfaces with different flows between any two interfaces, is that the component of the wave number along the flow direction be a constant and independent of the coordinate transverse to the flow direction. This can be easily proven from the continuity of acoustic pressure across each interface. In a 2-D system (Figure B-1), let

$$P^I(x, y, \omega) = F^I(y) e^{\pm jk_x^I x + j\omega t} \quad (B-1)$$

$$P^{II}(x, y, \omega) = F^{II}(y) e^{\pm jk_x^{II} x + j\omega t} \quad (B-2)$$

$$P^{III}(x, y, \omega) = F^{III}(y) e^{\pm jk_x^{III} x + j\omega t} \quad (B-3)$$

In the above, the x-coordinate is chosen to be in the flow direction.  $F^I(y)$ ,  $F^{II}(y)$ ,  $F^{III}(y)$  represent the amplitude variation of the sound field across each layer and can be represented by a pair of positive and negative going waves along the y-direction and when combined with the x and t dependent terms represent an incident and a reflected wave. In each region a separate  $k_x$  is initially assumed, but as shown below is found to be constant and independent of the region. A necessary condition is that the above expressions be continuous across each interface, and for arbitrary values of x. Thus, at  $y=y_1$  first interface,

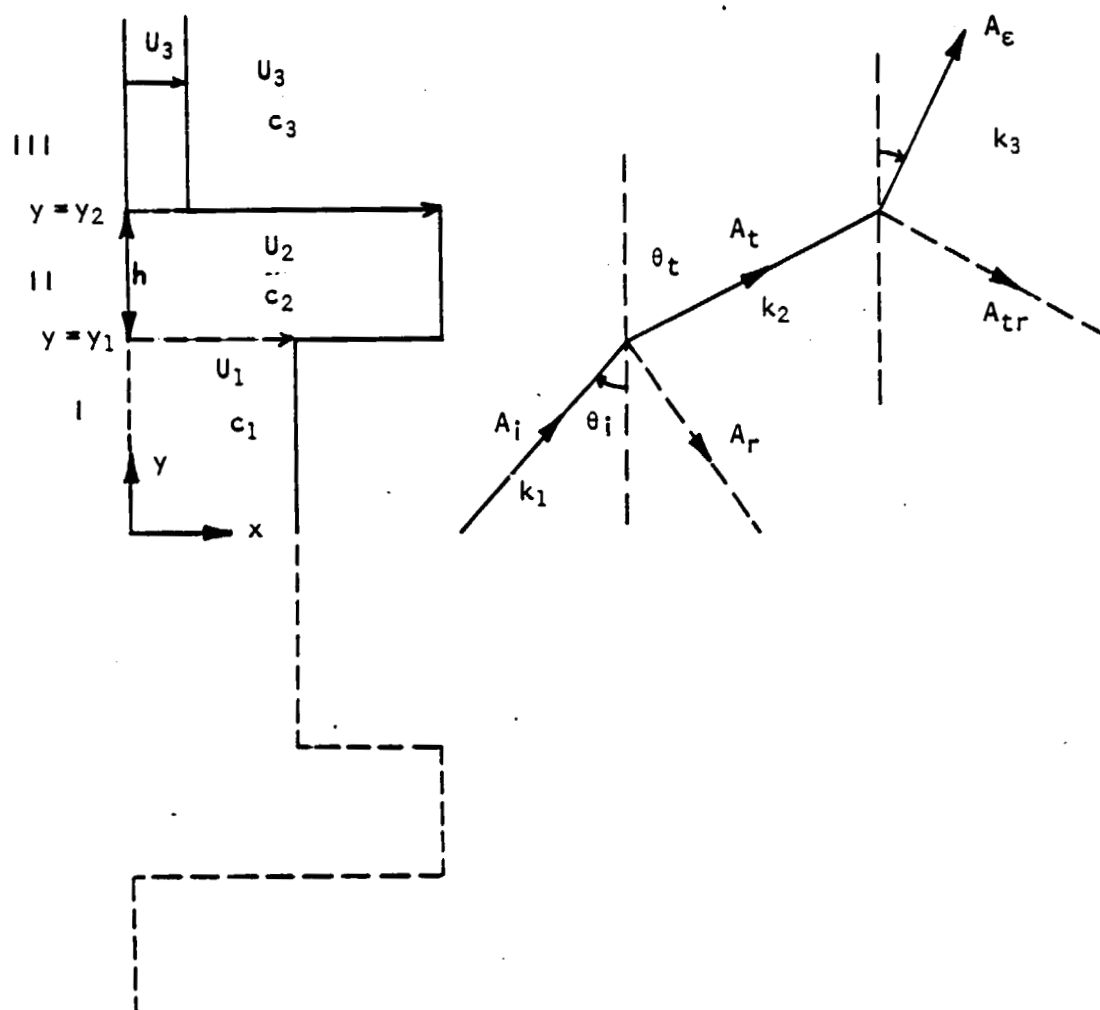


Figure B.1 Acoustic transmission across a system of plane parallel multi-layer flow fields.

$$P^I(x, y_1, \omega) = P^{II}(x, y_1, \omega) \quad (B-4)$$

Also  $P^I(x + \Delta x, y_1, \omega) = P^{II}(x + \Delta x, y_1, \omega)$  (B-5)

$P^I(x + \Delta x, y_1, \omega)$  and  $P^{II}(x + \Delta x, y_1, \omega)$  can be expanded in terms of their values at  $x$ . Thus

$$P^I(x, y_1, \omega) + \frac{\partial P^I}{\partial x}(x, y_1, \omega) \Delta x = P^{II}(x, y_1, \omega) + \frac{\partial P^{II}}{\partial x}(x, y_1, \omega) \Delta x \quad (B-6)$$

Substituting (B-1), (B-2) and (B-4) in (B-6), it can be shown that

$$\pm j k_x^I = \pm j k_x^{II} \quad (B-7)$$

Similarly at  $y = y_2$ , it can be shown that

$$\pm j k_x^{II} = \pm j k_x^{III}$$

Thus, it has been shown that

$$\pm k_x^I = \pm k_x^{II} = k_x^{III} = \pm k_x \quad (B-8)$$

The negative sign refers to propagation along flow direction and positive sign refers to propagation against flow direction. The wave-vector component are related by the dispersion equation which varies from region to region. Thus, in

region I:  $k_x^2 + k_y^{I2} = k_1^2(1 - M_1 k_x/k_1)^2 = \bar{k}_1^2$  (say) (B-9)

region II:  $k_x^2 + k_y^{II2} = k_2^2(1 - M_2 k_x/k_2)^2 = \bar{k}_2^2$  (B-10)

and region III:  $k_x^2 + k_y^{III2} = k_3^2(1 - M_3 k_x/k_3)^2 = \bar{k}_3^2$  (B-11)

From equations (B-9), (B-10) and (B-11), angles  $\theta_i$ ,  $\theta_t$  and  $\theta_e$  can be defined, such that (see Figure B-1)

$$k_x = \bar{k}_1 \sin \theta_i = \bar{k}_2 \sin \theta_t = \bar{k}_3 \sin \theta_e \quad (B-12)$$

and corresponds to Snell's law. (Note  $\bar{k}_1$  and  $\bar{k}_2$  are Doppler modified wave numbers.)

From equation (B-11),  $(k_x/k_3)$  can be expressed in terms of  $\theta_e$  and  $M_3$ , namely

$$k_x/k_3 = \sin\theta_e / (1 + M_3 \sin\theta_e) \quad (B-13)$$

Similarly,  $k_x/k_2 = \sin\theta_t / (1 + M_2 \sin\theta_t) \quad (B-14)$

and  $k_x/k_1 = \sin\theta_i / (1 + M_1 \sin\theta_i) \quad (B-15)$

From equations (B-9) and (B-12), it can be shown that

$$\frac{\sin\theta_e}{\sin\theta_i} = \frac{\bar{k}_1}{\bar{k}_3} = \frac{c_3}{c_1} \frac{(1 + M_3 \sin\theta_e)}{(1 + M_1 \sin\theta_i)}$$

and  $\sin\theta_e$  can be solved for with the following results

$$\sin\theta_e = \frac{(c_3/c_1) \sin\theta_i}{1 + (M_1 - M_3 c_3/c_1) \sin\theta_i} \quad (B-16)$$

Thus, the angle of emergence is a function of  $M_1$ ,  $M_3$ ,  $(c_3/c_1)$ , and angle of incidence  $\theta_i$ . Although equation (B-16) allows evaluation of  $\theta_e$  as a function of  $\theta_i$  for specified values of  $(c_3/c_1)$ ,  $M_3$  and  $M_1$ ,  $\theta_i$  is bounded by  $\theta_{ic}$ , the critical angle of incidence. Sound incident at angles greater than  $\theta_{ic}$  will be totally internally reflected.  $\theta_{ic}$  can be computed by using equation (B-12) and equation (B-10), from which it can be shown that

$$\frac{\sin\theta_e}{\sin\theta_t} = \left(\frac{c_3}{c_2}\right) \frac{(1 + M_3 \sin\theta_e)}{(1 + M_2 \sin\theta_t)} \quad (B-17)$$

It follows that

$$\sin\theta_t = \{(c_2/c_1) \sin\theta_i\} / \{1 + (M_1 - M_2 \frac{c_3}{c_1}) \sin\theta_i\} \quad (B-18)$$

Thus  $\theta_e$  is now a function of  $\theta_t$ ,  $c_3/c_2$ ,  $M_2$  and  $M_3$ .  $\theta_t$  is not an independent variable and is a function of  $c_2/c_1$ ,  $M_1$ ,  $M_2$  and  $\theta_i$ . However, to obtain the critical angle  $\theta_{ec}$  and  $\theta_{ic}$  above which total internal reflection takes place,  $\theta_t$  is set to  $+\pi/2$  for *downstream propagation*. One then obtains

$$\theta_{ec} = \sin^{-1} \left[ \frac{(c_3/c_2)}{1 + M_2 - M_3 (c_3/c_2)} \right] \quad (B-19)$$

Corresponding to this critical emergence angle, there exists a critical incidence angle which is obtained by solving for  $\theta_i$  from equation (B-16) and if this is done, one obtains

$$\sin\theta_{ic} = \frac{\sin\theta_{ec}}{(c_3/c_1) + (M_3 c_3/c_1 - M_1) \sin\theta_{ec}}$$

$$= \frac{1}{(c_2/c_1) (1 + M_2) - M_1} \quad (B-20)$$

Thus, for  $\theta_i > \theta_{ic}$ , total internal reflection takes place from *inner* layer (see Fig. B-2).

Now, if the sound is incident such that it propagates and emerges upstream, as  $\theta_i$  reduces from 0 to  $-\theta_i$ ,  $\theta_t$  ( $|\theta_t| < |\theta_i|$ ) reduces from 0 to  $-\theta_t$  and  $\theta_e$  ( $|\theta_e| > |\theta_t|$ ) reduces from 0 to  $-\theta_e$ . When  $\theta_e = -\pi/2$ ,  $\theta_t = -\theta_{tc}$  and  $\theta_i = -\theta_{ic}$ .

Thus, for upstream propagation ( $\theta_i < 0$ ), the criterion for total internal reflection is  $\theta_e = -\pi/2$ . From equation (B-16),

$$\sin\theta_{ic} = \frac{-1}{[(c_3/c_1) + M_1 - M_3(c_3/c_1)]} \quad (B-21)$$

and

$$\sin\theta_{tc} = \frac{-1}{[(c_3/c_2) + M_2 - M_3(c_3/c_2)]} \quad (B-22)$$

For angle  $\theta_t < \theta_{tc}$ , total internal reflection takes place at the *outer* layer.

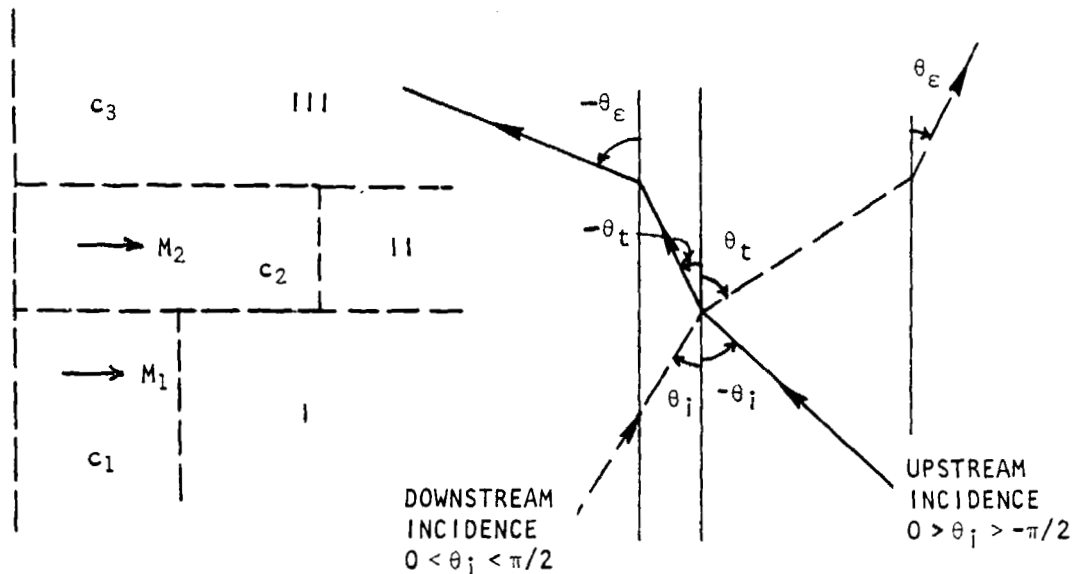


Figure B.2 Schematic representation of rays for upstream and downstream incidences.



Table B-1 shows variation of  $\theta_{ec}$  and  $\theta_{ic}$  for a fixed secondary flow  $M_2 = 1.4$  with variation of the primary flow  $M_1$ . For this case the temperatures are assumed to be the same so that  $c_1 = c_2 = c_3 = 344.5$  m/s, and outer-most layer is assumed to be stationary ( $M_3 = 0$ ).

TABLE B-1

$M_1$	$M_2$	$\theta_{ec}$	$\theta_{ic}$
0.0	1.4	24.6°	24.6°
0.2	1.4	24.6°	27.0°
0.4	1.4	24.6°	30.0°
0.6	1.4	24.6°	33.75°
0.8	1.4	24.6°	38.7°
1.0	1.4	24.6°	45.6°
1.2	1.4	24.6°	56.4°
1.4	1.4	24.6°	90.0°

Table B-2 shows a variation of  $\theta_{ec}$  and  $\theta_{ic}$  for a fixed primary flow  $M_1 = 0.8$  and a variable secondary flow  $M_2$ . Again, it is assumed that  $c_1 = c_2 = c_3 = 344.5$  m/s and  $M_3 = 0$ .

TABLE B-2

$M_1$	$M_2$	$\theta_{ec}$	$\theta_{ic}$
0.8	0.0	90.0°	--
0.8	0.2	56.4°	--
0.8	0.4	45.6°	--
0.8	0.6	38.7°	--
0.8	0.8	33.75°	90.0°
0.8	1.0	30.0°	56.4°
0.8	1.2	27.0°	45.6°
0.8	1.4	24.6°	38.7°

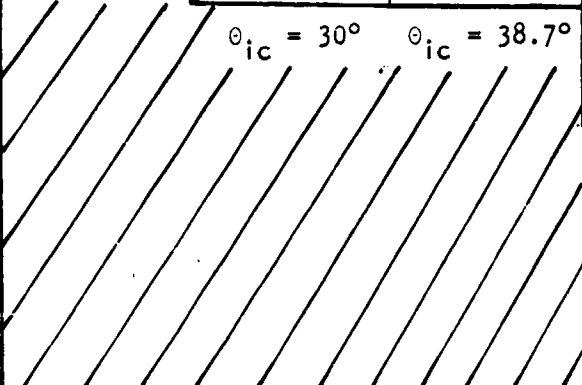
In Table B-3,  $\theta_{ec}$  and  $\theta_{ic}$  are computed for a set of  $M_1$  and  $M_2$  for constant temperatures or adiabatic speed of sound with  $c_1 = c_2 = c_3 = 344.5$  m/s and  $M_3 = 0$ .

TABLE B-3

$M_1$	$M_2$	$\theta_{EC}$	$\theta_{ic}$
0	0	90.0°	90.0°
0	1.2	27.0°	27.0°
0.4	0.6	38.7°	56.4°
0.8	0.9	31.8°	65.4°
0.8	1.2	27.0°	45.6°
0.8	1.4	24.6°	38.7°
1.2	1.4	24.6°	56.4°

Table B-4 shows the variation of  $\theta_E$  as a function of  $\theta_i$ , for a set of values for  $M_1$ . Again, the flow is assumed to be at ambient temperature with  $c_3 = c_1 = 344.5$  m/s.

TABLE B-4 VARIATION OF  $\theta_E$  WITH  $\theta_i$ 

$\theta_i$	$\theta_E$ ( $M_1=0$ )	$\theta_E$ ( $M_1=0.2$ )	$\theta_E$ ( $M_1=0.4$ )	$\theta_E$ ( $M_1=0.8$ )	$\theta_E$ ( $M_1=1.2$ )	$\theta_E$ ( $M_1=1.4$ )
0°	0°	0°	0°	0°	0°	0°
10	10°	9.7°	9.3°	8.8°	8.26°	8.0°
20	20°	18.7°	17.5°	15.6°	14.0°	13.4°
30	30°	$\theta_{ic} = 27.0^\circ$	24.6°	20.9°	18.2°	17.1°
40	40°	$\theta_{ic} = 30^\circ$		$\theta_{ic} = 38.7^\circ$	21.3°	19.8°
50	50°				23.5°	21.7°
60	60°				$\theta_{ic} = 56.4^\circ$	23.0°
70	70°					23.9°
80	80°					24.5°
90	90°					24.6°

In each column, the zones of silence are indicated by hatched areas.

Table B-5 shows the values of  $\theta_{ec}$  and  $\theta_{ic}$  (referred to the downstream axis) for all the test conditions covered in the present test program. It is to be noted that for constant Mach number and temperature of the primary jet, the effect of increasing the secondary Mach number or temperature is to increase the value of  $\theta_{ec}$ . Changing the temperature of the primary jet, however, affects only  $\theta_{ic}$ .

TABLE B-5  $\theta_{ic}$  AND  $\theta_{ec}$  VALUES\* FOR THE TEST CONDITIONS OF THE PRESENT PROGRAM

$M_1$	$M_2$	$T_{R1}$ (K)	$T_{R2}$ (K)	$\theta_{ic}$ (deg)	$\theta_{ec}$ (deg)
0.8	0.9	294.5	294.5	24.6	58.2
0.8	0.9	294.5	600.0	58.6	67.1
0.8	0.9	294.5	758.9	64.2	70.0
0.8	0.9	294.5	900.0	67.6	72.0
0.8	0.9	450.0	600.0	43.8	67.1
0.8	0.9	562.8	758.9	45.0	70.0
0.8	0.9	675.0	900.0	45.2	72.0
0.8	1.2	294.5	294.5	63.0	44.4
0.8	1.2	294.5	1080.0	63.2	69.5
0.8	1.2	294.5	1366.0	67.9	72.2
0.8	1.2	294.5	1620.0	70.9	74.1
0.8	1.2	810.0	1080.0	52.0	69.5
0.8	1.2	1013.0	1365.0	53.2	72.2
0.8	1.2	1215.0	1620.0	54.1	74.1
0.4	0.6	294.5	294.5	33.6	51.3
0.8	1.4	294.5	294.5	51.3	65.4
1.2	1.4	294.5	294.5	33.6	65.4
0	1.2	294.5	294.5	63.0	63.0

\*With respect to jet axis.

### B.3 AMPLITUDE AND PHASE CHANGES ACROSS MULTI-LAYER FLOW FIELDS

To determine the transmitted coefficient, that is the ratio of the amplitude and phase of the emergent field in terms of the amplitude and phase of the incident field, a matching of the pressures and normal displacements at the interfaces is necessary.

Since the normal velocity in any region of the fluid flow is given by the substantial derivative of the normal displacement, it follows that

$$\xi_Y^I = - \frac{j k_Y^I / k_1^2}{\rho_1 c_1^2 (1 - M k_X / k_1)^2} (A_i^I e^{-j k_Y^I y} - A_r^I e^{+j k_Y^I y}) e^{-j k_X x + j \omega t} \quad (B-23)$$

and  $A_r^I / A_i^I$  is the reflection coefficient at the inner layer, namely  $y = y_1$  see (Figure B.1).

Similarly in region II and III

$$\xi_Y^{II} = - \frac{j k_Y^{II} / k_2^2}{\rho_2 c_2^2 (1 - M_2 k_X / k_2)^2} \{ A_t^{II} e^{-j k_Y^{II} y} - A_{tr}^{II} e^{+j k_Y^{II} y} \} e^{-j k_X x + j \omega t} \quad (B-24)$$

$$\text{and } \xi_Y^{III} = - \frac{j k_Y^{III} / k_3^2}{\rho_3 c_3^2 (1 - M_3 k_X / k_3)^2} A_e^{III} e^{-j k_Y^{III} y} e^{-j k_X x + j \omega t} \quad (B-25)$$

At  $y = y_1$  the inner interface, the continuity of pressure and normal particle displacement lead to

$$A_i^I e^{-j k_Y^I y_1} + A_r^I e^{+j k_Y^I y_1} = A_t^{II} e^{-j k_Y^{II} y_1} + A_{tr}^{II} e^{+j k_Y^{II} y_1} \quad (B-26)$$

$$\begin{aligned} \text{and } A_i^I \sigma^I e^{-j k_Y^I y_1} - A_r^I \sigma^I e^{+j k_Y^I y_1} &= A_t^{II} \sigma^{II} e^{-j k_Y^{II} y_1} \\ &\quad - A_{tr}^{II} \sigma^{II} e^{+j k_Y^{II} y_1} \end{aligned} \quad (B-27)$$

$$\text{where } j^I = \frac{(k_Y^I / k_1^2)}{\rho_1 c_1^2 (1 - M_1 k_X / k_1)^2} \quad (B-28)$$

$$\text{and } \sigma^{II} = \frac{(k_Y^{II} / k_2^2)}{\rho_2 c_2^2 (1 - M_2 k_X / k_2)^2} \quad (B-29)$$

Similarly at  $y = y_2$

$$A_t^{II} e^{-jk_y^{II} y_2} + A_{tr}^{II} e^{+jk_y^{II} y_2} = A_\epsilon^{III} e^{-jk_y^{III} y_2} \quad (B-30)$$

and  $A_t^{II} \sigma^{II} e^{-jk_y^{II} y_2} - A_{tr}^{II} \sigma^{II} e^{+jk_y^{II} y_2} = A_\epsilon^{III} \sigma^{III} e^{-jk_y^{III} y_2} \quad (B-31)$

where  $\sigma^{III} = \frac{k_y^{III}}{\rho_3 c_3^2 k_3^2 (1 - M_3 k_x/k)^2} \quad (B-32)$

From equations (B-30) and (B-31)

$$A_{tr}^{II} = A_t^{II} \left[ \frac{\sigma^{II} - \sigma^{III}}{\sigma^{II} + \sigma^{III}} \right] e^{-jk_y^{II} 2y_2} \quad (B-33)$$

and

$$A_t^{II} = A_\epsilon^{III} \left[ \frac{\sigma^{II} + \sigma^{III}}{2\sigma^{II}} \right] e^{-j[k_y^{III} - k_y^{II}] y_2} \quad (B-34)$$

then

$$A_{tr}^{II} = A_\epsilon^{III} \frac{\sigma^{II} - \sigma^{III}}{2\sigma^{II}} e^{-j(k_y^{III} + k_y^{II}) y_2} \quad (B-35)$$

Substituting (B-34) and (B-35) in (B-26), one obtains

$$\begin{aligned} A_i^I e^{-jk_y^I y_1} + A_r^I e^{+jk_y^I y_1} &= A_\epsilon^{III} \frac{\sigma^{II} + \sigma^{III}}{2\sigma^{II}} e^{-jk_y^{III} y_2 + jk_y^{II} h} \\ &+ A_\epsilon^{III} \frac{\sigma^{II} - \sigma^{III}}{2\sigma^{II}} e^{-jk_y^{III} y_2 - jk_y^{II} h} \end{aligned} \quad (B-36)$$

where  $h = y_2 - y_1$ .

Similarly substituting (B-34) and (B-35) in (B-27) one obtains

$$\begin{aligned} A_i^I \sigma^I e^{-jk_y^I y_1} - A_r^I \sigma^I e^{+jk_y^I y_1} &= A_\epsilon^{III} \frac{\sigma^{II} + \sigma^{III}}{2} e^{-jk_y^{III} y_2 + jk_y^{II} h} \\ &- A_\epsilon^{III} \frac{\sigma^{II} - \sigma^{III}}{2} e^{-jk_y^{III} y_2 - jk_y^{II} h} \end{aligned} \quad (B-37)$$

The amplitude of the emergent sound field  $A_e^{III}$  can be solved for in terms of the amplitude of the incident sound field by eliminating the reflected amplitude  $A_r^I$ .

This is done by multiplying equation (B-36) by  $\sigma^I$  and then adding equation (B-28) which then yields

$$(A_e^{III}/A_i^I) = 2 e^{j(k_y^{III} y_2 - k_y^I y_1)} / (f_1 + j f_2) \quad (B-38)$$

where 
$$f_1 = \frac{\sigma^I + \sigma^{III}}{\sigma^I} \cos k_y^{II} h \quad (B-39)$$

and 
$$f_2 = \frac{\sigma^I \sigma^{III} + \sigma^{II} \sigma^{II}}{\sigma^I \sigma^{II}} \sin k_y^{II} h \quad (B-40)$$

Equation (B-38) expresses the amplitude and phase of the *emergent* sound field in terms of the amplitude and phase of the incident field and in terms of its directionality and frequency and the Mach numbers of the intermediate layers.

#### Evaluation of $f_1$ , $f_2$ and $k_y^{II}$

From equation (B-28)

$$\sigma^I = \frac{1}{\rho_1 c_1^2} \frac{k_y^I}{\bar{k}_1^2} = \frac{1}{\rho_1 c_1^2} \frac{k_y^I}{\bar{k}_1} \frac{1}{\bar{k}_1} \quad (B-41)$$

Now 
$$\frac{k_y^I}{\bar{k}_1} = \cos \theta_i, \quad \bar{k}_1 = k_1 (1 - M_1 k_x/k_1) \quad (B-42)$$

Since  $k_x = k_1 (1 - M_1 k_x/k_1) \sin \theta_i$ , it follows that

$$\frac{k_x}{k_1} = \frac{\sin \theta_i}{1 + M_1 \sin \theta_i} \quad (B-43)$$

$$\bar{k}_1 = k_1 \left( 1 - \frac{M_1 \sin \theta_i}{1 + M_1 \sin \theta_i} \right) = \frac{k_1}{1 + M_1 \sin \theta_i} \quad (B-44)$$

then 
$$\sigma^I = \frac{1}{\rho_1 c_1^2} \frac{\cos \theta_i}{\bar{k}_1} (1 + M_1 \sin \theta_i) \quad (B-45)$$

Similarly, it can be shown that

$$\sigma^{II} = \frac{1}{\rho_2 c_2^2} \frac{\cos \theta_t}{k_2} (1 + M_2 \sin \theta_t) \quad (B-46)$$

and

$$\sigma^{III} = \frac{1}{\rho_3 c_3^2} \frac{\cos \theta_e}{k_3} (1 + M_3 \sin \theta_e) \quad (B-47)$$

Thus

$$\begin{aligned} f_1 &= \left(1 + \frac{\sigma^{III}}{\sigma^{II}}\right) \cos k_y^{II} h \\ &= \left[1 + \frac{\rho_1 c_1^2}{\rho_3 c_3^2} \frac{k_1}{k_3} \frac{\cos \theta_e}{\cos \theta_i} \left(\frac{1 + M_3 \sin \theta_e}{1 + M_1 \sin \theta_i}\right)\right] \cos(k_y^{II} h) \end{aligned} \quad (B-48)$$

and

$$\begin{aligned} f_2 &= \left(\frac{\sigma^{III}}{\sigma^{II}} + \frac{\sigma^{II}}{\sigma^{I}}\right) \sin k_y^{II} h \\ &= \left[\frac{\rho_2 c_2^2 k_2}{\rho_3 c_3^2 k_3} \frac{\cos \theta_e}{\cos \theta_t} \left(\frac{1 + M_3 \sin \theta_e}{1 + M_2 \sin \theta_t}\right) + \frac{\rho_1 c_1^2}{\rho_2 c_2^2} \frac{k_1}{k_2} \frac{\cos \theta_t}{\cos \theta_i} \left(\frac{1 + M_2 \sin \theta_t}{1 + M_1 \sin \theta_i}\right)\right] \sin k_y^{II} h \end{aligned} \quad (B-49)$$

Let

$$Z_{13} = \frac{\rho_1 c_1^2 k_1}{\rho_3 c_3^2 k_3} = \frac{\rho_1 c_1}{\rho_1 c_3} = \sqrt{\frac{\gamma_1}{\gamma_3}} \sqrt{\frac{T_3}{T_1}} \quad (B-50)$$

Similarly

$$Z_{23} = \sqrt{\frac{\gamma_2}{\gamma_3}} \sqrt{\frac{T_3}{T_2}} \quad (B-51)$$

and

$$Z_{12} = \sqrt{\frac{\gamma_1}{\gamma_2}} \sqrt{\frac{T_2}{T_1}} \quad (B-52)$$

then

$$f_1 = \left\{1 + Z_{13} \frac{\cos \theta_e}{\cos \theta_i} \left(\frac{1 + M_3 \sin \theta_e}{1 + M_1 \sin \theta_i}\right)\right\} \cos k_y^{II} h \quad (B-53)$$

and

$$f_2 = \left[ Z_{23} \frac{\cos \theta_c}{\cos \theta_t} \left\{ \frac{1 + M_2 \sin \theta_c}{1 + M_2 \sin \theta_t} \right\} + Z_{12} \frac{\cos \theta_t}{\cos \theta_i} \left\{ \frac{1 + M_2 \sin \theta_t}{1 + M_1 \sin \theta_i} \right\} \right] \sin k_y^{II} h \quad (B-54)$$

Note if  $\theta_i = \pm\pi/2$ ,  $\cos \theta_i = 0$ ,  $k_y^I = 0$  or  $\sigma^I = 0$  and  $f_1$  and  $f_2$  suffer a singularity at  $\theta_i = \pm\pi/2$ . For calculation purposes singularity is avoided by making  $\theta_i$  not exactly  $\pm\pi/2$ .

Now  $\theta_c$  and  $\theta_t$  can be computed in terms of  $\theta_i$  from equations (B-16) and (B-17).  $k_y^{III}$  is evaluated from:

$$k_y^{II} = k_2 \left[ (1 - M_2 k_x/k_2)^2 - (k_x/k_2)^2 \right]^{1/2} = k_2 \frac{\cos \theta_t}{(1 + M_2 \sin \theta_t)} \quad (B-55)$$

Similarly, 
$$k_y^I = \frac{K_1 \cos \theta_i}{(1 + M_1 \sin \theta_i)} \quad (B-56)$$

and 
$$k_y^{III} = \frac{K_3 \cos \theta_c}{(1 + M_3 \sin \theta_c)}$$

Thus,  $f_1$ ,  $f_2$  and  $k_y^I$ ,  $k_y^{II}$ ,  $k_y^{III}$  can be evaluated in terms of  $\theta_i$ ,  $M$ ,  $M_2$ ,  $(c_2/c_1)$  and  $(c_3/c_1)$ . Hence,  $A_c^{III}/A_i^I$ .

Effects of varying  $M_2$  for fixed values of  $M_1$ , namely 0.4, 0.8 and 1.2 on  $A_c^{III}/A_i^I$  as calculated from equation (B-38) are plotted in figure B.3. Both streams are assumed to be unheated. Sharp decrease in the values of  $A_c^{III}/A_i^I$  at low and high values of  $\theta_i$  is caused by the total internal reflection phenomena. For values of up to  $\theta_i < 80^\circ$  (with respect to the jet axis) neither  $M_1$  nor  $M_2$  appear to have a strong influence on the transmitted to incident ratio. For values of  $\theta_i \geq 120^\circ$  (with the jet axis), however, these ratios are almost independent of  $M_2$  but decrease considerably with increasing values of  $M_1$ . Also, note that in the regions of total internal reflection the above ratios have finite values instead of being zero as expected from ray acoustics. The sound reaching the zone of silence in this case is actually due to diffraction, and hence has a finite value.

In the analysis presented so far, the sound rays cross two interfaces before reaching layer III. Thus, the results for amplitude changes are strictly applicable for the case when the source is located in the zone in our coaxial-nozzle system. To extend the analysis to source located in the jet, whereby the sound rays cross only one interface, all parameters in the layer I are made equal to the corresponding parameters in layer II (i.e.  $M_1 = M_2$ ,  $T_1 = T_2$  and  $h = y_2 - y_1$  is made equal to zero. It is found that the expression  $A_c^{III}/A_i^{II}$  is then given by



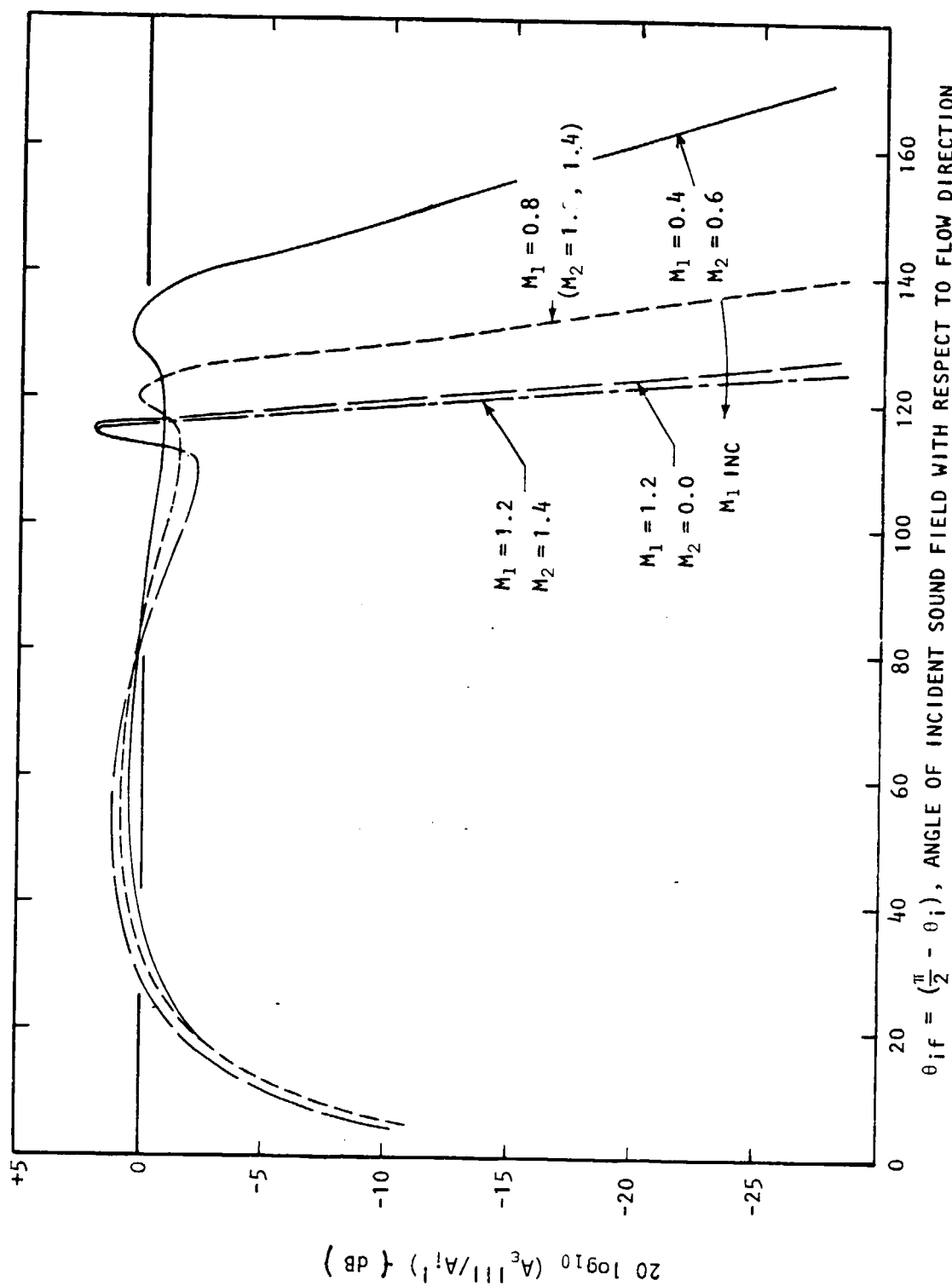


Figure B.3 Effects of  $M_2$  for fixed  $M_1 = 0.4, 0.8$  and  $1.2, T_R = 294K$  (ambient).

$$\frac{A_{\epsilon}^{|||}}{A_i^{||}} = \frac{2}{f_1} e^{jy_2} \left( \frac{k_3 \cos \theta_{\epsilon}}{1 + M_3 \cos \theta_{\epsilon}} - \frac{k_2 \cos \theta_i}{1 + M_2 \sin \theta_i} \right) \quad (B-56)$$

Thus, the amplitude of the transmitted to incident sound is calculated from

$$\frac{A_{\epsilon}^{|||}}{A_i^{||}} = \frac{2}{f_1} \cdot \quad (B-57)$$

## APPENDIX C

### ANALYTICAL STUDIES OF THE ACOUSTIC PROPERTIES OF CONVERGING CONICAL NOZZLES IN THE ABSENCE OF MEAN FLOW

## C.1 INTRODUCTION

The acoustic properties of a conical nozzle like those of a straight pipe can be characterized by parameters such as the far-field directivity, the radiation impedance and the reflection coefficient spectra. Such acoustic properties can be influenced by the mean flow and its gradients as well as the nozzle geometric properties such as the convergence angle  $\theta_0$ , the exit radius which can be combined with the sound frequency in the form of a non-dimensional frequency parameter  $kR_j$ , and the ratio of the nozzle length to the nozzle radius.

Of particular interest in this study is the influence of the angle of convergence on all three of the above mentioned acoustic parameters. Except in the case of no mean flow, the nozzle angle of convergence effect cannot be explicitly isolated for it also affects the mean flow field, which in turn affects the acoustic properties. *This analysis is restricted to the case of no mean flow.*

For nozzles with small angles of convergence, it may be expected that the acoustic properties will not differ markedly from those of a straight pipe which have been studied initially by Levine and Schwinger (ref. 2.5) and Ando (ref. 2.7). The analysis described below makes use of an extension of the method of spherical harmonics. This is then used to study the effects of angle of convergence on the acoustic near- and far-fields by comparing the far-field directivity, the acoustic radiation impedance and the reflection coefficient for three nozzles with angles of convergence equal to 6, 10, and 20 degrees. These results are also compared with data derived from the measurements described in earlier sections of this report.

## C.2 ANALYTICAL APPROACH

The acoustic reflection coefficient of a nozzle, like that of a straight pipe orifice, is a measure of the relative mismatch between the acoustic properties (including boundary conditions) inside and outside the nozzle. Inside a conical nozzle the rigid conical surface constrains the sound field in such a manner that a "plane" incident wave propagates with a curved (segment of a spherical surface) wave front will amplify as the wave propagates to the nozzle exit, following inverse square law (from virtual origin) relationship. At the nozzle exit, reflection back into the nozzle and diffraction to the far field take place. The diffracted near- and far-field is a function of the outer surface condition of the nozzle and its angle of convergence as well as the phase variation across the nozzle exit plane of the incident wave.

The present analysis is a study of the influence of the nozzle convergence angle,  $\theta_0$ , on the diffracted field, and the radiation impedance. The "plane" reflection coefficient is computed from the corresponding radiation.

radiation impedance taking into account the angle of convergence of the inner surface of the nozzle.

Consider an infinite convergent conical nozzle of half angle  $\theta_0$  as shown in Figure C.1.

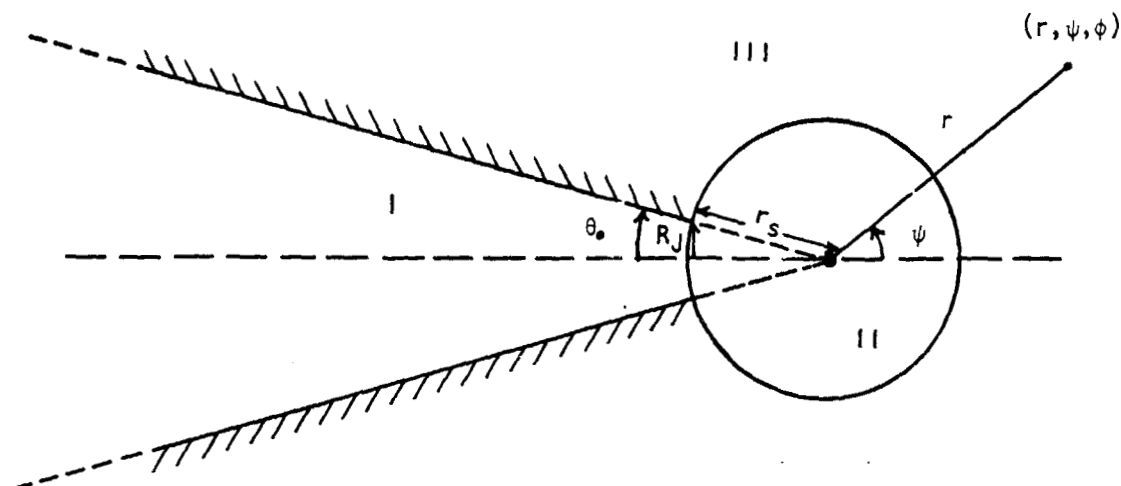


Figure C.1 Nozzle geometry and the coordinate system.

If a spherical surface of radius  $r_s = R_J / \sin \theta_0$  (where  $R_J$  is the nozzle exit radius) is drawn with center at the virtual origin of the nozzle, three acoustic regions can be distinguished. The incident and reflected sound field are restricted to region III. Region II corresponds to an intermediate region in which the input sound field,  $(\pi - \theta_0) < \psi < \pi$ , is radiated and diffracted to far field in the range  $0 < \psi < (\pi - \theta_0)$ .

The sound in each of the three regions can be advantageously expressed by a modified form of spherical harmonic analysis due to the fact that the nozzle surfaces (inner and outer) are coincident with those of a spherical coordinate system. For example, in regions I, II and III, assuming the sound field to be axisymmetric, the temporal Fourier transform of the acoustic pressure can be expressed in the following forms.

$$P^I(r, \psi, \omega) = \left\{ A_0 h_0^{(1)}(z) + \sum_m B_m h_m^{(2)}(z) \right\} n(q_m \psi) e^{j\omega t} \quad (C-1)$$

$$P^{II}(r, \psi, \omega) = \sum_k D_k L_k(\theta) j_k(z) e^{j\omega t} \quad (C-2)$$

$$P^{III}(r, \psi, \omega) = \sum_{\ell} E_{\ell} Q_{\ell}(z) \Lambda(\beta_{\ell} \psi) e^{j\omega t} \quad (C-3)$$

In equation (C-1) above,  $n(q_m\psi)$  represents the transverse distribution of the pressure field in the nozzle;  $n(q_m\psi) \rightarrow J_0(q_m\psi)$  (Bessel function of zero order) as the nozzle inner surface angle of convergence tends to zero; and the deviation between  $n(q_m\psi)$  and  $J_0(q_m\psi)$  is very slight even for  $\theta_0$  as high as  $20^\circ$ . For plane waves,  $q_0 = 0$ . The first term inside the bracket of equation (C-1) corresponds to a plane spherical wave converging towards the nozzle exit and represents the incident wave. The reflected waves are represented in general by a set of non-integral Hankel functions, except for the plane wave ( $q_0 = 0$ ). The function  $L_k(\psi)$  in equation (C-2) is the Legendre polynomial of integral order, for in region II, the sound field extends in the range  $0 < \psi < \pi$ . Also, because region II contains the virtual origin,  $j_k(z)$  is the spherical Bessel function expressing the radial variation of the sound field. In region III, since  $\theta$  is restricted to  $0 < \psi < (\pi - \theta_0)$ ,  $\Lambda(\beta_\ell\psi)$  is a modified form of Legendre polynomial and  $Q_{\epsilon_\ell}$  is a correspondingly modified form of non-integral Hankel function.

In the above equations (C-1) through (C-3), the amplitude coefficient  $A_0$  is assumed specified and the other amplitude coefficients, namely  $B_m$ ,  $D_k$  and  $E_\ell$  need to be determined in terms of  $A_0$ . The other functions  $J_0(q_m\psi)$  and  $\ell(\beta_\ell\psi)$  are functions of only the nozzle inner and outer angles of convergence and for a given nozzle can therefore be computed once for all.

Equations (C-1) through (C-3) are subject to the following two sets of boundary conditions at interfaces of the three regions:

$$P^I(r_s, \psi) + P^{III}(r_s, \psi) = P^{II}(r_s, \psi) \quad (C-4)$$

and 
$$\frac{\partial P^I}{\partial z}(r_s, \psi) + \frac{\partial P^{III}}{\partial z}(r_s, \psi) = \frac{\partial P^{II}}{\partial z}(r_s, \psi) \quad (C-5)$$

By making use of the orthogonal properties of  $L_k(\psi)$  and  $\Lambda(\beta_\ell\psi)$  in their respective ranges, the ratio of  $D_k/A_0$  and  $E_\ell/A_0$  and  $B_k/A_0$  have been computed. Substituting these values back in equations (C-1) through (C-3) allows explicit evaluation of  $P^I(r, \psi)$  and  $P^{III}(r, \psi)$ , the acoustic near and far fields respectively in terms of the incident wave. On integration of  $P^{II}(r_s, \psi)$  over the nozzle exit plane allows evaluation of the radiation impedance. Such evaluations have been carried out for three nozzles and are discussed next.

### C.3 NUMERICAL RESULTS

#### Directivity

The three nozzles used in the numerical study have the following geometric properties. The length-to-nozzle-exit ratio is assumed infinite in each case, that is, there is no junction with a straight pipe. The half angles

of convergence are  $6.12^\circ$ ,  $10^\circ$  and  $20^\circ$ . The far field is computed at  $kr = 6kR_J / \sin\theta_0$ , where  $r$  is the spherical radial coordinate measured from the virtual origin, and  $R_J$  is the nozzle exit radius.

Figure C.2 shows the effect of nozzle convergence angle  $\theta_0$  on the computed far-field directivity for a nondimensional frequency of  $kR_J = 1.85$ . The corresponding directivities for sound radiated from a baffled and an unbaffled straight pipe based on Kirchhoff's and Levine and Schwinger's analysis are also shown. The main observation is that as the angle of nozzle convergence increases, the SPL at any angle does not drop (relative to that on the axis) as much as that for the unbaffled straight pipe. In other words the beam width increases with nozzle angle. In the rear arc ( $0 - 90^\circ$ ), the SPL radiated by the  $6^\circ$  nozzle is similar to the unbaffled straight pipe to within half a decibel. In the forward arc, the deviation is of the order of one decibel. These deviations increase as the nozzle angle of convergence increases. Although the directivity for the baffled straight pipe should not strictly be used for comparison for reasons discussed later, it does appear to provide an upper limit.

Figure C.2 shows the far-field directivities for these three nozzles for three other frequencies, namely  $kR_J = 2.5$ ,  $1.4$  and  $0.5$ . For the two higher frequencies the effects of nozzle convergence angle is similar to those for the case of  $kR_J = 1.85$  already discussed above. For the low frequency case, the effect seems to suggest the existence of a critical frequency at which sensitivity to nozzle convergence is unimportant.

#### Comparison With Measurement

Although the analysis does not account for the effect of a shoulder (junction with a straight pipe) on the acoustic far field, a comparison with a set of measured directivities for nozzles of finite lengths may not be too inappropriate. Figure C.4 shows two sets of data corresponding to radiation from a straight pipe and a  $6^\circ$  convergent conical nozzle (radii 4 and 2 inches and length 10.25 inches). As indicated earlier, the difference between an unflanged straight pipe and a  $6^\circ$  nozzle is very small especially in the rear arc. Although this comparison is good but is not adequate to confirm the trends predicted by the numerical analysis.

#### Radiation Impedances

Figures C-5 and C-6 show the influence of nozzle angle on the radiation reactance spectra. The corresponding spectra for the radiation impedance from a baffled and an unbaffled straight pipe are also included for comparison. One observation is that in the low frequency range *the radiation resistance is significantly increased* compared to that of an unbaffled straight pipe. The baffled straight pipe spectrum seems to be higher in the low frequency range and in the relatively higher frequency range seems to be lower than the  $10^\circ$ - and  $20^\circ$ -degree nozzles.

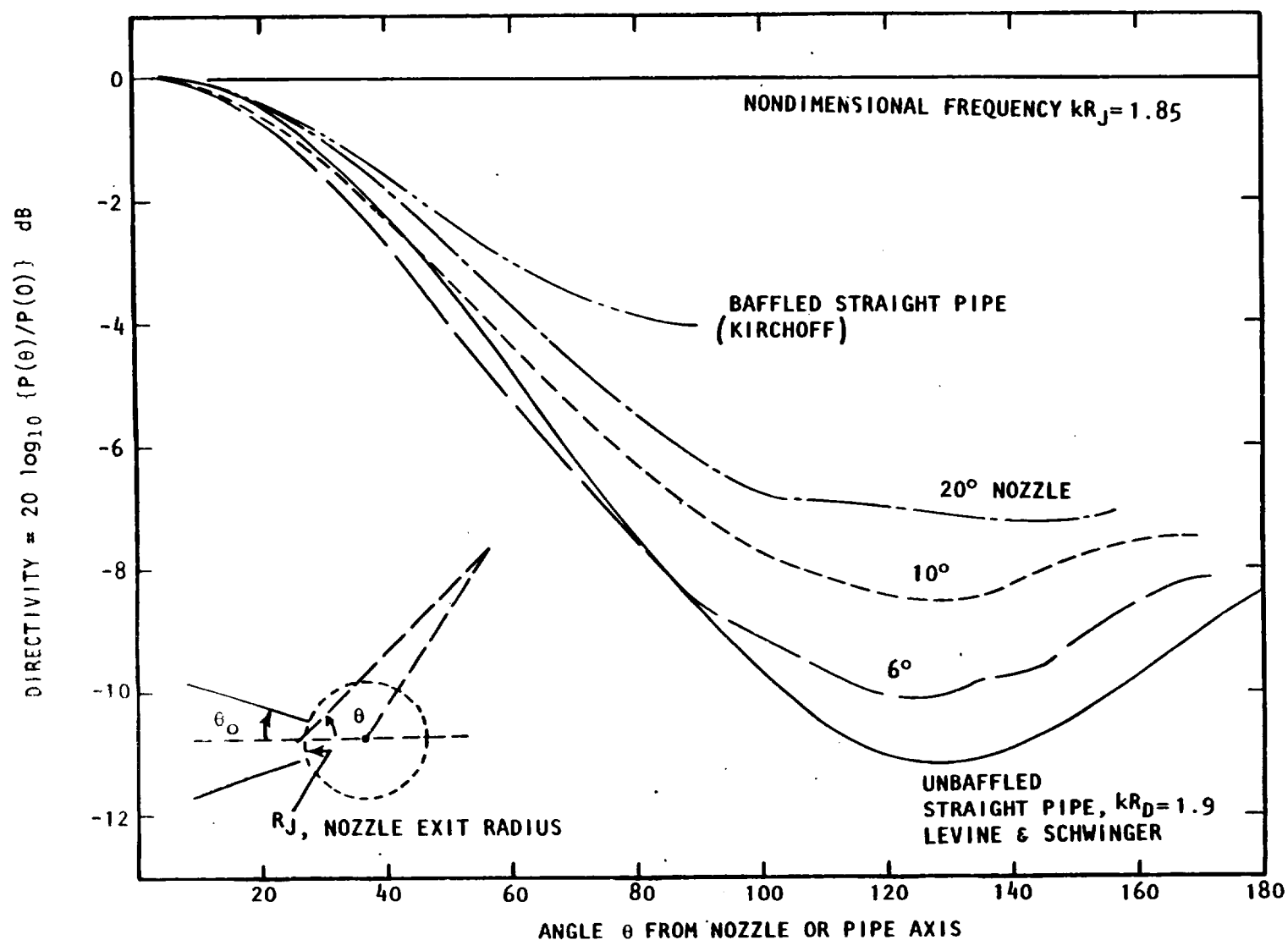


Figure C.2 Effect of nozzle convergence angle  $\theta_0$  on far-field SPL (numerical analysis) and comparison with baffled and unbaffled straight pipe solutions.



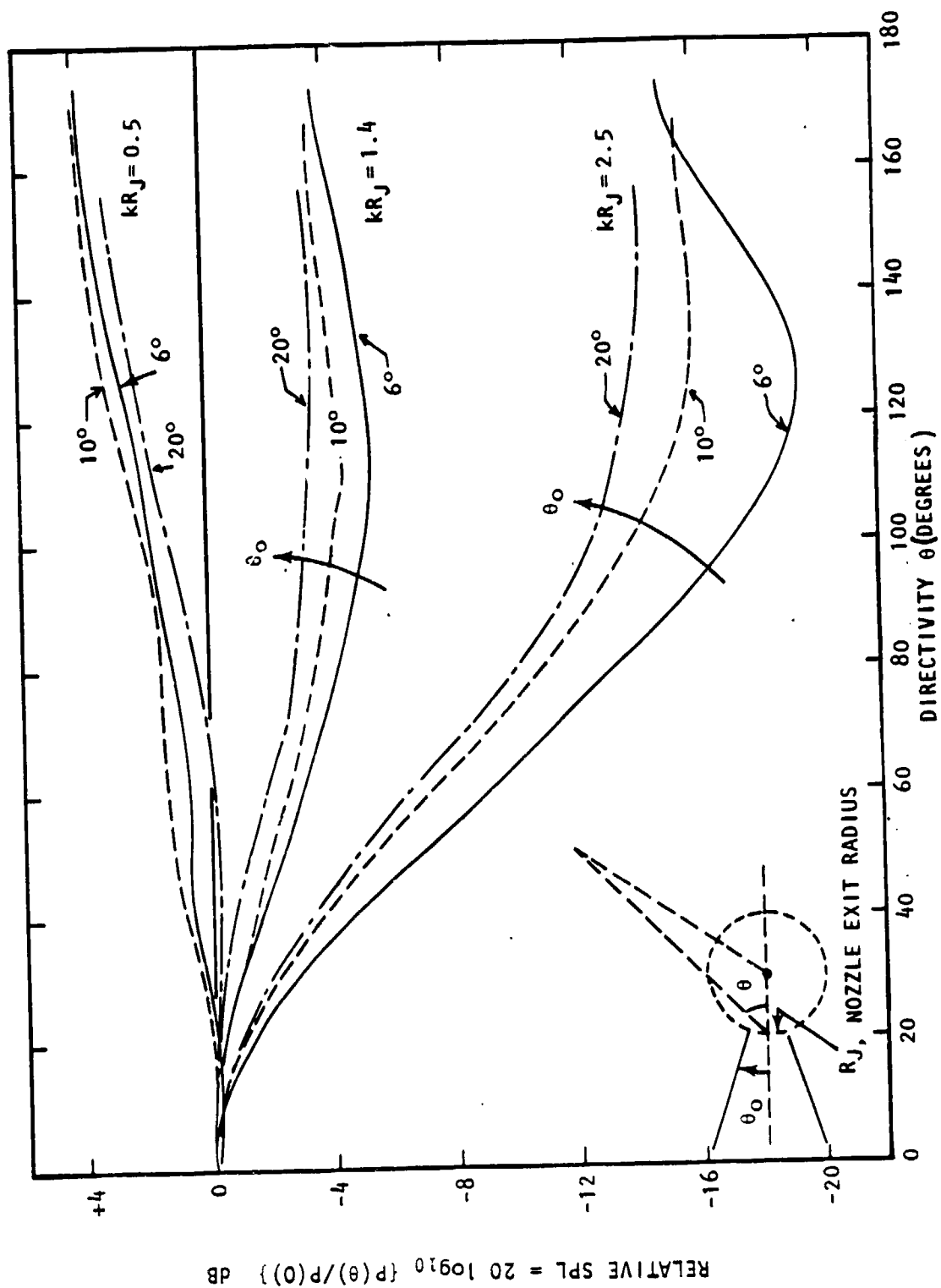


Figure C.3 Effect of nozzle angle of convergence  $\theta_0$  on acoustic far-field directivity for three nondimensional frequencies.

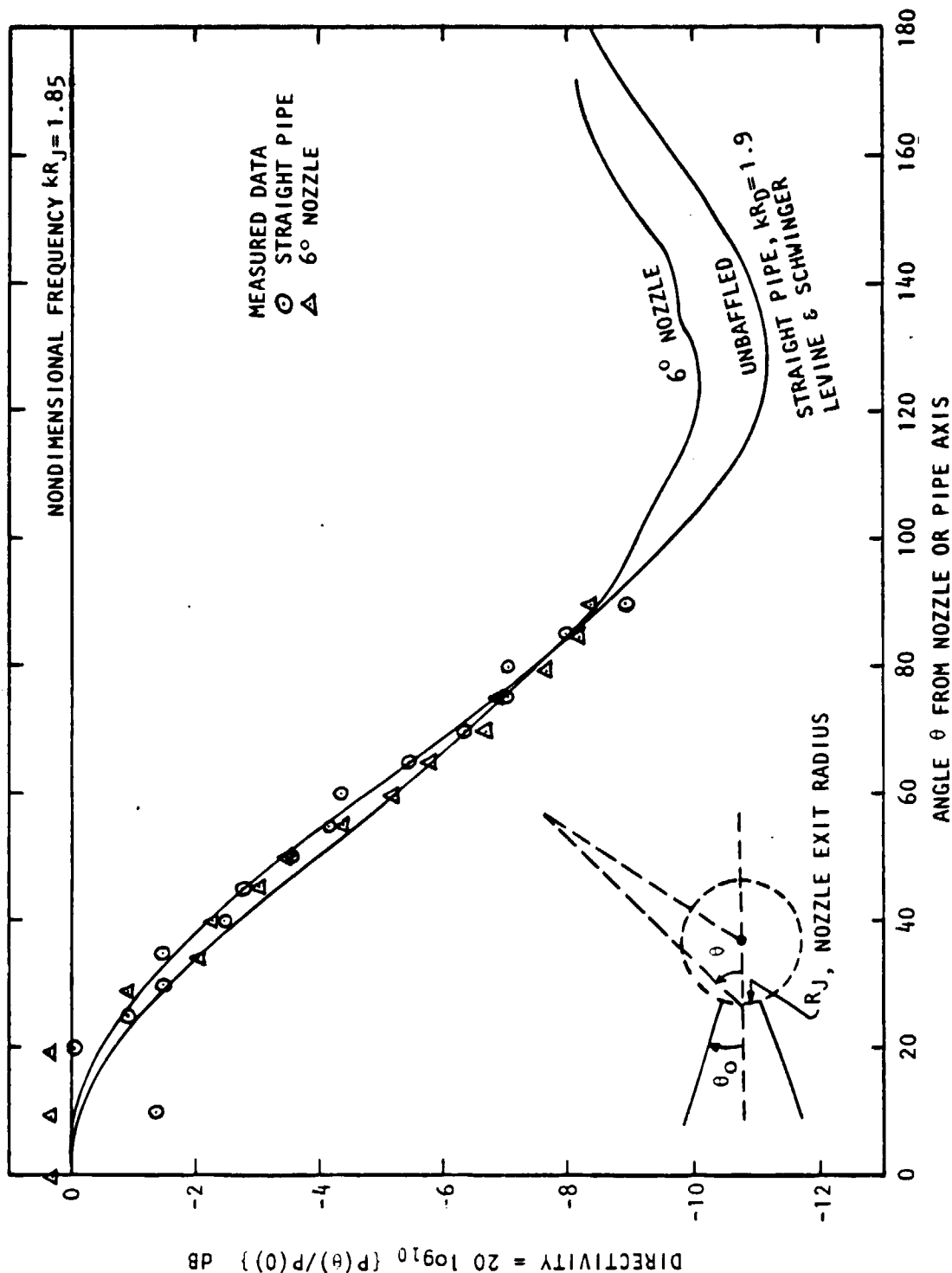


Figure C.4 Comparison of measured directivity for a straight pipe and a 6° nozzle with present analysis (for 0° and 6° nozzles) and that of Levine and Schwinger for straight pipe.

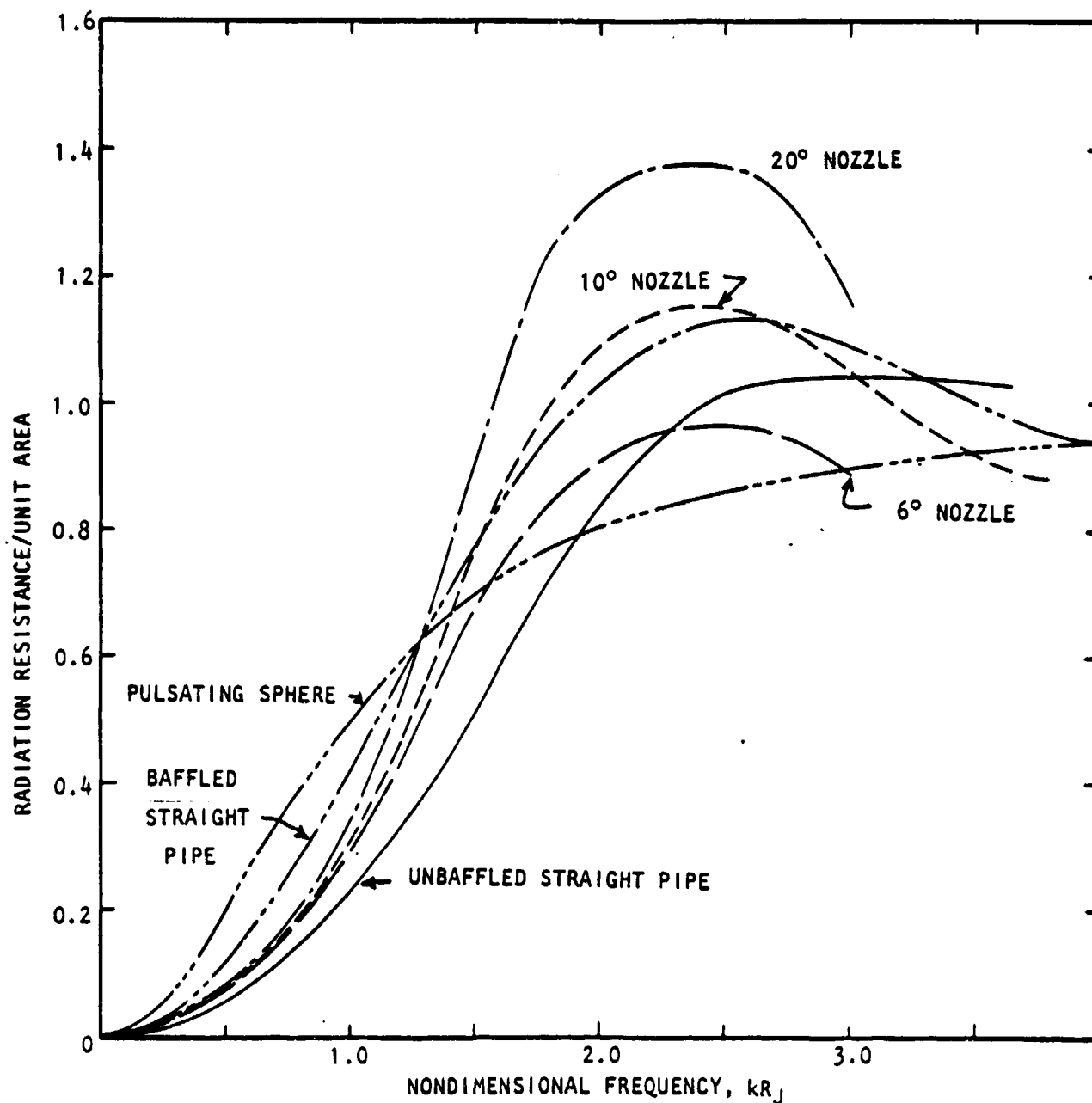


Figure C.5 Computed effects of conical nozzle convergence angle on the acoustic radiation resistance spectrum of nozzle orifice and comparison with corresponding solutions for baffled and unbaffled straight pipes (Kirchoff and Levine & Schwinger, respectively).

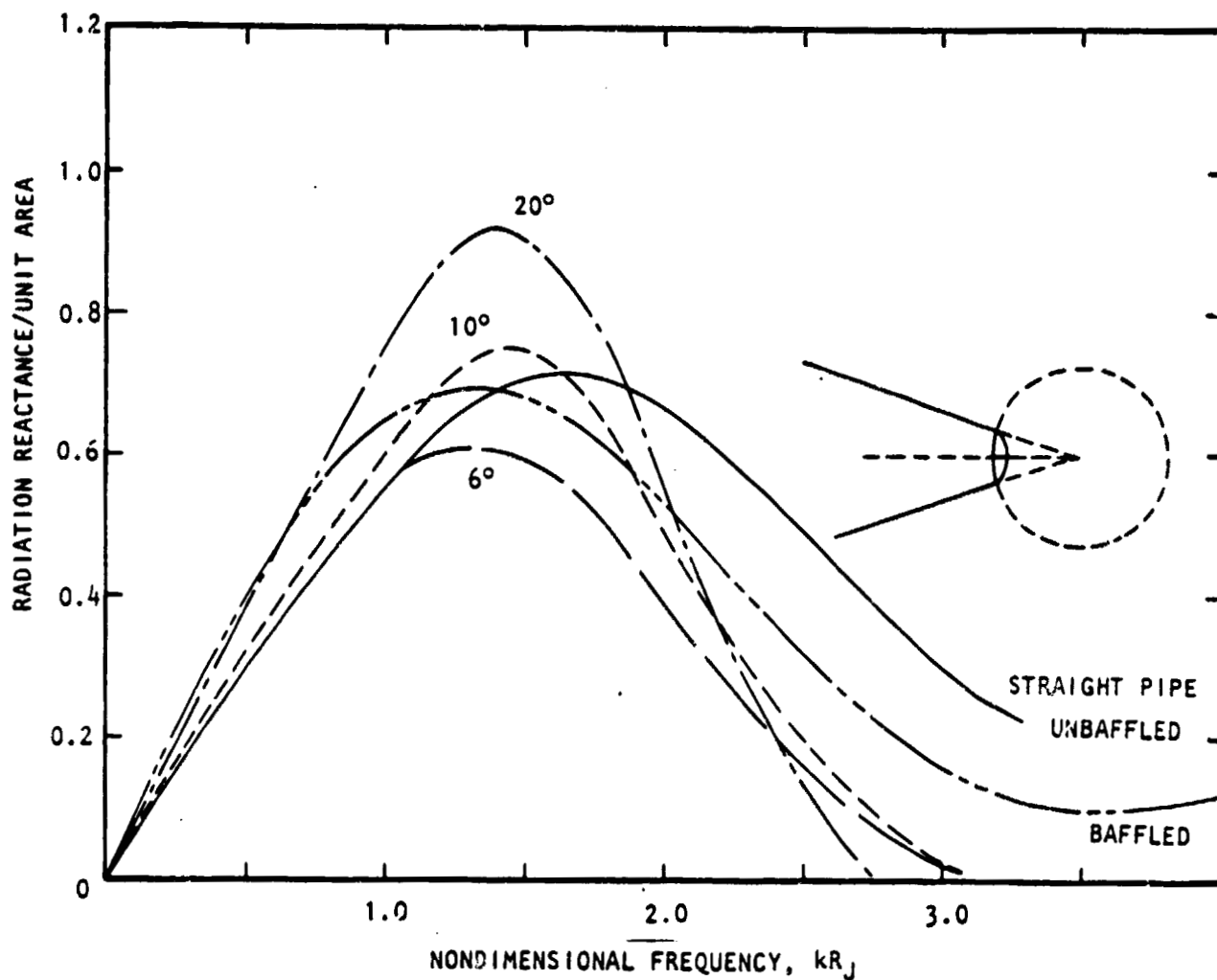


Figure C.6 Computed effects of conical nozzle convergence angle on the acoustic *radiation reactance* spectrum of nozzle orifice and comparison with corresponding solutions for baffled and unbaffled pipes (Kirchoff and Levine and Schwinger, respectively).

Like the far-field directivity plot, one would have expected the baffled pipe radiation resistance to be the upper limit as the nozzle angle is increased. The expectation is unjustified for the simple reason that in the conical nozzle case, the *velocity fluctuation* at the nozzle exit is *distributed across a curved surface* whose origin is the nozzle virtual origin; in the baffled straight pipe case, the velocity fluctuations are parallel and along the pipe axis. The curved velocity distribution in the nozzle case apparently must give rise to some form of focussing. In the *near field*, this focussing effect is opposed by acoustic spreading due to diffraction. On the other hand, in the *far field* (in the present analysis, this is six times the focal length which may be defined as the distance from the nozzle exit plane to the virtual origin), the two effects add together giving rise to increased spreading as already shown in figures C.2 and C.3.

In figure C.6 relative to the radiation reactance spectrum of an unbaffled straight pipe, the corresponding spectra for the nozzles are higher in the low frequency range and lower in the high frequency range. The 6° nozzle spectrum in the low frequency range is in fact identical to that of the unflanged straight pipe. Another point of observation is that at the higher frequency of  $kR_j = 3.0$ , and for the 20° nozzle, the radiation reactance is negative. This could be due to a resonant effect of the sound field in the imaginary spherical "cavity". A confirmation of this has not been made but could be done by computing the sound field distribution inside the cavity and will be investigated later.

#### The Acoustic Reflection Coefficient

The reflection coefficient,  $\sigma$ , is related to the normalized radiation impedance  $Z_R$ . For a straight pipe, the well-known relation for plane wave reflection is given by

$$\sigma_{\text{pipe}} = \frac{Z_R - 1}{Z_R + 1} \quad (\text{C-6})$$

In a conical nozzle, when account is taken of the variation of the amplitude during propagation, it can easily be shown that

$$\sigma_{\text{nozzle}} = \frac{Z_R - 1 + j Z_R \sin \theta_0 / kR_j}{Z_R + 1 - j Z_R \sin \theta_0 / kR_j} \quad (\text{C-7})$$

Making use of the computed radiation impedance spectra of figures C.5 and C.6, the spectrum of the amplitude of the reflection coefficient has been evaluated using equation (C-7) and are shown in figure C.7. For comparison the reflection coefficient for an unbaffled straight pipe as computed by Levine and Schwinger (ref. 2.5) is also included. The only point of observation is that in the low frequency range the amplitude of the reflection is not too sensitive to the convergence angle of the nozzle.

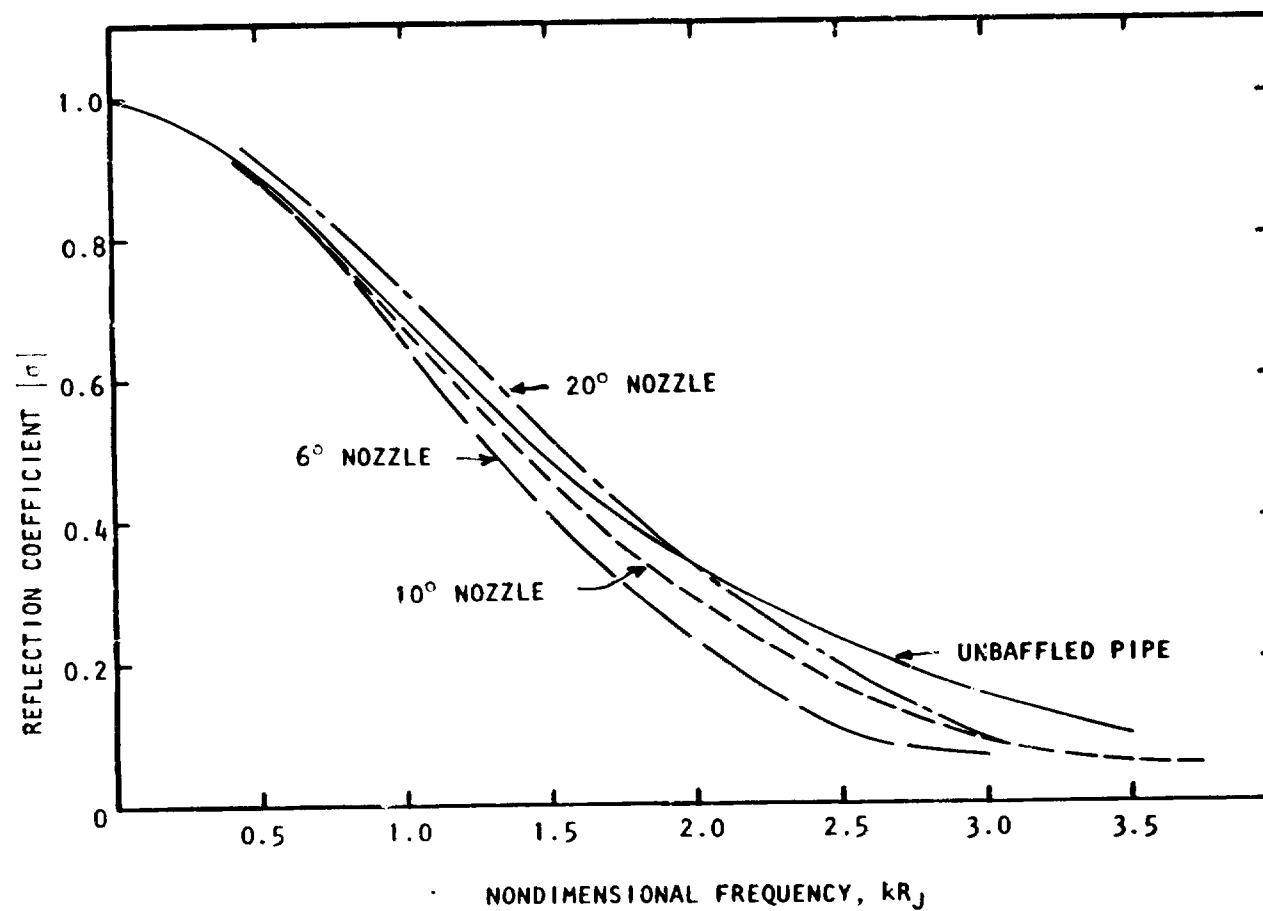


Figure C.7 Influence of angle of convergence of conical nozzle on acoustic reflection coefficient.

#### C.4 CONCLUSIONS

The principal results are as follows:

- (1) The far-field directivity radiated from a  $6^\circ$  nozzle is similar to that from a straight pipe orifice to within half a decibel in the rear arc and about one decibel in the forward arc.
- (2) As the nozzle angle of convergence ( $\theta_0$ ) is increased the SPL relative to that on the nozzle axis increases at all frequencies except at the lowest frequency case  $kR_j = 0.46$ .
- (3) The limited comparisons between the predicted and the measured acoustic far-field directivities are good.
- (4) In the low frequency range,  $kR_j < 2.25$ , the radiation resistance spectrum of the nozzle ( $6^\circ$ ,  $10^\circ$ ,  $20^\circ$ ) is higher than that of an un baffled straight pipe and rises as  $\theta_0$  is increased. For frequencies higher than critical values  $kR_j > 2.25$  for  $6^\circ$  nozzle,  $kR_j > 7.75$  for  $10^\circ$  nozzle and  $kR_j > 3.75$  for  $20^\circ$  nozzle, the corresponding radiation resistance is lower than that of an un baffled straight pipe.
- (5) The radiation reactance spectrum for the  $6^\circ$  nozzle is identical to the un baffled straight pipe up to  $kR_j = 1.1$ , and is lower at higher frequencies. The corresponding values for the  $10^\circ$  and  $20^\circ$  nozzles are higher than the  $6^\circ$  nozzle up to  $kR_j = 2.4$ , ( $20^\circ$  nozzle being highest). At frequencies greater than  $kR_j = 1.7$  for the  $10^\circ$  nozzle and  $kR_j = 1.9$  for the  $20^\circ$  nozzle, the radiation reactance of each nozzle is lower than that of the straight pipe.
- (6) The amplitude of reflection coefficient in the low frequency range is not very sensitive to the nozzle convergence angle.
- (7) Relative to a straight pipe, the nozzles radiate somewhat more acoustic power in the low frequency range and less at higher frequencies.

## APPENDIX D

### SYMBOL LIST

A, B	constants appearing in equation (A-12)
$A_D$	duct area
$\bar{c}$	local speed of sound
$\bar{c}_0$	stagnation speed of sound
D	diameter
f	frequency, Hz
h	annulus height
j	$\sqrt{-1}$
k	wave number, $2\pi f/\bar{c}$
$k_0$	wave number based on $\bar{c}_0$ , $2\pi f/\bar{c}_0$
$\lambda, L$	length
M	mean flow Mach number
$M_D$	duct Mach number
$M_J$	jet Mach number
p	acoustic pressure
$p_i$	incident pressure wave
$p_r$	reflected pressure wave
$p_{rad}$	far-field acoustic pressure (radiated acoustic pressure)
R	resistance
$R_D$	duct radius
$R_J$	nozzle exit radius
$R_m$	far-field measurement radius
r	radial coordinate



$T$	temperature
$t$	time
$\bar{U}$	mean flow velocity
$u_r$	velocity perturbation along $r$
$W$	acoustic power
$X$	reactance
$x$	axial coordinate
$Z$	transfer impedance
$Z_R$	radiation impedance
$\alpha$	convergence angle for the outer nozzle
$\gamma$	specific heat ratio
$\lambda$	wavelength
$\rho$	density perturbation
$\bar{\rho}$	mean flow density
$\sigma$	reflection coefficient
$\theta$	far-field measurement angle (degrees) with the jet axis
$\theta_c$	angle of impulse wave front to duct wall
$\theta_o$	nozzle convergence angle
$( )'$	first derivative with respect to $r$ or $x$
$( )''$	second derivative with respect to $r$ or $x$

## REFERENCES

- 1.1. Matta, R. K. et al.: G.E. Core Engine Noise Investigation. FAA Report RD-77-3, February 1977.
- 1.2. Lowrie, B.: Rolls Royce Core Engine Noise Compared With Various Prediction Schemes. Presented at DOT/FAA Jet Noise/Core Noise Status Review, February 1977.
- 2.1. Chung, J. Y.: Cross-Spectral Method of Measuring Acoustic Intensity Without Error Caused by Instrument Phase Mismatch. *J. Acoust. Soc. America*, Vol. 64, No. 6, 1978, pp. 1613-1616.
- 2.2. Brown, W. H.; and Dean, P. D.: Evaluation of a Hot-Wire/Microphone Acoustic Intensity Probe. Lockheed Report LG79ER0093.
- 2.3. Otnes, R. K.; and Enochson, L.: *Digital Time Series Analysis*. John Wiley and Sons, 1972.
- 2.4. Kinsler, L. E.; and Frey, A. R.: *Fundamentals of Acoustics*. John Wiley and Sons, Second ed., 1962.
- 2.5. Levine, H.; and Schwinger, J.: On the Radiation of Sound from an Unflanged Pipe. *Phys. Rev.*, Vol. 75, No. 4, 1948, pp. 383-406.
- 2.6. Lansing, D. L. et al.: Radiation of Sound from an Unflanged Circular Duct with Flow. Paper presented at 79th Meeting of Acoust. Soc. of America, 1970.
- 2.7. Ando, Y.: On the Sound Radiation from Semi-Infinite Circular Pipe of Certain Wall Thickness. *Acustica* 22, 1969, pp. 219-225.
- 2.8. Mungur, P.; and Plumblee, H. E.: Influence of the Jet Exhaust Flow Field on the Acoustic Radiation Impedance of a Jet Pipe Opening. AIAA Paper 79-0676, Presented at AIAA 5th Aeroacoustics Conf., Seattle, 1979.
- 2.9. Pinker, R. A.; and Bryce, W. D.: The Radiation of Plane Wave Duct Noise from a Jet Exhaust, Staticallly and in Flight. AIAA Paper No. 76-581, 1976.
- 3.1. Burrin, R. H.; and Tanna, H. K.: The Lockheed-Georgia Coannular Jet Research Facility. Lockheed Report LG77ER0243.
- 3.2. Shields, F. D.; and Bass, H. E.: Atmospheric Absorption of High Frequency Noise and Application to Fractional-Octave Bands. NASA CR-2760, 1977.

- 4.1 Dean, P. D., et al.: Studies of the Acoustic Transmission Characteristics of Coaxial Nozzles with Inverted Velocity Profiles, NASA CDR- (to be assigned).

1. Report No. NASA CR-159698		2. Government Accession No.		3. Recipient's Catalog No.	
4. Title and Subtitle STUDIES OF THE ACOUSTIC TRANSMISSION CHARACTERISTICS OF COAXIAL NOZZLES WITH INVERTED VELOCITY PROFILES - Volume I				5. Report Date May 1979	
				6. Performing Organization Code	
7. Author(s) P. D. Dean, M. Salikuddin, K. K. Ahuja, H. E. Plumblee, and P. Mungur				8. Performing Organization Report No. LG 79 ERD17B	
9. Performing Organization Name and Address  Lockheed-Georgia Company Marietta, Georgia 30063				10. Work Unit No.	
				11. Contract or Grant No. NAS3-20797	
12. Sponsoring Agency Name and Address  National Aeronautics and Space Administration Washington, D. C. 20546				13. Type of Report and Period Covered  Contract Report	
				14. Sponsoring Agency Code	
15. Supplementary Notes Final Report. Project Manager, A. M. Karchmer, V/STOL and Noise Division, NASA-Lewis Research Center, Cleveland, Ohio. Lockheed Program Manager, H. E. Plumblee, Jr.					
16. Abstract An experimental study to determine the efficiency of internal noise radiation through coannular exhaust nozzle with an inverted velocity profile was conducted. A preliminary investigation was first undertaken (1) to define the test parameters which influence the internal noise radiation, (2) to develop a test methodology which could realistically be used to examine the effects of the test parameters, and (3) to validate this methodology. The result was the choice of an acoustic impulse as the internal noise source in the jet nozzles. Noise transmission characteristics of a coannular nozzle system were then investigated. In particular, the effects of fan nozzle convergence angle, core extension length to annulus height ratio and flow Mach numbers and temperatures were studied. The results are presented as normalized directivity plots.					
17. Key Words (Suggested by Author(s)) Acoustic Measurements, Acoustic Sources, Duct Acoustics, Electric Spark, Engine Noise, Gun Shot, Internal Noise, Inverted Velocity and Temperature Coaxial Jets, Impulse Noise, Multilayer Flow Nozzle Transfer Function, Refraction				18. Distribution Statement  Unclassified - Unlimited STAR Category 71	
19. Security Classif. (of this report)  UNCLASSIFIED		20. Security Classif. (of this page)  UNCLASSIFIED		21. No. of Pages 186	
22. Price*					